UNIVERSITÀ
DEGLI STUDI
DI BRESCIA

DOTTORATO DI RICERCA IN PRECISION MEDICINE

settore scientifico disciplinare CHIM/03

CICLO

XXXV

TITOLO TESI

Extracellular vesicle engineering across length scales

DOTTORANDA

Rossella Zenatelli

RELATORE

Prof. Paolo Bergese

CORRELATORI

Prof. Annalisa Radeghieri

Prof. Giuseppe Pomarico

Index

Chapter 1

Riassunto

1 Riassunto

I materiali nano ingegnerizzati sono materiali sintetici con proprietà e comportamenti unici che emergono su scale di lunghezza nanometriche (da 1 a 100 nm). Attualmente la ricerca su questo tipo di materiali è focalizzata sulla loro transizione biotecnologica e medica per la creazione di bio-nanomateriali. I bio-nanomateriali possono interagire attivamente con sistemi biologici a livello molecolare, cellulare, di organismo e di ecosistema. Tra le nano particelle organiche naturali, le vescicole extracellulari (EVs) sono tra le più studiate nano particelle all'interno del secretoma. Le EVs si sono naturalmente evolute per la comunicazione cellula-cellula, sono in grado di attraversare le barriere biologiche, come la barriera ematoencefalica, e trasportano vari tipi di biomolecole come proteine, lipidi e acidi nucleici. Queste caratteristiche le ha rese promettenti strumenti utilizzabili in applicazioni biomediche sia diagnostiche (es. biopsia liquida) che terapeutiche (sistemi di somministrazione di farmaci, agenti rigenerativi). Unire le proprietà di trasporto delle EVs e le proprietà uniche dei nanomateriali sintetici, le renderle sfruttabili per le applicazioni biomediche. Per affrontare queste transizione cruciale, nanomateriali multifunzionali, combinazioni tra nanomateriali sintetici e le vescicole extracellulari, possono generare nanomateriali ibridi di nuova generazione, utilizzati nella somministrazione di farmaci, nell'ingegneria dei tessuti e nella medicina rigenerativa che sfruttano sia le proprietà dei nanomateriali sintetici che le proprietà delle EVs.

Nella prima parte di questo progetto di dottorato, il lavoro è stato focalizzato nella produzione e caratterizzazione di nano particelle ibride (nanoparticelle super paramagnetiche e nanoparticelle lipidiche organiche sia naturali che sintetiche). L'identificazione di un protocollo per la sintesi e la caratterizzazione è fondamentale per poter verificare il caricamento. Dopo aver eseguito diversi protocolli di caricamento, la resa di produzione delle nanoparticelle ibride è stata verificata utilizzando due tecniche ortogonali: I) il trasferimento di energia per risonanza (FRET) e II) una versione modificata del saggio colorimetrico nanoplasmonico (CONAN). In particolare questo secondo saggio sfrutta le proprietà nanoplasmoniche delle nanoparticelle d'oro per valutare il rivestimento delle membrane biologiche sulle nanoparticelle sintetiche senza bisogno di nessun trattamento ulteriore (es. colorazione o marcatura).

Nella seconda parte di questo progetto di dottorato, il lavoro si è concentrato sull'ingegnerizzazione della superficie delle EVs finalizzata al "*targeting*" specifico contro un particolare sottotipo di tumore al seno. Per poter ingegnerizzare queste vescicole extracellulari è stato necessario ottimizzare i protocolli di produzione, isolamento e caratterizzazione da diverse sorgenti come linee cellulari, plasma, siero, e globuli rossi. In questo lavoro l'obbiettivo è quello di fornire conoscenze all'avanguardia sulla produzione, sull'isolamento, la caratterizzazione delle EVs. Inoltre, grazie agli innovativi metodi di "*targeting*" molecolare, realizzati tramite "*click chemistry*", la superficie delle vescicole extracellulari è modificata con molecole indirizzano le vescicole verso specifici bersagli. Su queste vescicole, la superficie è stata funzionalizzata con un anticorpo monoclonare chiamato Cetuximab, attualmente utilizzato in clinica per diversi tipi di tumori. La funzionalizzazione (attiva e passiva) è stata effettuata e valutata tramite diversi test funzionali come la risonanza plasmonica di superficie (su chip) e mediante stress test mitocondriale e prove di *uptake* cellulare (in vitro).

Chapter 2

Abstract

2 Abstract

Nanotechnological materials are synthetic materials with unique properties and behaviours that emerge on length scales from 1-100 nm. Research on this type of material is currently focused on their biotechnological and medical transition. These materials interact with biological systems at the molecular, cellular, organism and ecosystem levels. As natural organic nanoparticles, extracellular vesicles are the principal nano-exponents within the secretome. They evolved for cell-to-cell communication and carrying various biomolecules (e.g. proteins, lipids, and nucleic acids). Quickly, they emerged as promising nanoplatforms for many biomedical applications in diagnostics (e.g. liquid biopsy) and therapeutics (drug delivery systems, regenerative agents). Despite their enormous potential, their heterogeneity in size and surface composition, the high complexity of their biomolecular load and inefficient absorption by the recipient cells are the main obstacles to overcome to allow their translation into real biomedical applications. To address these crucial issues, multifunctional nanomaterials (e.g. superparamagnetic nanomaterials with their particular physical and chemical properties) can play fundamental roles by combining with the diagnostic and therapeutic properties of extracellular vesicles and generate next-generation hybrid nanomaterials, used in drug delivery, tissue engineering and regenerative medicine.

The goal is to provide cutting-edge knowledge on extracellular vesicle production, isolation, characterisation and engineering. The engineering is obtained thanks to the innovative loading and surface modification (e.g. click chemistry) methods. The surface of the extracellular vesicles is modified with specific molecules that can direct the vesicles to defined targets. They can also be used as a means of delivering biomolecules or drugs. Combining the delivery properties of extracellular vesicles and the unique properties of synthetic nanomaterials make them exploitable for biomedical applications.

In the first part of this PhD project, work focused on the hybrid nanoparticles (superparamagnetic nanoparticles and natural and synthetic organic lipid nanoparticles) production and characterisation. The identification of a defined protocol for synthesis and characterisation is essential to be able to verify the load. After running several loading protocols, the production yield of the hybrid nanoparticles was verified using two orthogonal techniques: I) resonance energy transfer (FRET) and II) a modified version of the colorimetric nanoplasmonic test (CONAN). In particular, this second test exploits the nanoplasmonic properties of gold nanoparticles to evaluate the coating of biological membranes on synthetic nanoparticles without any further treatment (e.g. staining or labelling).

In the second part of this PhD project, work focused on engineering the surface of extracellular vesicles for specific targeting against a particular subtype of breast cancer. To modify these extracellular vesicles, it was necessary to optimise protocols for production, isolation and characterisation from different sources such as cell lines, plasma, serum and red blood cells. On these vesicles, the surface was functionalised with a monoclonal antibody called Cetuximab, which is currently used in the clinic for several types of tumours. Functionalisation (active and passive) was performed and compared with different functional tests such as Surface Plasmon Resonance (*on chip*) and mitochondrial stress test, and cellular uptake test (*in vitro*).

Chapter 3

Disclosure statement, collaborations, and publications

3 Disclosure statement, collaborations, and publications

3.1 Disclosure statement

The results presented in this thesis have been obtained during my PhD studies (November 2019 – November 2022) at the University of Brescia (Brescia, Italy) and ETH Zürich (Zürich, Switzerland). All the experimental chapters, hereafter described, contain several not-yet-published data.

3.2 Collaborations

The main laboratory activity was carried out at the laboratory of Prof. Paolo Bergese. In collaboration with Prof. Giuseppe Pomarico and Prof. Annalisa Radeghieri, Dr. Lucia Paolini and Dr. Andrea Zendrini and with the support of Dr. Serena Ducoli, Dr. Miriam Romano, Silvia Alacqua, Angelo Musico and ing. Franco Rabbi. The experiments of this PhD project were carried out also thanks to the collaboration with various research groups within the University of Brescia and with Italian and European research groups.

The first project (chapters 9-10) was framed within the highly international context of the Biogenic Organotropic Wetsuits (BOW) FET Proactive European project [2] and carried out at the Eidgenössische Technische Hochschule Zürich (Switzerland) and in collaboration with international academic and industry partners, Nanomag (University of Santiago de Compostela), the National Research Council of Palermo and Rigenerand Srl. In particular, I have to thank Prof. Paolo Arosio for hosting me in his laboratory, and his collaborators Karl Normak and Dr. Michael Sebastian Gerlt; Prof. José Rivas Rey and his collaborators Dr. Yolanda Piñeiro Redondo and Dr. Manuel A. González Gómez; and Dr. Antonella Bongiovanni and her collaborators Dr. Giorgia Adamo and Sabrina Picciotto and all the Rigenerand Group.

The second research project (chapters 11-12) focused on engineering biological EVs through surface modification aimed to obtain a specific targeting ability towards a particular subtype of breast cancer. The collaborations in this project involved Prof. Marco Rusnati and Eva Chiara Urbinati, Prof. Alessandra Valerio and Dr. Maurizio Ragni.

3.3 Publications

During my PhD studies, I contributed to other collateral projects regarding extracellular vesicles that brought to the publication of one book chapter, one paper, and one manuscript in preparation.

3.3.1 Book chapter

N. Zarovni, F. Loria, **R. Zenatelli,** D. Mladenovic, L. Paolinic, G. Adamo, A. Radeghieri, A. Bongiovanni, P. Bergese. *Standardization and commercialization of extracellular vesicles.* In Extracellular Vesicles, Wojciech Chrzanowski, Chwee Tek Lim and Sally Kim Editors. The Royal Society Of Chemistry. October 29, 2021.
https://www.amazon.com/Extracellular-Vesicles-Applications-Regenerative-Therapeutics/dp/178801894X

3.3.2 International journals and impact factor

M. Gabrielli, I. Prada, P. Joshi, C. Falcicchia, G. D'Arrigo, G. Rutigliano, E. Battocchio, **R. Zenatelli,** F. Tozzi, A. Radeghieri, O. Arancio, N. Origlia, C. Verderio. Microglial large extracellular vesicles propagate early synaptic dysfunction in Alzheimer's disease. Brain. 2022 Aug 27;145(8):2849-2868. doi: 10.1093/brain/awac083. PMID: 35254410; PMCID: PMC9420022.
https://academic.oup.com/brain/article/145/8/2849/6541881?login=false
Impact Factor: 15.255; 5-year Impact Factor: 16.173

F. Antonaros, **R. Zenatelli**, G. Guerri, M. Bertelli, C. Locatelli, B. Vione, F. Catapano, A. Gori, L. Vitale, MC. Pelleri, G. Ramacieri, G. Cocchi, P. Strippoli, M. Caracausi, A. Piovesan. The transcriptome profile of human trisomy 21 blood cells. Hum Genomics. 2021 May 1;15(1):25. doi: 10.1186/s40246-021-00325-4. PMID: 33933170; PMCID: PMC8088681.
https://humgenomics.biomedcentral.com/articles/10.1186/s40246-021-00325-4
2-year Impact Factor (2021): 6.481; 5-year Impact Factor (2021): 5.407

3.3.3 In preparation

A. Musicò, **R. Zenatelli,** M. Romano, A. Zendrini, S. Alacqua, S. Tassoni, L. Paolini, C. Urbinati, M. Rusnati, P. Bergese, G. Pomarico, A. Radeghieri. Assessing the effect of protein corona formation during extracellular vesicle engineering

3.4 Pandemic situations

This work was affected by the COVID-19 outbreak, including, without limitation, the office and laboratory closures, inaccessibility of files or other materials, delays in the delivery of the lab materials, travel delays and blocks, and personal or family illness, mandatory quarantine. The timetable of the mandatory total quarantine and the distribution of work activity is shown in **Figure 1**.

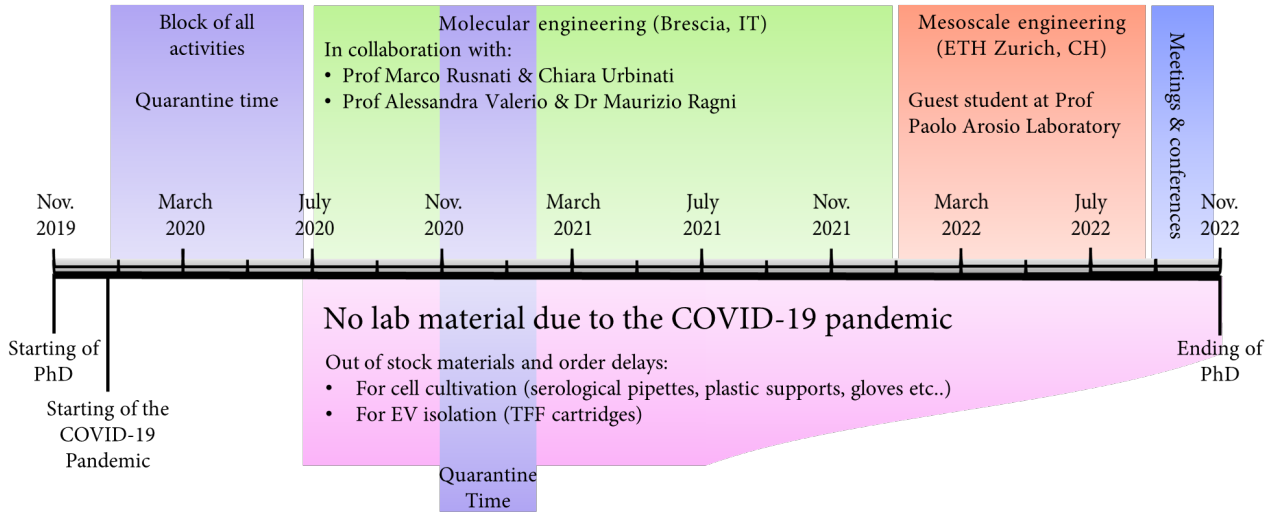

Figure 1. Mandatory quarantines are shown in purple. These blockages not only blocked and delayed the orders of the material but also completely blocked the work of growing and expanding the cell lines to obtain the extracellular vesicles. In green and orange, the two projects that I followed during the PhD course, PRIN and BOW project, respectively. Self-made image.

Chapter 4

Abbreviations

4 Abbreviations

4.1 Material and chemicals

Abbreviation	Complete name
Buffer	
Buffer - PBS	Phosphate Buffered Saline 1X
Buffer - TBS	Tris-buffered saline
Cell culture materials	
Cell culture materials - Cipro	Ciprofloxacin
Cell culture materials - CM	Conditioned Medium (culture medium containing EVs)
Cell culture materials - DMEM	Dulbecco's Modified Eagle's Medium
Cell culture materials - F12	Ham's F12
Cell culture materials - FBS	Foetal bovine serum
Cell culture materials - G418	Geneticin
Cell culture materials - Glu	Glutamine
Cell culture materials - MEM-Alpha	Minimal Essential Medium Alpha
Cell culture materials - P.S.	Penicillin Streptomycin
Cell culture materials - P.S.	Penicillin-Streptomycin
Cell culture materials - PBS 1X	Phosphate-Buffered Saline 1X w/o Ca Mg
Cell culture materials - PLP	Human Platelet Lysate
Cell culture materials - PLP	Human Platelet Lysate
Cell culture materials - RPMI 1640	Roswell Park Memorial Institute 1640
Cell culture materials - TrypLE	TrypLE Select
Cell lines	
Cell lines - EDT-MSC/MSC	Human endometrial decidual tissue derived MSC
Cell lines - HEK293	Human embryonic kidney cell line - adherent growth
Cell lines - HEK293F	Human embryonic kidney cell line - suspension growth
Cell lines - MBA-MB-453	Human epithelial TNBC breast cancer cell line -EGFR negative
Cell lines - MDA-MB-231	Human epithelial TNBC breast cancer cell line -EGFR positive
Cell lines - MSC	Human mesenchymal stromal cells
Cell lines - PC3	Human epithelial prostate cancer cell line
Cell lines - PC3-CD63-GFP	PC3 transfected with the GFP-CD63
Chemicals	
Chemicals - DCC	N,N'-Dicyclohexylcarbodiimide
Chemicals - Cy3	Azido-Sulfo Cyanine 3
Chemicals - Cy7.5	Sulfo Cyanine 7.5 NHS ester
Chemicals - DBCO	DBCO STF ester
Chemicals - DMSO	Dimethyl Sulfoxide
Chemicals - FCCP	Carbonyl cyanide-4-(trifluoromethoxy) phenylhydrazone

Chemicals - HEMA	2-Hydroxyethyl methacrylate
Chemicals - KPS	Potassium persulfate
Chemicals - NHS	N-Hydroxysuccinimide
Chemicals - PEG4	N_3-$(Peg)_4$-NHS-Ester
Chemicals - PEO / PEG	Poly(oxyethylene / poly(ethylene glycol
Chemicals - PTX	Paclitaxel
Chemicals - R/A	Rotenone/antimycin A
Chemicals - PFA	Paraformaldehyde
Chemicals - Tris	Tris(hydroxymethyl)aminomethane
Dye	
Dye-DiO	Rhodamine B isothiocyanate
Dye-RhB	Rhodamine B
Dye-RITC	(3,3'-Dioctadecyloxacarbocyanine Perchlorate
EV	Extracellular vesicle
EV - LEV	Large extracellular vesicle
EV - MEV	Medium extracellular vesicle
EV - MEV	Medium extracellular vesicle
EV - pEV	Pristine SEV
EV - SEV	Small extracellular vesicle
NPs	Nanoparticles
NPs - AgNP	Silver Nanoparticle
NPs - AuNP	Gold Nanoparticle
NPs - EV	Extracellular vesicle
NPs - Lipo	Liposomes
NPs - MBD	Magnetic Bead Devices
NPs - MMA-NP	fluorescent methyl methacrylate Nanoparticle
NPs - MNPs	Magnetic Nanoparticles
NPs - PdNP	Palladium Nanoparticles
NPs - PS standards	PolyStyrene nanoparticle standards
NPs - PtNP	Platinum nanoparticle
NPs - SGNP	Nano-spike gold Nanoparticles
NPs - SPION	Superparamagnetic iron oxide Nanoparticle
NPs - SPM	Superparamagnetic Nanoparticle
P.I.	Protease Inhibitor Cocktail
Protein	
Protein - Ab	Antibody
Protein - BSA	Bovine Serum Albumin
Protein - CTX	Cetuximab
Protein - EGF	Epidermal growth factor
Protein - EGFR	Epidermal Growth Factor Receptor
Protein - EPC	Exogenous protein contaminants
Protein - ER	Oestrogen Receptor
Protein - GFP	Green fluorescent protein
Protein - HER2/neu	Human epidermal growth factor receptor 2
Protein - mCTX	Modified CTX
Protein - PR	Progesterone receptor
Protein - SAP	Soluble exogenous single and aggregated protein
Protein - VEGF	Vascular endothelial growth factor
Support	
Support - CD	CELLdisc (cell culture vessel)
Support - PVDF	Polyvinylidene difluoride

Support - T75	Cell culture vessel 75 cm^2
Virus	
Virus - CMV	Cytomegalovirus
Virus - HbcAb	Hepatitis C surface antigen
Virus - HbsAg	Hepatitis B surface antigen
Virus - HCV	Hepatitis C Virus
Virus - HIV 1-2	H+A2:B98uman Immunodeficiency Viruses 1 and 2

4.2 Techniques

Abbreviation	**Complete name**
AFM	Atomic Force Microscopy
BCA	Bicinchoninic acid protein assay
CONAN assay	COlorimetric NANoplasmonic assay
Cryo-TEM	Cryo-Transmission Electron Microscopy
DC	Differential Centrifugation
DLS	Dynamic Light Scattering
dUC	Differential Ultra Centrifugation
FACS	Fluorescence Activated Cell Sorting
MRI	Magnetic Resonance Imaging
NTA	Nanoparticle Tracking Analysis
QC	Quality Control
SDS-PAGE	Sodium Dodecyl Sulphate-PolyAcrylamide Gel Electrophoresis
SEC	Size-Exclusion Chromatography
SMLM	single-molecule localization microscopy
TFF	Tangential Flow Filtration
TPHA	Treponema pallidum Haemoagglutination Assay
UC	Ultra centrifugation
VDRL	Veneral Disease Research Laboratory
WB	Western blot

4.3 Others

Abbreviation	**Complete name**
APCs	Antigen-presenting cells
BD	Biodistribution
chemo-PTT	Chemo-photothermal therapy
CNS	Central Nervous System
CuAAC	Copper(I)-catalyzed azide-alkyne cycloaddition
DDSs	Drug delivery systems
EPR	Enhanced permeability and retention
ICI	Immune checkpoint inhibitor
Index	
Index - AI	Aggregation index
Index - PDI	Polydispersity index
LSPR	Localized surface plasmon resonance
MOFs	Metal-organic frameworks
MPS	Mononuclear phagocyte system
N.A.	Not applicable
NDDS	Nanosized Drug-Delivery Systems

NMs	Nanomaterials
NMs - 0DNMs	Zero-dimensional nanomaterials
NMs - 1DNMs	One-dimensional nanomaterials
NMs - 2DNMs	Two-dimensional nanomaterials
NMs - 3DNMs	Three-dimensional nanomaterials
NMs - ENMs	Engineered nanomaterials
NMs -NSMs	Nanostructured materials
PK	Pharmacokinetics
RT	Room Temperature
SF	Sucrose gradient fraction
SPAAC	Strain-promoted azide-alkyne cycloaddition
SPM	Superparamagnetic
TAA	Tumour-associated antigen
TNBC	Triple-Negative Breast Cancer

Chapter 5

Nanotechnology

5 Nanotechnology

The prefix “nano” derives from the Greek word “Nanos” (i.e., "very small"), which describes the nanoscale (1nm–100nm). Many scientists agree that the worldwide attention to nanotechnology started on December 29th of 1959, when Richard Feynman delivered the lecture “There’s Plenty of Room at the Bottom” [3] to the annual American Physical Society at the California Institute of Technology (Caltech). However, it was not until the early 1990s that nanomaterial science exploded into a gigantic field [4] due to generous public funding for nanotechnology. The prefix “nano” quickly became the fashion and no one wanted to miss the “nano revolution” [5].

The difference between nanoscience and nanotechnology is that nanoscience is the study of structures and molecules on the scales of nanometers ranging between 1 and 100 nm, and the technology that uses it in practical applications, developing nanomaterials, nanostructures, nanodevices and nanosystems, is called nanotechnology [6]. Nowadays, nanotechnology, one of the most promising technologies of the 21st century, is rapidly expanding with new applications in different fields. For instance, nano-engineering brings new opportunities for progress in healthcare, energy, environmental protection, construction, agriculture and food processing, and other sectors [7]. The term nanotechnology (or ‘“nanotech”) combines distinct domains (engineering, chemistry, physics, biology, and medicine) with the ultimate aim of manipulation of matter. The manipulation by chemical, molecular, and supramolecular methods in the molecular length scales and the mesoscale, fabricate nanoparticles (NPs), nanomaterials (NMs), and nanostructured materials [7].

Generally, any material classified as a nanomaterial (NMs) has a size between 1–100nm and exhibits exclusive properties compared with bulk particles [7]. The specific features observed upon the dramatic size reduction of the NPs alter the nanomaterial’s optical, electrical, and magnetic properties. For example, 20nm gold (Au), platinum (Pt) and silver (Ag) NPs have characteristic wine red colour, yellowish grey, black and dark black colours, respectively. The AuNPs, with 20 nm of diameter, have a Localized Surface Plasmon Resonance (LSPR) at a wavelength of 520nm in water, which redshifts to 600nm as the AuNPs diameter increases to 100nm [7, 8] (**Figure 2**). These NPs showed characteristic colours and properties with variations in size and shape, which can be used in bio-imaging applications.

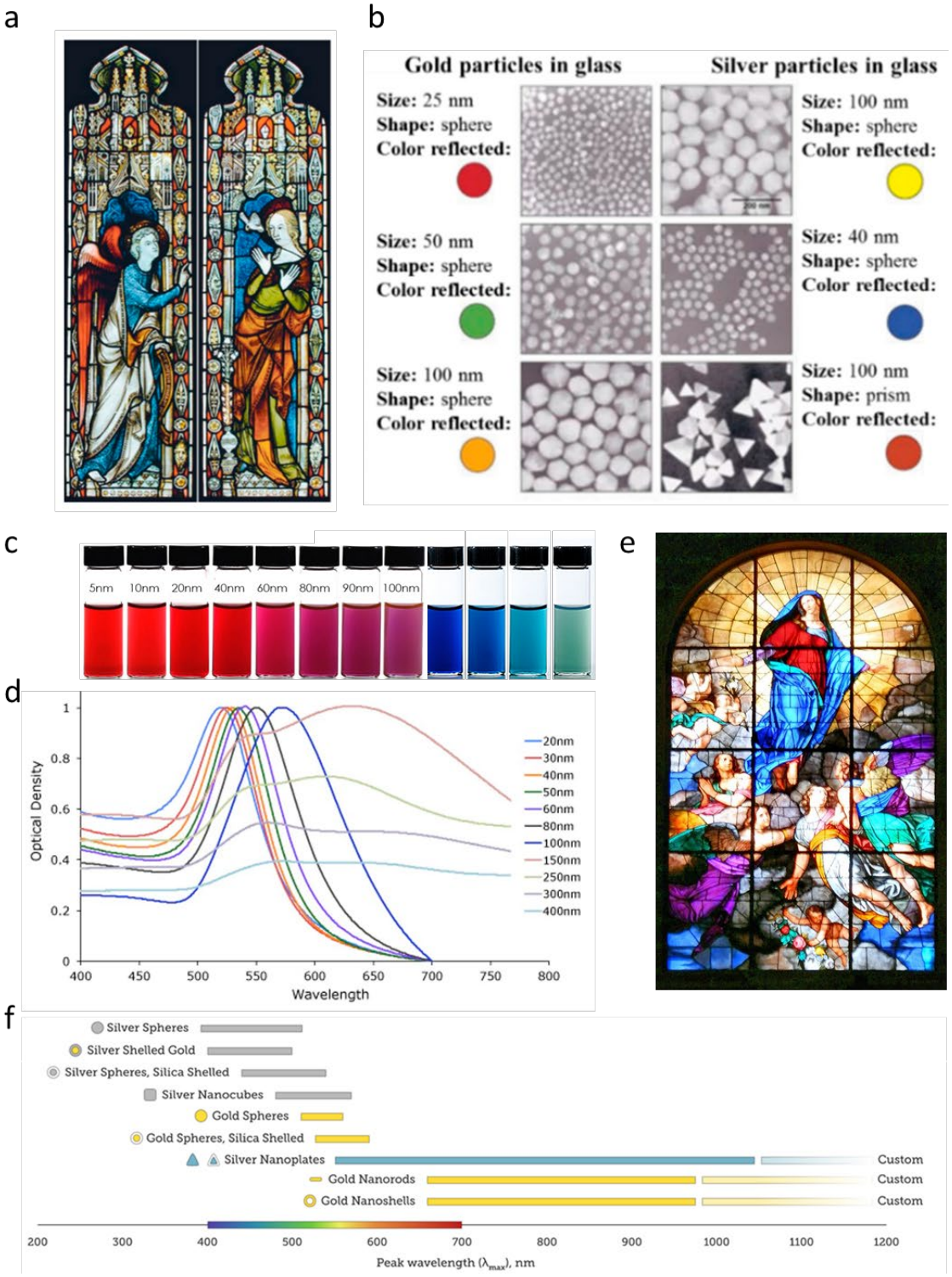

Figure 2. (a) Glass windows of late medieval churches. The shining bright and luminous red and yellow colours are due to the fusion of AuNPs and AgNPs in the molten state glass [6]. **(b)** Transmission electron microscopy (TEM) images of the AuNPs and AgNPs used in coloured window glasses in medieval churches [6]. **(c)** The 20nm AuNPs produce a red colour result of light absorption (at 520 nm). The red-purple colour is due to the absorption by the bigger particles, while the green colour is attributed to the light scattering of a colloidal dispersion of AgNPs with a size > 40 nm. **(d)** Spectra of AuNPs with different sizes in diameter from 20nm to 400nm [9]. **(e)** Feast of the Assumption of the Blessed Virgin Mary, Dome of Milan (Italy) show nanoparticle coloured glasses [10]. **(f)** Optical properties of different types of AgNPs and AuNPs [11].

5.1 Classification of nanomaterials

As there are many different sources of NMs, NMs must be classified to understand them [7]. NMs differ in origin, shape, size, and composition, and several classifications have been used. This section presents the sorting of NMs according to their source and configuration (**Figure 3**).

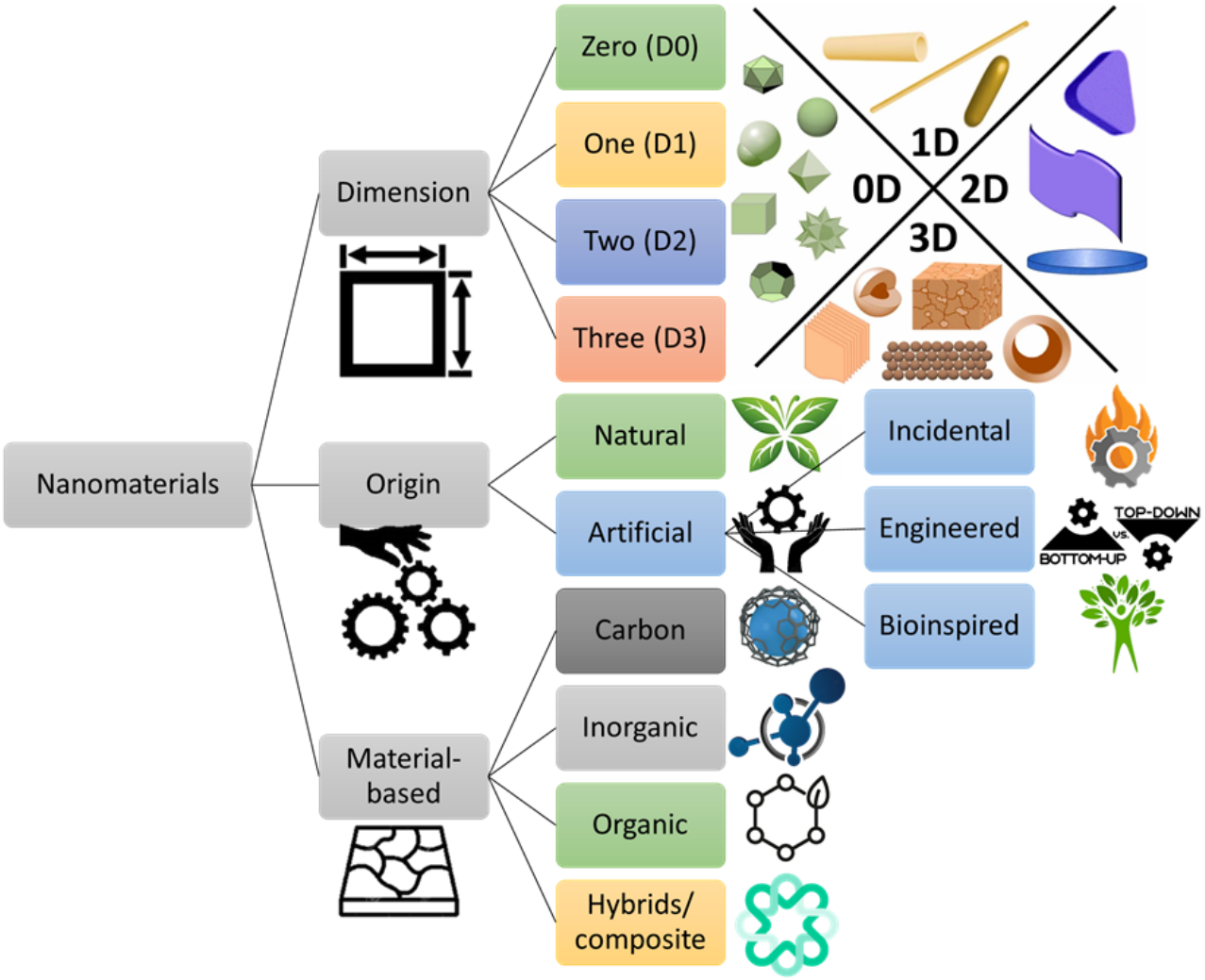

Figure 3. Classification of nanomaterials (NMs) in function of their I) dimensionality, II) origin, and III) composition. **I)** Schematic representation of different morphologies of NMs. Schematic representation of different morphologies of NMs. NMs are classified into 0D, 1D, 2D, and 3D nanostructures based on their morphology. 0D NMs have all dimensions inside the nanoscale. 1D NMs have one dimension, and 2D NMs have two dimensions beyond the nanoscale. 3D NMs are microstructures with nanofeatures, such as hollow microstructures with nanoshells and nanoparticle-based micro assemblies [12]. **II)** NMs can be classified into a) naturally occurring, b) anthropogenic (incidental, engineered, and bioinspired NMs) in the function of their origin. **III)** NMs can be organized into four material-based categories: a) Carbon-based NMs; b) Inorganic-based NMs; c) Organic-based NMs and d) Composite-based NMs. Self-made image.

5.1.1 Classification of nanomaterials based on their dimensions

NMs can be differentiated from the macroscale materials on Earth based on their dimensionality (size and morphology) into four main types of NMs (0D, 1D, 2D, and 3D). Therefore, NMs can be classified based on the number of dimensions outside the nanometer scale.

5.1.1.1 Zero-dimensional (0D) nanomaterials

Zero-dimensional NMs (0DNMs) have all three dimensions on the nanometer scale, so different NPs with different shapes (spherical NPs, many polyhedral shapes, such as cubes, tetrahedra, icosahedra, pyramids, stars, tripods, and tetrapods) [12]. Some examples are fullerenes inorganic/carbon-based quantum dots and polymer/magnetic/noble metal NPs. Due to their optical stability, wavelength-dependent

photoluminescence, chemical inertness, cell permeability, and biocompatibility, 0DNMs are interesting for optoelectronic and biomedical applications [13].

5.1.1.2 One-dimensional (1D) nanomaterials

One-dimensional NMs (1DNMs) have only one dimension >100 nm. 1DNMs include metal, metal oxides and carbon-based nanotubes, nanowires, nanofibers, nanoribbons, polymer nanofiber layers, veils, and webs that present huge surface-to-volume ratios with high porosity and small-scale pores that are exploited for decontamination, catalysis, filtration, and as a super-absorbent and scaffold nanomaterials for tissue engineering and wound dressings [7].

5.1.1.3 Two-dimensional (2D) nanomaterials

The two-dimensional NMs (2DNMs) type has two dimensions >100 nm. 2DNMs have plate-like shapes and have thin layers with a thickness of at least one atomic layer. It is possible to find a wide range of NMs, including round disks, hexagonal/triangular/quadrangular plates, nanosheets, and nanofilms. Among them, nanosheets and films are probably the most studied ones, not only because of their structural integrity but also due to their highly accessible surface [13]. Their unique physical, chemical, optical, and biological characteristics explain their uniform shapes, high surface-to-volume ratio (in contrast with the bulk material), and surface charge. Some examples of 2DNMs are Graphene/graphene oxide/reduced graphene oxide, silicate clays, black phosphorus, graphitic carbon nitride, antimonite, boron nanosheets, and tin telluride nanosheets [7].

5.1.1.4 Three-dimensional (3D) nanomaterials

These materials are NMs with three dimensions >100 nm. This class includes but is not limited to box-shaped graphene nanostructured and bundles of nanowires (graphite) and nanotubes, hollow micro-/nanostructures, which exhibit nanofeatures such as nanowalls or nanoshells, 3D assemblies comprising 0D, 1D, and 2D nanocomponents or a combination thereof [12], but also polycrystalline and diamond structures, dendrimers, aerogels, liposomes, and extracellular vesicles (EVs). Materials with complex 3D structures can display unique features, such as the critical transition to bio stability of a square twist origami and high mechanical strength. Complex 3D structures are crucial components of micro-electromechanical systems, biomedical devices, robotics, and solar cells. The synergic integration of NMs with 3D printing technologies enables the creation of architecture and devices with unprecedented functional levels [7].

5.1.2 Classification of nanomaterials based on their origin

NMs can be classified into naturally occurring, anthropogenic, incidental, engineered, and bioinspired NMs in the function of their origin.

5.1.2.1 Natural Nanomaterials

Natural NMs are produced by natural bio-geochemical or mechanical processes without any link with anthropogenic activities/processes. Natural NMs are present in all the Earth's spheres (hydrosphere, atmosphere, lithosphere and biosphere). Natural inorganic NMs sources include: I) forest fires (combustion materials); II) volcanic ash; III) ocean spray; VI) radon gas decline; and V) weathering of metal- or anion-containing rocks and acid mine drainage sites; but also VI) crystal growth and clays that show complex nanostructures. Some examples of natural organic NMs are viruses (capsid structures), extracellular vesicles, the wax crystals that coat lotus leaves, the gecko foot spatulas, some butterfly wing scales, or also natural colloids like milk and blood, horny materials (claws, skin, feathers, hair), and the human bone matrix [7, 13]. Both incidental and natural NPs may have regular or irregular shapes.

5.1.2.2 Anthropogenic Nanomaterials

Anthropogenic NMs are both incidental, engineered and bioispired NMs.

Incidental Nanomaterials, also known as waste particles, occur because of man-made processes. These NPs and NSMs are unintentionally produced through direct or indirect human influences or anthropogenic processes, such as mechanical or industrial processes, vehicle exhaust gases, welding gases, solid fuel heating (home heathers), and combustion during cooking. Incidental atmospheric NMs, inadvertently formed, might increase air pollution. Incidental NMs, by-products of human activities, generally have poorly controlled sizes and shapes. Incidental NMs have high environmental impacts. The deliberate or accidental release of anthropogenic NMs into the environment has high environmental impacts and is becoming a major public issue.

Engineered Nanomaterials (ENMs) are fabricated in the laboratory/industry to obtain materials with specific features (top-down and bottom-up methods). The engineered NMs are produced for defined applications based on their dimensionality and peculiar characteristics. They are extensively characterised to reduce or minimise their unplanned negative effects. Engineered NPs have regular shapes, such as rings, spheres, tubes, and so on.

Bioinspired Nanomaterials are engineered NMs whose properties mimic the natural NMs or living matter [7]. Using advanced nanofabrication technologies, many bioinspired NMs with specific functions can be fabricated by modulating their structures.

5.1.3 Classification base on the material-based categories

Most current NPs and NMs can be organized into four material-based categories: I) Carbon-based NMs; II) Inorganic-based NMs; III) Organic-based NMs and IV) Composite-based NMs.

5.1.3.1 Carbon-based nanomaterials

Carbon-based NMs are crucial for human activities (e.g., combustibles, composite materials, pigments, reinforcement materials). Carbon-based NMs contain carbon and include nano-diamonds, fullerenes, graphene, single- and multi-walled carbon nanotubes, carbon nanofibers, activated carbon, carbon black, nano-horns, nano-onions, nano-graphite, and graphene. Carbon-based NMs are a specific NMs class but they could also be considered organic NMs because they include C-C bonds [7].

5.1.3.2 Inorganic-based nanomaterials

Inorganic-based NMs include metal, metal salts, and metal oxides. These NMs can be synthesised into metals such as Au or Ag NPs, metal oxides such as TiO2 and ZnO NPs, and semiconductors such as silicon and ceramics. They have different shapes (spheres, cylinders, oblates, ellipsoids, cubes, and stars) in the function of the atom packing and the crystallinity nature of metal-based compounds. However, there can be also amorphous inorganic NPs. The surface is highly reactive and sensitive due to the dangling bonds of atoms at the surface. This problem overcomes by functionalisation [7]. Inorganic NPs have several advantages over organic NPs, including mechanical, thermal, optical, and magnetic properties. In the metal category, Au, Ag, and Cu NPs exhibit unique electronic, optical, and catalytic properties that vary according to their size, magnetic NPs (MNPs) are fascinating due to the high coercive fields and superparamagnetic behaviour at the reduced nanoscale (e.g. magnetite Fe_3O_4)[14–18].

5.1.3.3 Organic-based nanomaterials

Organic-based NMs include NMs made from organic matter. This class presents dendrimers, micelles, ferritin, lipid NPs (liposomes) and polymer NPs. Usually, Organic NPs are nanospheres or have a nano-encapsulated shape ranging from 10 to 1000 nm. The mimic lipid bilayers are synthetic films that assemble nanoparticulated micelles, liposomes, and single or bilayer films by taking advantage of the fact that the "head" is hydrophilic and the "tail" is hydrophobic. Micelles and liposomes contain a hollow core. They are considered biodegradable and non-toxic NPs. Lipid bilayer films are self-assemblies formed by polar lipids found in cell membranes, some microorganisms, and viruses [7].

5.1.3.4 Hybrid/Composite-based nanomaterials

Composite-based NMs may be any combination of carbon-based, metal-based, or organic-based NMs and any form of metal, ceramic, or polymer bulk materials [13]. Organic/inorganic hybrids are expected to be better physicochemical properties than the sum of their components due to the synergy between the NMs. For example, water-non-dispersible inorganic NPs (e.g., AuNPs, iron oxide (Fe3O4)NPs, quantum dots etc.) can become dispersible in water by surface modification [7]. Organic/inorganic hybrid materials can be divided into two categories according to the binding force responsible for the interaction between their organic and inorganic components: **I) Class 1**. The hybrid materials interact weakly through van der Waals, electrostatic, or hydrogen bonds between the organic and inorganic components [19] and **II) Class 2.** The hybrid materials are held together by strong interactions, such as covalent or ionic-covalent bonds [19]. Based on the physicochemical properties of hybrid NMs, organic/inorganic hybrid NMs have attracted a deal of attention in the development of various pharmaceuticals and medical devices (e.g., diagnostic or therapeutic agents, drug delivery carriers, biomedical imaging by taking advantage of the optical or physical properties of the inorganic NPs etc.) [19].

5.2 Nanoparticles

The term "nanoparticles" (NPs) usually defines minute particles of matter (1 to 100 nm in diameter), but other names can be used to describe larger particles (up to 500 nm in diameter). For example, nanorods, nanowires, and nanofibers are NPs with a diameter in the 1–100 nm range but with one dimension outside the nanoscale dimension (**Figure 4**). NPs provide useful opportunities to investigate changes in material properties as a function of particle size [5].

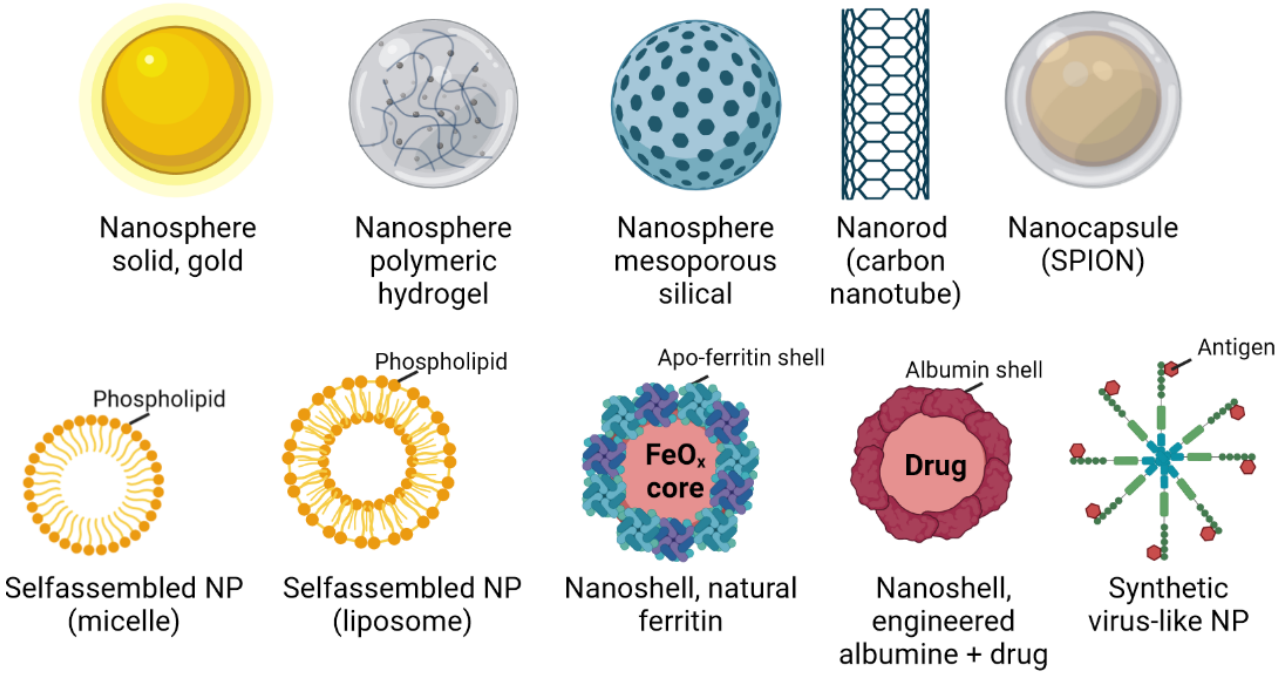

Figure 4. Schematic illustration of different architectures of most common inorganic and organic nanoparticles. Self-made image.

The properties of these NPs differ significantly from those of bulk metals or molecular compounds and depend strongly on particle size, particle shape, inter-particle distance, and the nature of the organic shell if any. Many research groups are focusing on the surface functionalisation of NPs by introducing synthetic ligands and/or natural biomolecules, which have become a critical component regarding the overall performance of the NP system for its use in the biological field. Hybrid NPs not only have the characteristics of both inorganic and organic NPs but can also have unique properties that surpass those of the original components (**Figure 5**). Accordingly, hybrid NPs can be harnessed in a variety of biomedical applications, including biomedical imaging, drug delivery, phototherapy, and image-guided therapy [19].

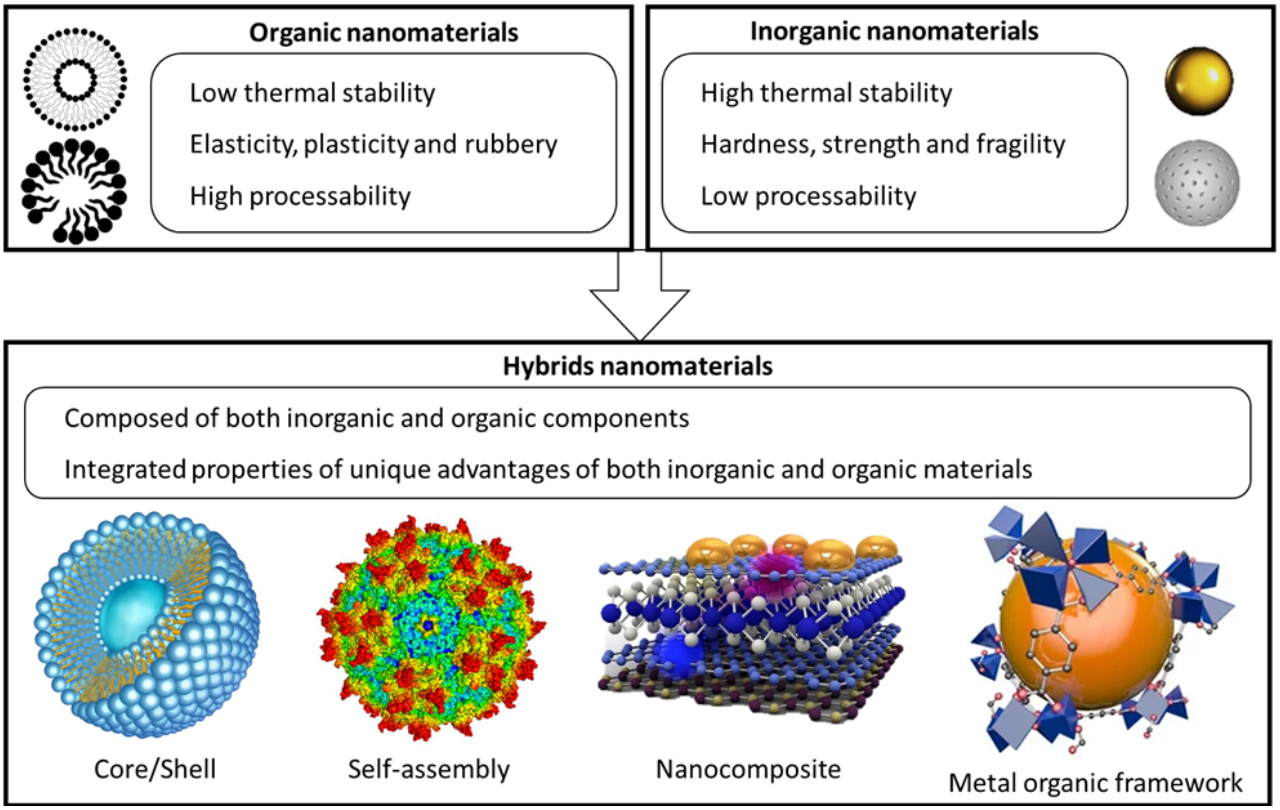

Figure 5. Schematic representative of organic and inorganic NMs property comparison. The desirable characteristics of each NMs are incorporated into various types of hybrid NMs. Self-made image.

5.3 Synthesis of advanced nanoparticles

In recent years, many researchers have sought to utilise the desirable biomedical properties of both inorganic, organic, and hybrid NPs (**Figure 6**). To expand the application of NPs in various fields, the spacing and alignment of individual NPs must be controlled to exploit their desirable properties. Various methods can be employed for the synthesis of NPs, but these methods are broadly divided into two main classes: I) Bottom-up approach and II) Top-down syntheses (**Figure 6**) [6, 8]. The resulting NPs have excellent colloidal properties. The size of the NPs obtained by both methods varied from 10 nm to 500 nm.

5.3.1 Top-down syntheses

In a top-down syntheses method, a destructive approach is employed. Large bulk materials are decomposed into small units, and the units are converted into suitable NPs (**Figure 6a**). Examples of this approach are mechanical milling, chemical etching, sputtering, laser ablation, optical lithography, electro-explosion, E-beam lithography, soft and nanoimprint lithography, block co-polymer lithography, scanning probe lithography, grinding/milling, and other decomposition techniques.

5.3.2 Bottom-up approaches

The bottom-up approach refers to the build-up of nanostructures from the bottom: atom-by-atom or molecule-by-molecule via physical and chemical methods, which are in a nanoscale range (1-100 nm) using controlled manipulation of self-assembly of atoms and molecules (**Figure 6b**). These approaches further divide into various subclasses based on the operation, reaction condition and adopted protocols [8].

Chemical synthesis is a method of producing rough materials, which can be used directly as the building blocks of unorganized-bulk materials or for more advanced ordered materials.

Self-assembly is a bottom-up approach in which atoms or molecules organise themselves into ordered nanostructures by chemical-physical interactions.

Positional assembly is the only technique in which single atoms, molecules or clusters can be positioned one by one freely[6]. Some examples are atomic layer deposition, sol-gel nanofabrication, molecular self-assembly, chemical vapour deposition (CVD), physical vapour deposition (PVD), and DNA scaffolding.

Biological synthesis via biological organisms. Green/biogenic bottom-up synthesis attracts many researchers for the feasibility and less toxic nature of processes. These processes are cost-effective and environmentally friendly, where synthesis of NPs is accomplished via biological systems such as plant extracts, bacteria, yeast, fungi, Aloe Vera, tamarind and even human cells are used for the synthesis of NPs. AuNPs have been synthesised from the biomass of wheat and oat and using the microorganism and plant extracts as reducing agents [8]. The category "nano-organisms" are naturally occurring NMs that include a massive range of organisms, (nanobacteria, viruses, fungi, algae, and yeast), that can produce NPs in their bodies [8]. Generally, bacteria produce metal NPs, binding to soluble, toxic heavy metals and precipitating them on their surface. The nanobacteria and are useful in the biosynthesis of low-toxicity NPs. Magnetotactic bacteria produce magnetic oxide NPs that possess SPM properties, which can be utilised for biological separation and in biomedicine fields. Generally, biocompatible magnetite (Fe_3O_4), iron oxide, iron sulfides and maghemite (Fe_2O_3) are synthesised using magnetotactic bacteria that help in targeted cancer treatment via magnetic hyperthermia, magnetic resonance imaging (MRI), DNA analysis and gene therapy. Algae support the formation of AgNPs, nanocomposite and nanoporous structures via coccoliths and diatoms. Since limited studies are available, the possible mechanisms for algae-mediated NP formation are still unidentified. Similarly, fungi are excellent candidates for metal and metal sulfide NPs synthesis with various sizes and shapes [8].

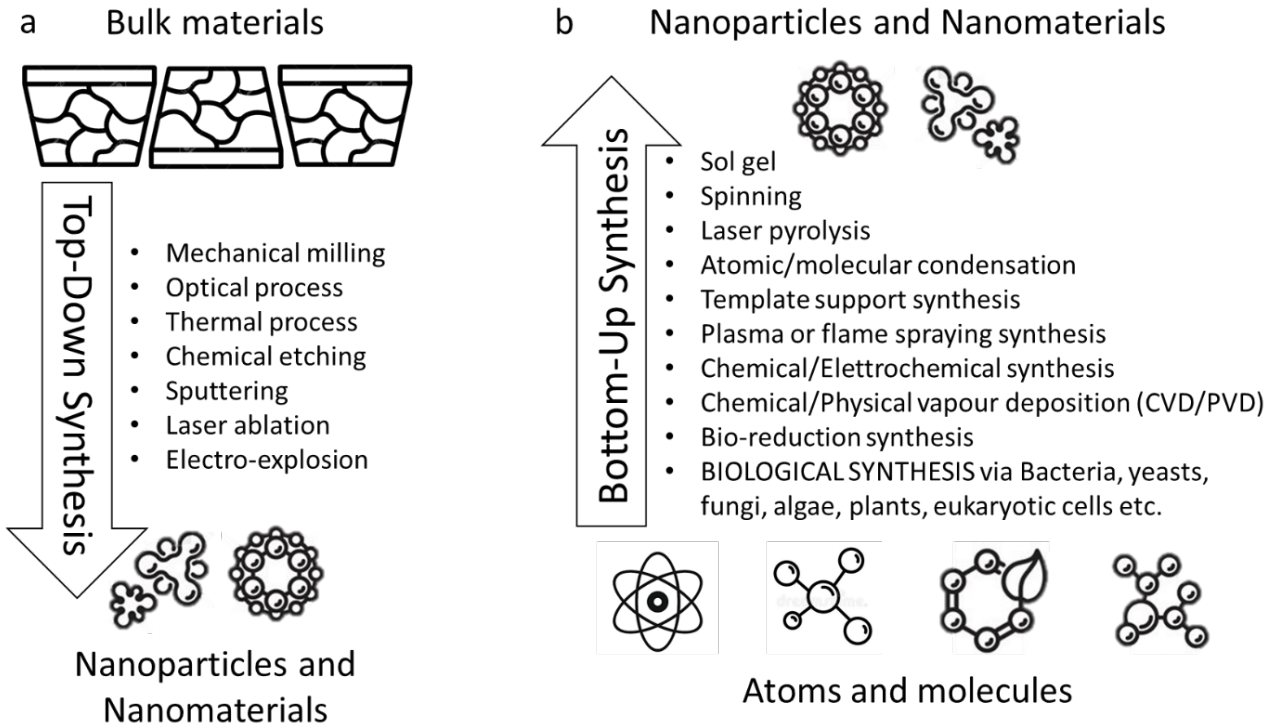

Figure 6. The concept of top down and bottom up technology and typical synthetic methods for NPs for the (a) top-down and (b) bottom-up approaches. Self-made image.

Chapter 6

Nanoparticle engineering and biomedical applications

6 Nanoparticle engineering

Over the past decades, inorganic NPs have shown remarkable potential for numerous applications. Multiple synthetic methods, including metal-organic frameworks (MOFs), self-assembly, physical blending, surface modification, and in situ deposition by altering the surface properties of NPs and controlling their arrangement, have been developed to obtain desired physicochemical properties [19]. Surface modification, a simple method for overcoming surface incompatibility between NPs and polar/non-polar solvent or polymer matrices, involves the introduction of small molecules or synthetic polymers into the NP surface. This simple method not only enhances the dispersion of the NPs in polymer matrices but also enables further modification of the NPs, thereby expanding their range of applications. In addition, various methods have been developed to obtain reinforced physicochemical properties by controlling the alignment of NPs. Assembled NPs can manifest new intriguing characteristics or/and properties relative to the original forms [19]. Therefore, different hybrid NPs have been developed using various methods, such as self-assembly and MOFs, to control the NP arrangements. Some inorganic NPs have distinguished physical and chemical bulk properties, but their surface properties (especially biocompatibility and colloidal stability) are often unsuitable for biomedical applications. In addition, due to their high specific surface-to-volume ratio, inorganic NPs are prone to form agglomerates/aggregates, resulting in fast clearance by the reticuloendothelial system (RES). To broaden the application of inorganic NPs, it is necessary to modify their physicochemical properties by coating them with organic components, thereby improving their biocompatibility and prolonging their stability in blood.

The biological compatibilities and interplay of NPs have been extensively studied for expanding their development in biomedical applications such as a vaccine or antimicrobial activity, bioimaging and biosensing for diagnostic applications, and drug delivery systems (DDSs) [19]. In searching for useful and biocompatible materials, numerous approaches are presently studied. The basic architecture used in many of these approaches consists of three components: I) scaffold, II) core and III) surface.

The scaffold. The scaffold provides mechanical and physicochemical stability. The scaffolds should have a defined size range and a suitable surface that allows the addition of functional groups.

The core. The core can be hollow, porous, or cavernous. The core is used to accommodate therapeutic and diagnostic agents, alone or together with a solvent. Although the ‘core’ of the NPs may not interact directly with the biological environment, it is needed to stabilise the NPs, protect, and release the cargo. There are also requirements for it to be biocompatible [18]. It will have either to degrade to smaller components or be small enough to be cleared at the kidney level.

The surface. The "surface" is modified to become biocompatible and immune-resistant and interacts with cells, tissues, and biological fluids. It can be conjugated with different agents direct the particle to a biological target, for example the antibodies (ABs).

Despite the impressive technological advancement in the design of “smart” NPs, the lacking of knowledge about the safety of the NPs in biological organisms (interaction with the immune system, biodistribution, toxicity, and fate) has limited their effective clinical translation [19].

6.1 Surface modification

The surfaces of inorganic NPs can be modified by physical (adsorption) and chemical (grafting) methods. **Adsorption methods.** Physical modifications are achieved through surface adsorption or the reaction with small molecules on the NP surface. Silane coupling agents, the most common modifiers for inorganic NP surfaces, have bifunctional groups that can react with both phases, thereby forming a bridge between them. Further surface modification can be achieved using the terminal functional groups of the silane coupling agent. The synthesised silica-coated nanomaterials have numerous amine groups on the surface, resulting positively charged surface [19].

Grafting methods. Another approach to modifying the surface of inorganic NPs is a chemical method. Chemical modifications involve the grafting of synthetic polymers to the substrate surface to functional groups on the NP surface, which enhances the chemical functionality and alters the surface topology of the native inorganic NPs. Two chemical grafting methods have been reported [19]. The first is the “grafting to” method, a convenient way to link end-functionalized polymers to the surface of complementary functionalised inorganic NPs. Despite its simplicity, the grafting approach typically results in low grafting density due to entropic limitations imposed on the reactivity of end-functionalized polymer chains [19]. Higher grafting density can be achieved by surface-initiated controlled polymerisation (the “grafting from” method). This polymerisation process, including radical, anionic, and cationic polymerisation methods, involves the propagation of the grafted polymers from the surface of the NP. In the grafting-from method, the monomers are polymerised from the surface of the inorganic NPs. Due to the low molecular weight of monomers, they can penetrate aggregated NPs and react with activated sites on their surfaces. The thickness and especially the density of the polymer layer can be controlled by adjusting monomer feeding and polymerisation time, ultimately yielding well-defined organic/inorganic hybrid NPs [19].

6.1.1 Chemical surface modification and hydrophilization

From a physicochemical point of view, the NP surface must be compatible with the pH, ionic strength, temperature, and other parameters imposed by the surroundings and must help to prevent particle association [20]. Conventional colloid techniques prevent the association of pristine NP by introducing capping agents to the surface to induce electrostatic or steric repulsion between neighbouring NP. This is a popular means of controlling colloidal stability [20]. Poly(oxyethylene) (the PEO abbreviation comes from the source-based name poly(ethylene oxide), is also referred to as poly(ethylene glycol) (PEG)), can also be employed to create a steric barrier that reduces non-specific binding of the NP and has proven a popular surface coating in many DDSs. The two terms are often used interchangeably. However, the systematic term PEO is recommended by IUPAC, but to describe the process of attaching PEO to surfaces, the term ‘PEGylation’ was used, which is widely used in the literature. PEO segments are available in a variety of forms (short or long chains or multiple chains in the same substituent) [20]. They are hydrophilic, neutral, and biocompatible and can be conjugated with other biomolecules. Other macromolecules have also been used to create sterically stabilised NP, such as dextran or dendrimers, which are more biocompatible and can be used for biomolecule attachment. PEGylation of the surface has been used in liposomal technologies because it enhances NP circulation half-life, pharmacokinetics and bio-distribution in vivo [20].

6.1.2 Surface modification with biomolecules

The surface functionalisation of NPs involves a process that aims to improve properties functional for medical applications. These methodologies can be exploited to achieve structures with multiple functions, such as diagnosis and therapy and implement the theranostic approach [21].

In general, the choice of a suitable immobilisation strategy is determined by the physicochemical and chemical properties of both the nanoparticle surface and the biomolecules [20]. Different nanomaterials have peculiar functional groups on the surface to be used in the first functionalisation steps. Generally, the first phase of surface modifications is based on the organic functional-group addition (R-NH2, R-COOH, etc.) to bind biological molecules [21]. For silica NPs, the most used linkers are amino-silanes that introduce an amino group on the NP surface for the next bio-conjugation. Noble metals, like AuNPs, can be functionalised using crosslinkers with -SH or -NH2 groups able to react with the metal and produce a covalent bond. Metal oxides can be easily modified using a ligand exchange strategy based on the original surface substitution with functional groups like amine, carboxylic acid, and thiol [21].

The attachment of a targeting biomolecule is usually necessary when an NP is engineered to target specific cell types. The biomolecule attachment capable of specific target recognition (e.g. antibodies, enzyme substrates, ligands for membrane receptors/transporters, RNA/DNA) to NP surfaces is a universal strategy with many applications [20]. Possible targeting molecules are I) antibodies (ABs) for cell-surface receptors or membrane transporters in specific tissues; II) ligands (like peptides or proteins); III) surface components of microorganisms for vaccination IV) antibacterial agents and others (**Figure 7**) [20]. In particular, the ABs are excellent targeting agents due to their high affinity for their antigens. They can recognise specific biomarkers on the surface of cancer cells, which makes AB-coated NP useful for biomedical diagnostics or bio-imaging [20]. Target recognition can also be improved by employing monoclonal ABs, which bind a single specific epitope of an antigen [20]. However, because monoclonal ABs are expensive and protein-coupling strategies are inefficient, polyclonal ABs are often preferred, despite their reduced biomolecular recognition capability and potential for non-specific binding [20]. The choice of AB is application-dependent. After the functionalisation, it is crucial to evaluate the purity and the performance *in vitro/in vivo* of the bio-functionalized NPs. Therefore, it is necessary to evaluate the "fraction of active biomolecules" on the surface of the NPs (ie the fraction of molecules capable of recognizing the target) and to optimize the bioconjugation strategy. [20]. There are two general methods for generating AB-coated NP: I) passive adsorption and II) covalent attachment (**Figure 7**) [20]. This methodology can be exploited to achieve structures with multiple functions, such as diagnosis and therapy and implement the theranostic approach. Usually, the covalent bond of ligands to the NP surface can be achieved using various linker molecules. Generally, non-covalent interactions are used to load nanoparticles with molecules that must be released in target cells, such as drugs or genetic materials (DNA, RNA). On the other hand, the covalent bonds are employed to bind ligands useful to achieve targeting or to reduce the toxicity of NPs [21].

Passive adsorption. Passive adsorption is straightforward to conduct, cost-efficient and leads to the adsorption of protein layers (corona) on the NP surface. However, because the proteins are immobilised non-covalently, they can be removed and replaced by other biomolecules that exhibit higher affinity towards the NP surface [20]. Moreover, changes in AB conformation or local pH can influence an AB's isoelectric point and its electrostatic interactions with the NP surface, leading to more rapid desorption of the targeting AB [20]. However, the sensitive bond usage, such as pH-sensitivity or heat-sensitivity, to develop nanoplatforms for controlled drug release has been explored. pH-sensitive nano-platforms can be designed for controlled drug release into the tumour environment [21]. The drug release is triggered by the acidity inside the tumour microenvironment, more acid if compared with the healthy extracellular space. Despite this, the passive absorption method is not very popular for drug delivery systems but is widely accepted in biomedical diagnostics. One of the best examples is the passive adsorption of AB-coated AuNP on a gold surface for use in COVID-19 and pregnancy tests [20].

Covalent attachment. The most common covalent coupling strategies that are applied to NPs utilise standard chemistry employing -NH2/-COOH groups, which was first exploited for radio- and fluorescent-labelling of proteins (**Figure 7**). One of the simplest examples of covalent conjugation of antibodies to NP involves the use of carbodiimide agents. For example, the zero-length 1-ethyl-3-[(3-dimethylamino)propyl] carbodiimide

hydro-chloride (EDC) reacts with carboxylated NP in the presence of sulfo-N-hydroxylsulfosuccinimide (sulfo-NHS) to form amine-reactive sulfo-NHS esters [20]. The subsequent addition of antibodies results in coupling between the NP and primary amines on the AB to form a stable amide bond [21]. Another common approach to covalently coupling antibodies on the NP surface is based on two subsequent chemical reactions employing a variety of hetero- and homo-functional linkers [21]. The linkers act like a spacer between the protein and the NP surface, thus avoiding denaturation of the typically expensive biomolecule and undesirable biomolecule-nanoparticle interactions. For example, the PEG/PEO can be synthesised with specific functional groups at the ends and used as homobifunctional or heterobifunctional linkers to perform a wide range of functionalisation processes [21]. Thanks to its polymeric nature, PEG/PEO can be used as a spacer for high molecular weight molecules to space them across the surface of the NPs and to reduce steric hindrance of bonded ligands, allowing bioconjugation. Specific heterobifunctional PEG molecules are still an active research field [21]. However, these molecules can be used to design efficient nano-platforms for medical applications. Because nonspecific AB coupling methods do not result in site-specific binding, the orientation of the antibodies on the NP surface is not controlled, and the binding epitopes may not be accessible for target recognition [20]. Approaches that attempt to influence the site-specific orientation of antibodies focus on the Fc portion of IgG. For example, oxidising the oligosaccharide moieties of the Fc region generates aldehydes, which can be reacted with amine- or hydrazine-terminated surfaces, resulting in the variable region of the AB being oriented away from the ENM surface and available to recognise target molecules [21].

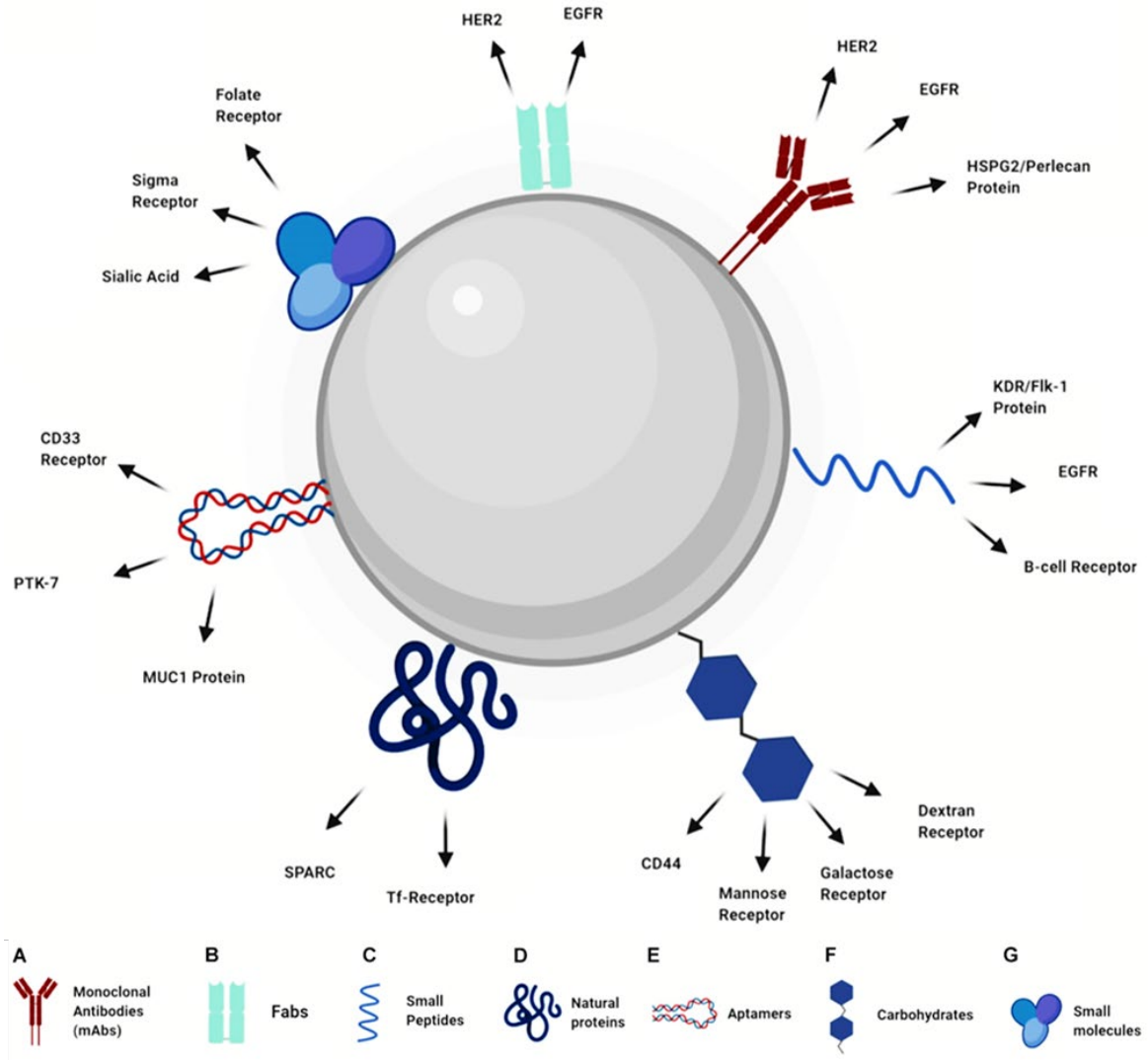

Figure 7. Design of nanoparticles for active uptake (Created with BioRender.com). **(A)** Monoclonal Antibodies, **(B)** Fabs, **(C)** Small Peptides, **(D)** Natural Proteins, **(E)** Aptamers, **(F)** Carbohydrates, **(G)** Small molecules. Modified from [21].

6.1.3 Protein corona

Despite efforts to improve the colloidal stability of NMs through the grafting of sterically or electrostatically repelling coatings, additional surface modification often occurs inside the body by the adsorption of substances present in body fluids. Such surface 'fouling' is primarily attributed to protein adsorption onto the NP surface to form a 'protein corona', also referred to as a 'biomolecular corona'[20]. Two types of the protein corona, 'hard' and 'soft', have been shown to form on many types of NP, including gold, polystyrene, titanium, silica, and zinc oxide.

Hard protein corona. A hard protein corona is a near-monolayer of biomolecules tightly bound (not irreversibly but with possible effect denaturant) to the particle surface.

Soft protein corona. The 'soft' protein corona is composed of more loosely associated and rapidly exchanging biomolecules and surrounds the hard protein corona. According to the article 'What the Cell "Sees" in Bionanoscience, this corona provides the 'extrinsic environmentally- derived identity' that a cell would actually 'see' and interact with [22].

The emergence of the protein corona field highlights the importance of performing analytical characterisation in complex biological media. The idea of protein corona engineering runs in parallel with the concept of 'cell vision', where different cell types can elicit significantly different responses to nanomaterials based on their protein corona composition [20].

6.1.4 Drug targeting

Drug pharmacokinetics and biodistribution can be modulated by chemically modifying the structure of the drug itself or its formulation. Formulations are developed to solubilise drugs or improve bioavailability. NP formulations can be used to modulate the absorption, distribution, metabolism, excretion, and toxicity, which include but go beyond drug pharmacokinetics and biodistribution [4]. Three main strategies to localise nanoparticles to tumours involve: I) passive accumulation into tumours via leaky vasculature; II) incorporation of targeting molecules for binding to cancer cells; and III) targeting nanoparticles to endothelial cells, stromal cells, macrophages or other immune cell types in the tumour microenvironment. For the other diseased tissues, currently, the approaches for targeted drug delivery can be distinguished into two concepts: I) passive and II) active [4].

Passive targeting. The size, charge, geometry, and composition of nanoparticles affect their localisation, cell penetration, and rate of payload release. Optimisation of these parameters helps to maximise efficacy and mitigate the toxicity of the payload [23]. Passive targeting in the tumour microenvironment is attributed to passive extravasation by the enhanced permeability and retention (EPR) effect, a phenomenon observed in cancerous tissue, including many solid tumours. The tumours have defective blood vessels with high permeability, which leads to NP accumulation [23]. This phenomenon is due angiogenesis of highly fenestrated, disordered, and discontinuous vessels in the tumour microenvironment. Such conditions ensure that the tumours are sufficiently supplied with nutrients and oxygen for rapid proliferation. Irregularities in the tumour vasculature, especially in fast-growing tumours, increase the permeability of macromolecules and nanomaterials relative to healthy tissue [23]. The NPs preferentially localise to tumours due to leaky vasculature that enables NPs to diffuse into the tumour microenvironment. The EPR effect has been reported in mice and humans; however, it has not been fully characterised across tumour types. Leaky vasculature was cited as the mechanism by which a lipid NP formulation of cisplatin attained 10- to 200-fold increased drug concentration in tumours during a phase I clinical trial [23]. The EPR effect is responsible for the clinically successful NP-based therapeutic Doxil® (doxorubicin encapsulated in a liposomal formulation) [4]. Despite the clinical success of Doxil®, the EPR effect is complicated by many variables like irregular blood vessel distribution, type and location of the tumour, and limited blood flow in the tumour. As a result, many NP-based strategies designed to take advantage of the EPR effect were less successful than anticipated however

these findings suggest that the EPR effect may be strategically used in clinical nanomedicine efforts going forward [4, 23]

Active targeting. The development of NPs modified to localise and be retained in disease microenvironments is often referred to as active targeting. Disease-specific receptors on tumour cell membranes are reasonably well described in the literature. Active targeting of NP drug carriers to cancer cells involves the functionalisation or decoration of NPs with targeting molecules to promote internalisation into tumour cells and the surrounding microenvironment [23]. Specific surface transporter markers that mediate the uptake can lead the targeting uptake. Some of the most studied targets for nanomedicines include the folate receptor, transferrin receptor, and epidermal growth factor receptor (EGFR) [23]. There are two prominent concerns with this strategy: I) the targeting receptors are not specific to diseased cells; whereas they may be overexpressed on the diseased cell surface, they are also typically available on healthy cells. II) The formulation of NP with ligands, such as antibodies, immobilised in their active form on the surface tends to be difficult due to AB denaturation during long-term storage, corona formation, or nonspecific ionic interactions and challenges with large-scale production [4]. In addition, NP conjugated to targeting moieties are chemically complex species, and detailed characterisation of their specifical and quantitative ability to target the desired receptor and their biological activity and r is often lacking [4].

6.1.5 Drug release

Many new NDDs are currently focused on applications related to cancer therapy, neurodegenerative disorders (Alzheimer's and Parkinson's disease), type 1 and 2 diabetes, and cardiovascular and infectious diseases (i.e. tuberculosis). In general, NDDS favour a slow release of a therapeutic agent that is either encapsulated in the core of the NP or attached to the surface of the nano-carrier (**Figure 8**) [4]. NDDS aims to release their loaded cargo progressively via diffusion or degradation phenomena (or both), and the speed of the release processes must be adequate to achieve therapeutic drug concentrations that remain below toxic levels. In the new hybrid multifunctional NMs, the NPs are made of a combination of organic/inorganic NMs [4]. The drug is incorporated inside the core/shell. The choice of where the drug is encapsulated, inside the core or the shell or even attached on the surface of the NMs, depends on I) the desired application; II) the nature of the drug. III) The composition of the NMs, IV) if the drug can diffuse through the shell or not, and V) if the core/shell has a different function than transporting and protecting the drug (e.g. photothermal effects, imaging contrast, or magnetic properties). However, NDDS have little relevance for bioactive molecules that are soluble in body fluids and diffuse out rapidly. They are of more interest to hydrophobic species, which usually have longer retention times [4].

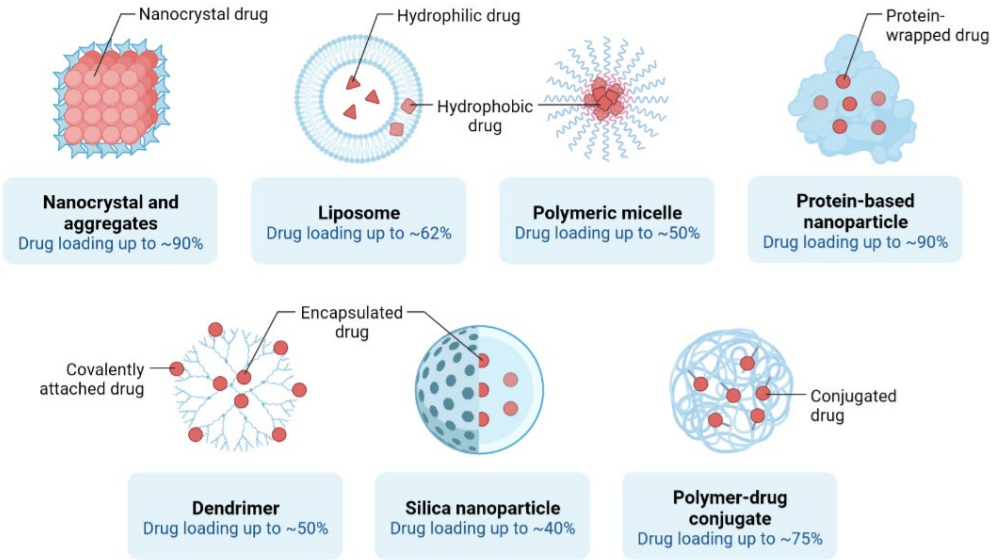

Figure 8. Schematic illustration of different encapsulation inside of inorganic and organic nanoparticles. Modified from [23].

6.2 Biomedical applications

Nano-sized inorganic particles display unique physical and chemical properties and represent an increasingly important material in the novel nanodevices development, which can be used in numerous physical, biological, biomedical and pharmaceutical applications [8]. NPs have drawn increasing interest from every branch of medicine for their ability to deliver drugs in the optimum dosage range, often resulting in increased therapeutic drug efficiency, weakened side effects and improved patient compliance (**Figure 9a**) [19].

Most semiconductor and metallic NPs (**Figure 9a**) have immense potential for cancer diagnosis and therapy due to their Surface Plasmon Resonance (SPR) enhanced light scattering and absorption. The selection of NPs for achieving efficient contrast for biological and cell imaging applications and photothermal therapeutic applications is based on the optical properties of NPs (absorption, scattering, optical resonance wavelength).

AuNPs, silica-AuNPs and Au nanorods efficiently convert the strongly absorbed light into localized heat, which can be exploited for the selective laser photothermal therapy of cancer (**Figure 9a**). The detection of analytes in tissue sections can be accomplished through antigen-antibody interactions using antibodies labelled with fluorescent dyes, enzymes, radioactive compounds or colloidal Au [8]. Besides this, the antineoplastic effect of NPs is also effectively employed to inhibit tumour growth [8]. Superparamagnetic iron oxide NPs, such as magnetite (Fe_3O_4) or its oxidized form maghemite (Fe_2O_3), with appropriate surface chemistry can be used for numerous in vivo applications such as magnetic resonance imaging (MRI) contrast enhancement, immunoassay, tissue repair, drug delivery, and cell separation [8].

AgNPs are being used increasingly in wound dressings, catheters and various household products due to their antimicrobial activity (**Figure 9a**). Antimicrobial agents are extremely vital in medicine. Therefore, the antimicrobial characteristics of inorganic NPs add more potency as compared to organic compounds, which are relatively toxic to biological systems [8, 19].

In recent decades, there has been considerable interest in biodegradable NP development as active devices for drug delivery. Various types of NPs have been used in drug delivery research (**Figure 9**), as they can effectively deliver the drugs to the target site, thus increasing the therapeutic benefit while minimising side effects. The controlled release of pharmacologically active drugs to the precise action site at the therapeutically optimum degree and dose regimen has been one of the prime goals in designing such devices [8, 19]. Liposomes (**Figure 9b**) have been used as a potential drug carrier instead of conventional dosage forms because of their unique advantages, which include I) the ability to protect drugs from degradation, II) the targeting of the site of action and III) the reduction of the noxiousness and other side effects. However, developmental work on liposome drugs has been restricted due to inherent health issues, such as encapsulation efficiency, rapid water leakage in the commodity of blood components and very poor storage and stability [8, 19].

6.2.1 Application in nanomedicine

Nanomedicine is defined as the medical application of nanotechnology for the prevention, diagnosis and treatment of different diseases. Nanoscale agents have remarkable potential in biomedical applications such as biosensors, diagnosis systems, and DDSs [19]. DDSs are designed to alter the pharmacokinetics (PK) and biodistribution (BD) of their associated drugs. In particular, the distinct properties of NPs, including their small size, large surface area, ideal in vivo kinetics, high loading capacity and the ability to protect a drug from degradation by encapsulation on NPs, are ideal properties of NPs as tools for nanomedicine. One of the most intriguing properties of nanomedicines is that they can preferentially accumulate in cancer tissue through the leaky vascular structure of a tumour [19]. This phenomenon has served the development of nanomedicine that delivers drugs to tumours. Passive tumour-targeted delivery increases the therapeutic effect of delivered drugs, minimising their off-target side effects relative to their original forms [19].

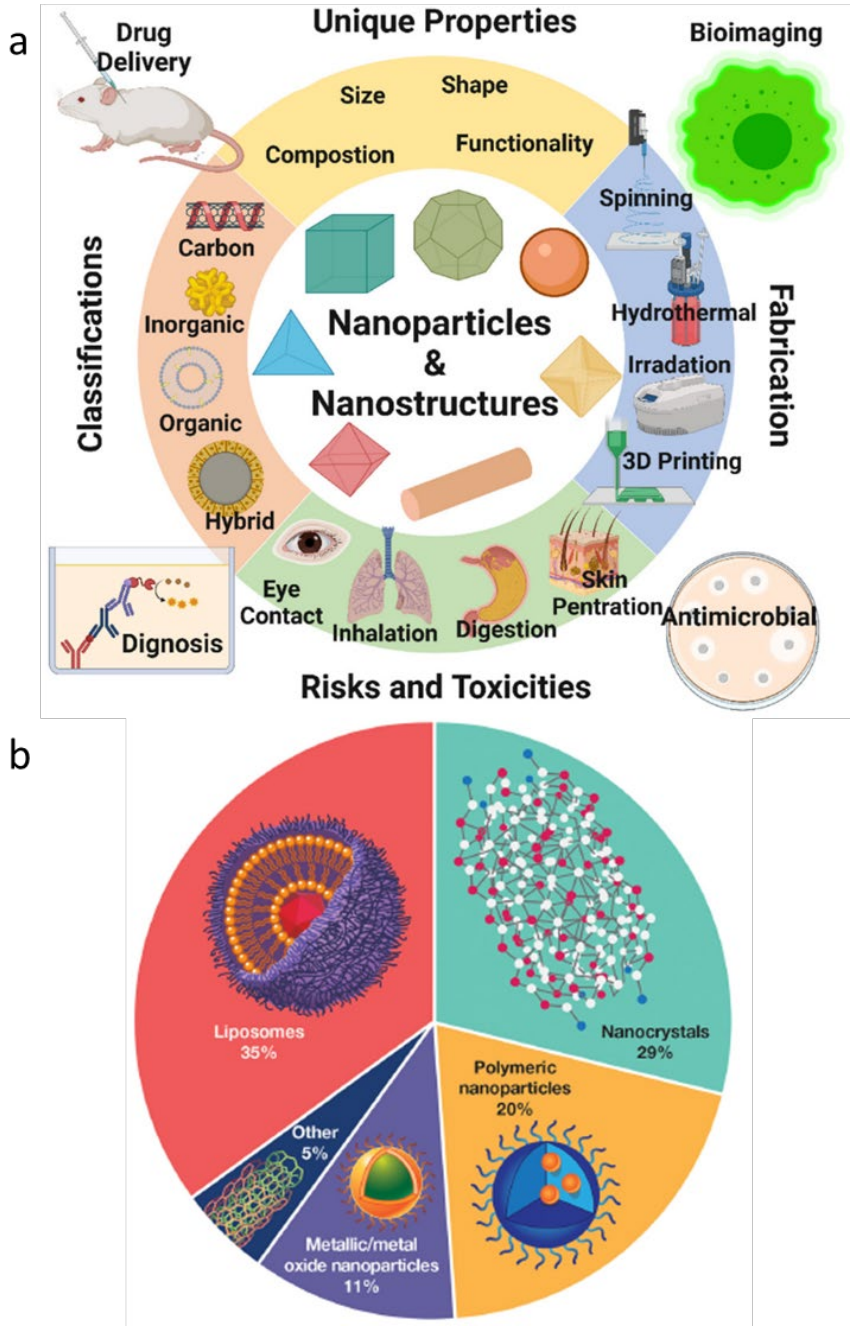

Figure 9. **(a)** Summary of the recent topic on nanoparticles and nanostructured materials from morphology and composition to fabrication and their applications in bioimaging, biosensing, drug delivery, and antimicrobial and toxicities features. [24]. **(b)** Most common nanomaterial-containing drug classes submitted to FDA [25].

6.2.2 Cancer immunotherapy

As NP technology for drug delivery has advanced, its application has spread to various fields. In particular, NPs have the potential to be used as nano-vaccines, and nano-vaccines in cancer immunotherapy (**Figure 5a**), a promising strategy for inhibiting cancer pro-aggression that involves activation and recruitment of the patient's immune system [19]. NPs have also been used as a vehicle to deliver immunostimulants (antigen/adjuvant) and agents that induce the generation of endogenous cancer antigens to elicit an adaptive immune response. The binding or encapsulation of antigens and adjuvants within NPs has yielded significantly improved antitumor immune responses (i.e., T- and B-cell responses) relative to non-NP-based antigens and adjuvants [19]. Unlike NPs that aim to deliver chemotherapeutics into tumour cells bypassing surveillance by antigen-presenting cells (APCs) and other phagocytes, nano-vaccines act directly on APCs or direct trigger activation of tumour-associated antigen (TAA)-specific T-cells [19]. Nano-spike gold NPs

(SGNPs) were coated with polydopamine (PDA) to provide photothermal stability to SGNPs and improve their photothermal efficiency. In addition, sub-therapeutic doses of doxorubicin were co-administered with PDA-coated SGNPs to elicit a robust antitumor immune response (chemo-photothermal therapy, chemo-PTT) [19]. In vivo results in the CT26 colon carcinoma model revealed that chemo-PTT exerted a remarkable therapeutic effect by inducing antitumor immunity, as well as long-term resistance against tumour-rechallenge. The immunotherapeutic effects of hybrid NP-based modalities can be further improved by combination with an immune checkpoint inhibitor (ICI) which is blocking the immune-inhibitory pathway and amplifying T cell activation [19].

6.2.3 Theranostics

The aim of nanomedicine is also the improvement of the drug targeting for specific sites to minimise side effects and maximise therapeutic efficiency. As drug delivery technology evolves and new types of molecular probes have led to advances in imaging technology, demand has grown for combinations of imaging and drug delivery technologies that enable accurate diagnosis and treatment of cancer, a concept termed theranostics (**Figure 5**) [4, 19]. Theranostics refers to integrating both diagnostic and therapeutic functions into a single platform. This platform would enable simultaneously real-time disease monitoring and treatment. The capability to monitor drug accumulation in target tissues and therapeutic responses empowers the development of personalised medicine by optimising treatment strategies. The organic/inorganic hybrid NPs have emerged as promising theranostic agents due to their novel bioimaging properties (CT, MR, and optical) and disease-specific targeting ability, which are derived from their inorganic NP and organic components, respectively [19]. Tumour-specific accumulated hybrid NPs enable accurate disease diagnosis and delivery or release of therapeutic agents, including small-molecule chemotherapeutics (such as cisplatin, doxorubicin, and paclitaxel) and biotherapeutics (such as protein drugs, antibodies, DNA, siRNA, and miRNA). Theranostic agents provide both diagnosis and treatment with the same nanoformulation [19].

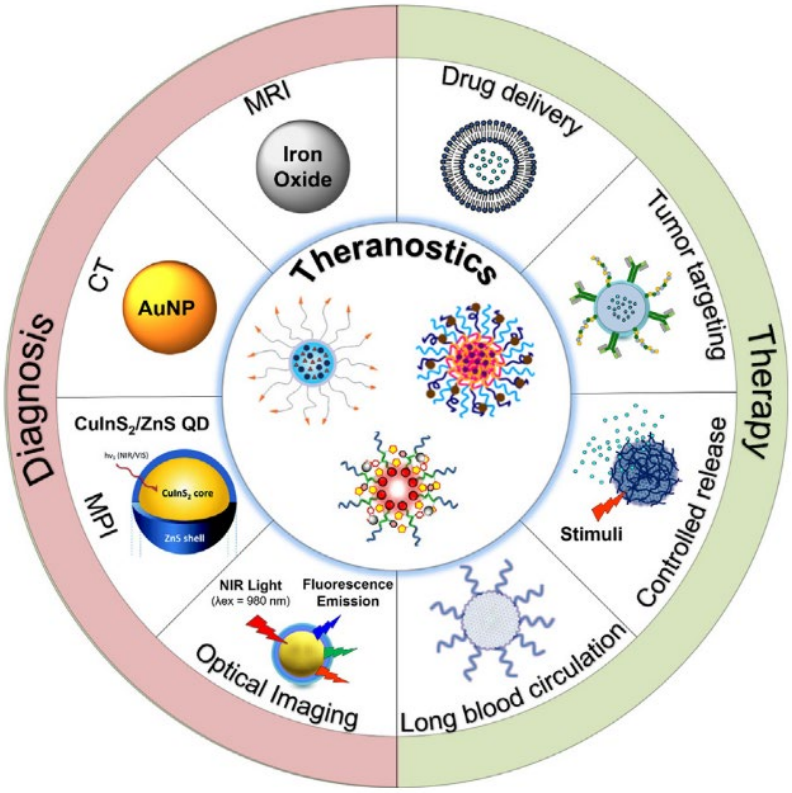

Figure 10. Schematic illustration of the theranostics concept. Theranostics is defined as combined modality, both therapy, and diagnosis in a single platform. More advanced theranostics agents have developed with the progress of different nanocarriers and imaging agents. Abbreviations: MPI: magnetic particle imaging; CT: Computed tomography; MRI: Magnetic resonance imaging [4].

Chapter 7

Liposomes and Extracellular Vesicles

7 Liposomes and Extracellular Vesicles

Increasing advances in nanotechnology and nanoscience have raised great hopes in biomedicine. Inside these fields, the liposomes and the extracellular vesicles (EVs) circumvent many challenges in the medical field, including prevention, diagnosis, and therapy and the lipo-NPs being one of the most widely used nanoparticles in biomedicine. Based on the NM classification, these lipid-based NPs can be considered 3D organic NMs, and liposomes and extracellular vesicles (EVs) are synthetic and natural NMs, respectively. Due to the unique structure, both natural and synthetic phospholipids-based NPs are considered suitable as drug delivery systems. Liposomes, artificial lipid NPs, are long known for their capacity to encapsulate a diverse range of bioactive molecules and release the cargo in a stimuli-responsive manner. They have already been widely explored as drug, vaccine/gene delivery, biosensors fabrication, diagnosis, and imaging agents. They are also extensively used in cancer immunotherapy and theranostics. On the other hand, exosomes, the tiniest type of EVs (sEVs), have proven their capability to carry an array of active pharmaceuticals and diagnostic molecules. The EVs are naturally occurring NPs that serve a fundamental role in cell-cell communication. However, only 14 types of liposomal products are available on the market for the cancer treatment, which means the advantages of liposomes are not fully exploited [26]. Recently, efforts have been directed toward developing smart-bioengineered hybrid NPs to improve all medical applications.

By definition, liposomes (**Figure 11a**) are self-assembled artificial/synthetic lipid vesicle, spherical in shape, having at least one membranous lipid bilayer surrounding an aqueous volume (**Figure 11b**), with a different size, from 20-30 nanometres to 5 micrometres. Typically, the bilayer lipid membrane comprises cholesterol and natural-non-toxic phospholipids, especially phosphatidylcholines but may also include other types of lipids as long as they are compatible with the lipid bilayer structure (**Table 1**). The phospholipids contain a hydrophobic tail and a hydrophilic head that provide both hydrophilic and hydrophobic environments, so at the end, the final structure of a liposome presents an amphiphilic feature [27]. Due to their similarity to the cell membrane, liposomes are considered an appropriate membrane model for revealing the fundamental nature of cell membranes. The liposome types can be classified based on their size and amount of layers. They can be subdivided into four main categories based on these two structural parameters: MVV, multi-vesicular vesicle (MVV), MLV, multilamellar vesicle (MLV), and unilamellar vesicles (ULV). Furthermore, the ULV can be divided into giant unilamellar vesicles (GUV), large unilamellar vesicles (LUV), and small unilamellar vesicles (SUV) [28].

On the other hand, EVs are non-replicating lipid bilayer-delimited NPs that are naturally released from almost all types of cells and organisms. EVs range in diameter from near the size of the smallest physically possible unilamellar liposome (20-30 nanometres with a phospholipid bilayer thick of 4–5 nanometres) to as large as 10 microns or more, although most EVs are smaller than 200 nm in size. The EV phospholipid membrane includes an abundance of cholesterol, sphingomyelin, ceramide, and lipid rafts and contains more than one hundred types of lipids (**Table 2**). Moreover, nucleic acids (DNA and RNA), metabolites, enzymes, and cytosolic and cell-surface proteins (**Figure 11c**). However, the specific composition depends on the EV types and EV sources.

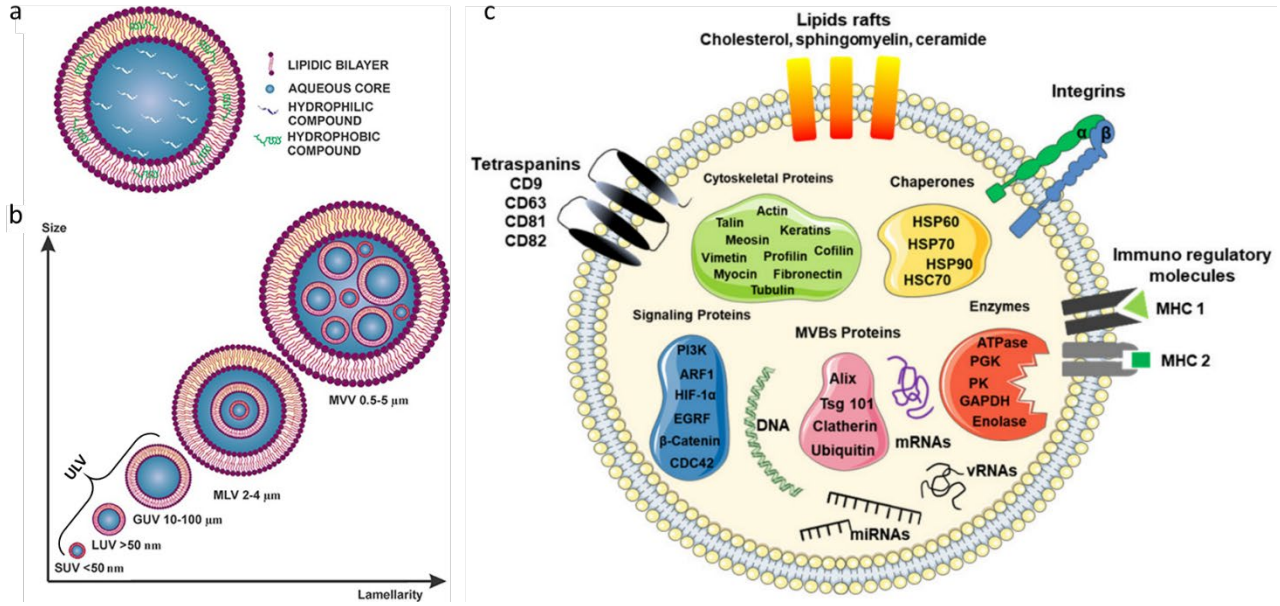

Figure 11. (a) Schematic representation of a liposome [28]. **(b)** Classification by vesicle number based on the size and amount of layers [28]. **(c)** Schematic model of a typical EV. The model shows an extracellular vesicle with a diameter between 30 and 200 nm, expressing several proteins as a protein marker. Inside the core, there are MVBs proteins (i.e. Alix, Tsg101), heat shock proteins (HSP-60, -70, and -90), cytoskeletal proteins, signalling proteins, enzymes, and nucleic acids, such as coding RNAs (mRNAs) and non-coding RNAs (miRNAs and lncRNAs), as well as surface proteins, such as tetraspanins (CD9, CD63, and CD81), integrins, immunoregulatory proteins (MHC-I and MHC-II) [29]. Abbreviations: MLV, multilamellar vesicle; MVV, multi-vesicular vesicle; ULV: unilamellar vesicles; GUV, giant unilamellar vesicle; LUV: large unilamellar vesicles; SUV: small unilamellar vesicles.

Table 1. The common lipids used to prepare liposomes. Table modified from [27, 30]

Charge (neutral pH)	*Abbreviation*	*Name in full*	*Mol. Formula*	*Mol. Weight*
	Chol	*Cholesterol*	C27H46O	38.665.354
Anionic	DLPA	1,2-dilauroyl-sn-glycero-3-phosphatidic acid	C27H53O8P	558.7
	DLPG	1,2-dilauroyl-sn-glycero-3-phosphoglycerol	C30H58O10 PN a	633
	DLPS	1,2-dilauroyl-sn-glycero-3-phospho-L-serine	C30H57NO10PNa	645.74
	DMPA	1,2-dimyristoyl-sn-glycero-3-phosphatidic acid	C31H60O8PNa	614.77
	DMPG	1,2-dimyristoyl-sn-glycero-3-phosphoglycerol	C34H67O10P	666.9
	DMPS	1,2-dimyristoyl-sn-glycero-3-phospho-L-serine	C34H65NNaO10P	701.8
	DOPA	1,2-dioleoyl-sn-glycero-3-phosphatidic acid	C39H71Na2O8P	744.93
	DOPG	1,2-dioleoyl-sn-glycero-3-phosphoglycerol	C42H79O10P	775.0
	DOPS	1,2-dioleoyl-sn-glycero-3-phospho-L-serine	C42H78NO10P	788
	DPPA	1,2-dipalmitoyl-sn-glycero-3-phosphatidic acid	C35H67Na2O8P	692.9
	DPPG	1,2-dipalmitoyl-sn-glycero-3-phosphoglycerol	C38H75O10P	723
	DPPS	1,2-dipalmitoyl-sn-glycero-3-phospho-L-serine	C38H73NNaO10P	757.9
	DSPA	1,2-distearoyl-sn-glycero-3-phosphatidic acid	C39H75Na2O8P	749
	DSPG	1,2-distearoyl-sn-glycero-3-phosphoglycerol	C42H82NaO10P	801.1
	DSPS	1,2-distearoyl-sn-glycero-3-phospho-L-serine	C42H82NO10P	792.1

	PG	Phosphatidylglycerol	C8H23O7P	262.24
	PI	Phosphatidylinositol	C9H21O17P3	494.17
	PS	Phosphatidylserine	C42H77NO10P-	787
	DCP	dipalmityl phosphate	C32H67O4P	546.8
Cationic	DDAB	Dimethyldioctadecylammonium	C38H80NBr	630.95
	DODAP	1,2-dioleoyl-3-dimethylammonium-propane	C41H77NO4	648.1
	DODMA	1,2-dioleyloxy-3-dimethylaminopropane	C41H81NO2	620.1
	DOTAP	1,2-dioleoyl-3-trimethylammonium-propane	C42H80ClNO4	698.5
	DOTMA	1,2-di-O-octadecenyl-3-trimethylammonium propane	C42H84ClNO2	670.6
Zwitterionic	DLPC	1,2-dilauroyl-sn-glycero-3-phosphocholine	C32H64NO8P	633
	DLPE	1,2-dilauroyl-sn-glycero-3-phosphorylethanolamine	C29H58NO8P	579.75
	DMPC	1,2-dimyristoyl-sn-glycero-3-phosphocholine	C36H72NO8P	678
	DMPE	1,2-dimyristoyl-sn-glycero-3-phosphorylethanolamine	C33H66NO8P	635.85
	DOPC	1,2-dioleoyl-sn-glycero-3-phosphocholine	C44H84NO8P	786
	DOPE	1,2-dioleoyl-sn-glycero-3-phosphorylethanolamine	C41H78NO8P	744
	DPPC	1,2-dipalmitoyl-sn-glycero-3-phosphocholine	C40H80NO8P	734.053
	DPPE	1,2-dipalmitoyl-sn-glycero-3-phosphorylethanolamine	C37H74NO8P	692.0
	DSPC	1,2-distearoyl-sn-glycero-3-phosphocholine	C44H88NO8P	790
	DSPE	1,2-distearoyl-sn-glycero-3-phosphorylethanolamine	C41H82NO8P	748
	PC	Phosphatidylcholine	C46H84NO8P	810.1
	PE	Phosphatidylethanolamine	C9H18NO8P	299.21
	POPC	1-palmitoyl-2-oleoyl-sn-glycero-3-phosphocholine	C42H82NO8P	760.08
	SOPC	1-stearoyl-2-oleoyl-sn-glycero-3-phosphocholine	C44H86NO8P	788.1
	HSPC	1-Palmitoyl-2-linoleoyl-sn-glycero-3-phosphocholine	C42H84NO8P	783.774

Table 2. Lipid composition of sEVs from different cell types. Table modified from [30, 31]. %: Percent of total lipid quantified;

Cells	**EVs**	**CHOL (%)**	**PC (%)**	**PC ethers (%)**	**PE (%)**	**PE ethers (%)**	**SM (%)**	**PS (%)**	**PI (%)**	**Cer (%)**
PHC	Cells		44,90		25,10	5,40	11,10	7,40	4,80	1,40
	EV		29,80		10,30	6,30	34,80	11,30	4,10	3,40
PC-3	Cells	19.25	49,06	2,04	10,59	2,67	6,87	5,54		0,24
	EV	43.52	15,28	0,81	5,78±	3,27	16,26	11,66	0,13	0,32
PC-3 + HG	EV	59	10,80	0,70	1,10	4,70	9,10	6,90	0,30	0,70
HT29	Cells		50,40		8,20	18,50	7,20	6,40	7,50	1,80
	EV		61,60		0,90	0,90	34,00	1,40	0,40	1,00
SW480	Cells		53,60		10,80	13,40	6,00	8,40	6,40	1,50
	EV		60,30		1,30	1,20	0,34	1,30	1,10	0,80
LS174t	Cells		49,20		11,70	14,80	9,00	8,50	5,60	1,20
	EV		58,40		1,30	1,10	35,40	1,90	0,60	1,30
Colo 201	Cells		53,60		11,60	13,90	7,80	7,10	5,40	0,60
	EV		48,60		3,30	7,90	28,40	10,30	0,90	0,60
Oli-neu	EV	43	26,70		10,90		8,20	14,90		NR
HepG2/C3a	EV	43	20,00		7,40		9,70	15,60	4,10	0,63

B-lymphocytes	EV	42.1	20,30		14,60	14,60	23,00	20,30	20,30	
Monocity	Cells		0,08		0,47		0,24	0,05		0,11
	EV		0,34		0,41		0,19	0,02		0,01
Mast cell	EV	15	28,00		24,00		12,00	16,00	16,00	
Dendritic cell	EV	NR	26,00		26,00		20,00	19,00	19,00	
Reticulocytes	EV	47	23,50		12,70		8,4c	5,90	2,40	
Platelets	EV	42.5	15,90	1,40	3,10	3,20	12,50	10,50	5,20	0,40
Mouse adipocytes	EV	43	33,00		4,00		12,50	1,10	2,30	0,20
	Large EVs		0,58			4,25	24,20	0,70	4,50	0,57
	Small EVs		0,58			0,07	22,90	0,02	0,04	0,35

Annotations and abbreviations: HG: Hexadecylglycerol; Chol: Cholesterol. PC: Phosphatidylcholine. PC/PE ethers: Ether-linked lipids may be present in all glycerophospholipid classes shown (Phosphatidylglycerol (PG) and Phosphatidic acid (PA)), but are for simplicity shown for PC/PE only. Ether lipids with an alkyl group are abbreviated as exemplified for PC O and ether lipids with an alkenyl group are abbreviated PC P (the alkenyl ether phospholipids are often called plamalogens). PE: Phosphatidylethanolamine. SM: Sphingomyelin. PS: Phosphatidylserine. PI: Phosphatidylinositol. Cer: Ceramide. PHC: Primary healthy colon cells; PC-3 prostate cancer cell lines; HT29, SW480, and LS174t colon cancer cell lines from primary site; Colo 201 colon cancer cell line from metastatic site; HepG2/C3a human hepatocellular carcinoma cell line; Adipocyte from mouse 3T3-L1 adipocytes.

7.1 Milestones of liposomes and extracellular vesicles

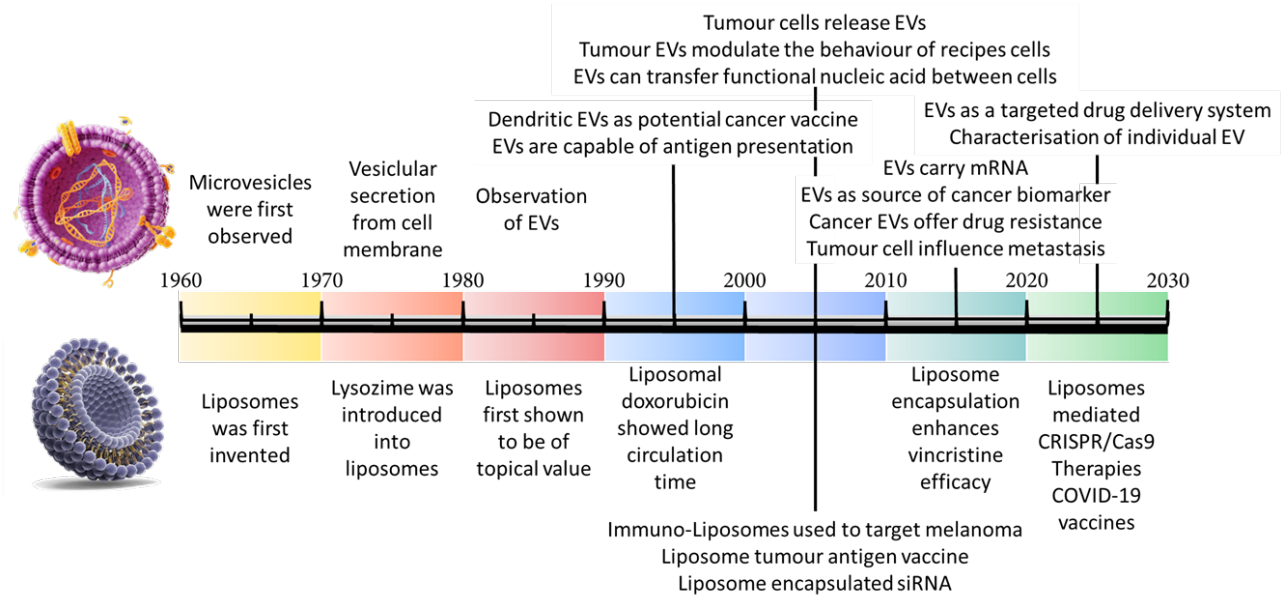

Figure 12. History comparison of the discoveries/application of the extracellular vesicles and liposomes. Self-made image.

In 1961, liposome structure was described for the first time by the British haematologist A.D. Bangham. From the terminology point of view, liposome consists of "*Lipos*" and "*Soma*" attributed to fat and body, respectively. In the same years, as shown in the timeline (**Figure 12**), the first observation of multivesicular bodies (MVBs), and thus of (intraluminal) exosomes -which are the smallest class among EVs- was first recognised in flagellated algae and mammalian cells. Liposomes were recruited as a drug carriers for the first time in the early 1990s. After the 2000s, the role of liposomes and EVs began to become fundamental in the nano biomedical field. The possible applications of bionanotechnology, in the vaccine, diagnostic, therapeutic, and regenerative fields of liposomes and EVs, led to the "*nano*" revolution. In contemporary times, the most obvious application of these technologies has been the development of COVID-19 vaccines

7.2 BOX 1- Liposomes into the PhD projects

The liposomes inside these projects are made with two different compositions. In the BOW project, the liposomes are made with a solution of cholesterol, sphingomyelin and POPC (molar ratio 1: 0.38: 0.87, respectively), while for the CONAN calibration curve, the solution includes only the POPC (**Figure 13**).

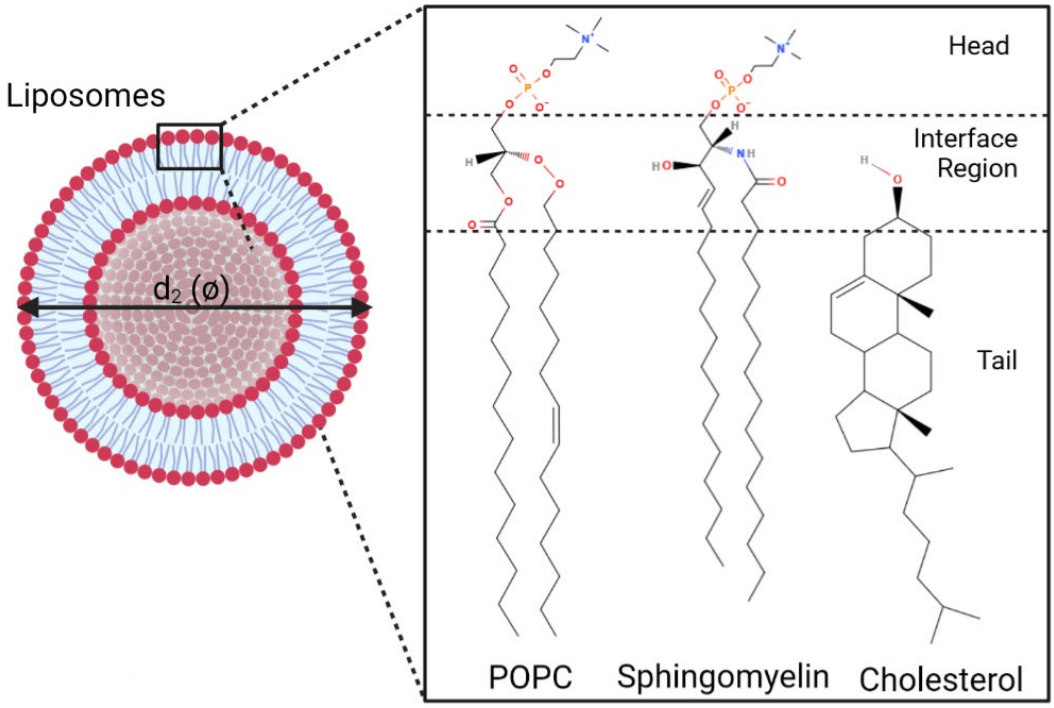

Figure 13. Schematic representation of the liposome used inside these projects. Self-made image.

Cholesterol (Chol). Chol is one main component of the liposome bilayer and can be used in almost all commercial products. The addition of chol can promote the packing of lipid chains and bilayer formation, modulate the fluidity/rigidity of the membrane, and further affect the stability of liposomes, the kinetics of exocytosis, and drug release[26, 27]. Studies have shown that chol as a non-ionic molecule has revealed interesting effects on the zeta potential, especially increasing the highest zeta potential of cationic liposomes.

Palmitoyl-2-oleoyl-sn-glycero-3-phosphocholine (POPC). POPC has one saturated and one unsaturated alkyl chain. As a result, they have different phase behaviours at 25 °C, which allows liposome preparation in situ at room temperature. POPC has a phase transition melting temperature (Tm) of −2 °C; thus, it is in the liquid crystalline phase [26, 27].

Sphingomyelin (SM). SM significantly decreases lipid hydrolysis in an acidic environment and prompts the stability of liposomes. That is because an acid environment (pH 2.0–4.0) is routinely used for producing a transmembrane pH gradient for active drug loading. Under the condition of 37 ◦C and pH 2.0, the rate of hydrolysis for liposomes was approximately 100-fold slower in SM/Chol (55/45 mol/mol) liposomes than in dis-tearoylphosphatidylcholine (DSPC) DSPC/Chol liposomes [26]. In addition, liposomes with SM/Chol showed optimal pharmacokinetic properties. They increased circulation time and enhanced the delivery of the drug into target tissues [26, 27].

7.3 Origin and classification

Naturally, all cell types produce and secrete different EV types. The EVs have been found in all biological fluids counting tears, aqueous humour, saliva, gastric acid, plasma, bile, urine, serum, lymph, cerebral spinal fluid (CSF), bronchial fluid, synovial fluid, semen, amniotic fluid, breast milk and pleural ascites. Depending on their size, origin (biogenesis mechanisms), or function, the EVs are classified as exosomes (50–200 nm), microvesicles (200–1000 nm) that include the oncosomes (1-10 µm), or apoptotic bodies (generally > 1000 nm/ 1µm). EVs are classified based on their origin (endosome vs plasma membrane) and dimension [29].

7.3.1 Exosomes

Exosomes (size <200 nm [32]), also referred to as intraluminal vesicles (ILVs), represent endosomal-derived EVs (**Figure 14**). Typically, exosomes' membranes are made by a phospholipid membrane (containing cholesterol, sphingomyelin, ceramide, and lipid rafts) with evolutionarily conserved biomarkers like tetraspanins (CD9, CD63, CD81, and CD82) and immunoregulatory proteins (major histocompatibility component classes I (MHC-I) and II (MHC-II)) and integrins. Inside the core, there are MVBs proteins (Alix, Tsg101) heat shock proteins (Hsp60, 70, and 90), cytoskeletal proteins, enzymes, signalling proteins, and nucleic acids, such as coding RNAs (mRNAs) and non-coding RNAs (miRNAs and lncRNAs) [29].

7.3.1.1 Exosome biogenesis

Exosome production requires double invagination of the plasma membrane, leading to intracellular multivesicular bodies (MVBs) containing intraluminal vesicles (ILVs). The first membrane invagination forms a cup-shaped structure including cell-surface proteins and soluble proteins present in the extracellular environment. This process results in the formation of the early endosome. In this process, the endoplasmic reticulum and the trans-Golgi network contribute to the formation of the early endosome, which matures into late endosomes. MVBs form by inward invagination of the late endosomal, resulting in MVBs containing multiple ILVs (second invagination). The exosome biogenesis pathway includes two pathways for the inward invagination of the endosome membrane: I) ESCRT-dependent regulated by the endosomal sorting complex required for transport (ESCRT) machinery; II) ESCRT-independent pathway regulated by lipids (ceramide), tetraspanins (CD63, CD81), and small integral membrane protein of lysosome and late endosome. After the MVB formation, MVB can follow two different pathways: I) Degradation pathway. MVBs can fuse with lysosomes or autophagosomes, which leads to the degradation and recycling of their protein, nucleotide, and lipid components. II) Secretion pathway. Upon maturation, MVBs destined for exocytosis are transported to the plasma membrane along microtubules by the Rab GTPase family. After transport to and docking in the plasma membrane, secretory MVBs couple to the soluble N-ethylmaleimide-sensitive component attachment protein receptor (SNARE) membrane fusion machinery.

7.3.1.2 Exosome uptake

Exosomes are continuously generated by and taken up by other cells, resulting in paracrine signalling, or by the parental cells, resulting in autocrine signalling. The exosomes contain specific proteins and transcripts, which are responsible for eliciting the regulation of recipient cells. The recipient cells absorb exosomes by I) membrane fusion, II) endocytosis, III) receptor-mediated internalisation through a caveolin-, clathrin-, VI) lipid-raft-mediated phagocytosis or V) endocytosis mechanism. Inside the cell, the exosomes can I) release their content into the cytoplasm, II) be degraded by lysosomes or III) may fuse with the pre-existing early endosome.

7.3.2 Microvesicles and oncosomes

Microvesicles (200 nm to 1 μm) are plasma membrane-derived EVs secreted by the direct outward budding and pinching of the plasma membrane (**Figure 14**). This process involves ESCRT and ADP-ribosylation factor 6 (ARF6) proteins. Similar to exosomes, the microvesicles carry proteins, nucleic acids, and bioactive lipids to recipient cells; however, they are larger than exosomes.

Oncosomes refer to atypical large-EVs, produced from non-apoptotic plasma membrane blebbing from cancer cells and carrying abnormal and transforming macromolecules, including oncoproteins (**Figure 14**). Typically, EVs derived from cancer cells are greater than those derived from non-cancer cells. Their size difference can be attributed to the heterogeneous nature of cancer cells since different overexpression of genes related to the carcinogenic process produces different subclones of cancer cells. For this reason, microvesicles derived from cancer cells have been referred to as oncosomes (100–400 nm) or large oncosomes (LOs, 1–10 μm).

7.3.3 Apoptotic bodies

The Apoptotic bodies (1-5 µm) are formed from the plasma membrane during apoptosis (**Figure 14**) [33]. These are a peculiar family of extracellular vesicles, heterogeneous in size and content and appear after the cell disassembly into a variable number of subcellular fragments as a final phase of apoptotic death. Moreover, they may contain numerous cellular components: micronuclei, chromatin remnants, cytosol portions, degraded proteins, DNA fragments, or even intact organelles. During the early stages of apoptosis, a membrane lipid rearrangement occurs, which involves phosphatidylserine (PS), commonly localized in the inner leaflet of the plasma membrane. The PS is translocated from the inner to the outer leaflet. The exposure of the PS acts as an "eat me" signal. This signal facilitates the recognition and uptake of apoptotic cells by phagocytes. After releasing in extracellular space, apoptotic bodies are phagocytosed by macrophages, parenchymal cells, or neoplastic cells. Afterwards, they are degraded within phagolysosomes to deliver exploitable materials to healthy recipient cells.

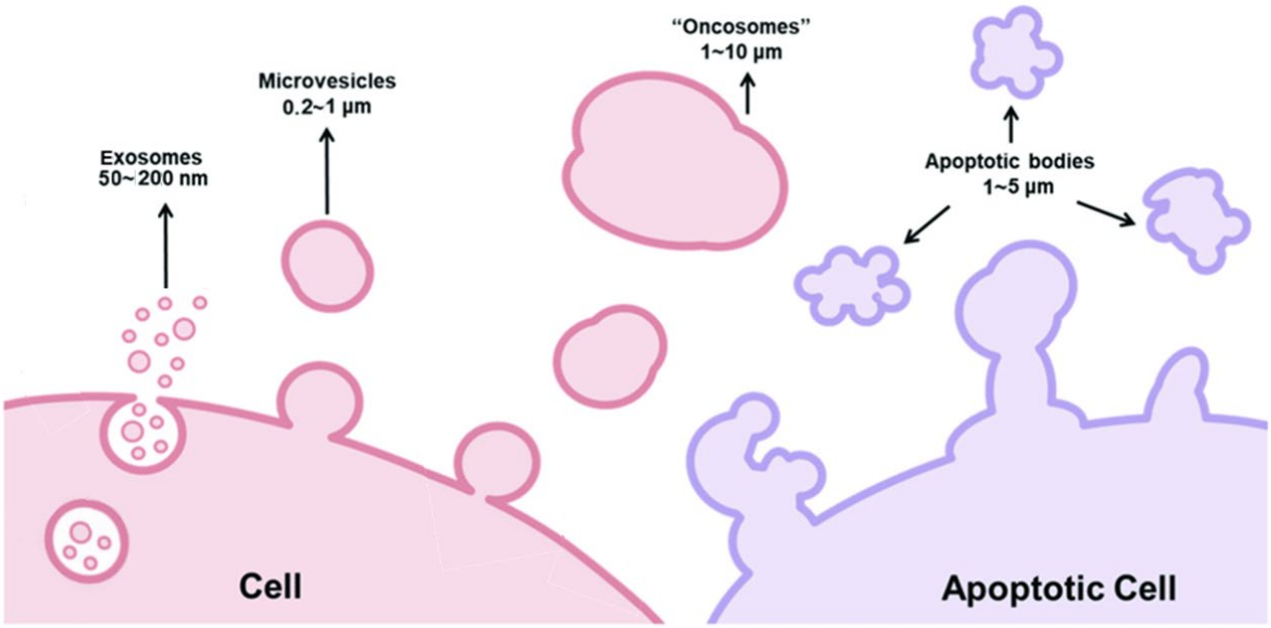

Figure 14. Classification of extracellular vesicles (EVs) according to their size. EVs are classified as exosomes (50-200 nm), microvesicles (200-1000 nm) and oncosomes (1-10 µm), and apoptotic bodies (1-5 µm). Image modified from [29].

7.4 BOX 2- Extracellular vesicle history

EVs across the kingdoms of life. Timeline in green. All types of cells from all organisms (archaea, gram-negative and –positive bacteria, algae, plants, fungi, and mammalian cells) produce EVs. The first time multi-vesicular bodies (MVBs) were recognised in algae (1957) and mammalian cells (1959). At the same time, outer membrane vesicles (OMVs) were found in bacteria. In 1965, after almost a decade, MVBs were found in higher plants. In 1973, EVs were reported in fungi. In 2000, the ubiquity of EVs in all Kingdoms of life was confirmed when they were accounted for in the archaea. EVs were observed throughout all kingdoms of life, underlining their high evolutionary importance [34].
EV functions. Timeline in orange. Today, it is well known that extracellular vesicles (EVs) play a central role in diverse cellular communication processes. Initially, when EVs were discovered, no function could be identified. The EVs were identified as cellular waste due to cell damage or by-products of cell homeostasis. They were considered "trash cans". 1996 marked a turning point in the thinking of EV function when Raposo *et al*. observed that EVs influence antigen presentation in the adaptive immune system in vivo. In 2007, it was revealed that EVs carry messenger RNA (mRNA) and small noncoding RNA (sncRNA), enabling cells to exchange genetic information. These fundamental discoveries have led to discovering and deepening the authentic function of EVs.
EV nomenclatures/EV society/Events. Timeline in blue. In the early years of the field, a variety of terms were used to describe the structures that were observed, including "*ectosomes*", "extracellular microvesicles", "*microparticles*", "small particles", and "virus-like particles". In 1981, the term 'exosome' was used for the first time by Trams et al. to describe vesicles produced directly by outward budding at the plasma membrane. In 1987, Johnstone et al. used "exosome" to describe vesicles released after the fusion of MVBs with the plasma membrane. This has become ISEV's recommended term for this type of EV. As the field grew, it became clear that a precise nomenclature was required. It was suggested to use "extracellular vesicles" to describe a non-replicating structure delimited by a lipid bilayer, and this was formalised into the current recommendations within the Minimal Information for Studies of Extracellular Vesicles (MISEV) guidelines [32].

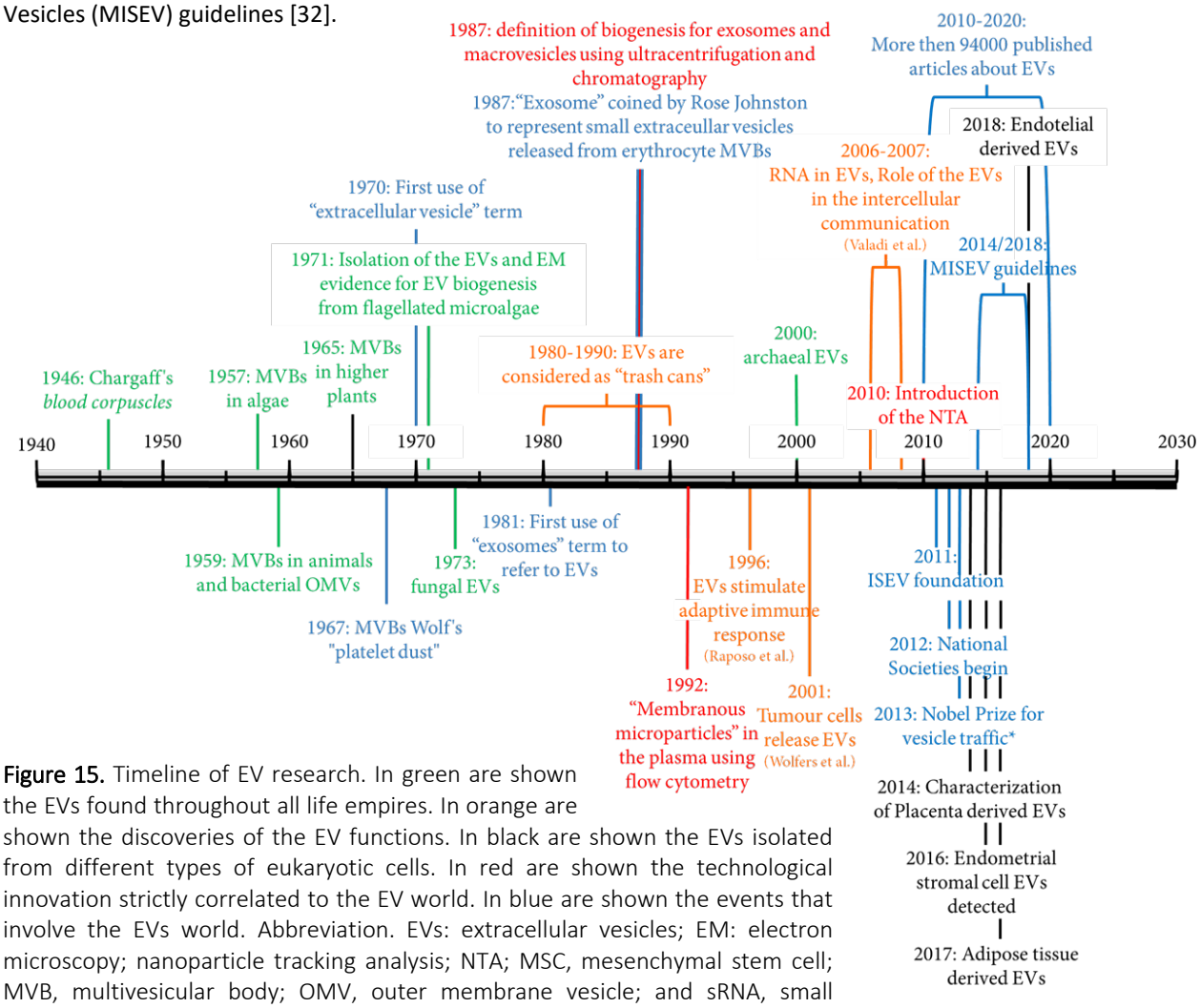

Figure 15. Timeline of EV research. In green are shown the EVs found throughout all life empires. In orange are shown the discoveries of the EV functions. In black are shown the EVs isolated from different types of eukaryotic cells. In red are shown the technological innovation strictly correlated to the EV world. In blue are shown the events that involve the EVs world. Abbreviation. EVs: extracellular vesicles; EM: electron microscopy; nanoparticle tracking analysis; NTA; MSC, mesenchymal stem cell; MVB, multivesicular body; OMV, outer membrane vesicle; and sRNA, small noncoding RNA; ISEV: International Society of Extracellular Vesicles; MISEV: Minimal Information for Studies of Extracellular Vesicles [32]. Self-made image.

7.5 Organic NP engineering

The current chemical pathways for lipid-NP surface engineering span a wide range of different materials and interactive forces. Broadly, the materials used for surface engineering can be classified as synthetic/artificial, biological, or hybrid (metal–organic). Each of these three categories allows different interactive forces to anchor the material into or onto the lipid surface. For example, biological materials (EVs) have been anchored using hydrophobic forces (lipids), receptor–ligand interactions (proteins and nucleic acids), and covalent conjugation. Synthetic materials (liposomes) have been attached with hydrophobic forces and covalent modification. The only hybrid material so far explored is the MPNs, a supramolecular coordination complex consisting of metal ions and polyphenols. It has complex interactive forces allowing for its deposition onto EVs. The crucial point with chemical modification is confirming that the modification strategy does not disrupt the EV membrane. Moreover, chemical modification strategies require additional purification steps, which increase the complexity and chance of loss [35].

7.6 Surface engineering

The surface modification of lipid NPs is necessary for many practical applications as it endows lipo NPs with additional functionality. The main objectives are I) to improve targeting, II) to improve pharmacokinetics and III) to label the particles. One of its most important uses is the introduction of targeted portions on the surfaces of the lipid NPs could help improve their cell specificity and their selective enrichment in specific cells. Passive or active targeting strategies can help to deliver lipid NPs to target cells or tissues. Passive NP targeting uses natural particle tropism, while active targeting achieves targeted delivery of vesicles through surface engineering using various technical approaches. There are two main active targeting strategies about the EVs: I) genetic engineering of the parental cells that produce the EVs II) non-genetic approaches that directly engineer the surface of the vesicle with exogenous modifications by the physical modification or the chemical modification [35–37]. Although the former method is effective for displaying genetically engineered proteins on the surface of EVs, it has many limitations, as it cannot be applied to molecules other than the genetically encodable peptides and proteins. Chemical modification can introduce a wide range of molecules onto EV surfaces by utilizing noncovalent or covalent interactions (**Figure 16**). However, it remains challenging because of the complexity of membrane surfaces and various issues with the purification steps necessary to separate the unreacted chemicals from the EVs [35]. The EVs showed a preferential interaction with the target cells. However, there have been reports that this innate targeting ability is not very efficient in vivo. After systemic administration, native EVs do not show improvements compared to liposomes in terms of circulation time in the bloodstream and tumour accumulation. The pharmacokinetics of lipid NPs could be improved by protecting them from uptake by non-target cells. In the synthetic NP field, the reduction of interaction with the mononuclear phagocyte system (MPS) is mainly achieved by coating the surface of the particles with polyoxyethylene/polyethylene glycol (PEO / PEG) or other peptides that inhibit phagocytosis [36, 37]. Also, for the lipid NPs, to extend the blood circulation time, PEG-lipid conjugates were inserted into the lipid membranes [35]. Lipid NP surface modification can be used for the labelling of the NPs. The Lipid NPs can be modified by loading hydrophilic fluorescent dyes inside or on the surface of vesicles or by staining the membranes with lipophilic dyes. The lipophilic dyes (e.g. BODIPY TR ceramide, carbocyanine dye, PKH-26, PKH-67, DiI, DiO and DiR) are often used to stain EV membranes by intercalating their aliphatic chains into lipid bilayers. However, they have several potential drawbacks that might limit their usefulness. I) Due to their lipophilic nature, these dyes tend to form NPs, which are nearly indistinguishable from stained NPs in terms of size and fluorescence intensity. These dyes are thus difficult to remove with the standard technique (e.g. ultracentrifugation). II) Therefore, stained-NPs need meticulous control experiments to rule out the possibility of the contamination of self-assembled dye NPs, which causes false-positive signals. III) They can label other lipid-containing contaminants (e.g. lipoproteins), IV) they can pass from the vesicles to other plasma membranes without vesicle uptake, leading to false positive results, and V) the long half-life of some dyes might also lead to a false distribution of labelled lipo NPs in the body [35, 36].

7.6.1 Indirect engineering of extracellular vesicles by modifying EV-producing cells

The EV surface can be engineered indirectly via genetically modifying the EV-producing cells, which holds several advantages over directly modifying EVs in terms of expression yield and stability of targeting moiety displayed on engineered exosomes [37]. The genetic modification of EV-producing cells is achieved by transfecting genes expressing I) targeting moiety on the surface of EVs (e.g. peptides, receptors, and antibodies) which is fused with EV membrane components such as tetraspanins, II) can be used to immobilise proteins on the inner surface of EVs. III) can be labelled with fluorescent and luminescent molecules via genetic engineering (**Figure 16a** – **Figure 16b**) [35–37]. The cells transfected with these vectors generate surface-modified EVs expressing the targeting moieties via the natural EV biogenesis process [37]. In terms of applications, biological modification approaches have been primarily used to target EVs to tumours for drug delivery or to study their biodistribution. However, it can be envisioned that similar approaches could be used to target pathological disease states with fluorophores or radiolabels as a form of diagnostic vehicle [35–37]. These EVs produced from genetically engineered cells stably display introduced targeting moiety on their surface and are that the standard EV isolation and purification protocols can be used without modification, which is not necessarily the case for chemical modification approaches [35]. However, cell-based EV functionalisation strategies typically package only a poor fraction of the total modified content into the secretome. Such inefficient incorporation offers a poor return on reagents and costs. In contrast, the direct functionalisation of purified EVs ensures that all modified sites or encapsulated species are localised at the EVs. [35] In addition, the plasmid design, cell lines transfection, and EV production can be challenging and expensive and still risks having the engineered biomolecules appear on the internal EV surface rather than the desired external surface [35].

7.6.2 Direct engineering of extracellular vesicles

EV surface modification can also take place after the isolation. During surface modifications, EVs have one main advantage over cells; they are non-living entities. It is possible to use reagents and reaction conditions that could not be used for live cell functionalisation [38]. Nevertheless, there are still constraints to be considered. For instance, excessive temperatures, pressures, or solvent exposure can cause surface protein denaturation and membrane disruption, while exposure to low or high salt concentrations will lead to osmotic stress. Moreover, certain chemical modifications and many reaction conditions can induce vesicle aggregation [38]. The post-isolation-based methods can be employed for all kinds of molecules or ligands, do not require engineering of the parent cell, can be applied to EVs derived from different sources (biological fluids), and no extensive knowledge about peculiar EV surface proteins is needed [36]. Direct engineering of extracellular vesicles requires more steps and time to achieve the desired final product and it can be divided into methods based on chemical modifications on the EV surface using covalent attachments of targeting moieties such as ‘‘click chemistry’’ and based on physical interactions using non-covalent methods [36, 37]. All the direct surface modifications present one crucial challenge: unincorporated material removal. Here a suitable purification and analytical method need to be employed that guarantees the purity of the modified EVs while maintaining their integrity and activity [36].

7.6.2.1 Covalent Modification of the EV Membrane

Common bioconjugation and “click chemistry” are convenient prosecutions of chemical reactions to modify EVs. They have great potential as a standardized method that can be readily applied to EVs derived from different sources with a wide variety of targeting moieties, fluorescent dyes or PEG derivatives [38]. Moreover, Due to mild reactions that rapidly form chemical bonds under ambient conditions, "click chemistry" has become a natural candidate for covalent EV modification [38]. However, the drawback of utilizing covalent bond is that covalent bonds are very stable bond and mostly requires toxic chemicals (copper), thus increasing caution in vitro/in vivo experiments [37]. Moreover, it is possible that such

bioconjugation strategies could impair biological functions by altering or obscuring the active site of modified surface proteins. To avoid this problem, covalent reactions could be performed upon previously transfection-modified EVs to express additional or bio-orthogonal moieties. Another problem could be the presence of non-vesicular material, which can lead to unwanted side reactions that could interfere with the surface modification of the vesicles. Thus, during the development and optimization of chemical surface engineering, the purity of EV samples needs to be taken into account [36]. In chemical approaches to EV surface modification, vesicles are engineered through the covalent linkage of molecules to their surface [36]. The most abundant suitable functional groups on the EV surface are the amino groups available in lysine side chains and the N-termini of EV surface proteins and they can be easily bound using activated esters, like NHS esters. Amino groups can be used directly as the anchor- point for chemically simple molecules, such as fluorescent dyes or PEG derivates (**Figure 16c**). PEGylation, which is a modification of the exosome's surface with polyethylene glycol (PEG), is one of the most common examples of a chemical conjugation method that uses covalent attachments [37]. However, in the case of more complex biomacromolecules (like antibodies); a two-step approach needs to be employed. Click chemistry utilises covalent interactions between an alkyne and azide residue to form a stable triazole linkage. This can be applied to attach targeting moieties on the surface of EVs in a variety of aqueous buffers that include water, alcohols, and dimethyl sulfoxide (DMSO) [37]. This approach was based on sequential chemical reactions that exploit the amino group on the EV surface. The amino group are a reactive functional group naturally expressed on membrane proteins and, therefore, represents a reasonably straightforward target. First, the activated ester is used to endow the vesicles with a functional group that subsequently selectively reacts with the molecules used for surface modification in biorthogonal reactions (**Figure 16d**). In details, a carbodiimide coupling was used to graft the alkyne onto EV membrane amines. The introducing a reactive alkyne base allowed a second-click chemistry reaction with an azide-tagged molecule [38]. These reactions can be divided into Copper (I)-catalyzed azide-alkyne cycloaddition (CuAAC) and its Strain-promoted azide-alkyne cycloaddition (SPAAC). CuAAC reaches higher rate constants and the alkynes needed in these reactions are chemically more accessible and less large than the strained cyclooctynes employed in SPAAC. However, the latter approach does not require the addition of Cu[I]-ions. These ions might cause oxidative damage to EV surface proteins and need to be thoroughly removed from the vesicles before EV application in vitro and in vivo, due to their toxicity. The mild reaction conditions and high selectivity of SPAAC that have led to its wide application, even for direct labelling in vivo, predestine it as the reaction of choice for EV-labeling [36]. Also, it has been reported that azide-Fluor 545 fluorescent molecules could be attached to the surface of EVs via alkyne-based cross-linking reactions without altering the size and characteristics of EVs [37]. As a proof-of-principle, this example demonstrates that common chemical reactions can be applied to EV surface modification, without any observed effects on the structure of the vesicles or their ability to interact with cells [38]. However, to reach this goal the effects of chemically linking molecules to the EV surface protein amino groups warrant further evaluation, as these modifications might affect the natural protein activity of EVs to an unknown extent [36].

7.6.2.2 Noncovalent Modification of the EV Membrane

The physical surface modification of EVs can be achieved through fusion with liposomes, the insertion of lipophilic moieties into the membrane and the adsorption of molecules to their surface [36]. The stability of any surface modification is highly dependent on the strength of the bond that links the exogenous species to the EVs [38]. Covalent bonds typically have bond energies in the region of 200−900 kJ/mol, which is much greater than the values for noncovalent interactions (2−13 kJ/mol). Consequently, covalently bonded species are less prone to dissociation by chemical displacement or changes in ionic strength, temperature, or solvent. Three noncovalent strategies are commonly used to provide stable modification of biological membranes: I) multivalent electrostatic interactions, II) receptor-ligand binding, and III) hydrophobic insertion [38].

Multivalent electrostatic approaches. Multivalent electrostatic approaches rely on the cumulative action of multiple charge interactions, which typically involves a highly cationic species adhering to negatively charged

functional groups present on EV biological membranes [38]. For instance, electrostatic interactions were used to bind cationic lipids to the surface of EVs. In turn, this produced EVs with a positively charged surface potential that enhanced binding and uptake into recipient cells (**Figure 16g**). However, there are concerns that some cationic nanomaterials can cause cytotoxicity through membrane thinning and hole formation. Moreover, a more relevant issue is that cationic nanomaterials are typically taken up into the cell via endocytosis, which could lead to the lysosomal degradation of delivered payloads [38].

Receptor-ligand binding. The second noncovalent strategy involves receptor-ligand binding. Receptor binding strategies offer a bioinspired approach that can be transferred from cell modification to EV functionalisation (**Figure 16e**). Indeed, the specificity of this approach suggests fascinating opportunities, particularly if the receptor is enriched on the EV surface. For instance, targeting EV surface receptors use a strategy to bind and eliminate vesicles implicated in pathological processes, such as cancer metastasis [38]. Qi et al. [39] reported a notable example of the use of reticulocyte-derived EVs. Reticulocytes are a principal source of EVs in the bloodstream and release EVs during their maturation into erythrocytes. The EV reticulocyte contains transferrin receptors in their membranes and synthesised transferrin-conjugated superparamagnetic Fe3O4 NPs clusters that are effectively bound to the surface of EVs by the specific interaction between transferrin and transferrin receptor [38].

Hydrophobic insertion. Liposomes can be effortlessly produced in large quantities and adapted to specific drug delivery problems. The fusion between liposomes and EVs is a very flexible and attractive approach to obtaining mimetic EVs (**Figure 16f**). [36]. Furthermore, several liposome-based formulations have been successfully translated to the clinic and could provide necessary information for the clinical development of liposome-EV-hybrids [35, 36]. The primary complications of this method are I) how to achieve the fusion of EVs and liposomes and II) separating the resulting three populations of native EVs, native liposomes and their fusion product. The fusion of EVs and liposomes is more challenging, and it is difficult to adapt the cell fusion strategy to the EVs. The high level of cholesterol, sphingomyelin, and ganglioside in the membrane of EVs create a more rigid bilayer structure than observed in the parent cells [40]. This prevents the facile fusion of lipid-based particles, such as liposomes or micelles. For example, while cells will take up micellar structures under ambient conditions, EVs require aggressive freeze−thaw (T = −196 °C) or high-temperature (T =40 °C) cycling to disrupt the vesicular membrane and promote fusion [38]. The fusion can be achieved through freeze-thaw cycles, where the mixture of EVs and liposomes was shock-frozen in liquid nitrogen and then thawed at room temperature ten times [35, 36]. The fusion efficiency was characterised by FRET and increased with an increasing number of freeze−thaw cycles [35]. The fusion itself can be monitored through Förster resonance energy transfer (FRET). After fusion with EVs, the complementary pair of lipophilic fluorescent dyes contained in the liposome membrane is diluted, and the measurable fluorescence of the donor-dye increases [36]. However, the dilution of dyes and lipids can also occur by hemifusion, i.e. the interaction of only the outer leaflet of two lipid-bilayer enclosed entities. As hemifusion not necessarily proceeds to complete fusion, further assessment is needed. To confirm the fusion of EVs and liposomes, it is necessary to use the method of Meers et al. [41].The evaluation can be achieved through content mixing or oxidation assays with the inactivation of one of the FRET partners in the outer leaflet using dithionite to assess the fusion of the inner leaflet. Interestingly, microvesicles or exosomes could be fused with liposomes with the same efficiency, suggesting that the size of the EVs had little effect on this fusion process. The EV-liposome hybridisation method could be used to optimise the properties of the EV surface to reduce immunogenicity, promote colloidal stability, increase blood pharmacokinetics, and therefore enhance target cell uptake of in vivo administered EVs [37]. The drawback of this method is the risk of altering the integrity and direction of membrane proteins on the exosomes, thus weakening their biological functionalities [37].

7.7 Loading strategy

7.7.1 Passive loading

Hydrophobic interactions are highly effective at driving the spontaneous integration of small lipophilic species into the EV membrane. This can be achieved using a simple co-incubation under ambient conditions (25−37 °C), with loading efficiencies that positively correlate with the hydrophobicity of the exogenous species. This approach is used in most commercial EV membrane stains, including commonly used dyes like BODIPY TR ceramide, carbocyanine dye, PKH-26, PKH-67, DiI, DiO and DiR [38]. Furthermore, hydrophobic sequestration is used to load EVs with small lipophilic drugs, such as anti-inflammatory curcumin, common porphyrin photosensitisers, and chemotherapeutic agents like curcurbitacin, doxorubicin, paclitaxel, and methotrexate. The incorporation of large and polar cargo molecules into EVs can be challenging. Thus, the surface of EVs rather than their internal space could provide an easily accessible location for exogenous vesicle cargo [38].

7.7.2 Active Loading of EVs.

Passive loading strategies that rely on spontaneous interactions are limited by poor loading efficiency. To address this, membrane permeabilisation strategies have been adapted from the bacterial transformation field and liposome modification and repurposed for the active loading of EVs [38]. For example, electroporation and sonication are commonly used to transiently permeabilise the EV membrane to enhance the uptake of siRNA, small molecule drugs, and SPIONs [42]. A higher loading efficiency can be achieved using saponin treatment and hypotonic dialysis. Saponin permeabilises biological membranes by complexing with cholesterol, while hypotonic dialysis, commonly used to load erythrocyte “ghost” cells, uses osmotic pressure to enhance drug internalisation efficiency. Such strategies are inherently more disruptive than passive approaches, and careful handling and characterisation should be employed to ensure the integrity and functionality of the EVs are retained post-modification. For these reasons, membrane stabilisers can be employed to improve the colloidal stability of EVs. Moreover, it is necessary not to mistake EV precipitation with micellar aggregation for loaded EVs [38].

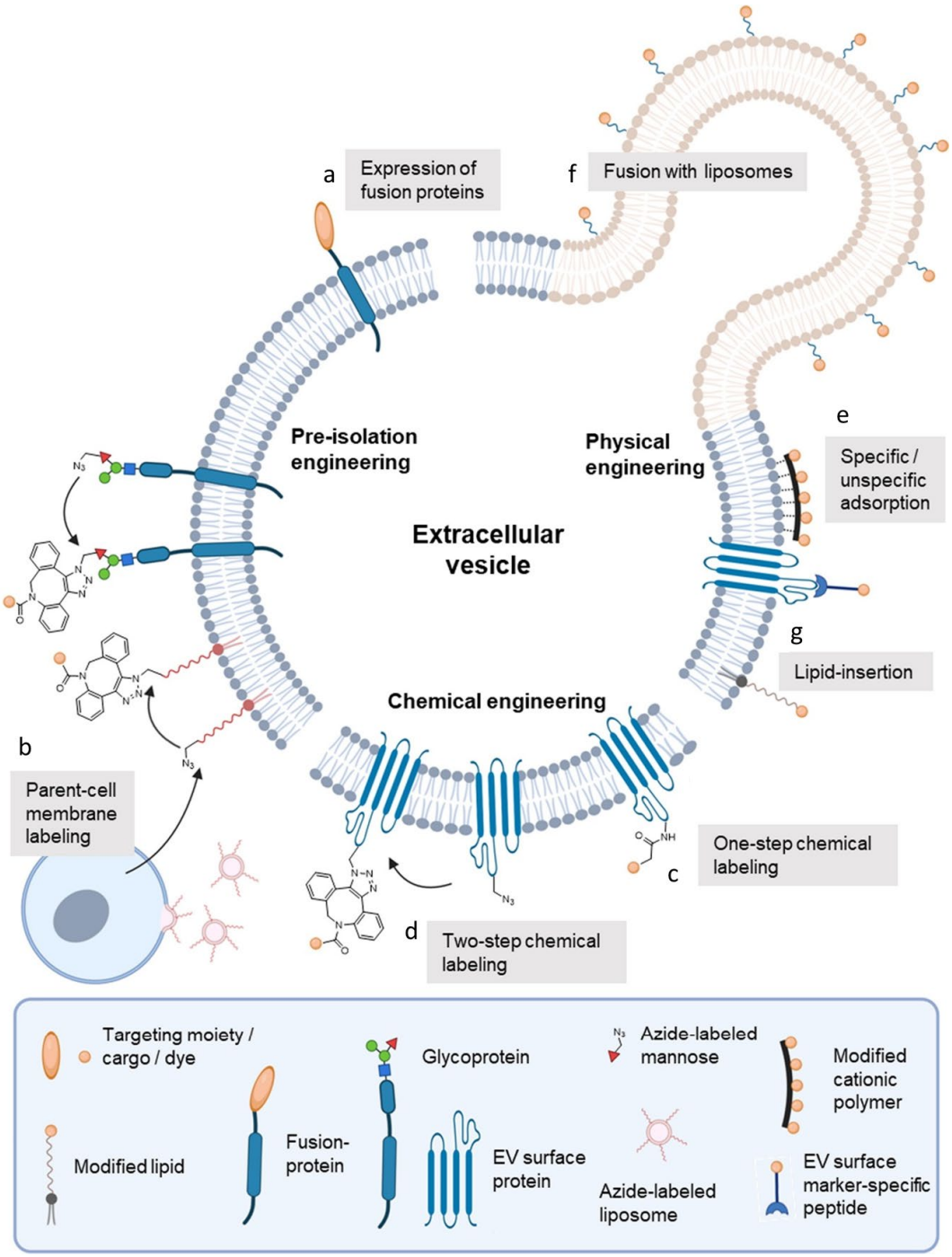

Figure 16. Overview of EV surface engineering methods. There are multiple approaches to the surface engineering of EVs. **(a)** Modification can take place before EV isolation, by expressing fusion proteins of EV membrane-proteins and the protein of interest. **(b)** Alternatively, EVs bearing azide groups can be generated by fusing them with azide-labelled liposomes, and parent-cell membrane labelling. Azide-labeled EVs can subsequently be functionalized using e.g. strain-promoted alkyne-azide cycloaddition (SPAAC). After EV isolation, the vesicles can be engineered by chemical or physical means. Chemical engineering with simple molecules can be carried out in **(c)** one step through a reaction with amino acid side chains of EV surface proteins. **(d)** More complex molecules can be coupled chemically to EVs by first introducing azide groups that may subsequently be labelled by SPAAC. Physical engineering can take place through **(e)** specific or unspecific adsorption of molecules to the EV surface, **(f)** fusion with liposomes, and **(g)** the insertion of lipids. Image modified from [36].

7.8 Biomedical application

7.8.1 Liquid biopsy

EVs can be used as biomarkers for diagnostic applications. Many approaches have been established for the efficient detection of EVs. However, most exosome detection approaches rely on CD63 and other biomarkers. CD63-based detection may not be accurate due to the heterogeneous properties of cancer cells and their exosomes. Furthermore, the purity of the EV preparations can affect the final detection. A different combination of different antibodies will become a more efficient approach for detecting exosomes. Furthermore, the discovery of more specific biomarkers of exosomes will significantly promote the applications of exosome-based diagnosis in clinical practice [43].

7.8.2 Vaccination against Infectious Disease

One of the first EV therapeutic applications was the vaccination against infectious diseases. In some cases, the immune response induced by EVs is more effective than the one produced by protein subunit–based vaccines. Typically, this type of vaccine uses vesicles with pro-inflammatory properties and provokes cell-mediated immunity and T helper 1 (Th1)-type immune responses, which are most effective for clearing viral and bacterial infections. If no effective antigen-based vaccine exists for a specific pathogen, EV-based vaccines provide a new therapeutic strategy [44].

7.8.3 Cell-to-cell communications

Before the "nano-revolution" of the 2000s, soluble molecules and direct interactions dominated research in the communication between cells. In 2013, the Nobel Prize in Physiology or Medicine was awarded to three scientists for their outstanding contributions to the EV mechanism in cell-to-cell communication. The number of studies about this topic exponentially increased and confirmed that EVs are a powerful tool for functional molecule delivery. Cell-to-cell communications via EVs have played essential roles in gene-guided anti-tumour applications. [43]

7.8.4 Intrinsic Therapeutic Activity

EVs from various cell sources have therapeutic potential. Vesicles derived from mesenchymal stem cells (MSCs) are promising for enhancing recovery from several injuries. In mice, the MSC EVs help to I) reduce hypoxia-induced inflammation and hypertension and II) decrease myocardial infarct size. III) MSC EVs can have a neuroprotective effect after brain injuries, IV) can promote remyelination of the central nervous system (CNS), and V) can deliver specific micro-RNAs and other molecules to mouse breast cancer cells and downregulate the expression of vascular endothelial growth factor (VEGF) and decrease tumour growth. EVs can bring therapeutic benefits by alternatively attenuating or promoting immune responses and inflammation. Placental EVs inhibit maternal immune rejection of the foetus and protect non-placental cells from viral infection by upregulating autophagy through the transfer of miRNAs. EVs from tolerised immune cells suppress various inflammatory diseases in mice, including contact sensitivity. Moreover, EVs can be harnessed as antiviral therapeutics by activating specific types of immune function. [44]

7.8.5 Vaccination to Treat Cancer

EV vaccines have the potential to prevent and treat cancers. Usually, tumours are highly heterogeneous, their surface biomarker expression is unstable. Vaccination with EVs derived by homogenisation and sonication of melanomas decreased tumour growth and metastasis in mice. These results have motivated the production of EV vaccines now in clinical trials. Highly active targeting capability, highly efficient drug delivery and low cytotoxicity are the main factors required for the final anti-tumour applications and efficacy. [44]

7.8.6 EV-mediated delivery of exogenous therapeutic biomolecules

The ideal NPs carries the drug load safely to a predefined target. En route, the NPs prevent unwanted interactions of the drug load with non-target tissues. The circulation time of the encapsulated drug is improved and sustained inside the body. At the target site, their cargo is released into the intracellular or extracellular space. Combined they could advance vesicles as drug-delivery entities. To obtain these ideal NPs, three main strategies have emerged to integrate the best of both worlds, merging the advantageous properties of synthetic NPs with those of EVs.

I) Generation of hybrid EVs. The first strategy is to generate hybrid EVs, consisting of both EV and synthetic NP components. This confers the tunability of synthetic NPs onto natural EVs and enables modification of the EV lipid bilayer. This may tune the cellular uptake of the EV and could aid in enhancing EV stability, circulation time, targeting properties, etc.

II) Bioinspired lipo NPs. Second, the inherent biocompatibility of EVs serves as an inspiration for the liposome field to generate synthetic vesicles that incorporate the advantageous characteristics of natural EVs. As such, the lipid compositions of liposomes are becoming increasingly complex to resemble the lipidomic characterisation of EVs. Furthermore, the addition of targeting moieties to the liposome surface takes inspiration from the findings of EVs. This type of bioinspired approach, which retains extensive control over the content of the vesicles generated, could be highly advantageous for future clinical approval.

IV) Increase the scale of production and the control of cargo. A third approach is the generation of vesicles from cellular membranes using a cell shearing procedure. As elucidation of the underlying processes by which cells select the incorporated EV cargo is still ongoing, the control over the EV composition is limited. This method aims to retain biocompatibility and increase the scale of production and internal cargo control.

EVs display characteristics of ideal delivery vehicles, including a lipid composition that enhances vesicle stability in circulation and proteins that slow EV clearance, like complement inhibitors and phagocytosis. Targeting EVs to specific cell types can reduce off-target effects and increase specific uptake by target recipient cells. Moreover, EVs can deliver therapeutic biomolecules like nucleic acids to small molecules [44]. For nervous system disease therapy, the main obstacle is the blood-brain barrier (BBB). Traditional macromolecular drugs and NMs have failed to cross the BBB. This EV-based approach has prominent advantages over the conventional NM-based DDSs because the EVs have excellent biocompatibility and high nanoscale stability. The EVs can easily cross the BBB and deliver therapeutic agents to cure neurogenic-related diseases [43]. The research demonstrated that EVs could be used for biomedical imaging and tumour diagnosis. However, the active targeting ability needed to be further improved [43].

In sum, there is mounting preclinical evidence that EV-based therapeutics are promising and uniquely well suited to various applications. In the future, convenient and low-cost strategies should be intensively exploited instead of expensive methods. The packaged therapeutic agents could be controllably released via near-infrared laser irradiation. The EV-based immunotherapy should focus on decreasing the immunogenicity and stabilising the surface molecule expression. Besides, the immune content loading efficiency also needs to be improved [43].

7.8.7 COVID-19

The 2020s changed the world with the Coronavirus (COVID-19) pandemic. Many treatments have been employed to overcome it. Exosome-based technology has also been used to fight this terrible pandemic. In 2021, a novel therapy for COVID-19 was developed. During COVID-19 infection, a cytokine storm takes place in the lung. This happens when the immune system goes into overdrive and starts attacking healthy cells. As a result, inflammation arises, becoming the principal cause of patient health deterioration and a death prognosis in COVID-19. Some evidence suggests that the small protein CD24, which is involved in the control of T-cells proliferation and can negatively regulate inflammation. Therefore, as exosomes are involved in cell-

to-cell communication, their use for CD24 protein delivery to the lungs helps calm down the immune system. NCT04747574 is a phase I study, which includes CD24-exosomes. The exosomes deliver CD24 directly to the target organ and inhibit the cytokine storm. This novel treatment is administrated to patients through an inhalation device by aerosol. This direct administration route throughout an inhalation device opens new possibilities for engineered exosomes as a new therapy for lung cancer treatment [45].

Chapter 8

Aims and rationale of the thesis

8 Aims and rationale of the thesis

Strictly focusing on organic NPs, most nanomedicines currently on the market are simple liposomes, extensively used as carriers for numerous molecules in the cosmetic and pharmaceutical industries. The liposomes are small artificial NPs, which consist of a sphere-shaped bilayer that usually comprises cholesterol, up to three non-toxic natural lipid types, and up to two therapeutic agents, enclosed as cargo (hydrophilic drugs/molecules) or embedded in the membrane (lipophilic drugs/molecules). Despite liposomes being clinically used combined with a wide variety of therapeutic agents, the realisation of the true potential of bio NPs awaits the implementation of more complex multifunctional designs. The ideal design of a bio-nanocompatible system is presumably to require a level of complexity similar to that of the biological environment to enable successful evasion of obstacles, including degradation, clearance, and physical barriers, such as the blood-brain barrier (BBB), the endothelium, and the cell membrane, and enable the delivery of the cargo in the desired localisation. Theoretically, multiple design and manufacturing challenges in nanomedicine could be bypassed by exploiting the evolutionary selection of extracellular vesicles (EVs) occurring and preserved in all organisms of all kingdoms of life. The EV structures are naturally designed for the specific and selective transport of molecular cargo. EVs resemble liposomes in size, shape and structure. However, they have a more complex lipid bilayer containing hundreds of distinct types of lipids, proteins and carbohydrates, as well as surface-associated molecules and internal cargo. EVs play a vital role in intercellular communication in multifarious physiological and pathological processes. EVs can be obtained from biological materials like tissues and fluids but also from the conditioned medium of cell cultures. However, the heterogeneity of EVs and the existence of other biological NPs (i.e. secretome NPs [1]) with overlapping properties make EV isolation extremely challenging. The ability of EVs to transport biomolecules, on the surface or as cargo, to recipient cells has made them attractive for drug delivery purposes. The implementation of various techniques of targeting directly against specific cell types using engineering approaches on the EV membrane and the optimisation of loading protocols (passive incubation, osmotic shock, extrusion and electroporation, sonication, and freeze-thaw) to combine the EVs and synthetic NPs or incorporate therapeutic agents have led to significant advances in the field of bio nanomedicine. However, the potential of hybrid EVs for drug delivery remains uncertain due to challenges in hybrid-EV isolation and characterisation that have hampered basic and translational studies.

8.1 BOW project

Inorganic NPs have shown remarkable potential for broad applications over the past decades. Among others, the biological compatibilities and interplay of NPs have been extensively studied for expanding their development in biomedical applications such as bioimaging, biosensing, and drug delivery systems (DDSs). Magnetic metal oxide NPs can be exploited as nanocarriers of substances optically active either that can emit optical signals upon excitation. However, using magnetic metal oxide NPs in bioimaging is challenging due to I) their loading capability, II) synthesis complexity, III) regulatory hurdles, IV) imaging efficiency, V) toxicity of the intrinsic ingredients, VI) batch reproducibility, VII) production cost, VIII) in vivo stability, and IX) storage.

In recent times, magnetic NPs have gained notable interest because of their progress in image-guided therapy (e.g., fluorescence, magnetic resonance, X-ray CT) and cancer theranostics favourable properties I) tunable size, II) generating reactive oxygen species (ROS) or heat, III) simple fabrication, IV) energy transfer, and V) X-ray absorption properties. Moreover, their long-term toxicity and dispersion stability must be specifically investigated [24]. Despite the impressive technological advancement in the design of "smart" NPs, the functionalisation of NPs that satisfies the clinical need for safety, interaction with the immune system, targeting, biodistribution, fate and toxicity is yet to come. On the other hand, extracellular vesicles (EVs) promise to be the necessary switch to unlock NP power in precision medicine. The EV innate precision, circulation capacity, and targeting performance of EVs are derived from the unique cell-tailored composition and structure of their membrane, which is inaccessible to synthetic mimic NPs. The composition and structure of the EV membrane contain specific proteins and lipid structures that regulate the inflow and outflow of small molecules, transmit electrical currents, and modulate ligand-receptor interactions as a part of cellular communication. Moreover, the EV membrane protects and destines the EV cargo to specific cells and mediates cell interaction. Biomedical engineering has become more precise and sophisticated and the demand for highly functionalized biomaterials has increased. In particular, novel organic/inorganic hybrid biomaterials with two or more chemical, physical, and optical properties are currently being developed and applied in various biomedical fields [19].

The Biogenic Organotropic Wetsuits (BOW) project [2] plans to take the combination of synthetic and biological NP to the next level by developing a technology that assembles hybrid biogenic-synthetic nanodevices (evMBD). The evMBDs are made by an inorganic core in the specific, magnetic iron oxide NPs (MBDs) [14] enveloped by a “wetsuit” made of biological EV membrane from sustainable sources (microalgae [46–48] and mesenchymal stromal cells from endothelial decidual-tissue, EDT-MSCs). These hybrid ENMs represent the first brilliant examples of suitable NPs, providing exciting solutions for combining the surface complexity of biological systems with the convenient properties of NPs. Among the other leading challenges of the BOW project are included I) the production of high-grade extracellular vesicles with biomimetic and organotrophic functions; II) the synthesis and functionalisation of MBDs; III) the design of a microfluidic device for the fabrication of hybrid EVs and IV) the control of biological performance and nanotoxicity *in vitro, ex vivo and in vivo*.

This part of the project was performed at the Biochemical Engineering Laboratory of Prof. Paolo Arosio at Eidgenössische Technische Hochschule Zürich (ETHZ) [49], and in collaboration with the Nanomag laboratory of Prof. José Rivas Rey at the University of Santiago de Compostela (USC), the Cellular Dynamics Laboratory of Dr. Antonella Bongiovanni National Research Council (CNR) of Palermo and Rigenerand Srl.

The project included the characterisation of the EVs produced by different sources (HEK293-F cell lines, EDT-MSCs, and Algae). Furthermore, exploiting the plasmonic properties of citrate-capped gold NPs (AuNPs) [50, 51], a modified-label-free colorimetric nanoplasmonic (CONAN [50]) assay was developed to evaluate the hybrid nanodevice synthesis obtained through an acoustic-microfluidic device. The estimated loading results were correlated and validated throw an orthogonal technique, the Föster Resonance Energy Transfer [36, 41] (FRET) Assay. First, the evaluated the single components, MBD and the vesicles, was performed. MBDs consist of two elements I) magnetic iron oxide nanospheres that form the single or multi-core enclosed within a II) silica shell. Core and shell form superparamagnetic iron oxide NPs (MBDs). As biological membranes were employed different formulations of vesicles, including liposomes with different diameters (~100 nm and ~200 nm) made of 1-palmitoyl-2-oleoyl-glycero-3-phosphocholine (POPC), sphingomyelin and cholesterol, and EVs derived from various sources (Hek239F cell culture, mesenchymal stromal/stem cell culture (MSCs), and *Tetraselmis chuii* microalgae culture). Afterwards, an anionic gold NPs (AuNPs) with a diameter of 16 nm was synthetised and characterised. Then the interaction between citrate-stabilised AuNPs (**Figure 17a - 18**), and I) the MBDs (single and multicore) (**Figure 17b - 18**)); II) the biological NPs (Liposomes (**Figure 17c - 18**) and EVs (**Figure 17d - 18**)); III) hybrid NPs composed of MBDs covered by biogenic lipid membranes (evMBD

(**Figure 18**)) was characterised. The peculiar AuNP physical-chemical interaction with the phospholipid membrane was exploited to estimate the coverage of MBDs and to quantify the coating. This specific interaction with the organic and inorganic NPs provides insight into the "dressing" ratio of the NPs thanks to the unique properties of AuNPs. The characterisation of the biogenic-synthetic hybrid nanodevice was validated with different approaches by coupling orthogonal methods and techniques that produced qualitative data and quantitative measurements of the coverage of the MBDs (FRET, single-molecule localization microscopy (SMLM), cryo Transmission Electron Microscope (cryo-TEM) etc.).

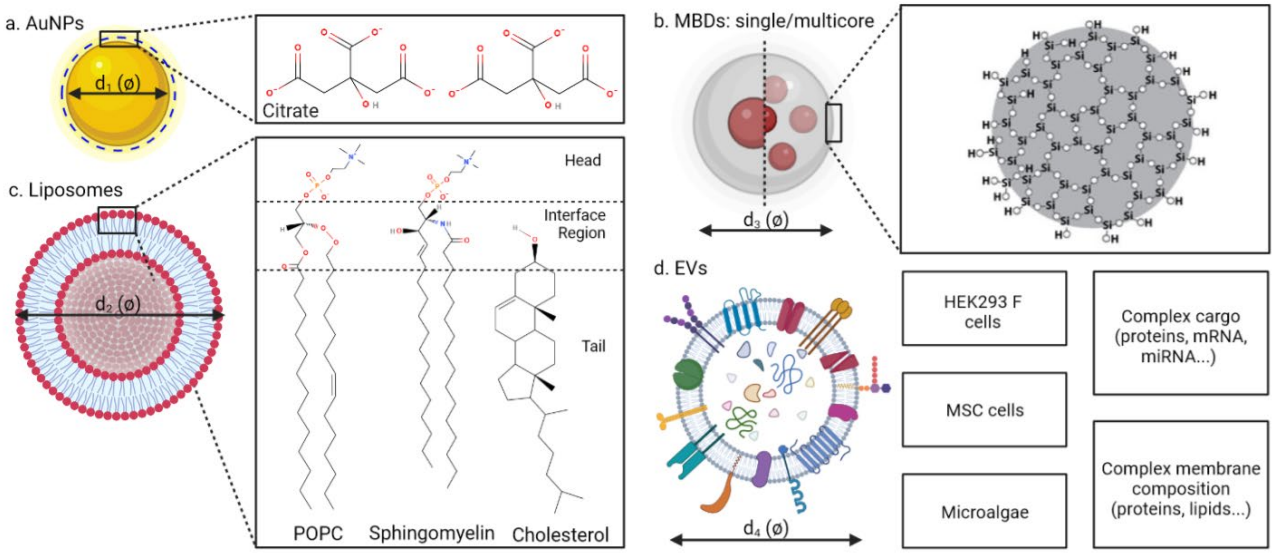

Figure 17. Summary of the main NPs used in the BOW project. AuNPs: citrate-stabilised gold nanoparticle. EVs: extracellular vesicles. MBDs: magnetic beads devices. MSC: mesenchymal stromal/stem cells. POPC: 1-palmitoyl-2-oleoyl-glycero-3-phosphocholine. Self-made image.

8.2 PRIN project

Conventional small-molecule drugs consist of single chemical entities with dimensional ranges from about 0.6 to 2 nm [19]. Although the pharmacology of a small molecule drug can often be improved by designing analogues, some restrictions remain. For example, failure to solubilise when applied intravenously, unfavourable half-life, or failure to cross biological barriers will limit the delivery of a drug to the target organ or correct cellular location. Post-administration capture by the molecular and cellular elements of body fluids, lack of activation at the target site, and premature export from target cells via membrane carriers can further limit the therapeutic efficacy of the drug. It is a central goal of NP drug design to overcome such restrictions. It is well-established that nano-sized particles have been used in pharmacology and diagnostics before the onset of NP engineering. For example, colloidal gold has been applied in disease treatment and polymeric gold compounds are used to treat otherwise therapy-resistant rheumatoid arthritis. However, the engineering of more complex nanostructures to improve therapeutic and diagnostic possibilities started only some 20 years ago.

Breast cancer is the second cause of cancer-associated mortality worldwide [52]. The triple-negative breast cancer incidence (TNBC, deadliest subtype) is increasing in young women and represents approximately 15-20% of newly-diagnosed breast cancers [53].TNBC is associated with high metastasis rates, drug resistance, and poor prognosis. TNBC relapses are scarcely sensitive to endocrine and trastuzumab-based therapies, being cytotoxic drugs (Paclitaxel (PTX), Taxol) the only alternative. Unfortunately, many chemotherapeutics have low aqueous solubility, thus requiring the use of specific formulations (e.g. micelles, liposomes or Extracellular Vesicles (EVs)) for parenteral administration [54]. Currently, the treatment of TNBC is hindered by drug toxicity and resistance, and there are no targeted therapies due to the lack of specific surface markers. However, bio-nanotechnology has brought new opportunities, offering the possibility to develop innovative DDSs in TNBC, such as extracellular vesicle EV-based carriers. Cells naturally release EVs that

circulate between tissues and organs and can cross biological barriers, shuttling bioactive molecules. EVs are involved in the regulation of immune processes, in particular, in anti-tumour responses. They are suitable for DDS for cancer therapy.

My PhD project has therefore the objective to produce EVs on a large scale and engineers them to develop an EV-based nanocarrier for the targeted delivery of anti-cancer drugs to TNBC cells and obtain a targeting specificity. CTX [55–58] is an monoclonal antibody recognising Epidermal Growth Factor Receptor (EGFR) [55–58]. EGFR is highly expressed in TNBC tumour cell (60%). The CTX-EVs (**Figure 18**) can target the EGFR on the cell surface and drive the targeting [55–58]. During this project, I worked on the modification of CTX (**Figure 18**) in collaboration with Prof. Giuseppe Pomarico (University of Brescia), coupling it to a fluorophore (CY7.5) to track it in solution and adding to it a functional group (Dibenzocyclooctyne-amine, DBCO) to bind CTX to a PEGylated-EVs (N3-(Peg)4-NHS-Ester) to perform a "Click Chemistry" reaction. First, CTX was modified binding the DBCO and the CY7.5 molecule and the reaction parameters were optimized. The modified CTX (mCTX (**Figure 18**)) was tested to evaluate if the modification hampered its ability to recognise EGFR. The binding tests were carried out using Surface Plasmon Resonance (SPR) spectroscopy in collaboration with Prof. Marco Rusnati (University of Brescia). Indeed, SPR [59, 60] is ideal for observing interactions between molecules in real time and obtaining kinetic data (e.g. binding constants). Meanwhile, the CTX metabolic activity *in vitro* [61] was evaluated thanks to the Cell mito-stress test assay on the Seahorse platform. In addition, these protocols were optimised. The first step was the selection of two suitable cell lines, positive and negative control, MDA-MB-231 (EGFR+) and MDA-MB-456 (EGFR-), respectively. Afterwards, the optimisation of the number of cells on both cell lines and the CTX activity was evaluated. Moreover, the concentration di CTX and Carbonyl cyanide-4-(trifluoromethoxy) phenylhydrazone (FCCP) concentration was explored for the MDA-MB-231. Afterwards, a massive amount of EVs (**Figure 18**) was produced (more than 10 litres of conditioned medium), isolated and characterised from different cell lines (PC3, PC3-CD63-GFP, MDA-MB-453, MDA-MB-231, MDA-MB-231-CD63-GFP, and HeLa cells) and human plasma. These EVs were used to set the experiments and optimised the EV engineering protocols and the SPR protocol. The final validation of the results was performed with the induced EV produced from the red blood cells (RBC-EVs) due to their high and effortless production level and uniform distribution (**Figure 18**).

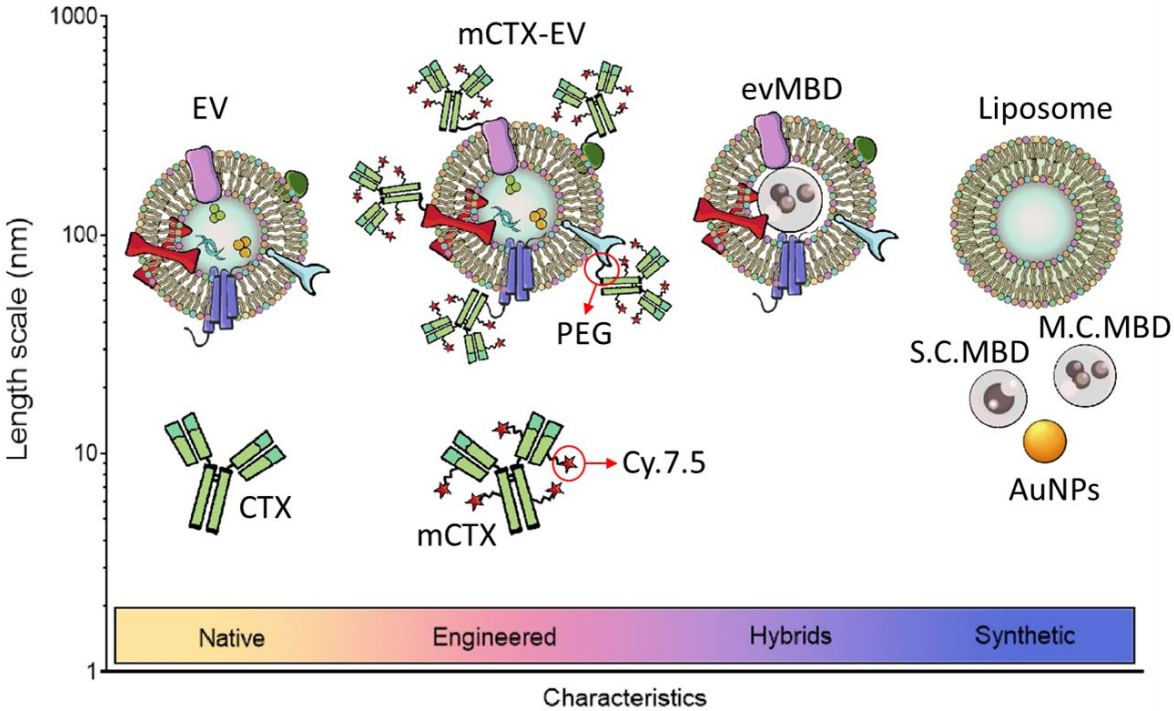

Figure 18. The length scale of all natural, engineered, hybrid, and synthetic NPs used in the projects. Self-made image.

Chapter 9

Materials and Methods

9 BOW project - Materials and Methods

9.1 Ethical statement and safety procedures

Cells from donors. The donation procurement, isolation, and testing were performed in full respect of national guidelines/regulations (Cells and Tissues Directive 2006/17/EC of 8 February 2006 implementing Directive 2004/23/EC and the national Italian Law DL 25/01/2010 n.16). After approval by the Modena Ethical Committee on human studies (http://www.aou.mo.it/ComitatoEticoProvinciale) by Rigenerand Srl (Medolla 41036, MO, Italy https://rigenerand-biotech.com/; now Evotec Srl https://www.evotec.com/en). Written consents of healthy donors and Local Ethical Committee approval were mandatory requirements to accept the starting material and for further processing.

All the cell manipulation procedures were performed under the Biohazard cabinet (Class II, Type2).

9.2 Cell lines culture and microalgae cultivation

Materials. CD 293 medium (Cat#11913019, Gibco), GlutaMAX (Cat#35050061, Gibco), Pluronic™ F-68 (Cat#24040032, Gibco). Minimal Essential Medium Alpha (MEM-Alpha, Cat#:12561056 Gibco), Fetal Bovine Serum (FBS, Gibco), Exosome-depleted FBS (Gibco), Penicillin-Streptomycin (P.S., Gibco), Ciprofloxacin (Cipro, Fresenius Kabi), Glutamine (Glu, Gibco), Heparin (Veracer), Human Platelet Lysate (PLP, Macopharma), Phosphate Buffered Saline pH 7.4 (1X) w/o Ca Mg (PBS, Glibco), TrypLE Select (TrypLE, Glibco). Flask T25/T75/T125 (Greiner Bio-One), CELLdisc 1/4/8 layer/s (Greiner Bio-One). f/2 medium (UTEX).

9.2.1 Human embryonic kidney cell line

EV source. Human Embryonic Kidney 293 (HEK293) cell line is a permanent line established from primary embryonic human kidney and transformed with sheared human adenovirus type 5 DNA[62]. HEK293 cells are tumorigenic and have high proliferation rates. The HEK 293-F cell line is a variant of the HEK293 cell line that has been adapted to suspension growth.HEK293-F cells were purchased from the Grand Island Biological Company (Gibco Thermo Fisher Scientific, Inc., MA, USA).

Cell cultures. The HEK293-F cell line was cultivated at the Department of Chemistry and Applied Biosciences, ETH Zurich, Zurich, Switzerland. HEK293-F cells were cultured in CD 293 medium supplemented with 4×10^{-3}M GlutaMAX and 250 mg L^{-1} Pluronic F-68 at 37°C, 8% CO_2, and 125 rpm for 96 hours. Conditioned media (200 mL) was harvested from ≈2.2×10^{8} cells with 97% viability [63]. The conditioned media was stored at -80°C before EV isolation.

9.2.2 Human endometrial decidual tissue-derived mesenchymal stromal cells

EV source. Human Endometrial Decidual Tissue derived Mesenchymal Stromal Cells (EDT-MSC/MSC) were collected, isolated and expanded, following optimized protocols from Rossignoli *et al.* 2013 and Álvarez *et al.* 2018 [64, 65]. Donors are aged between 18-45 years old and were checked for Hepatitis B surface antigen (HbsAg), Hepatitis B core antigen (HbcAb), Hepatitis C virus (HCV), human immunodeficiency virus 1-2 (HIV

1-2), Veneral Disease Research Laboratories (VDRL), Treponema Pallidum Hemagglutination Test (TPHA), Cytomegalovirus IgG, Toxoplasma, and Rubeo virus (IgG and IgM).

Cell cultures. The MSC cell lines were cultivated at Rigenerand facilities in Medolla, Modena, Italy. The culture medium for EDT-MSC isolation was composed of MEM-Alpha, 10% FBS, 1% P.S., and 1% Glu. The medium for MSC expansion was made by MEM-Alpha, 2.5% PLP, 1% Glu, 0.5% Cipro, and 0.2% Heparin. The culture medium for EV isolation was composed of MEM-Alpha, 10% Exosome-depleted FBS, 1% Glu, and 0.5% Cipro.

After the evaluation of the blood sample volume, the blood was diluted 1:2 with a PBS solution (PBS 1% heparin, 1% fluconazole, 1% P.S.). The sample was homogenized by 10 passages through a 19G needle using a 10-30 mL syringe. The homogenate was centrifuged at 450g for 10 min, RT with Benchtop centrifuges (SL8R and Heraeus Multifuge 1XR, ThermoScientific). The supernatant was carefully removed and the pellet was resuspended in the isolation medium with a ratio sample volume/cell culture surface equal to 0.33. The culture was incubated at 37°C, 5% CO_2 for 48-72 h. After the incubation, the cell culture was washed twice with PBS and the isolation medium was changed. These operations were performed every 48-72 hours until the cells reach 90-95% of confluency, around 12-16 days after the isolation. To expand the cell culture, the cell medium was removed and the cells were washed twice with PBS. The TrypLE (0,024 mL/cm^2) was added to the culture and the cells were incubated for 3-5 minutes at 37°C, with 5% CO_2. After the detachment of the cells, the TrypLE action was stopped by diluting it in an equal amount of PBS. The cells were collected and in centrifuge tubes and were centrifuged at 316 ×g for 5 min, at RT. The supernatant was removed and the cells were resuspended using I) Expansion medium for cell passage 0, 1, and 2. The culturing surface was evaluated considering 6.000-7.000 cells/cm^2 and the entire number of cells were seeded; II) PBS for cell passage 3-5. The remaining cells were seeded at 6.000-7.000 cells/cm^2 using the EV isolation culture medium. After 48-72 hours, the conditioned medium containing EVs was collected and was centrifuged at 800g for 20-30 minutes at 4°C (to pellet apoptotic bodies/cellular debris/cells). The supernatant was transferred into a new tube while the pellet was discarded. The supernatant was stored at -80°C before EV isolation.

9.2.3 Tetraselmis chuii microalgae

EV source. *Tetraselmis chuii* microalgae [47] is a chlorophyceaen photosynthetic marine microalga possessing an array of bioactive pigments and essential fatty acids identified as a suitable candidate for biogenic NP production, that offer an increased EV yield production [46].

Cell cultures. The cultivation of *Tetraselmis chuii* microalgae was performed at Institute for Research and Biomedical Innovation (IRIB) – National Research Council (CNR), Palermo, Italy. The marine chlorophyte Tetraselmis chuii CCAP 66/21b was grown in a borosilicate glass flask in an f/2 medium [66] up to its exponential growth phase and then used, via a 10% v/v inoculum, to inoculate a 7.5 L culture in a photobioreactor PB 200 (GroTech GmbH, Germany) at an initial concentration of 0.5 mg/ml (wet weight). The cultures were maintained at a temperature of 20 ± 2°C, with a white light intensity of 100 µEm−2s−1 and a 14:10 light/dark photoperiod for 30 days before processing by EVs separation [48].

9.3 EV isolation protocols

The isolation protocols were compared and optimised based on the sources of EVs to obtain pure and homogeneous preparations of EVs.

9.3.1 MSC and HEK293 EV isolation with differential ultracentrifugation

Cell culture supernatants were centrifuged at 800 ×g for 30 minutes (A-4-44 rotor, 5804R Eppendorf centrifuge) to obtain the first pellet (P1) containing the large EVs (LEVs). The supernatant was transferred in polycarbonate tubes (Cat#357003 Beckman Coulter) and was centrifuged at 16,000 ×g for 45 minutes (ja20 rotor, Avanti J25) to reap a medium EV (MEV)-enriched pellet (P2). The supernatant was transferred to polycarbonate tubes (Cat# 355622 Beckmann Coulter) and was ultracentrifuged at 100,000 ×g for 4 h (TY45i

rotor, Optima XP80, Beckman Coulter) to obtain a small EV (SEV)-enriched pellet (P3). The resulting pellets (P1, P2, and P3) were washed by resuspension in filtered PBS (final volume 1.5 mL). P1 and P2 were re-pelleted at the respective *g force* and time (45-30-11 rotor, 5417C Eppendorf centrifuge); P3 was re-pelleted at 100,000×g for 2 h (TLA-55 rotor, Optima MAX, Beckmann Coulter). All steps were performed at 4°C, centrifugations speed decreased with the max brake on [67]. Finally, EV pellets were re-suspended in 100 µL of PBS 1X (or pure water for the Atomic Force Microscopy analysis) supplemented with a 1:1000 P.I. Cocktail. The EV preparations were characterized and were frozen at −80 °C until further use.

9.3.2 MSC and HEK293 EV isolation with size-exclusion chromatography (SEC)

For EV isolation by SEC, 100 mL of harvested conditioned medium was filtered through a 0.22um syringe filter (Cat#99722, TPP). Pierce nuclease (0.5 units/mL, Invitrogen) was added to the filtered media and was incubated for 2.5 hours. The media was concentrated to less than 500 µL using Amicon 30 kDa ultrafilter (Cat#UFC9030, Millipore) and it was corrected to 500 µL using PBS. Afterwards, the media was centrifuged at 7,000 ×g for 10 minutes to remove any larger aggregates. The size exclusion chromatography (SEC) was performed using Sepharose CL-4B resin (Cat#17015001, Cytiva Lifesciences) packed into a Bio-Rad gravity flow column. The supernatant from the centrifugation was added to the top of the resin and the flow-through was discarded. PBS was continuously added while 500 µL fractions are collected. The fractions between five to eight contain the isolated EVs and were pooled and concentrated to 1-10E11 particles/mL using an Amicon 50kDa ultrafilter. The EV preparations were characterised and were frozen at −80 °C until further use [63].

9.3.3 MSC EV isolation using tangential flow filtration (TFF).

The EV isolation was performed using the KrosFlo® KR2i TFF System from (Repligen Spectrum Labs) and with the following set of cartridges: I) C1, with a cut-off of 650 nm (D04-E65U-07-N, Repligen Spectrum Labs), II) C2, with a cut-off of 200 nm (D04-P20U-10-N, Repligen Spectrum Labs), and III) C3, with a cut-off of 500KDa~25 nm (D05-E500-10-N, Repligen Spectrum Labs). Before use, the cartridges were washed with sterile water until the output flow solution reaches neutral pH. Moreover, at the end of the filtration, the TFF cartridges were cleaned using NaOH 0.2 M according to the manufacturer's datasheet and stored in NaOH 0.05 M.

Briefly, the EV-conditioned medium was centrifuged at 800 ×g for 30 minutes at 4°C (A-4-44 rotor, 5804R Eppendorf centrifuge). The resulting pellet was discarded while the supernatant was transferred to a clean bottle. The TFF system was set at the following parameters: I) Concentration mode, II) Concentration factor: 10x, III) Feed flow rate: between 100 mL/min and 200 mL/min, IV) transmembrane pressure (TMP): 0.5 psi. The supernatant was clarified through C1. The first retentate (R1) was collected and stored at 4°C while the first permeate (P1) was processed with C2. Again, the second retentate (R2) was collected and stored at 4°C and the second permeate (P2) was filtered through C3 to obtain the last retentate (R3) and the last permeate (P3). At the end of the protocol, four fractions were collected I) R1 containing particles with a size > 650 nm, II) R2 containing particles with a size between 650 nm and 200 nm, III) R3 containing particles with a size between 200 nm and 25 nm and, IV) P3 containing particles with a size < 25 nm. The collected fractions were concentrated using Centricon Plus-70 centrifugal filters (MWCO 100kDa, Millipore) following the manufacturer's instructions and the EV preparations were characterised and were frozen at −80 °C until further use.

9.3.4 Microalgae EV isolation using Tangential flow filtration

Briefly, microalgae clarification and EV concentration were performed using a TFF ÄKTA Crossflow system (GE Healthcare, USA) and three GE Healthcare polysulfone hollow fibre membranes. After 30 days of cultivation, the reactor (containing typically 7.5 L of cell culture) was connected to the TFF system and the cell suspension was clarified by microfiltration with a 450 nm hollow fibre cartridge (ÄKTA Crossflow). Feed flow was kept constant at 110 ml/min and transmembrane pressure (TMP) was set at 0.05 bar. The first

retentate (R1, particle size > 450 nm) was concentrated into a final volume of 100–200 ml and used to observe the integrity of cells by light microscopy. The 450 nm permeate (P1, particle size < 450 nm) was processed using a 200 nm hollow fibre membrane with a feed flow of 140 ml/min and 0.05 bar of TMP. The second permeate (P2, particle size < 200 nm) was concentrated using a 50 kDa MWCO hollow fibre membrane with a feed flow of 42 ml/min and a TMP of 0.45 bar (R3), while the permeate (P3) was discarded. This TFF preparation (R3) corresponds to the sEVs and is considered the TFF-isolated nanoalgosomes. Nanoalgosomes were characterized as described in previous work [46]. Afterwards, nanoalgosome preparations were frozen at −80 °C until further use [46].

9.4 EV characterisation

9.4.1 Purity CONAN assay

EV preparations purity was checked by the Colorimetric Nanoplasmonic (CONAN) assay. The CONAN assay exploits the nanoplasmonic properties of AuNPs and their peculiar interaction with exogenous protein contaminants (EPCs) composed of soluble single and aggregated proteins, and with lipid bilayers [51]. When the AuNP solution is mixed with pure EV formulations, the AuNPs cluster on the EV membrane, whereas, when the AuNPs are mixed with protein-contaminated EV formulation, the EPCs create a protein corona on the surface of the AuNPs, which prevents the clustering of the AuNPs on the EV membrane. The difference between these two conditions can be observed thanks to the LSPR phenomena.

When AuNPs cluster on the EV lipid membranes, a broadening and redshift of the LSPR is observed, resulting in a colour change of the AuNP solution from red to blue. The redshift can be evaluated through UV-Vis spectroscopy, and the UV/Vis/NIR absorption spectrum is correlated to the purity grade of the EV formulation. The aggregation index (AI) quantifies the purity grade of the EV samples. AI is described as the ratio between the absorbance at the LSPR wavelength of the AuNPs, which depends on the AuNP size, and the absorbance at 650 nm plus the absorbance at 850 nm, which describes the red-shift wavelength [50].

$$AI = \frac{Abs_{LSPR}}{Abs_{650nm} + Abs_{850nm}}$$

Briefly, the experiment was conducted in triplicate as described in [68]. EV samples were diluted by 1:1, 1:2, 1:5, and 1:10 in HPLC water. In a 96-multiwell plate, 2 µl of EV preparations were added to 23 µl of HPLC water (final volume 25 µl). Subsequently, 6nM AuNP solution (50 µl) was added to the EV preparation (final concentration 3 nM) and then mixed with 25 µl of PBS 1X (final volume 100 µl). The mixes were incubated for 30 minutes at RT and the UV/vis/NIR absorption spectra (from 400 nm to 900 nm) were collected using the multi-mode microplate reader CLARIOstar® Plus (BMG LABTECH). The elaboration of the dataset was performed using a custom Python script.

9.4.2 Protein concentration assay

BCA Protein Assay. The protein content of EV preparations was measured using the micro-bicinchoninic BCA Protein Assay Kit (Thermo Fishers Scientific) following the manufacturer's instructions. BCA Protein Assay is a colorimetric method that provides a relative concentration to a bovine serum albumin standard (BSA), which is used for the preparation of a calibration curve. The relative absorbance of the BCA soluble compound was measured at 562 nm using a CLARIOstar® Plus multi-mode plate reader (BMG LABTECH).

Bradford assay. The Bradford assay is a colorimetric protein assay based on an absorbance shift of the dye Coomassie Brilliant Blue G-250. The Coomassie Brilliant Blue G-250 dye exists in three forms: anionic (blue), neutral (green), and cationic (red). During the assay, the red form of the dye is converted into the blue form due to the formation of bonds with functional protein groups and the colour change can be measured using UV/Vis spectrophotometer. The blue form of dye has the maximum absorption at 595 nm. The increase of

absorbance at 595 nm is proportional to the amount of bound dye, and thus to the concentration of sample's proteins.

To determine the EV protein concentration, a BSA (Sigma) standard calibration curve was created with known concentrations (0, 2, 4, 8, 12 and 16 µg/µl). Absorbance values of standards, measured with spectrophotometer (Microplate reader, Model 680, Biorad) were correlated with the respective BSA concentration to create a calibration line. Absorbance values of the samples were interpolated with the calibration curve to obtain the protein concentration.

9.4.3 Dynamic Light Scattering Measurements (DLS)

Size distributions and polydispersity index (PDI) of the NPs and liposomes were measured using a Zetasizer Nano ZSP DLS instrument (Malvern) working in backscattering mode at 173°at 20°C. Particle-free PBS or water was used as dilution buffer based on the buffer of the sample [63].

9.4.4 Nanoparticle Tracking Analysis Measurements

NP size distribution and concentration were measured using a NanoSight NS300 (Malvern Panalytical, UK) at CNR of Palermo for the nanoalgosomes and a *ZetaView*® Nanoparticle Tracking Analysis (NTA) instrument (Particle Metrix) at ETH Zurich for the NPs and cell EVs measurements.

At CNR, the NanoSight NS300 was equipped with a 488 nm laser, a high sensitivity sCMOS camera and a syringe pump. Briefly, EV samples were diluted in pure water to generate a dilution in which 20–120 particles per frame were tracked (concentration range between 10^8 and 10^9 particles/mL as recommended). Five experiment videos (duration of 60-s) were analysed using NTA3.4 Build 3.4.003 (camera level 15–16). The frames were analysed by applying instrument-optimized settings [46]. Further settings, such as blur size and Max Jump Distance were set to 'automatic' and viscosity to that of water (0.841 - 0.844 cP).

At ETH Zurich, the NP size distribution and concentration were measured using a *ZetaView*® Nanoparticle Tracking Analysis (NTA) instrument (Particle Metrix) equipped with a CMOS camera and a 405 nm laser. Briefly, the sample chamber was calibrated with polystyrene NP (PS) standards according to the manufacturer's recommendation. EV or liposome samples were diluted in particle-free water or PBS (based on the buffer of the sample) to obtain a concentration within the recommended measurement range between 10^7 and 10^9 particles/mL. The samples were injected until the chamber was filled using a 1 mL syringe. Videos were acquired at 11 positions in the chamber at a frame rate of 30/s, with a trace length of 15 frames and using 85% scattering intensity and 150 shutter in light scattering mode [46, 63]. The experiments were repeated in triplicates and analysed with the ZetaView analysis software (ZetaView 8.04.02 SP2).

9.4.5 Western blot analysis

Materials of 293F-EVs. Lysis buffer (20 x 10^{-3} M Tris, 150 x 10^{-3} M NaCl, 5 × 10^{-3} M EDTA, 1% Triton-X, 25 × 10^{-3} M NaF, 1 x 10^{-3} M PMSF, 1 x 10^{-3} M Na_3VO_4, and protease inhibitors), blocking buffer (5% BSA in Tris-buffered saline (TBS) with 0.1% Tween-20, TBS-T).

The 293F-EVs characterisation by Western Blot was performed in previous work [63]. The HEK 293F cells were pelleted at 200 ×g for 5 minutes and were rinsed with PBS. The 293F-EVs and the 293F cells were treated with the lysis buffer for 30 minutes on ice at 4 °C. For the cell lysate preparation, the cell debris was pelleted by centrifugation at 15.400 ×g for 10min.

Immunoblotting of 293F-EVs. Cell lysate (35 µg) and EV lysate (12 µl) were loaded on 12% sodium dodecyl-sulfate polyacrylamide (SDS-PAGE) gels and separated at 100 V for 2 h in a Mini-PROTEAN Tetra Cell (Biorad). Proteins were transferred on a polyvinylidene difluoride (PVDF) membrane (Biorad) with a Mini Trans-Blot module (Biorad). The membrane was blocked with blocking buffer for 2 h, at RT and incubated overnight at

4 °C under agitation with 1:1000 primary antibody dilutions (CD63 antibody Mx-49.129.5, CD81 antibody 5A6, Alix antibody 1A12, TSG101 antibody C-2, Calnexin antibody AF18, GAPDH antibody G-9, Santa Cruz Biotechnology Inc.) in blocking buffer. The membrane was washed four times with TBS-T and was incubated for 2 h, at RT with a 1:1000 secondary anti-mouse HRP conjugated antibody dilution (m-IgG$_K$ BP-HRP, Santa Cruz Biotechnology)[63]. Blots were detected using enhanced chemi-luminescence solution (Western Blotting Luminol Reagent, Santa Cruz Biotechnology) and Chemidoc imaging system (Biorad).

Materials of MSC EVs. Loading buffer (reducing SDS sample buffer (80 mM Tris, pH 6.8, 2%SDS, 7.5% glycerol, 0.01% bromophenol blue) supplemented with 2% 2-mercaptoethanol (Sigma-Aldrich)), blocking buffer (5% (w/v) non-fat dried skim milk in PBS with 0.05% Tween-20, PBST).

Total cell homogenates and EV preparations were mixed with proper volumes of 6X loading buffer. The samples were boiled at 95°C for 5 minutes and separated by SDS-PAGE on acrylamide/bisacrylamide 10% gel.

Immunoblotting of MSC EVs. Samples were normalized for EVs concentration when possible (20 µg) or alternatively, equal volumes of each sample were loaded on a SDS−PAGE gel (25 µL). Total cell homogenates (20 µg) of and an equal volume of EVs preparations (25 µL) were loaded on a 10% SDS-PAGE gel and were separated for 1.30 h at 100 V. The proteins were transferred on a PVDF membrane (GE Healthcare) for 1h at 100 V. Membranes were blocked with blocking solution for 1h at 37°C and afterwards, they were washed three times with PBST before the incubation (under agitation, overnight at 4 °C) with primary antibodies diluted in 1% (w/v) non-fat dried skim milk in PBST. After three washes with PBST, the membranes were incubated with the HRP-conjugated secondary antibody diluted in 1% (w/v) non-fat dried skim milk in PBST for 1 h, at RT. After three washes with PBST, the detection of the immunocomplexes was performed using Clarity Western ECL (Biorad) on G:Box Chemi XT Imaging system (Syngene)

The following primary antibodies and dilutions were used: rabbit polyclonal anti-alpha Actinin 4 (1:1000, Cat#GTX101669, Genetex), mouse monoclonal anti-Alix (1:500, Cat#sc-53539, Santa Cruz), rabbit polyclonal anti-Annexin XI (1:1000, Cat#GTX33010, Genetex), mouse monoclonal anti-CD63 (1:1000, Cat#CBL553, Millipore), mouse monoclonal anti-CD9 (1:500, Cat#sc-7637, Santa Cruz), and rabbit monoclonal anti-CD90 (1:1000, Cat#ab133350, Abcam).

The following HRP-conjugated secondary anti- bodies and dilutions were used: rabbit polyclonal anti-mouse and (1:5000, Cat#A90-117P, Bethyl) and goat polyclonal anti-rabbit at (1:5000, Cat#A120-101P, Bethyl), rabbit monoclonal anti-CD63 (1:500, Cat#ab134045, Abcam), rabbit monoclonal anti-APO A1 (1:500, Cat#).

Materials of algae EVs. Loading buffer (0.25 M Tris-Cl pH 6.8, 10% SDS, 50% glycerol, 0.25 M dithiothreitol (DTT), 0.25% bromophenol blue), BSA-TBS-T solution (3% powdered with bovine serum albumin in TBST (50 mM Tris HCl pH 8.0, 150 mM NaCl with 0.05% Tween 20).

The algae EVs characterisation by Western Blot was performed in previous work [46–48].

Immunoblotting of algae EVs. Cell lysate and EV samples (30 µg) were mixed with proper volumes of 5X loading buffer. The samples were heated at 100°C for 5 minutes and were loaded in a 10% SDS-PAGE gel for electrophoretic analyses. Proteins were blotted onto PVDF membranes, which were blocked with BSA-TBS-T solution for 1 h, at RT, followed by primary antibody incubation overnight at 4°C. The antibodies anti-Alix (clone 3A9, dil. 1:150), anti-Enolase (clone A5, dil. 1:400), anti-β-actin (clone AC15 dil. 1:400) in 3%BSA/TBS-T1X and anti-HSP70 (cloneW27 dil. 1:500) in 5%Milk/TBS-T1X (Santa Cruz Biotechnology, USA). Anti H+/ATPase (dil. 1:1000 in 3% BSA/TBS-T1x, Agrisera), is incubated for 1 h at room temperature. After washing, the membrane was incubated for 1 h with secondary antibodies according to the manufacturer's instructions (horseradish peroxidase-conjugated secondary anti-mouse or anti-rabbit antibodies, Cell Signaling). The membranes was washed four times in TBST for 20 min. The immunoblots were revealed using SuperSignal Pierce ECL (Thermo Fisher Scientific).

9.4.6 Atomic force microscopy (AFM)

EV preparations were characterized by size and morphology thanks to the AFM analysis.

MSC EVs. All AFM experiments were performed in ultrapure water at room temperature. Briefly, EV pellets were diluted 1:10 v/v with sterile H2O (Milli-Q, Merck Millipore). Briefly, EV pellets were diluted 1:10 v/v with sterile H2O (Milli-Q, Merck Millipore). 5 to 10 µL of EV samples were then spotted onto freshly cleaved mica sheets (PELCO® Mica discs Grade V-1, thickness 0.15 mm, 10 mm diameter from Ted Pella, Inc) and air dried over a plate heated at 37-40°C for 10 minutes. Dried samples were imaged in tapping mode with NaioAFM (Nanosurf AG) equipped with Multi75AI-G (Budget Sensors) tip (Resonant Frequency ≈ 75 kHz; Force Constant ≈ 3 N/m). Images were collected over different length scales (scan size ranged from 1 µm to 15 µm with a scan speed of ranged from 0.8 sec/line to 1 sec/line). Images were collected over different length scales with a scan size ranging from 1µm to 25µm with a and a scan speed of 1 s per scanning line. The larger ones allowed the characterisation of the samples as a whole in terms of homogeneity or other collective parameters while those collected at higher magnification showed in detail the shape and size of individual vesicles. The obtained topography images were processed with Gwyddion ver. 2.61 software, while EVs size distributions were obtained analyzing with ImageJ (PSA macro).

Algae EVs. EV samples were concentrated by ultracentrifugation and were resuspended in MilliQ water to a final concentration of 5×10^{11} particles/ml, as previously estimated by NTA. For measurements on dry samples, a 30 µl drop of the samples was directly deposited on freshly cleaved mica, incubated for 10 min, and then gently dried under nitrogen flow. Atomic Force Microscopy images were captured by using a Nanowizard III scanning probe microscope (JPK instruments, AG Germany) equipped with a 12-µm scanner. Measurements were performed in tapping mode by using a NSC-15 (Mikromasch) cantilever (spring constant 40 N/m, typical tip radius 8 nm). Measurements with softer cantilevers (data not shown) were carried out with MSNL-10 cantilevers (Bruker; lever D, spring constant 0.03 N/m, nominal tip radius 2 nm) [46].

9.4.7 Cryo-transmission electron microscopy (cryo-TEM)

For the Cryo-TEM analysis, the acceleration voltage was 200 kV and the device was coupled with an axis Gatan US1000 2k CCD camera [46]. Liquid nitrogen was used as a cooling medium. The EV samples were concentrated using Amicon Ultra-2 µl Centrifugal Filters (Molecular weight cut-off (MWCO): 30 kDa, Merck, Germany). The samples (10 µl) were placed onto a 400 mesh copper grid covered with lacey film, which was treated with oxygen plasma to make it hydrophilic, and immobilized using high-pressure freezing (Engineering Office M. Wohlwend GmbH, Switzerland). The specimen (sapphire discs with cells) was enclosed and protected in a small volume between two specimen carriers and locked inside the specimen pressure chamber by blotting two times for 3 s each. After the preparation, the samples were carefully transferred into liquid nitrogen for further imaging. Imaging was performed on a TEM (FEI Tecnai F20) microscope [46].

9.5 Synthesis of MBD

9.5.1 Preparation of external polydopamine-derivatized Single-Core MBDs

Materials. 2-Propanol (CH_3CH (OH) CH_3, IPA, HPLC grade, Merck), Ammonium hydroxide (NH_4OH, Purity 28%, Panreac), Biological degree water (H_2O, Purity 100%, Corning), Cyclohexane (C_6H_{12}, CHX, Purity 99.7%, Scharlau), Dopamine Hydrochloride ($C_8H_{11}NO_2$, DA, Purity 98%, Merck), Ethanol (CH_3CH2OH, EtOH, Absolute, Scharlau), Hydrochloric acid (HCl, Purity 37%, VWR Chemicals). Iron(II) Sulfate Heptahydrate ($FeSO_4 \cdot 7H_2O$, Purity 99% , Merck), Iron(III) Chloride Hexahydrate ($FeCl_3 \cdot 6H_2O$, Purity 99%, Merck), Milli-Q water (H_2O, Purity 100%, Milli-Q), Oleic Acid ($C_{18}H_{34}O_2$, OA, Purity 90%, Merck), Polyoxyethylene(5)nonylphenylether ($(C_2H_4O)_5 \cdot [C_{15}H_{24}O]$, IGEPAL CO-520, Merck). Tetraethyl orthosilicate ($Si(OC_2H_5)_4$, TEOS, Purity 98%, Alfa-Aesar), rhodamine B isothiocyanate ($C_{29}H_{30}N_3O_3S$, RITC, mixed isomers, Merck), Sodium citrate dihydrate ($HOC(COONa)(CH_2COONa)_2 \cdot 2H_2O$, Purity 99%, Merck).

MG-544 was prepared according to the method described below.

S.C.MBD@SiO2-PDA. For the external polydopamine single core superparamagnetic (SP) iron oxide (IO) NPs (PDA-S.C.MBDs) the protocol includes three steps [14]: I) Co-precipitation method to produce Fe_3O_4 cores following Massart's approach [69] with some modifications; II) Microemulsion method to produce Fe_3O_4@SiO_2 NPs following the water-in-cyclohexane reverse microemulsion process technique reported by Moldes *et al*.[18, 70, 71] (experimental details can be found in S1) and; III) Application of external derivatization with PDA (MBD@SiO_2 -PDA NPs) through a polymerization method.

Co-precipitation method to produce Fe_3O_4 cores. The first reaction led to the production of iron oxide NPs coated with oleic acid (MBD@OA NPs) by co-precipitation, according to the reaction equation $Fe^{2+} + 2Fe^{3+} + 8OH^- \rightarrow Fe_3O_4 + 4H_2O \rightarrow 2Fe(OH)_3Fe(OH)_2 \rightarrow Fe_3O_4 + 4H_2O$.

Superparamagnetic (SP) Fe_3O_4 NPs (MBDs) coated with oleic acid (OA) were obtained by the co-precipitation method. In a typical synthesis, $FeCl_3 \cdot 6H_2O$ (45mmol) and $FeSO_4 \cdot 7H_2O$ (30mmol) were dissolved in 100 mL of HCl solution (10 mM) through mechanically stirring. The mixture was heated up to 60°C under mechanical stirring. Ammonium hydroxide (NH_4OH, 770nmol) and oleic acid (OA, 1.11mmol) were added, and the reaction was carried out for 1 hours in the same conditions. Afterwards, the obtained MBD@OA NPs (MNPs) were transferred to a beaker on a 100 °C plate to allow flocculation. The precipitate containing MBD@OA NPs was magnetically separated from the reaction medium using neodymium (NdFeB) permanent magnet and were washed three times with Milli-Q water. At the end, the MBD@OA NPs were redispersed in cyclohexane (CHX) and the remaining water was completely removed from the organic phase by using a decantation funnel [14]. The NPs were stored at room temperature (RT).

Microemulsion method to produce MBD@SiO_2 NPs. MBD@OA NPs were coated with silica (Fe_3O_4@SiO_2) by a water-in-cyclohexane reverse microemulsion process reported in Moldes *et al*.[18]. Experimental details can be found in S1.

Briefly, 128 mg of MBD@OA dispersed in 250 mL of CHX, were added to a mixture of IGEPAL CO-520 (19.5 mmol) and CHX (250 mL) and were mixed and mechanically stirred for 30 min. 2.1 mL of $NH_4(OH)$ and 2.4 mL of TEOS was added to complete the reaction at room temperature for 16 hours. MBD@SiO_2 NPs were retained with a using neodymium (NdFeB) permanent magnet and were washed four times using 2-propanol (IPA). MBD@SiO_2 NPs were washed twice with Milli-Q water, and were centrifuged at 9,000 rpm for 15 minutes. The pellet contain the MBD@SiO_2 NPs was redispersed in Milli-Q water.

External derivatization with PDA (MBD@SiO_2-PDA NPs) through a polymerization method. The last step led to the functionalisation of MBD@SiO_2 with polydopamine (MBD@SiO_2-PDA) based on the dopamine polymerization on MBD@SiO_2. MBD@SiO_2NPs (31 mg) were dispersed in 10mL of Milli-Q water. Then NH_4OH (1mmol) and dopamine hydrochloride (0.19 mmol) were added and the mixture was incubated at 70°C under orbital stirring at 300rpm for 16 hours. MBD@SiO_2-PDA were separated from the reaction medium by a magnetic field and were washed six times with Milli-Q water. Finally, MBD@SiO_2-PDA were re-dispersed in Milli-Q water to a final concentration of 0.1 % wt (256 µg MBDs).

9.5.2 Preparation of RITC-doped Single-Core and Multi-Core magnetite MBDs

MGAP-19 and MGAP-21 were prepared according to the method described below.

S.C.Fe_3O_4@SiO2-RITC-SiO_2. Rhodamine-derivatized S.C.MBDs (MBD@SiO_2-RITC-SiO_2 NPs) were obtained through a two-step procedure: I) thermal decomposition method to produce Fe_3O_4 cores and II) microemulsion method to produce fluorescent MBDs [18, 70, 71] .

Thermal decomposition method to produce Fe_3O_4 cores. OA-coated MNPs (MBD@OA) were prepared following Zhou's procedure [72]. Typically, iron-oleate complex (3mmol) and OA (1.5mmol) were added to a

flask containing ODE (50mL). After being filled with nitrogen atmosphere, the reaction mixture was heated at 320°C at a constant heating rate of 6°C/min and then kept at that temperature for 120 minutes. MNPs were precipitated, magnetically separated and washed with ethanol (x4) and cyclohexane (x4). Finally, MBD@OA NPs were resuspended in CHX [14].

Microemulsion method to produce MBD@SIO_2 NPs. In this case, MBD@OA NPs previously synthesized by thermal decomposition methods were used as magnetic cores for the design of MBD@SiO_2-RITC-SiO_2 following a water in cyclohexane reverse microemulsion process modified to incorporate the fluorescent molecule (RITC) into a silicate matrix and the silica coating on the MNPs.

RITC (0.037mmol) was dissolved in a sample vial in deoxygenated ethanol (35mL), and was kept under magnetic stirring (200rpm) for 30 minutes. Fe_3O_4@OA NPs (10 mg dispersed in CHX), Igepal CO-520 (3.6mmol) and cyclohexane (18.7mL) were mixed in a sample vial and orbital shaken using an incubator for 30 minutes. Finally, the addition of NH_3aq (210µL) and the tetraethyl orthosilicate (TEOS) were added in three stages to the reaction under the same orbital conditions during the entire procedure. First, TEOS (112mmol) was added to the synthesis and left 2 hours, followed by the addition of the RITC-fluorescent complex (30 µL). After 1h of incubation, TEOS (56mmol) was added to the mixture and left for 1 h to facilitate cross-linking. Finally, TEOS (56mmol) was introduced to the solution. The reaction required a further 16 hours at room temperature to complete the silica coating for the single core, and 63 hours for the multicore. After that, IPA was added to precipitate the fluorescent MNPs, which were magnetically separated and extensively washed with IPA (four times) and water (four times). Finally, the fluorescent single MBD@SiO_2-RITC-SiO_2 NPs were redispersed in Milli-Q water.

Sterilization and storage. The last step of the MNP washing procedure was carried out in a laminar flow hood using cell culture-grade water. All the obtained MNPs were submitted to UV light for 1 hours to sterilize each batch.

9.6 MBD characterisation

9.6.1 Microscopy Morphological Characterisation of MBDs

The morphology and size of the MBDs were studied by transmission electron microscopy (TEM) using a JEOL JEM-1011 microscope operating at 100 kV (JEOL, Tokyo, Japan). Samples were placed on copper grids with Formvar® films for analysis. The Image J program (distributed by NIH, USA) was used to measure the diameters of the MNPs [14].

9.6.2 Hydrodynamic Particle Size, Zeta Potential, and stability measurements

Hydrodynamic Particle Size. Measurements of hydrodynamic particle size and ζ-Potential of MBDs were routinely performed on the same instrument by a Zetasizer Nano ZS (Malvern Instruments, Worces- tershire, UK) equipped with a He–Ne laser (633nm) and operating at a scattering angle of 173° and at room temperature. All analysis were performed in triplicate. All multi- functional magnetic nanoprobes were dispersed in Milli-Q water with an iron or magnetic material concentration of 0.4mg/mL (approx.) and at pH 6.5 [14].

Zeta potential measurements. Zeta potential measurements were carried out using a Malvern Nano ZS instrument (Malvern Instruments,Worcestershire, UK) supplied by DTS Nano V7.11 software (Malvern Instruments, Worcestershire, UK) when the functionalized nanoprobes were dispersed in Milli-Q water with an iron or magnetic material concentration of 0.4mg/mL (approx.) and at pH 6.5. The Smoluchowski equation was used for zetametry measurements [14].

Stability in PBS buffer and after centrifugation. To verify stability in various buffer conditions, each MBD type was diluted to a stock concentration of 5E+11p/mL. The MBDs were dispersed in milli-Q water, 0.5X PBS or 1X PBS, and then the hydrodynamic particle size was evaluated by DLS analysis. To assess the eventual

aggregation after centrifugation protocols, the MBD preparations were centrifuged at 13,000 rpm for 15 minutes and washed with pure water (three times) before the hydrodynamic particle size (DH) was measured by DLS analysis. To avoid bias due to the different particle concentrations, the samples were measured trying to keep the same corps number during the measurement. The results are reported in (Figure X). For each type of MBDs, control samples without any centrifugation protocol and diluted in pure water were used.

Optical Properties. The optical properties were measured using a Fluorescent Spectrophotometer (Varian Cary Eclipse). Additionally, fluorescent MNPs imaging was performed with a fluorescence confocal multispectral imaging Confocal Laser microscope Leica TCS SP8 SMD. Technical specifications: resolution, 1024 × 1024; scan direction X, bidirectional; objective, HC PL APO CS 63×/1.40 OIL, using the 405 nm and 552 nm laser lines to PDA and RITC fluorescent visualization, respectively [14].

9.7 Nanoparticles preparations and characterisation

9.7.1 Preparation of fluorescent DIO and dye-free liposomes

Materials. Cholesterol ≥99% (Cat#C8667, Sigma-Aldrich Sigma Aldrich), 2-Oleoyl-1-palmitoyl-sn-glycero-3-phosphocholine ≥99.0% (POPC, 100 mg/mL, Cat#42773, Sigma Aldrich) Sphingomyelin from chicken egg yolk (Cat#85615, Sigma Aldrich), 3,3'-Dioctadecyloxacarbocyanine perchlorate (DIO, Cat#D4292, Sigma-Aldrich), Chloroform 100% (Cat#288306, Sigma Aldrich).

The POPC/sphingomyelin/cholesterol stock solutions (10mg/mL) and DiO stock solution (1mg/mL) were prepared in chloroform

Liposomes preparation via thin film hydration method. The solutions of cholesterol, sphingomyelin and POPC were mixed into a 50mL round bottom flask at followed ratio: 0.73mg of cholesterol, 0.5025mg of sphingomyelin, and 1.245mg of POPC, (molar ratio 1: 0.38: 0.87, respectively). For the DiO-stained liposomes, 0,0125mg of DiO were added to the mix. The chloroform was evaporated under a chemical hood under gentle nitrogen flux until a thin and homogeneous lipid film was formed at the bottom of the flask. The lipid film was completely dried under a vacuum by overnight rotary evaporation (25°C, 0.2bar). The film was hydrated with 5mL PBS (or pure water) and was incubated at 40°C in a water bath. The lipid solution was gently agitated every 5 minutes until the lipid film was completely dissolved. The lipid suspension was sonicated in a water bath for 3 minutes (Sweep mode, 30% power, 37 kHz frequency, 40°C). The lipid suspension was then extruded through polycarbonate membranes Whatman® Nuclepore™ Track-Etched Membranes (diameter 19mm, pore size 0.1µm or 0.2µm, Cat# WHA800309, Cytiva) for fifteen cycles per membrane to yield larger and smaller unilamellar lipid vesicles. Afterwards, every liposome batch was characterised via dynamic light scattering (DLS) and Nanoparticle tracking analysis (NTA) analysis. The liposome preparations were characterized via NTA and DLS, as described in [63], and were stored at 4°C.

9.7.2 Preparation of fluorescent methyl methacrylate NPs (MMA)

Materials. Methyl methacrylate (MMA, Sigma Aldrich), 2-hydroxyethyl methacrylate (HEMA, Sigma Aldrich), N-Hydroxysuccinimide (NHS, Carl Roth), N,N'-Dicyclohexylcarbodiimide (DCC, Sigma Aldrich), potassium persulfate (KPS, Sigma Aldrich), Rhodamine B (RhB, Sigma Aldrich) were used as received.

HEMA-RhB solution was prepared according to a previously published protocol [73]. Briefly, 50mg of RhB, 43mg of DCC, and 136mg of HEMA were dissolved in 63g of DCM and left to react overnight. The resulting HEMA-RhB solution was stored in the dark at 4°C before use.

Nanoparticles Synthesis. Fluorescent NPs covalently labelled with Rhodamine B were synthesized via surfactant-free emulsion polymerization of methyl methacrylate (MMA) by modifying previously published protocols [73, 74]. Briefly, 2.22g of HEMA-RhB solution was poured into a round bottom flask and purged with nitrogen to completely remove DCM. Subsequently, 2.22g of MMA and 73mg of KPS were dissolved in 25ml of a 40/60 vol/vol.% mixture of acetone/water and added to the round bottom flask. After purging with

nitrogen for 10 minutes, the mixture was heated to 70°C and left to react overnight under constant stirring. The obtained NPs were purified via dialysis against deionized water for 2 weeks with a dialysis tubing (Spectra/Por®, molecular weight cut-off (MWCO=3.5kDa)) by frequently changing the aqueous solution in order to remove the acetone and the unconjugated dye. The NPs were characterized via DLS as described in [73] (Dn=90 nm, PdI=0.187) and gravimetry (C_{NPs}= 21 mg/mL).

9.7.3 Preparation of gold nanoparticles

Materials. Gold(III) chloride trihydrate ($HAuCl_4$ $3H_2O$, Cat# 520918, Sigma Aldrich), Trisodium citrate dihydrate (Cat#W302600, Sigma Aldrich), HPLC grade water (Cat#270733, Sigma Aldrich).

$HAuCl_4$ solution (1mM, 20 mL) and trisodium citric aqueous solution (34.0 mM, 1.0%wt in pure water) were prepared in pure water.

Gold nanoparticles synthesis. Colloidal gold NPs (AuNPs) were synthesized through classic Turkevich's citrate reduction method [75]. Briefly, 20mL of HAuCl4 aqueous solution was brought to boiling temperature under constant and vigorous magnetic stirring. 2mL of trisodium citric solution were rapidly shot into the boiling solution under continuous heating and stirring. The formation of AuNPs was indicated by the colour change from the original pale yellow to deep red wine colour. The heating was turned off and after 10 minutes, the solution was cooled down in a water-ice bath.

Size and concentration of the gold nanoparticles. The evaluation of the size and concentration of the AuNPs was performed based on the UV-Vis spectrum according to the methods described in the literature [76, 77]. Briefly, the AuNPs solution was diluted in pure water (dilution 1:4) and the absorbance spectrum of the solution (from 400nm to 900nm) was measured with a multi-mode microplate reader CLARIOstar® Plus (BMG LABTECH) using a 96 multiwall plate (Cat#655080, GREINER) filled with 360µl of solution to reach 1cm of light path. The evaluation of the diameter (d/nm) of the monodispersed AuNPs was estimated thanks to the equation (**Eq. 1**) and the table (**Table 3**) reported in [77], where the Abs_{LSPR} corresponds to the maximum absorbance value of the spectrum and the Abs_{450} corresponds to the absorbance value at 450nm of wavelength.

Eq. 1 $$d(nm) = \frac{Abs_{LSPR}}{Abs_{450}}$$

Table 3. Correlation between the ratio of the absorbance of AuNPs at the localised surface plasma resonance peak (Abs_{LSPR}) to the absorbance at 450 nm (Abs_{450}) is correlated to the particle diameter (nm). Table modified from [77].

$\frac{Abs_{LSPR}}{Abs_{450nm}}$	$d\ (nm)$	$\frac{Abs_{LSPR}}{Abs_{450nm}}$	$d\ (nm)$	$\frac{Abs_{LSPR}}{Abs_{450nm}}$	$d\ (nm)$	$\frac{Abs_{LSPR}}{Abs_{450nm}}$	$d\ (nm)$	$\frac{Abs_{LSPR}}{Abs_{450nm}}$	$d\ (nm)$
		1.38	7	1.61	14	1.86	30	2.07	55
1.10	3	1.42	8	1.65	16	1.92	35	2.10	60
1.19	4	1.46	9	1.69	18	1.96	40	2.12	65
1.27	5	1.50	10	1.73	20	2.00	45	2.15	70
1.33	6	1.56	12	1.80	25	2.03	50	2.17	75

The concentration of AuNPs was determined using the Lambert-Beer law (**Eq. 2**).

Eq. 2 $$\mathrm{E}_\lambda = \varepsilon_\lambda \, \mathrm{l} \, \mathrm{c}$$

The data of ε_{450} can be used to calculate the particle concentration c in molarity (**Eq. 3**) from the absorption at 450 nm (Abs_{450}) for a standard path length l of 1 cm according to:

Eq. 3 $$c = \frac{Abs_{450}}{\varepsilon_{450}}$$

The molar concentration is equal to the ratio between the absorbance at 450nm and the molar extinction coefficient (ε). The ε is dependent on the d/nm and reported in table (**Table 4**).

Table 4. Correlation between diameter (nm) and the molar extinction coefficient. Table modified from [77].

$\boldsymbol{d}\ (\boldsymbol{nm})$	$\varepsilon_{450}\ (M^{-1}\ cm^{-1})$	$\boldsymbol{d}\ (\boldsymbol{nm})$	$\varepsilon_{450}\ (M^{-1}\ cm^{-1})$	$\boldsymbol{d}\ (\boldsymbol{nm})$	$\varepsilon_{450}\ (M^{-1}\ cm^{-1})$	$\boldsymbol{d}\ (\boldsymbol{nm})$	$\varepsilon_{450}\ (M^{-1}\ cm^{-1})$
		11	8.27E+07	**21**	6.31E+08	**31**	2.18E+09
2	4.25E+05	**12**	1.09E+08	**22**	7.31E+08	**32**	2.41E+09
3	1.49E+06	**13**	1.39E+08	**23**	8.42E+08	**33**	2.66E+09
4	3.62E+06	**14**	1.76E+08	**24**	9.64E+08	**34**	2.93E+09
5	7.20E+06	**15**	2.18E+08	**25**	1.10E+09	**35**	3.21E+09
6	1.26E+07	**16**	2.67E+08	**26**	1.24E+09	**36**	3.52E+09
7	2.03E+07	**17**	3.24E+08	**27**	1.40E+09	**37**	3.84E+09
8	3.07E+07	**18**	3.87E+08	**28**	1.58E+09	**38**	4.18E+09
9	4.43E+07	**19**	4.60E+08	**29**	1.76E+09	**39**	4.54E+09
10	6.15E+07	**20**	5.41E+08	**30**	1.96E+09	**40**	4.92E+09

9.8 Loading protocols

9.8.1 Common loading protocols

To compare and correlate the FRET and CONAN assays, these two analytical methods have been applied to assess loading in many commonly applied bulk-loading methods. Passive sonication, sonication, freeze-thaw and freeze-thaw plus sonication protocols were selected because they allow the same starting mixture to be used, avoiding distortions due to different initial preparations. The initial mixture (RhodamineB NPs (MMA NPs) or MBDs (with a RITC dye) and Liposomes (with or without DiO) was mixed with a 1:1 ratio, 2E+11p/mL each, final concentration of 1E+11p/mL) was split to be used in the loading protocols. In the sonication method, the mixture was sonicated into a sonicator bath at 37 kHz for 10 minutes at 35-40° C. For the freeze-thaw protocol, the mixture was immersed in liquid nitrogen for 1 minute to quickly freeze it and then the mixture was thawed in a water bath at 35°C for 10 minutes. The cycle was repeated 3 times. The Freeze-thaw plus sonication protocol is a fusion of sonication and freeze-thaw protocols. After 1 minute in liquid nitrogen, the mixture was sonicated for 10 minutes at 37kHz, 35-40°C, for two cycles.

9.8.2 Microfluidic device

The glass capillary devices were constructed using a glass capillary with an inner diameter of 0.5mm and four multiple piezoelectric transducers. The piezo elements were attached to the glass capillary using EPO-TEK H20E conductive epoxide. The epoxide was cured at 120°C for 30 minutes. Wires were attached to both terminals of the piezo elements using glue and conductive silver paste (Hans Wolbring GmbH). Each element was individually tested, before all the piezo elements were wired in parallel. The glass capillary was attached to PTFE tubing using heat shrink tubing.

The device was connected to an arbitrary wave function generator (GW Instek AFG-2225) generating and amplified to 1710kHz -2000kHz sine wave with a peak to peak amplitude of 20V-22V. The output of the wave generator was verified by connecting it to an oscilloscope (UNI-T UTD2025CL). At the resonance frequency, the actual peak-to-peak potential dropped to approximately 11V. The MBDs, Liposomes mixture (ratio 1:1, 2E+11p/mL each, final concentration 1E+11p/mL) was flown through the device at 10µL/min, which corresponded, to a residence time of approximately 1.30 minutes in the glass capillary.

9.9 Föster Resonance Energy Transfer (FRET) Assay

Förster Resonance Energy Tranfer (FRET) is based on the energy transfer between two fluorophores when they are in close proximity to one another. The required distance for FRET is generally considered to be between 1nm and 10nm. Therefore, the effective encapsulation of fluorescent NPs in fluorescent lipid membranes would lead to the proximity of the dye molecules incorporated in the two moieties inducing a successful energy transfer. The quantification of FRET fluorescence intensity provides a semi-quantitatively assess the encapsulation of the NPs since the FRET fluorescence signal is proportional to the number of encapsulated NPs. The RhodamineB NPs (MMA NPs) or MBDs (with a RITC dye) were mixed with DiO-liposomes (2E+11p/mL each, final concentration 2E+11p/mL). After the loading protocol, the sample was

diluted 20x before measurement with a multi-mode microplate reader CLARIOstar® Plus (BMG LABTECH). The sample was measured at three wavelength combinations: I) emission and excitation of the FRET acceptor (RhodamineB λex=550nm, λem=605nm), II) emission and excitation of the FRET donor (for Liposomes: DiO λex=460nm, λem=500nm), III) emission of the FRET acceptor and excitation of the FRET donor (FRET channel, λex=480nm, λem=605nm) (**Table 5**).

Table 5. Channels and wavelength of Excitation and Emission used in the FRET assay.

Channel name	Excitation (nm)	Emission (nm)	Gain
DiO (liposomes)	460-10	500-20	1600
FRET	480-10	605-40	1800
Rhodamine B (MMA NPs) / RITC (MBDs)	550-20	605-40	1600

The coefficients α and β (**Eq. 4**) account for the bleedthrough of the fluorophores into the FRET channel. They were obtained for each experiment by measuring a sample with only the donor or acceptor (i.e., liposomes or NPs only).

Eq. 4 $$\alpha = \frac{E_D^A\,(acceptor\ only\,)}{E_A^A\,(acceptor\ only)}; \qquad \beta = \frac{E_D^A\,(donor\ only)}{E_D^D\,(donor\ only)}$$

Where E denotes the measured fluorescence intensity at the emission wavelength of the superscript and the excitation wavelength of the subscript (A = FRET Acceptor wavelength, D = FRET Donor wavelength).

To calculate the FRET fluorescence signal the bleedthroughs of the dyes were subtracted from the overall signal (**Eq. 5**).

Eq. 5 $$FRET\ Fluorescence = E_D^A - \alpha \times E_A^A - \beta \times E_D^D$$

The FRET signal was normalized on the intensity of the Rhodamine/RITC signal inside the sample, which is proportional to the number of synthetic NPs in the sample.

Chapter 10

Results and discussion

10 BOW project - Results and discussion

10.1 EV characterisation

The following paragraphs describe an in-depth biochemical, biophysical and biological characterisation of the EV derived from the HEK293F cell line (HEK-EVs), the EV derived from Human endometrial decidual tissue-derived mesenchymal stromal cells (MSC-EVs) the microalgal-derived small extracellular vesicles (nanoalgosomes). The conditioned media was produced by culturing HEK293F cells, EDT-MSC starting from cryo-stock, followed by EV separation using differential ultracentrifugation (dUC) or size exclusion chromatography (SEC). The nanoalgosomes were isolated by dUC and TFF. The size and the isolated EV number were quantified using NTA. EV protein content was evaluated through the micro BCA protein assay or Bradford protein assay. Sample purity was verified using the CONAN assay. Finally, EV-marker expression was evaluated with WB. Additionally, isolated EV morphology was analysed at AFM and visualized using Cryo-TEM.

10.1.1 MSC EVs and nanoalgosomes isolated with dUC and TFF

The isolation of EVs from the MSC-conditioned culture media and microalgae-conditioned culture media was performed by the differential ultracentrifugation (dUC), a classic method for the EV enrichment [46, 67, 78], and by tangential flow filtration (TFF) [79, 80].

TFF has been increasingly applied in EV isolation, as gentler (low shear stress) purification method to optimize the recovery of intact EVs with consistent purity both in small and large-scale processes. Both dUC and TFF procedures allowed a reproducible separation of EVs. The AFM images (**Figure 19**) show the MSC-EVs sample obtained by dUC (**Figure 19a**) has less regular morphologies than the EV preparation isolated by TFF (**Figure 19b** and **Figure 19c**). This is probably because that dUC is a much more stressful method for the sample than TFF. By comparing the results obtained regarding the protein concentration (**Figure 19d**) and the concentration of particles (**Figure 19e**), it is possible to observe that both are superior using the TFF protocol compared to the dUC protocol. The protein content of the MSC-EVs is higher than that of the nanoalgosomes (**Figure 19f**) as the starvation medium of the MSC-EVs has the FBS which makes the purification of the MSC-EVs more challenging. For the nanoalgosomes, the yields, in terms of EV protein content and EV number, were consistent with the estimate of 10E+9 EV particles/μg EV proteins, as reported by Sverdlov [46, 81].

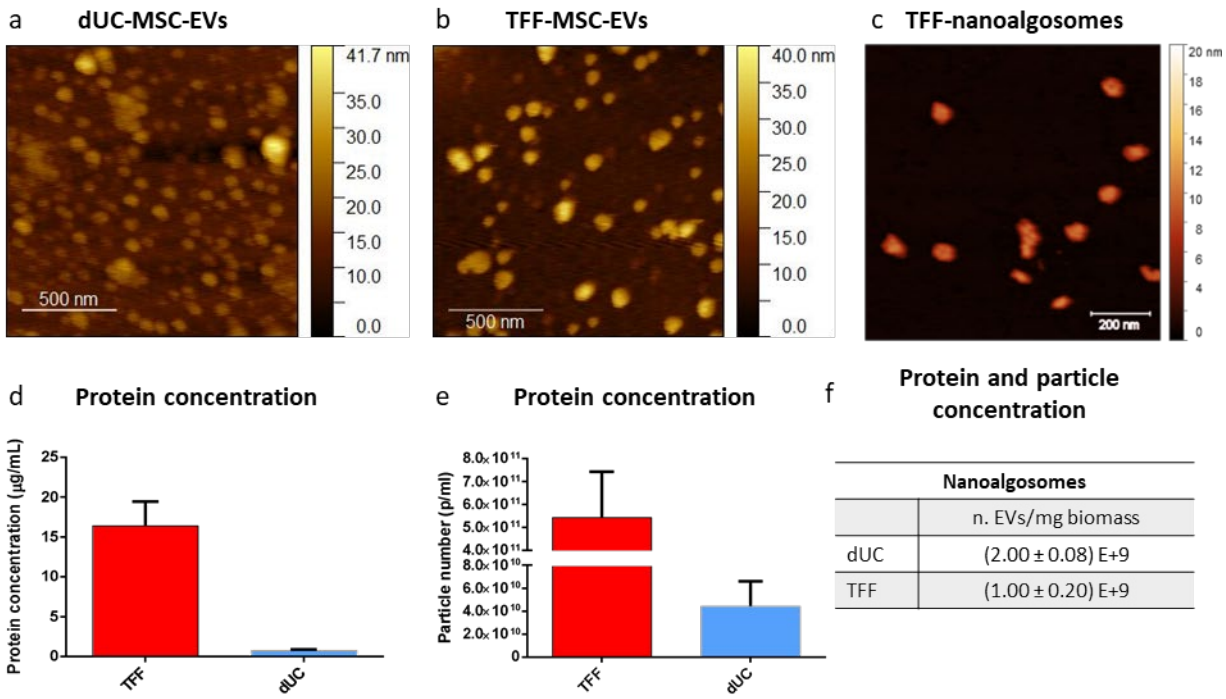

Nanoalgosomes	
	n. EVs/mg biomass
dUC	(2.00 ± 0.08) E+9
TFF	(1.00 ± 0.20) E+9

Figure 19. (a) Morphology of MSC-EVs isolated by differential ultracentrifugation. MSC-EVs (b) and nanoalgosomes (c) isolated by TFF. Wide-field tapping mode AFM images in air showing several EVs. The coloured scale on the right indicates the height for all AFM images. Representative images are presented at least three independent experiments (n ≥ 3). The MSC-EV yields is based on EV protein concentration (d), measured bymicro-bicinchoninic (BCA) colorimetric assay (µg/mL), and (e) particle numbers (p/mL), measured by Nanoparticle Tracking Analysis (NTA). (f) Table adapted from [46]. The EV yields is based on EV protein concentration, measured bymicro-bicinchoninic (BCA) colorimetric assay, and particle numbers (n. EVs), measured by Nanoparticle Tracking Analysis (NTA), both expressed per mg of dry weight microalgal biomass.

10.1.2 HEK293 EVs, MSC EVs and nanoalgosomes isolated by dUC and SEC

The size distribution and the particle concentration of the diluted EV samples were measured by NTA (**Figure 20**). The NTA experiments performed using ZetaView at ETH in Zurich were performed on HEK-EV (**Figure 20a**), MSC-EV (**Figure 20b**) and nanoalgosomes (**Figure 20c**). The HEK-EV samples were prepared with two isolation methods: I) dUC and II) size exclusion chromatography (SEC). The MSC-EV preparation was obtained by SEC. The protein content (µg / mL) and the particle numbers (p/mL), and the purity of all the preparations were measured using micro-bicinchoninic (BCA) colorimetric assay (**Figure 20e**), NTA (**Figure 20d**), and colorimetric nanoplasmonic assay (CONAN) assay (**Figure 20f, Figure 20g,** and **Figure 20h**), respectively. It can be observed from the size distribution (**Figure 20d**) how the different vesicular preparations are homogeneous and uniform in size among themselves, despite coming from various sources and a different isolation protocol. Significant differences in the results are highlighted regarding the CONAN protocol. Both preparations of HEK-EVs, purified with dUC and purified with SEC, respectively, show the same trend (**Figure 20f**). The trends changed with the SEC-MSC-EVs, in any case, present a positive outcome to the purity CONAN assay (**Figure 20g**). However, with this specific batch of nanoalgosomes, the response to the purity CONAN assay is unfavourable (**Figure 20h**). The negative test result can be determined by two different phenomena I) having a preparation contaminated with single and aggregate proteins (SAPs), or II) that there are not enough EVs within the preparation. This second hypothesis is confirmed by the concentration reported by the NTA and the TEM images, where few or no vesicles were detected. This may be due to problems in the delivery of nanoalgosomes preparation or to a problem during isolation.

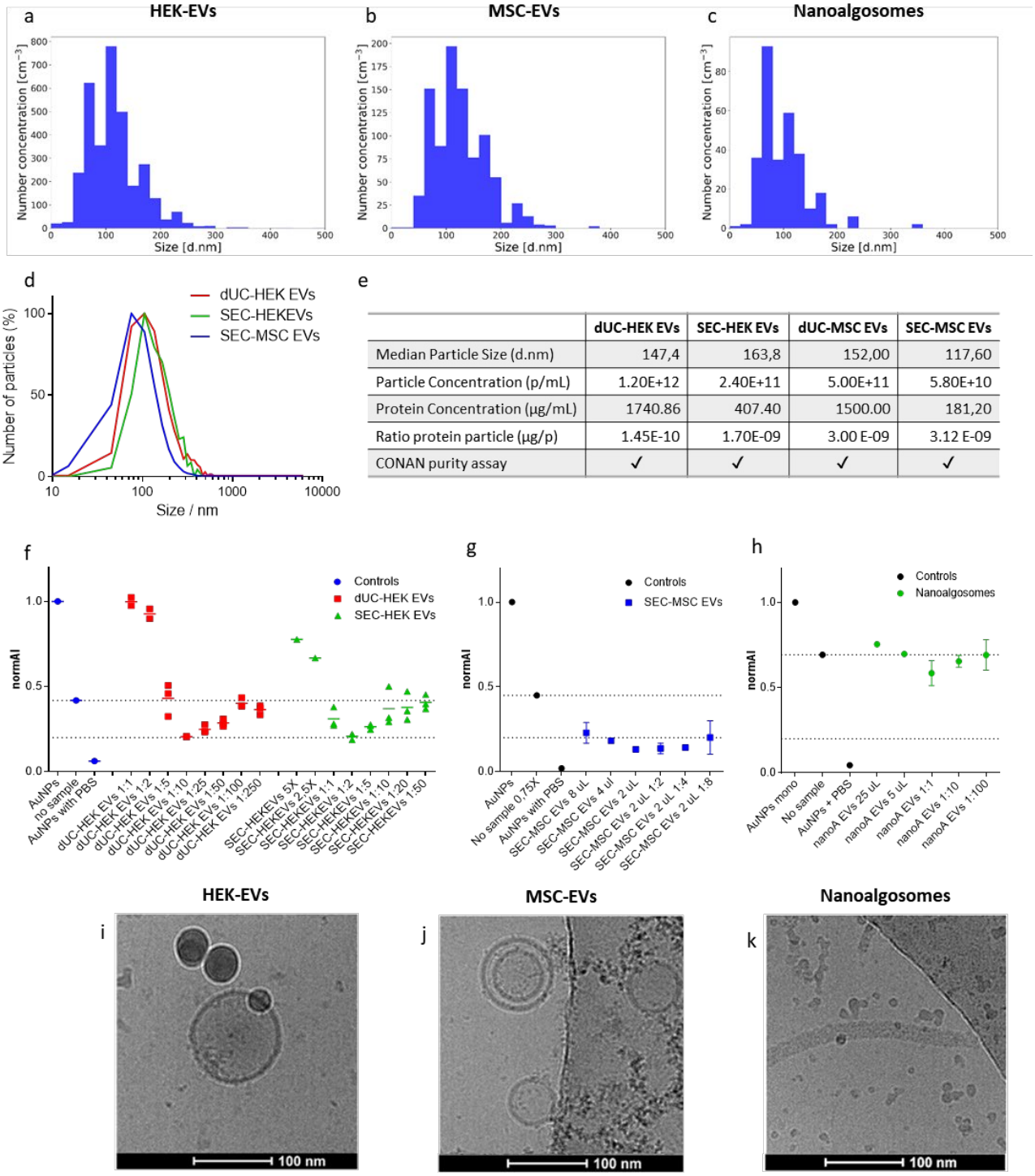

	dUC-HEK EVs	SEC-HEK EVs	dUC-MSC EVs	SEC-MSC EVs
Median Particle Size (d.nm)	147,4	163,8	152,00	117,60
Particle Concentration (p/mL)	1.20E+12	2.40E+11	5.00E+11	5.80E+10
Protein Concentration (µg/mL)	1740.86	407.40	1500.00	181,20
Ratio protein particle (µg/p)	1.45E-10	1.70E-09	3.00 E-09	3.12 E-09
CONAN purity assay	✓	✓	✓	✓

Figure 20. Size distribution measured by Nanoparticle Tracking Analysis (NTA) of HEK-EVs **(a)**, MSC-EVs **(b)**, and nanoalgosomes **(c)**. **(d)** Comparison between size distribution measured by Nanoparticle Tracking Analysis (NTA) of HEK-EVs isolated by dUC and SEC, MSC-EVs purified by SEC. **(e)** The table of EV yields is based on EV protein concentration (µg/mL) measured by micro-bicinchoninic (BCA) colorimetric assay, the particle numbers (p/mL) measured by Nanoparticle Tracking Analysis (NTA). Both of HEK-EVs and MSC-EVs were isolated by dUC and SEC. **(f)** Purity CONAN assay of HEK-EVs isolated by dUC and SEC. **(g)** Purity CONAN assay of MSC-EVs isolated by SEC. **(h)** Purity CONAN assay of nanoalgosomes purified by TFF. Morphology by cryo-TEM images of HEK-EVs **(i)**, MSC-EVs **(j)** and nanoalgosomes **(k)**. Representative images are presented of three independent experiments (n = 3).

10.1.3 Vesicle protein biomarkers

To perform a biochemical characterisation of HEK-EVs and MSC-EVs, a Western Blot analysis was carried out for EV markers (**Figure 21**), compared to the cellular lysate (**Figure 21a**) or cellular homogenate (H) (**Figure 21b**). Since there are no universal EV markers, the markers choice was made according to MISEV 2018 guidelines [32]. The HEK-EV preparations are shown enrichment of Alix, the tetraspanin CD63 and CD81, and TSG101. Calnexin was used as a potential contaminant of the EV preparations [63]. In the MSC-EV samples is shown an enrichment of Actinin4, Alix, CD63, and CD90. The cis-Golgi marker GM130 was visible only in the cellular homogenate (H), indicating an undetectable presence of intracytoplasmic membranous components. In the immunoblot analyses of nanoalgosome preparation (**Figure 21c**), selected biomarkers enriched in the EV fraction and putatively conserved during evolution were evaluated. Target protein biomarkers, chosen according to MISEV guidelines [32], were Alix, Enolase, β-actin, and H+/ATPase [46]. This analysis was crucial to discriminate EVs from other contaminants. Immunoblot results showed the enrichment of three target proteins (Alix, Enolase, and β-actin) in the EV samples compared to the lysates.

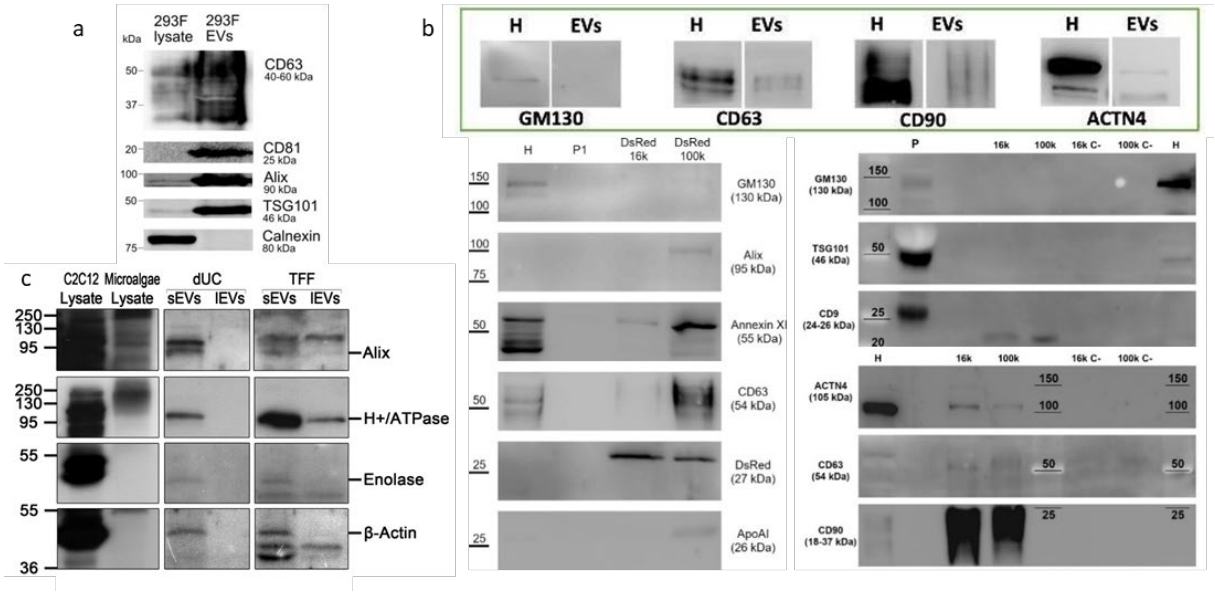

Figure 21. (a) Western blot for EV markers (CD63, CD81, ALIX, TSG101) and potential contaminant (Calnexin). The HEK293F lysate is used as positive control. Adapted from [63]. **(b)** Representative immunoblot analyses of EV markers (Actinin4, ALIX, AnnexinXI, CD63, CD81, CD90, and TSG101) and potential contaminant (APOA1, GM130) in MSC-EVs. The MSC homogenate is used as positive control. **(c)** Representative immunoblot analyses of Alix, H+/ATPase, Enolase and β-actin in *Tetraselmis chuii* cell lysates (Microalgae lysate), sEVs and lEVs isolated by dUC and TFF from Tetraselmis chuii cultures; a mammalian cell line is used as positive control (C2C12 lysate). C2C12 (10 µg) and microalgae (20µg) lysates, dUC-isolated and TFF-isolated sEV (13µg) and lEV (equal volumes) samples were loaded on gels. Alix, H+/ATPase, Enolase, and β-actin are enriched in the sEV samples. Three independent experiments (n = 3) were performed. Adapted from [46].

10.1.4 EV selection

Thanks to these experiments were possible to identify the ideal EV candidates to proceed with the subsequent experiments. For the selection of the EVs in the preliminary tests, the fundamental parameter was the purity-CONAN assay results. Therefore, the HEK-EVs isolated by dUC and SEC and MSC-EVs purified by SEC were selected.

10.2 Characterisation of S.C. PDA-MBDs and S.C. and M.C. RITC-MBDs

10.2.1 Microscopy Morphological Characterisation of MBDs

The morphology and size of iron oxide MNPs, characterized by TEM micrographs, are shown (**Figure 22**). The images show the single-core Fe3O4@PDA NPs (MG-544) (**Figure 22a**) and the single-core Fe3O4@SiO2-RITC-SiO2 (MGAP-19 (**Figure 22d**) and MGAP-21(**Figure 22e**)) and for the multi-core Fe3O4@SiO2-RITC-SiO2 (AP-20 (**Figure 22f**) and MG456-1C (**Figure 22g**)) respectively.

All MBDs types show a spherical morphology and size (**Table 7**). Regarding the single-core MBDs@PDA, from these images, it was possible to observe a higher cluster produced by the coprecipitation method (**Figure 22b**) compared to the Fe3O4@SiO2-RITC-SiO2 obtained by the microemulsion method (**Figure 22d** and **Figure 22e**), where magnetite cores, with a dark contrast (**Figure 22c**), are individually embedded within the silica (light contrast). On the other hand, the TEM images of the multi-core MBDs (**Figure 22f**) revealed particle size larger than the single-core MBDs and a clear core@shell structure, formed by small magnetic cores covered by a thick SiO2 shell, was observed [14]. The total average diameter of the MBDs@PDA is D_{TEM}≈14.90 nm. The total average diameter of the single-core@shell MBD@SiO2-RITC-SiO2 is D_{TEM}≈52.2 nm for the preparation of MGAP-19 and D_{TEM}≈32.3nm for the MGAP-21. The total average diameter of the multi-core@shell MBD@SiO2-RITC-SiO2 (AP-20 preparation) is D_{TEM}≈73 nm.

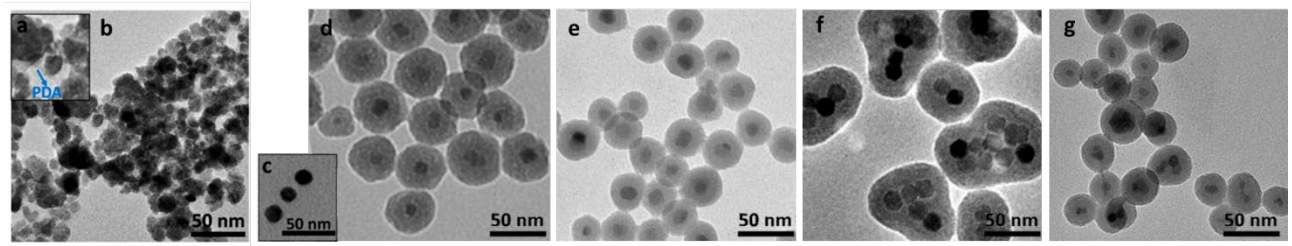

Figure 22. **(a)** The insets show a zoom of the MBD@PDA TEM micrographs. **(b)** Representative TEM micrographs of the fluorescent MBDs: single-core MBD@PDA. Adapted from [14]. **(c)** The insert shows magnetic cores before silica coating. Image modified from [14]. **(d)** Single-core@shell MBD@SiO2-RITC-SiO2 (MGAP-19 preparation). **(e)** Single-core@shell MBD@SiO2-RITC-SiO2 (MGAP-21 preparation). **(f)** Multi-core@shell MBD@SiO2-RITC-SiO2 (AP-20 preparation). **(g)** MBD@SiO2-RITC-SiO2 (MG-456-1C preparation).

10.2.2 Hydrodynamic Particle Size, Zeta Potential, and stability measurements

The colloidal stability of single- and multi-core MBDs was evaluated by hydrodynamic size, polydispersity index (PDI) and zeta potential analysis (**Table 6**).

Table 6. Hydrodynamic size (DH), TEM size obtained by TEM micrographs (D_{TEM}), polydispersity index (PDI) and zeta potential.

MBD@SiO2-RITC-SiO2 / PDA-derivative S.C.MBDs

Batch code	**MGAP-19**	**MGAP-21**	**AP-20**	**MG456-1C**	**MG-544**
Core	Single Core	Single Core	Multi Core	heterogeneous	Single Core
Dye	RITC	RITC	RITC	RITC	PDA
TEM Average size (D_{TEM} nm)	52.5	32.3	72.5	28.2	NA
Hydrodynamic size (DH. nm)	67.60	51.82	102.20	81.41	63.21
Polydispersity index (PDI)	0.06	0.30	0.10	0.25	0.24
ζ-potential (mV)	-50.60	-30.10	-63.50	-28.0	-19.90
NTA Average size (nm)	138,2	135.1	114.3	NA	NA
particle number (p/mL)	2,9E+12	1,0E+12	1,3E+12	NA	8.3E+13/ml

MBD@SiO2-RITC-SiO2. The single- and multi-core MBDs colloidal stability was evaluated with the zeta potential analysis and hydrodynamic size (Table 6). The negative zeta potential charges were found in the surfaces of the rhodamine S.C- and M.C-MBPs (MBD@SiO2-RITC-SiO2), indicating the presence of silanol groups from silica layers, confirming the silica coating of these NPs. The zeta potential of the RITC-MBDs

allows the evaluation of the NP stability. Based on the zeta potential, the more negative value corresponds to more stable MBDs. On this concept, the more stable MBDs should be the multicore AP-20, followed by MGAP-19, MGAP-21 and MG456-1C. The PDI allows the evaluation of the NP distribution uniformity. A higher index corresponds to a more heterogeneous NP solution. If the index becomes higher than 0.4, this indicates a moderate aggregation of MBDs in an aqueous medium. Based on these data, it is possible to classify the RITC-MBDs on a size stability scale. The more uniform preparation is MGAP-19, followed by AP-20, MG456-1C, and MGAP-21. DLS measurements revealed that the RITC-MBDs possess relatively small hydrodynamic diameters close to the particle size, except for the MG456-1C, whose hydrodynamic diameter increased by three times more than the particle size.

PDA-derivative S.C.MBDs. The negative zeta potential (-19.90mV) in the PDA-derivative S.C.MBDs (MBD@PDA) indicates some problems during the functionalisation with PDA on the surface of the MNPs. Indeed, with the PDA functionalisation, the zeta potential of the MBDs should be positive (+28.70 mV [14]).

10.2.3 Optical Properties

The optical characterisation of the fluorescent activity of PDA-(MBD@PDA) -functionalised MBDs, MG-544 preparation (**Figure 23a**), and RITC-(MBD@SiO2-RITC-SiO2)-functionalised MBDs (**Figure 23c**) reveals clear peaks, both excitation and emission, with maxima located at 424nm (Fe3O4@PDA) and 583nm (Fe3O4@SiO2- RITC-SiO2) agreeing with those reported theoretically for each fluorophore [14]. To verify whether fluorescent single-core MBDs have a sufficient response to be used in microscopy images for biological studies, these were analysed by confocal microscopy using laser excitation lines of 405 nm (**Figure 23b**) and 522 nm (**Figure 23d**) and allowing the visualisation of PDA and RITC, respectively. Unfortunately, the PDA functionalisation of the MG-544 preparation presents poor levels in both photoluminescence spectra and fluorescence confocal images. On the other hand, RITC-MBDs show clear fluorescent signals in both photoluminescence spectra and fluorescence confocal images. The confocal image confirms the correct integration of the fluorophore in the magnetic nanostructure.

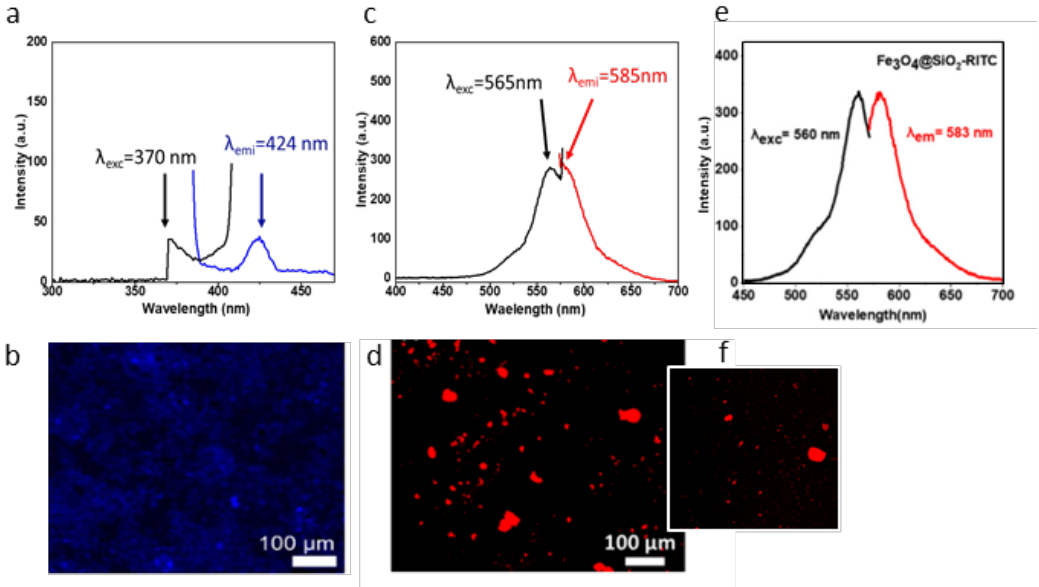

Figure 23. Photoluminescence spectra **(a, c)** and confocal fluorescence microscope images **(b, d)** of the fluorescent single-core MBDs, functionalised with fluorescent agent: PDA **(a, b)** and RITC **(c, d)**, respectively. Insets of (d) show the fluorescence of multi-core MBDs functionalised with RITC.

10.2.4 Stability measurements in PBS buffer and after centrifugation

MBD stability study. For a correct encapsulation into lipid membrane and for better quantification, MBDs need to be stable. Several tests were performed, investigating the role of centrifugation and resuspension buffer on MBD stability. Some explicative results are reported in (**Figure 24**). As a control sample for each type of MBDs, a mixture without any centrifugation protocol and diluted in pure water was used. All the

measurements were performed at least in triplicate. The results were summarized (**Table 7** and **Table 8**). Each type of MBD was assigned a score based on its results. The stability evaluation of the different types of MBDs was performed under various protocol conditions: I) type of buffer (Milli-Q water, 0.5X PBS or 1X PBS) II) after the centrifugation protocol. The hydrodynamic particle size (DH) was measured by DLS analysis. To avoid bias due to the different particle concentrations, the samples were measured to keep the same "corps number" for all the types of MBDs during the measurement. For both experiments, the most stable NPs can be identified. Regarding the aggregation, in different buffers, the stability order is MG544, followed by AP-

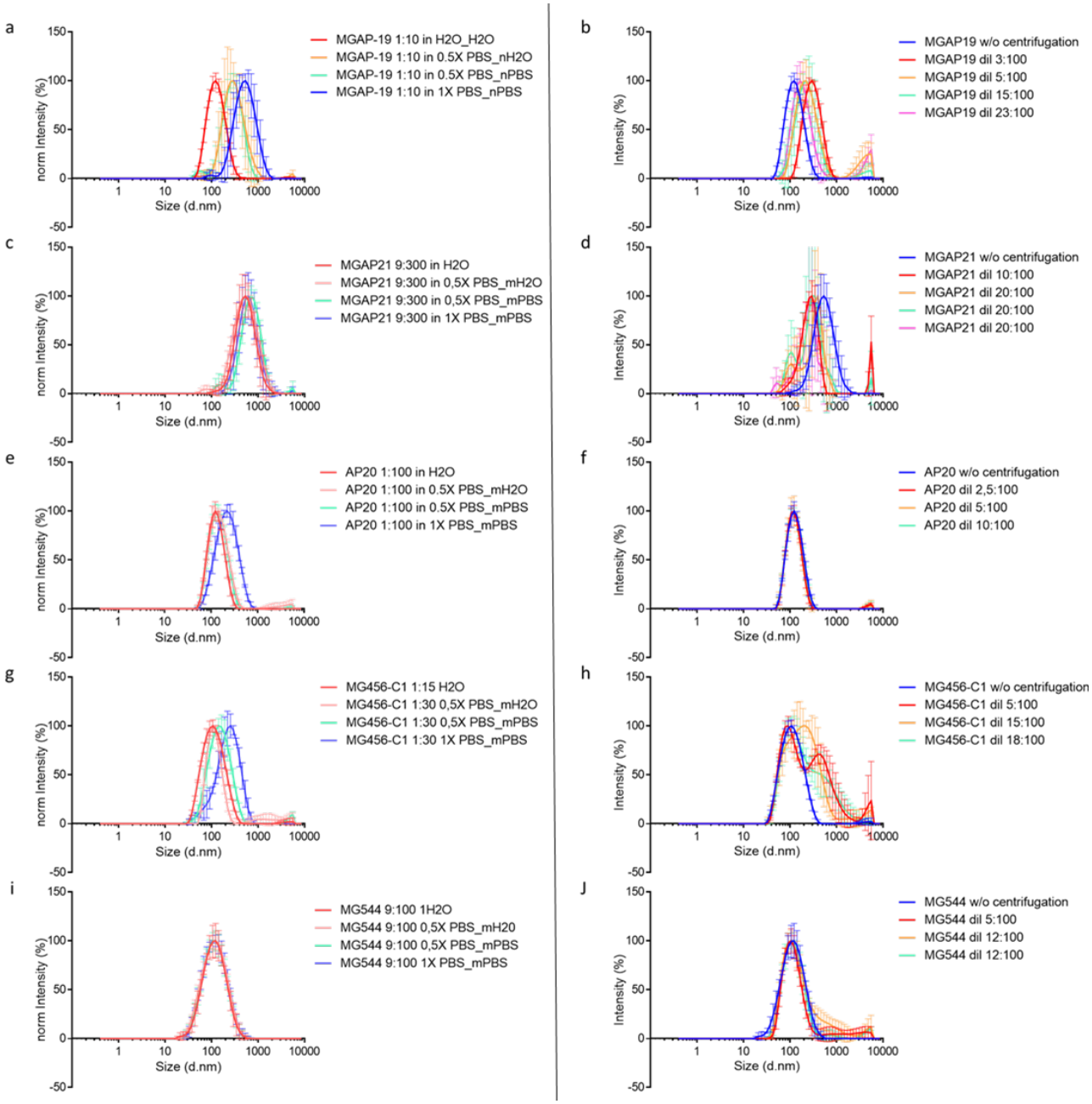

20, MG456-C1, MGAP-19 and MGAP-21. After centrifugation, the stability order is AP-20, followed by MG544, MG456-C, MGAP-19 and MGAP-21.

Figure 24. The figure was shown some exemplificative results of two different stability tests. The first column reported the size distribution of MBDs (MGAP-19 **(a)**, MGAP-21 **(c)**, AP-20 **(e)**, MG456-C1 **(f)**, and MG544 **(h)**) in pure water, PBS 1X and PBS 0.5X. The second column reported the size distribution of MBDs (MGAP-19 **(b)**, MGAP-21 **(d)**, AP-20 **(f)**, MG456-C1 **(g)**, and MG544 **(j)**) in pure water after a centrifugation protocol. In this experiment, an untreated sample for each MBDs type was used as a control.

Table 7. MBD stability in different buffers.

Name	Hydrodynamic size (**in H2O (DH.nm)**	Hydrodynamic size **at conc ~5E+9 p/mL in PBS 0,5X (DH.nm)**	Hydrodynamic size **at conc ~5E+9 p/mL in PBS 1X (DH.nm)**	**Stability Score**	**FRET**
MGAP-19	116,60 ± 7,90	238,67 ± 32,71	442,47 ± 84,46	*	✓
AP-20	120,27 ± 1,33	132,30 ± 1,95	188,60 ± 6,88	**	✓
MGAP-21	444,32 ± 57,93	575,70 ± 37,14	522,53 ± 126,79	*	✓
MG456-C1	99,45 ± 0,19	129,77 ± 2,32	180,85 ± 17,95	*	✗
MG544	99,50 ± 0,49	98,71 ± 0,73	101,90 ± 0,86	***	✗

Table 8. MBD stability after centrifugation.

Name	Hydrodynamic size **after centrifugation (DH.nm)**	Polydispersity index (PDI)	**Stability Score**	**FRET**
MGAP-19	238,5 ± 29,73	0,26 ± 0,07	*	✓
AP-20	119,9 ± 1,27	0,17 ± 0,01	***	✓
MGAP-21	636,7 ± 45,81	0,62 ± 0,03	*	✓
MG456-C1	152,7 ± 5,81	0,44 ± 0,06	**	✗
MG544	118,5 ± 4,04	0,30 ± 0,05	**	✗

10.2.5 MBD selection

Defining the stability of MBDs in the conditions used for their encapsulation into EVs is mandatory for the synthesis of functional evMBDs in BOW. The analysis performed allowed for the creation of a decision grid to score different MBD preparations and to select only those fulfilling the necessary criteria for evMBD synthesis. Moreover, the fact that some pristine MBDs showed incompatibility with the evMBD synthesis conditions (e.g. they cluster in saline buffers) shall not be interpreted as a limit, but rather as an opportunity to check evMBD formation. For instance, it is expected that MBDs that cluster in saline buffer stabilize once covered with EV membrane. In that sense, the screening of MBD stability pre- and post- putative encapsulation into EV membrane may become a way to assess evMBD formation.

Thanks to these experiments were possible to identify the ideal candidates to proceed with the subsequent experiments. For the selection of the MBDs in the preliminary tests, the size and stability of the MBDs of the MBDs and the possibility of performing both CONAN and FRET tests were taken into account. They were therefore selected as single-core MGAP-19 and MGAP-21, and the multicore AP-20 was selected.

10.3 AuNPs and Liposomes characterization

10.3.1 Liposome characterization

The size distribution (**Figure 25**) and the concentration of all the liposome preparations were characterised by dynamic light scattering (DLS) (**Figure 25a**) and nanoparticle tracking analysis (NTA) (**Figure 25b**). The summary of the result was reported (**Table 9**). The table shows all the main characteristics of the liposomal preparations. These include the pore size of the membrane used for extrusion, the presence or absence of

dye (Dio), the type of buffer used to create the liposomes (PBS/H2O), the hydrodynamic size (d.nm) measured via DLS, and the number of particles (p / mL) measured by NTA.

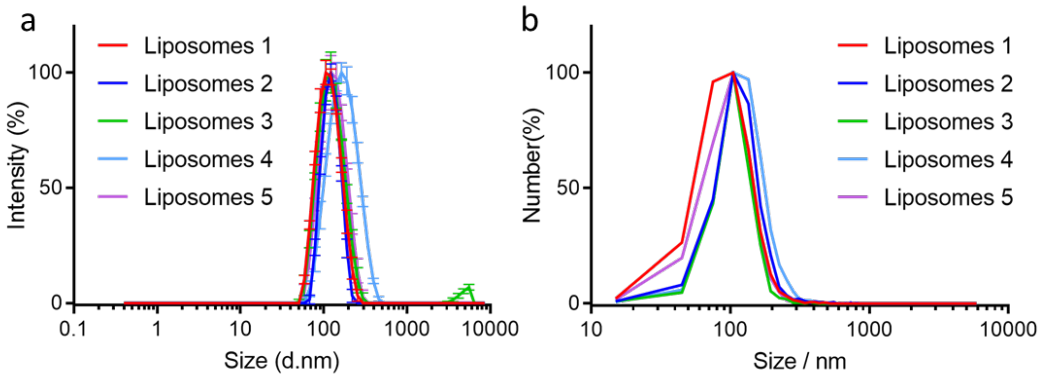

Figure 25. (a) The size distribution obtained with the DLS of all the liposome preparation was shown. **(b)** The size distribution was displayed for all the liposome types. The results are relative to the NTA measurement.

Table 9. In the table are reported all the main characteristics of the liposome preparations.

Batch	**Extrusion pore size (nm)**	**Buffer (H_2O/PBS)**	**Staining**	**Hydrodynamic size (d.nm)**	**Particle number (p/mL)**
Liposomes 1	100	H_2O	X	110	5.4E+11
Liposomes 2	100	H_2O	X	122	4.2E+11
Liposomes 3	100	H_2O	DiO	122	5,0E+11
Liposomes 4	200	H_2O	DiO	166	7,5E+11
Liposomes 5	100	PBS	DiO	122	1,6E+12

10.3.2 AuNP characterization

The different batches of AuNPs were characterised by UV-Vis spectroscopy and DLS, as reported in the materials and methods. The different batches of AuNPs were characterised by DLS and UV-Vis spectroscopy**,** as reported in the materials and methods. The typical absorption spectrum **(Figure 26a**) of an AuNPs preparation presents a well-defined peak at c.a. ~520nm (localized surface plasmon resonance (LSPR) peak). The absence of other peaks on the right of the first peak indicates that the NP preparation is monodispersed. Alterations of this typical absorption trend at 650 and 850 nm highlight synthesis problems, for example, the formation of larger NPs or a non-spherical NP shape (nanorods). The DLS analysis (**Figure 26b**) shows the same result. The AuNPs preparations are monodispersed with a hydrodynamic particle size of 24nm, close to the result obtained with UV-Vis spectroscopy. The little peak at 1-2nm probably represents the citrate, fundamental for the colloidal stability of the AuNP solution, and used in excess during the synthesis reaction. A summary of the principal features (size of the metallic core and concentration (nM)) was reported for all the NP preparations.

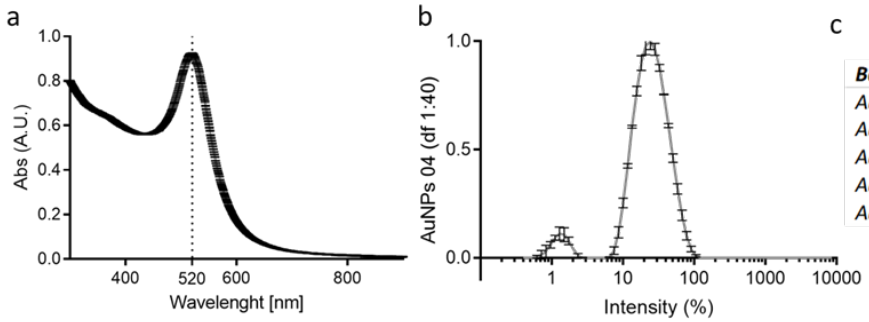

c

Batch	Size (d.nm)	Concentration (nM)
AuNPs 1	17	6.57
AuNPs 2	14/15	10.40
AuNPs 3	19	8,37
AuNPs 4	14/15	10.40
AuNPs 5	15	9.00

Figure 26. (a) A typical absorption spectrum of a monodispersed AuNP solution. **(b)** Size distribution by DLs of an AuNPs preparation. **(c)** The table reports the core size and the concentration of all used AuNP solutions.

An optical path of 1cm is required to measure the right concentration. To achieve this, two different strategies have been explored. The first consisted of three volumes of AuNP solution (100, 200, and 300 µL). The absorptions at the LSPR peak and 450nm were extrapolated from the spectra results (**Figure 27b**). Considering the absorbance as a linear parameter dependent only on the optical path, two calibration lines were interpolated and associated with their optical path dependent on the volume (**Figure 27a**). Then, the parameters for an optical path of 1cm were estimated and used to calculate the NP concentration. In the second strategy, by approximating the well to a cylinder, the volume relative to the 1cm optical path was estimated (360uL) (**Figure 27c**). The absorbance spectrum was measured and used to calculate the concentration (**Figure 27d**). Both these two strategies are consistent and reproducible (first strategy: diameter 17nm and concentration 6.45nM. Second strategy: 17nm diameter and 6.70nM concentration).

The aggregation capacity of the different preparations was evaluated. The first test consists in verifying whether the AuNPs can aggregate in the presence of a saline solution (PBS). The red solution of monodispersed AuNPs was compared with the positive aggregation control with PBS (**Figure 28a**). The PBS caused the aggregation of the AuNPs and consequent LSPR peak (and colorimetric) shift. The solution then changes from red to purple/blue. The quantity of PBS necessary for the aggregation is carefully calibrated (**Figure 28b**). Two different mixtures are evaluated. The first evaluates the ideal quantity of PBS to carry out the CONAN assay. 25µl of H_20 are mixed with 50µl of AuNPs (6nM) and 25ul of PBS at different concentrations (1X, 0.9X, 0.85X, 0.80X, 0.75X and 0.70X). The second mixture is made with 50µL of AuNPs (6nM) and 50µL of PBS at the same concentrations tested previously. The ideal result has an AI at ~0.5 for the first preparation and below 0.1 in the second.

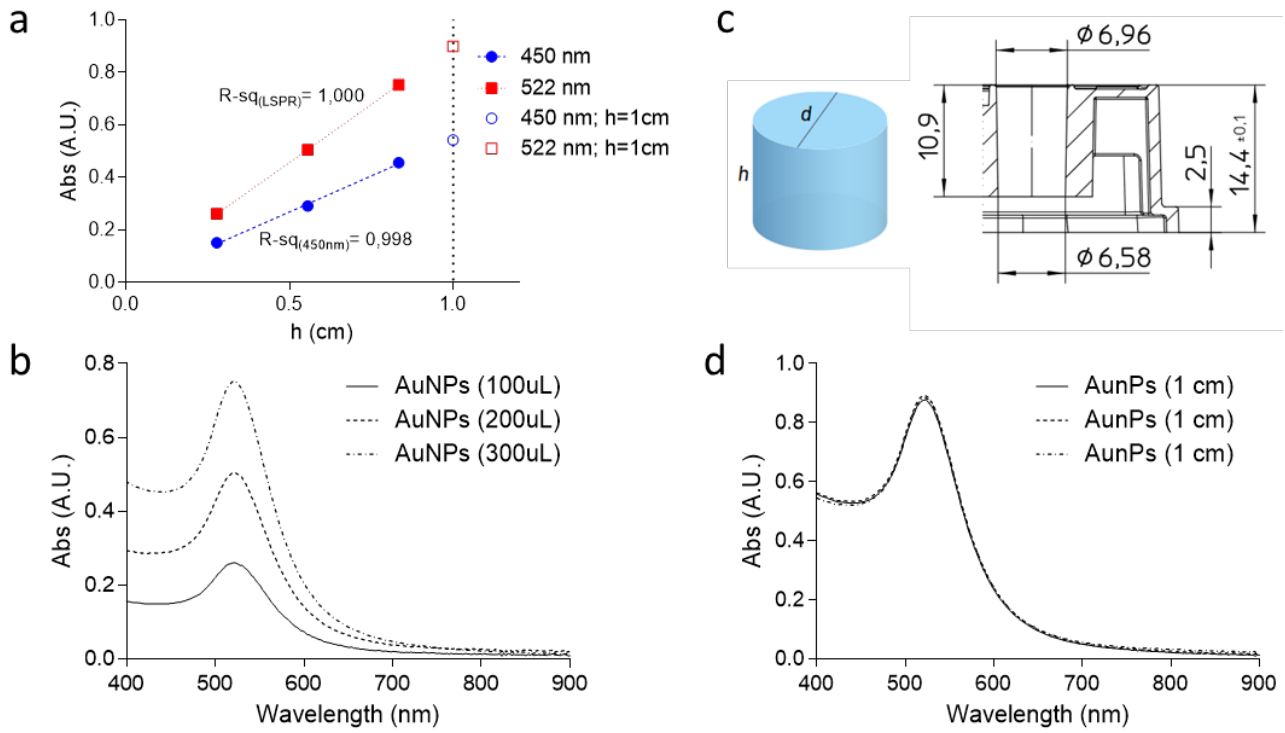

Figure 27. **(a)** The first strategy used to estimate 1cm of the optical path and thus the particle concentration. These data were extracted from the absorption spectra from three different volumes **(b)**. **(c)** The second strategy used a geometric formula to estimate the volume necessary to obtain 1cm of optical path. **(d)** The resulting spectrum was used to calculate the particle concentration.

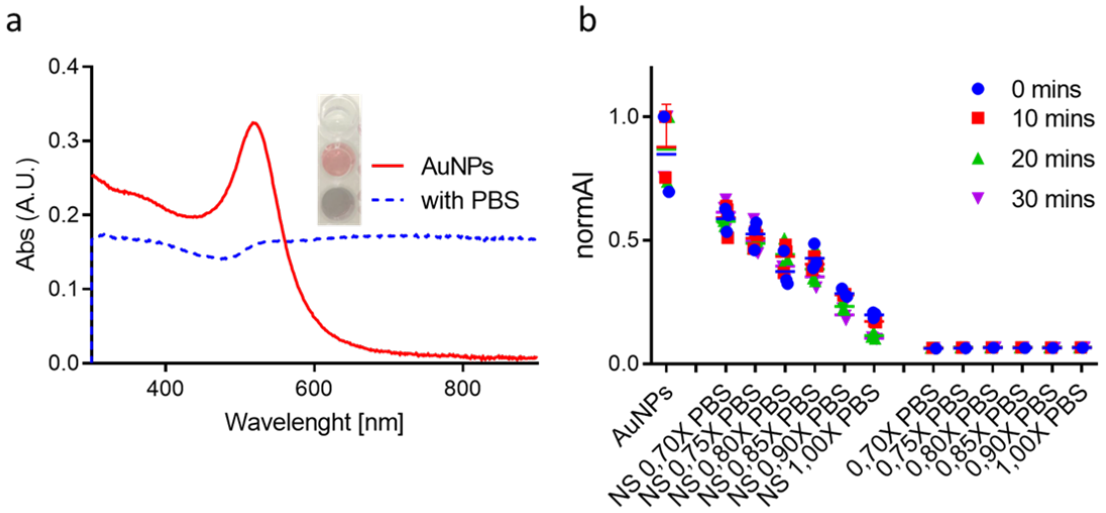

Figure 28. (a) The plate show three wells I) 100µL of H2O used as a blank, II) the monodispersed AuNPs (3nM), and III) the positive control of aggregation with the PBS. The colorimetric results are displayed in the absorption spectra. **(b)** The PBS concentration for each AuNPs preparation was set to obtain a good grade of aggregation with the biological samples.

10.4 Designing a modified CONAN assay

10.4.1 Behaviour of the liposomes and the MBDs with the AuNPs

AuNPs adsorb and cluster at the lipid membrane of liposomes or pure EVs [51] (i.e. without protein contaminants). The localized surface plasmon resonance (LSPR) of the AuNPs acts as a colour switch, giving a naked-eye colorimetric readout of the AuNP aggregation, quantified with the Aggregation Index (AI). Therefore, a modified CONAN assay was developed to evaluate the coverage of MBDs with a lipid membrane.

Due to the incompatibility of the MBDs with the PBS solution and the PBS component was removed from the assay (also the liposomes used as an EV model were produced in pure water).

The NPs taken into account were normalised at the same amount of particle concentration (5E+11 p/mL). 1.25E+10 particles were used for each preparation (liposomes, MGAP-19, AP-20, and MGAP-19), and brought to the volume of 50µL with pure water. The samples, 50µl of AuNPs (6nM) was added (final concentration 3nM) (**Figure 29a**). All the experiments were performed in triplicate (**Figure 29b**).

The behaviour of liposomes with the AuNPs is without mistake, which is expected considering the specific properties of AuNPs. As for the MBDs, from the absorption spectra and the normAI results, it can be seen that AP-20 M.C.MBDs are the least interacting with the AuNPs (normAI ~ 0.6). The S.C.MBDs (MGAP-19 and MGAP-21) interact with the AuNPs by decreasing the normAI (normAI ~ 0.35) (**Figure 29c** and **Figure 29d**).

The interaction between S.C MBDs and the AuNPs has been confirmed thanks to on-time evaluation. After 30 minutes, the S.C. MBDs + AuNPs started to become paler. After 1.15 hours, dark aggregates were visible at the bottom of the wells (**Figure 29e**). This phenomenon interests only the S.C.MBDs and could be due to a less silica coating coverage concerning the M.C.MBDs.

These results are unexpected because, by literature, the aggregation of the AuNPs is due only to surface charge interactions that are not observed with the commercial silica NPs that should have the same surface as the MBDs. The interaction and precipitation of pristine MBDs and AuNPs occurring under certain conditions may interfere with evMBD detection. However, such a phenomenon may be an indirect indicator of evMBD synthesis failure, and similarly, the instability of pristine MBDs could be exploited to remove them from the solution.

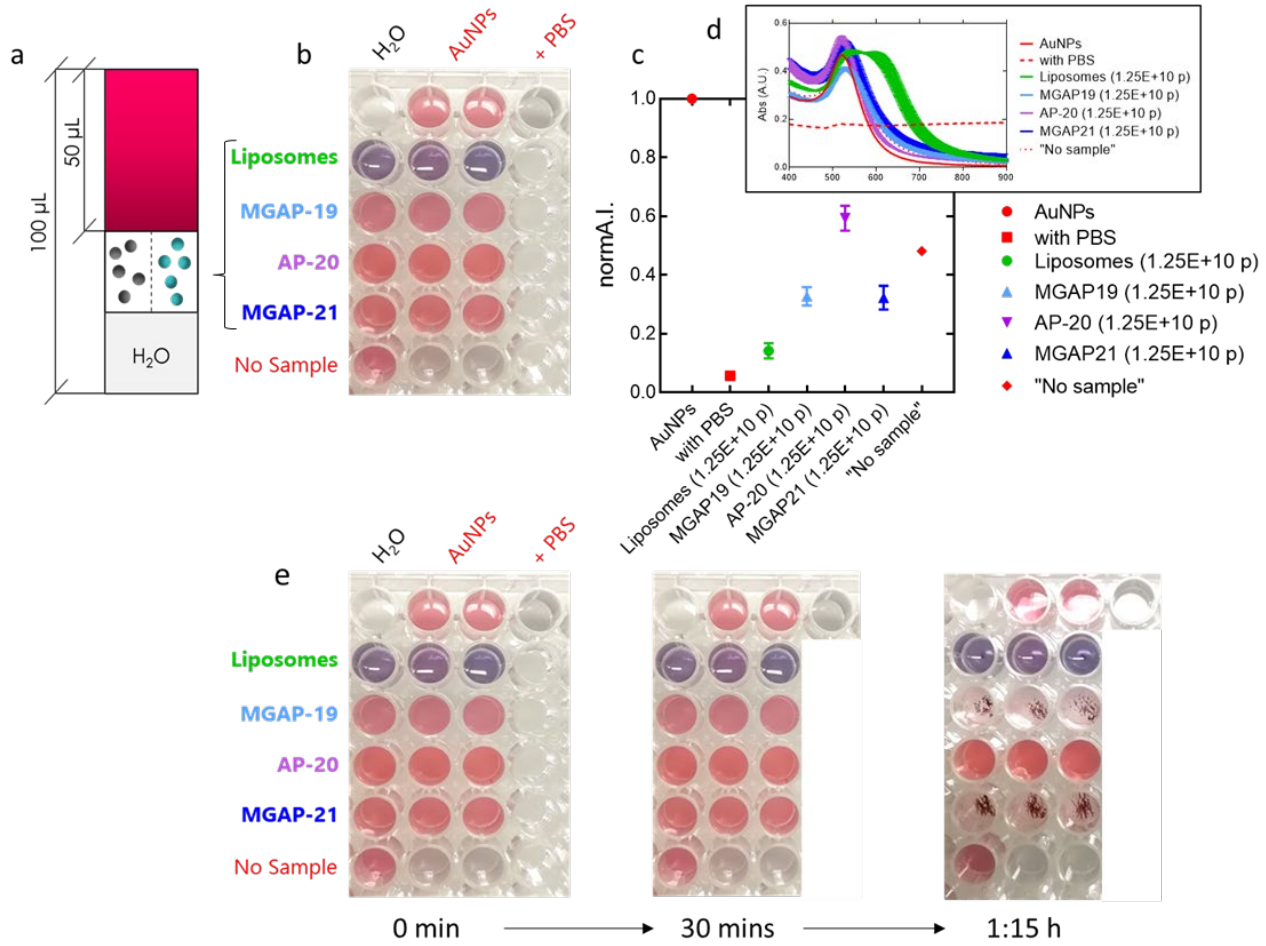

Figure 29. **(a)** The setup of the experiment is displayed. The NPs (Liposomes or MBDs) were brought to the final volume of 50µL, and 50µL of AuNPs (6nM) were added. **(b)** The results of the AuNP aggregation on liposomes and MBDs in the CONAN assay are shown. The colourimetric evaluation of the interaction between the NPs is perceptible with the naked eye. **(d)** The UV/Vis spectra are displayed and were used to calculate the aggregation index (norm AI). **(c)** The normAI quantifies the aggregation of the AuNPs with the liposomes and with three different types of MBDs (MGAP-19, AP-20, and MGAP-21).

10.4.2 Fluorescent evaluation of the MBDs mixed with the AuNPs

To evaluate the composition of the dark aggregate on the bottom of the wells, the idea was to exploit the fluorescence of the RITC in the MBDs silica shell. Unfortunately, this attempt has not produced any kind of results. Investigating the literature, this article emerged [82].

M. Stobiecka and M. Hepel write: *"... the large overlap of AuNP absorbance with RhB emission characteristics [...] is a prerequisite of an efficient energy transfer (FRET), provided that the distance between the interacting dipole molecule and surface multipole is sufficiently small. It is seen that the fluorescence peak of RhB at 578 nm observed, is completely quenched upon the addition of AuNPs"* [82].

This possible explanation was also evaluated for MBDs (**Figure 30**). As can be seen, the fluorescence of MBDs (MGAP-19) without AuNPs corresponds to ~ 8000 fluorescence intensity. If the MBDs are mixed with the AuNPs, the fluorescence is quenched, and the signal drops about four times.

A recent article confirms what was observed for MBDs and RITCs where Zhang et al. write: *"…We use the fluorescence change of an in situ quenching system to evaluate the surface coverage […]. AuNPs quench fluorophores attached to their surface, owing to the surface plasmon resonance and energy transfer. Fluorescent Rhodamine B isothiocyanate (RITC) binds to AuNPs and AuNPs quench its fluorescence..."* [83].

Quantification of MBDs must always be done before adding AuNPs.

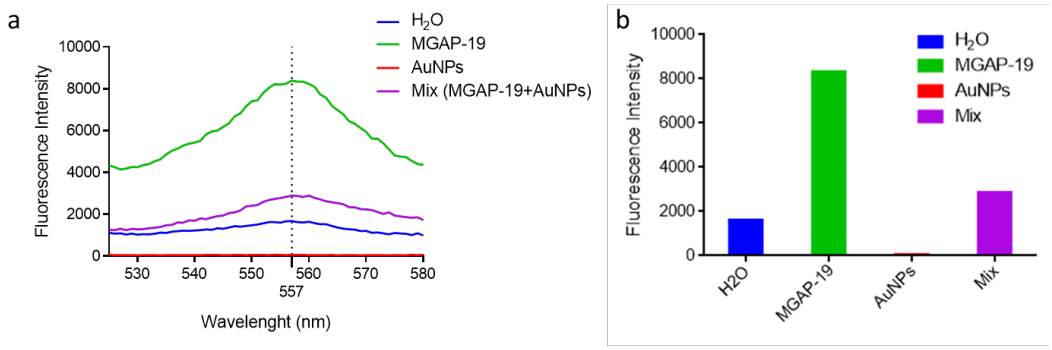

Figure 30. (a) Fluorescent spectra of H2O, MGAP-19, AuNPs, and the mix between the AuNPs and MGAP19. **(b)** Fluorescence reduction quantification after the mixture between the AuNPs and the MBDs.

10.4.2.1 Exploration of the aggregation conditions

To evaluate the interference of this aggregation on the assay optimisation, different conditions were explored I) evaluate the aggregation with different S.C MBDs particle numbers (**Figure 31a**) and II) keep constant the ratio between the number of S.C.MBDs and the number of AuNPs at the aggregation condition (**Figure 31b**). In the experiments, different standards were used I) dilution 1:3 of the S.C.MBDs ten times from the aggregation condition and II) 1:2 dilution five times from the aggregation condition of both S.C.MBDs and AuNPs (**Table 10**).

The aggregation is not triggered also in the other MBDs dilution of the MBDs (**Figure 31a**). However, by maintaining the same ratio between MBDs and AuNPs, the aggregation is trigger also in the diluted particle mixture (**Figure 31b**). In the first case, the results were quantified with the normAI (**Figure 31c**). In the second experiment, the reduction of the spectrum intensity in time without LSPR shift demonstrates the AuNPs did not aggregate in nanoclusters but that they had lost their nano shape and losing their nanoplasmonic proprieties (**Figure 31d**). Another useful information derived from this experiment is the range where the aggregation due to the presence of the MBDs becomes negligible in the assay. This range is between 1.54E+09 and 1.71E+08 particles (~4.63E + 08 p).

Table 10. In the table were reported the number of NP used in the experiments and their ratio.

	Number of S.C.MBDs (p)	Number of S.C.MBDs (M)	Number of AuNPs (M)	Ratio AuNPs/S.C.MBDs
Experiment 1 – Dilution of S.C.MBDs				
Aggregation condition	1.25E+10	2.08E-10	3.0E-9	**1,44E+01**
Standard 1	4,17E+09	6,92E-11	3.0E-9	**4,34E+01**
Standard 2	1,39E+09	2,31E-11	3.0E-9	**1,30E+02**
Standard 3	4,63E+08	7,69E-12	3.0E-9	**3,90E+02**
Standard 4	1,54E+08	2,56E-12	3.0E-9	**1,17E+03**
Standard 5	5,14E+07	8,54E-13	3.0E-9	**3,51E+03**
Standard 6	1,71E+07	2,85E-13	3.0E-9	**1,05E+04**
Standard 7	5,72E+06	9,49E-14	3.0E-9	**3,16E+04**
Standard 8	1,91E+06	3,16E-14	3.0E-9	**9,49E+04**
Standard 9	6,35E+05	1,05E-14	3.0E-9	**2,86E+05**
Standard 10	2,12E+05	3,52E-15	3.0E-9	**8,52E+05**
Experiment 2 – Constant Ratio				
Aggregation condition	1.25E+10	2,08E-10	3.0E-9	**1,44E+01**
Standard A	1,04E-10	1,04E-10	1.5E-9	**1,44E+01**
Standard B	5,19E-11	1,08E-08	7,50E-10	**1,44E+01**
Standard C	2,59E-11	5,41E-09	3,75E-10	**1,44E+01**
Standard D	1,30E-11	2,71E-09	1,88E-10	**1,44E+01**

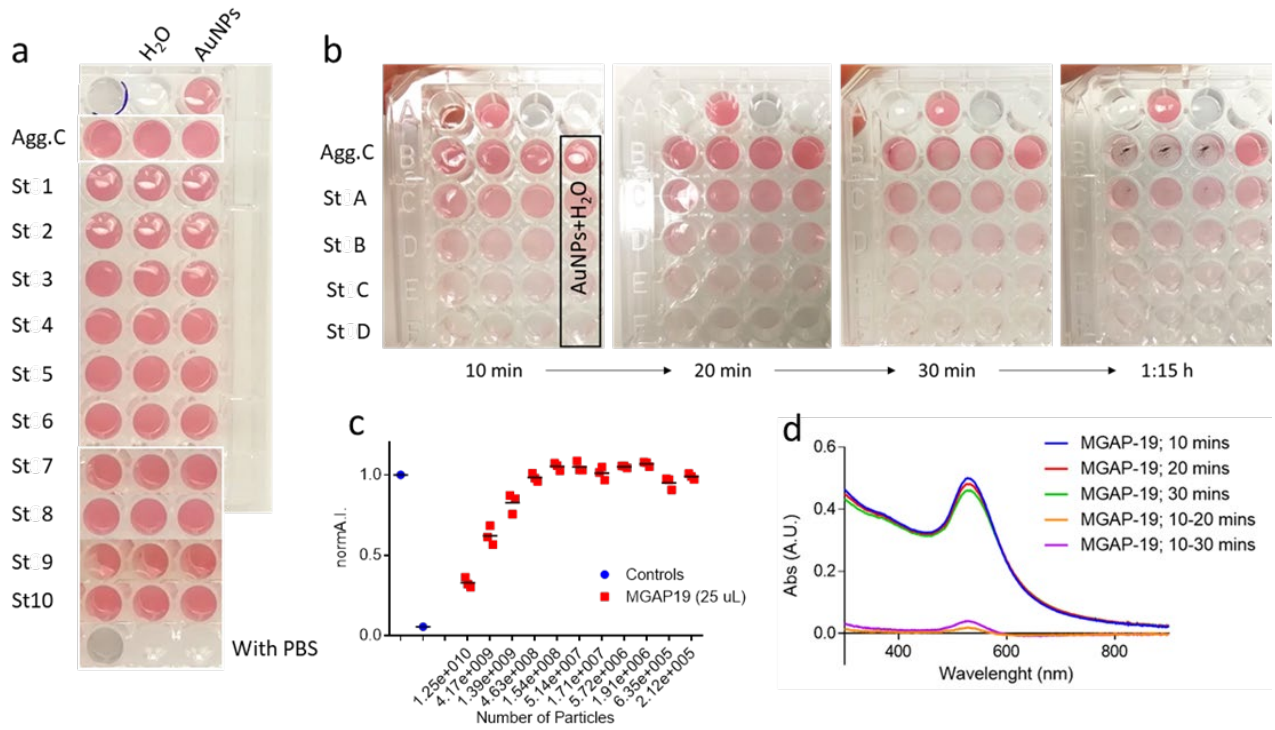

Figure 31. (a) The assay was made with different MBDs standards. The spectra were collected, and the aggregation index was calculated **(c). (b)** The assay was performed to keep the ratio between AuNPs and MBDs constant. **(d)** The spectra show that with the passing of time, the plasmonic peak decrease without any plasmonic shift.

10.4.3 Evaluation of the behaviour of the nanoparticle mixture

First, we verified the interaction between AuNPs and pristine MBDs. From the analysis, AuNPs seems to interact not only with lipid membranes but also with MBDs (in particular, MGAP-19 and MGAP-21 MBD batches), which induce a modification of the absorption spectra (without the LSPR shift → no AuNP clustering), also reflected in a modification of the normAI.

Second, we verified the interaction between MBDs, liposomes and AuNPs by simply mixing them. In the tested conditions (MBD/liposome ratio 1:1), AuNP cluster, and the aggregation is driven only by the liposomes (**Figures 32b** and **Figure 32d**). Similar tests were run also substituting liposomes with EDT-MSC EVs and EVs from HEK cells (HEK EVs). For such samples, the assay protocol was slightly modified adding 10µL of PBS 1X to trigger AuNP aggregation and stabilize the signal. Moreover, *ad hoc* aggregation indexes were calculated, to reduce data variability and reduce signal-to-noise ratio (**Figure 33a**)

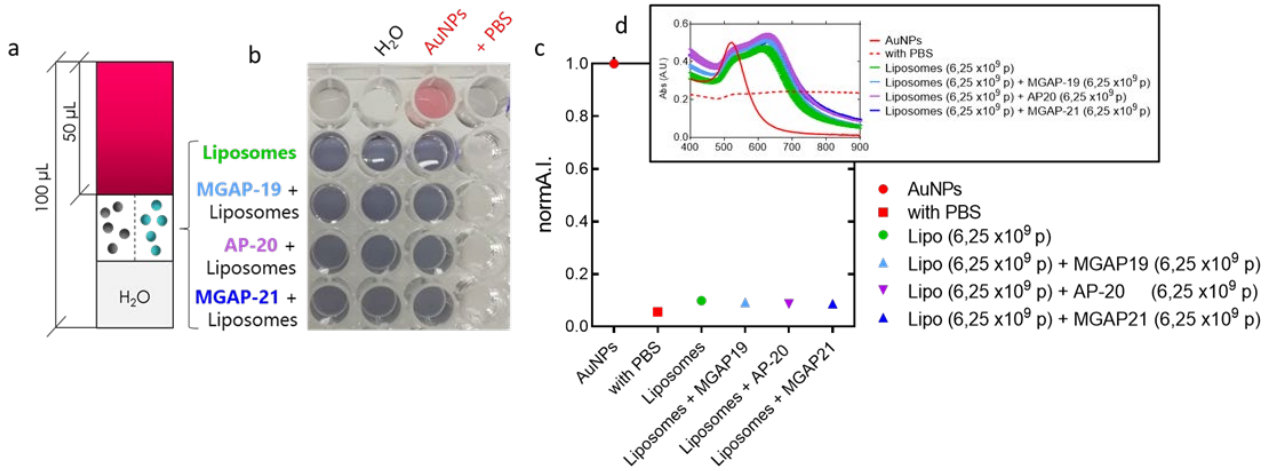

Figure 32. (a) The setup of the experiment is displayed. The NPs (Liposomes and liposomes plus MBDs) were mixed at a 1:1 ratio. The total amount of particles for the MBD plus Liposome mix corresponds to the total particle amount used in the experiment in Figure 30. The mixtures were brought to the final volume of 50µL with pure water, and 50µL of AuNPs (6nM) were added. **(b)** The plate shows the results of the interaction between the AuNPs. **(c)** The aggregation indexes are related to the number of liposomes present in the blend and are not influenced by the type of MBD added. **(d)** The results of AuNP spectra of the liposomes and the mixture of liposomes plus MBD in the assay were shown.

Finally, the testing range for all the types of NP used (**Figure 33**) for the assay to correctly work was measured MBDs: 2E+8–6E+8 particles; Liposomes: 8E+7–2E+9 particles (**Figure 33d**); HEK EVs: 3E+7–1E+9 particles (**Figure 33a**, **Figure 33b** and **Figure 33e**); MSC EVs: 6E+6–1E+8 particles (**Figure 33c** and **Figure 33e**) .

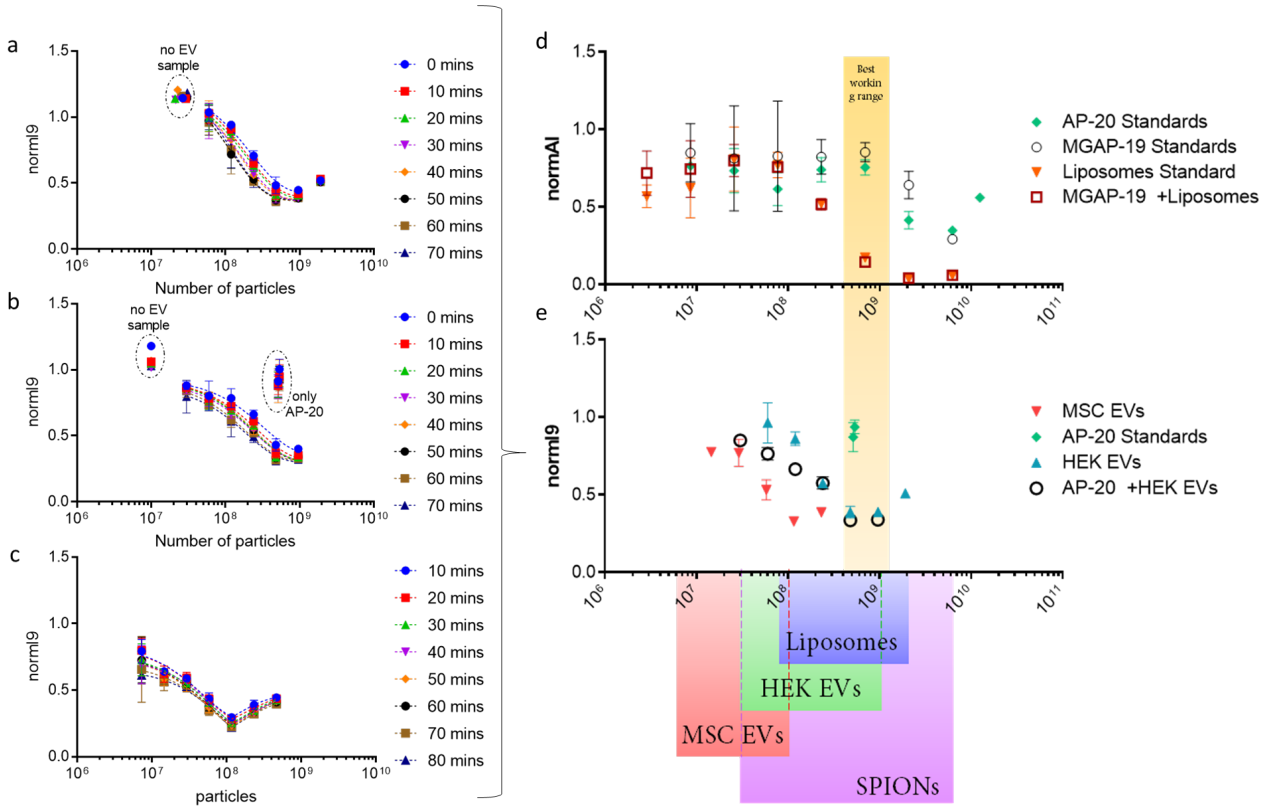

Figure 33. (d) The first graph shows the AI of different types of NPs and mixture: I) MBDs (AP-20 and MGAP-19), II) liposomes and, III) the mixture between MBDs and liposomes maintaining constant the number of MBDs fixed at 5E+8 particles. **(e)** The same analysis was carried out on I) the HEK EVs **(a)** and II) the mixture between HEK EVs and MBDs (constant in number)**(b)**, and VI) the MSC EVs **(c)**. This allowed the identification of the "ideal" working ranges for different types of NPs (highlighted in yellow). This ideal working range was chosen because it is the range that presents a higher difference between the aggregation of the MBDs alone and the MBDs mixed with the biological NPs (both liposomes and

HEK EVs). Instead, MSC EVs have a more limited working range than liposomes and HEK EVs due to the presence of protein contaminants in the preparation.

10.4.4 Evaluation of evMBD synthesis

The efficacy of the assay to detect MBD encapsulation into lipid membrane and, therefore, evMBD formation was evaluated. evMBD were synthesized with common loading methods and the formation of evMBDs was evaluated with the modified CONAN assay and the FRET assay (**Figure 34a**). The two methods showed a good grade of correlation, fostering the modified CONAN assay as a good way to verify the synthesis of evMBDs (**Figure 34b**).

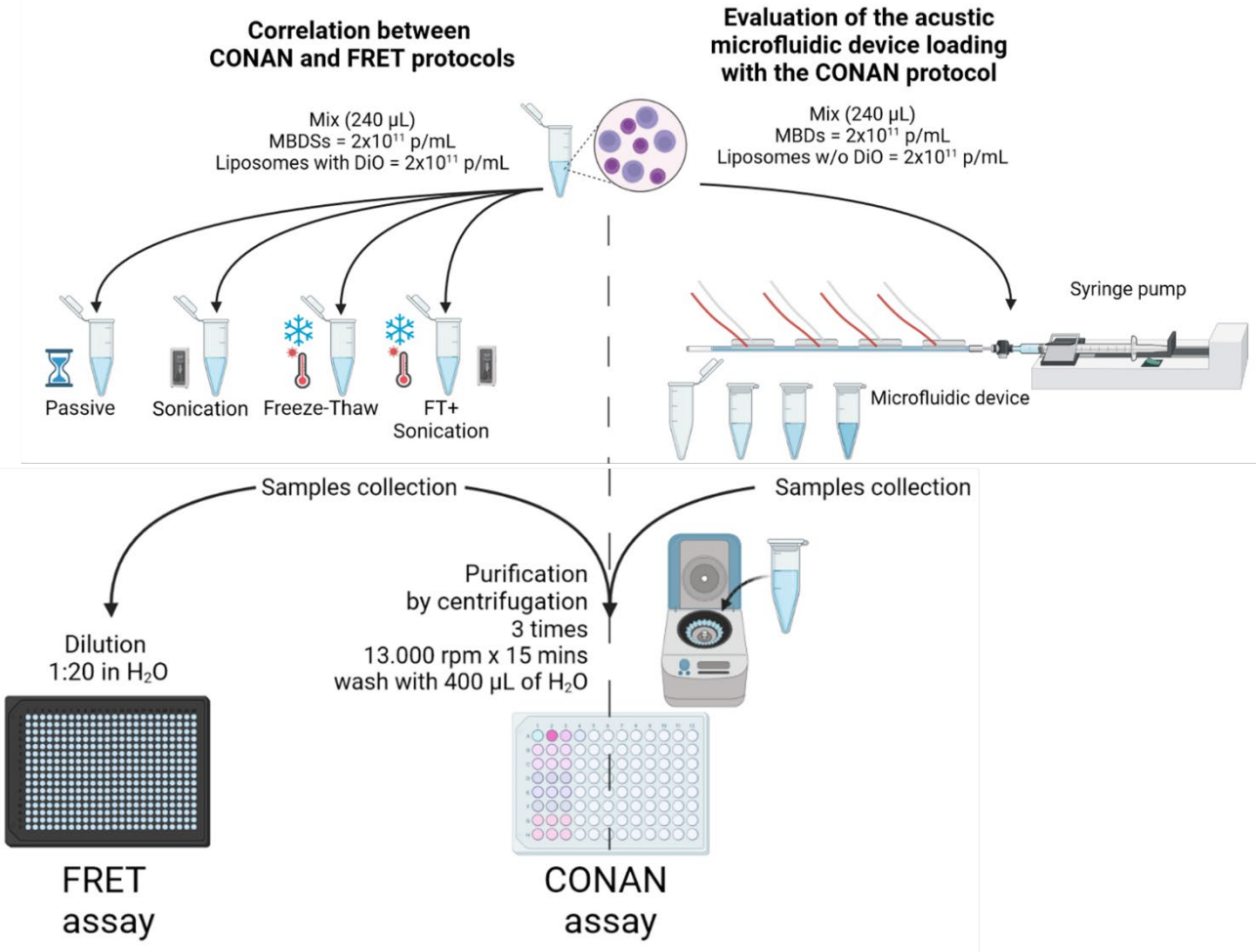

Figure 34. The Figure shows the workflow of the experiment. **(a)** In the left section, starting from the same mix (MBDs and DiO liposomes), four loading protocols (passive, sonication, freeze and thaw, and freeze and thaw plus sonication) were performed to validate the correlation between CONAN and FRET. The FRET experiment and the CONAN assay were performed in parallel. **(b)** In the right section, the acoustic microfluidic device loading protocol was performed using a mixture of MBDs and liposomes (without any staining).

Furthermore, the evMBD synthesis is more efficient when performed in H_2O comparing to PBS. This may occur for two reasons: I) MBDs alone aggregates in saline buffers, thus limiting their encapsulation; and II) saline buffers cause liposome to interact with MBDs aggregates without covering them, thus giving rise to false positives when checked with both CONAN and FRET assays.

After verifying the correlation with the FRET and verifying that this assay can be used with different loading protocols, it was possible to apply the same technique on the evMBDs created with the acoustic microfluidic device (**Figure 35a** and **35b**).

Acoustofluidics has been generally applied to larger species than NPs and EVs [84]. The microfluidic device (**Figure 34b**) and the electrical circuit (**Figure 34a**) made it possible to detect variations in frequency, voltage and current intensity. Moreover, thanks to a thermal imaging camera, it was possible to detect the temperature of the piezo and the device.

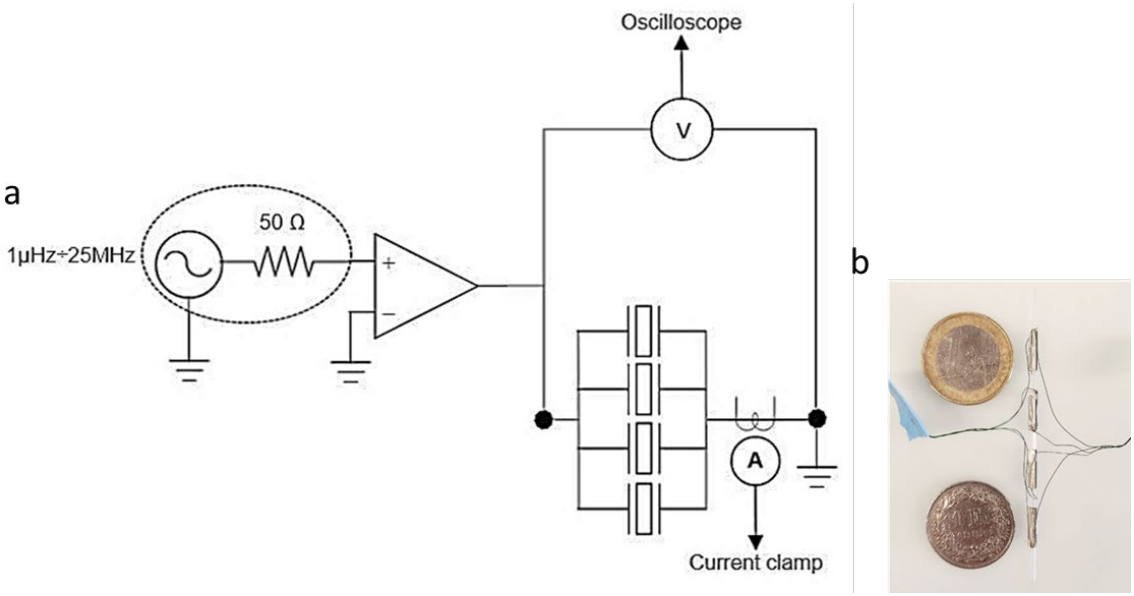

Figure 34. (a) The electric circuit and (b) the effective dimension of the microfluidic device compared with a euro or a Swiss franc.

The mixture of MBDs and liposomes (ratio 1:1, 2E+11p/mL each, final concentration 1E+11p/mL) was flown through the device at 10µL/min in the glass capillary with a syringe pump. The loading protocol was performed in four different conditions (**Table 11**). The first experiment represents the reference control (Ref), the mixture that passes through the capillary without any loading protocol. The second and third conditions were two load protocols close to the best resonant frequency of the device (Test 1 and Test 2), and the last experiment was performed with a resonant frequency further away from the resonant frequency of the device (Test 3). The samples were collected and centrifuged (13 000 rpm for 15 minutes). The pellets were washed three times with pure water to remove the unreacted liposomes.

Table 11: Condition used to test the loading inside the microfluidic device.

Name	Ref		Test 1	Test 2	Test 3
Ratio (Liposomes : MBDs)	1:1		1:1	1:1	1:1
Passage throw the glass capillary	✓		✓	✓	✓
Loading Protocol	✗		✓	✓	✓
f [MHz] initial	✗		1.30	1.30	1.30
f [MHz] final	✗		1.74	1.76	2.09
Voltage [Vpp]	control		21.50	21.00	20.50
Flow [µL/min]	10		10	10	10
Purification Protocol (centrifugation)	✗	✓	✓	✓	✓

The samples (Ref, Test1, Test2, and Test3) were normalized to have the same amount of MBD particles (~6E+8 particles) and the CONAN assay was performed. As shown (**Figure 35c**), the presence of the liposome membrane was highlighted by the presence of the peak in the absorption curve at 650nm of wavelength. The aggregation index of the samples was interpolated with a liposome calibration curve to related AuNP aggregation with the amount of lipids (and liposome, by extension) in solution. Finally, evMBD synthesis yield was evaluated considering the number of liposomes after the purification evaluated with the CONAN assay and the number of MBDs quantified by fluorescence (**Figure 35d**).

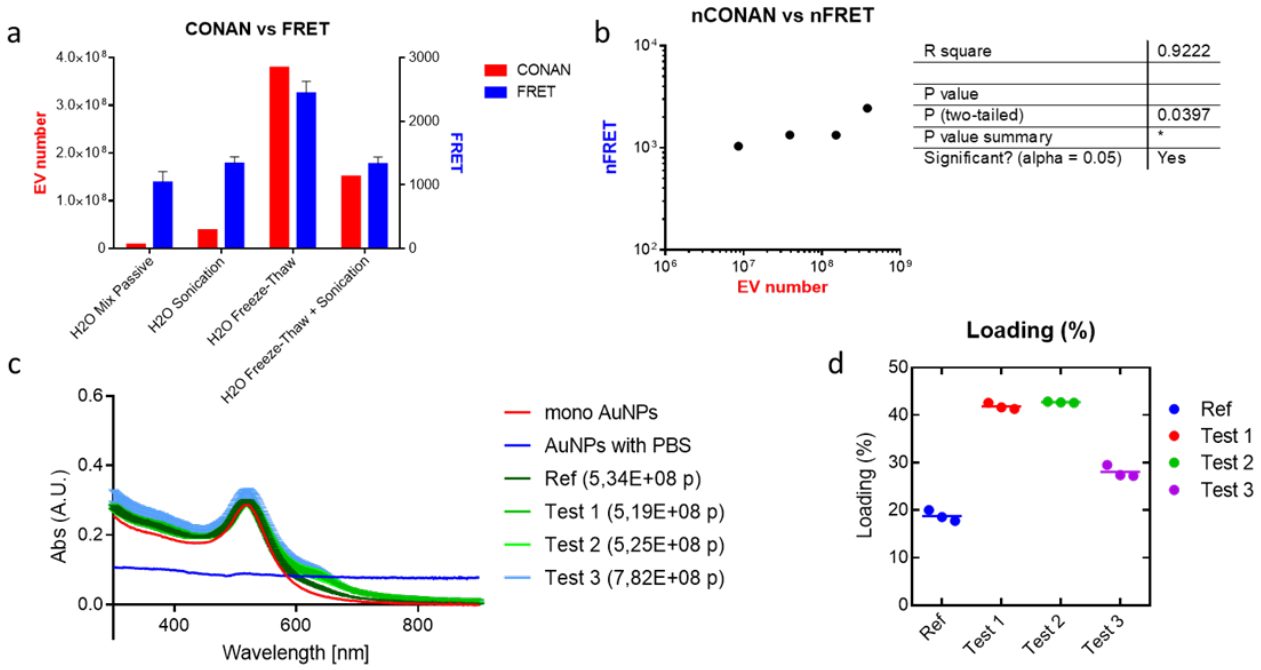

Figure 35. (a) shows the results of the loading protocols for the FRET (blue) and the CONAN assay (red), and (b) shows the correlation between the CONAN and FRET results for the different loading protocols (p-value<0.05). (c) shows the absorption spectra (between 300-400nm) of the CONAN assay, with a wavelength from 300nm to 900nm. The loading experiments were performed with the microfluidic device in four different conditions. The number of MBDs in the samples was evaluated thanks to a calibration curve (data not shown). The peaks at 650nm of wavelength confirm the presence of liposome membranes in the samples. (d) shows the evaluation of the device loading protocol performed, considering the aggregation level quantified with the I5 index. The data were normalized on the number of liposomes (evaluated by CONAN) and the number of MBDs (evaluated by fluorescence) in the sample

10.5 Conclusion

The design of a plasmonic assay to detect MBD encapsulation into EV membrane is not trivial, as several parameters must be considered. First, the interaction and precipitation of pristine MBDs and AuNPs occurring under certain conditions may interfere with evMBD detection. However, such phenomenon may be used as an indirect indicator of evMBD synthesis failure, in a similar way instability of pristine MBDs could be exploited. Second, soluble co-isolates found in contaminated EV preparation (e.g. proteins, probes for membrane staining) interfere with AuNP aggregation and, therefore, with evMBD detection. Although it may be possible to limit the assay sensitivity for such contaminants - e.g. by modifying the amount of AuNPs or by inducing AuNP aggregation with small amounts of saline buffers – such sensitivity to co-isolated species should not be interpreted as a limitation of the assay, as the use of pure EV samples is always preferred. Indeed, the pure preparations of EVs could also enhance evMBD synthesis. Third and last point to consider is the assay sensitivity. This aspect is better discussed in the following subsection.

Evaluation of evMBD synthesis. In the tested experimental setup, the modified CONAN assay proved able to detect model evMBD (MBDs + liposomes) formation, and its results are in good correlation with the ones obtained using a complementary technique (FRET). However, it fails to detect the hybrids when evMBD synthesis efficiency below 10%. Such threshold does not constitute a problem when evMBDs are synthesized from MBDs and liposomes (encapsulation yield > 10%), but it is insufficient when measuring evMBDs. Indeed, when substituting liposomes with EVs the encapsulation yield falls below 5%, making the modified CONAN assay unreliable to measure “real” evMBD formation. However, since evMBD synthesis in is expected to greatly improve soon, the assay LOD is a minor limitation. It is also worth of notice that, to estimate the evMBD synthesis, the assay relies on a calibration line of liposomes, which feature a lower stiffness compared to model evMBDs. Stiffness is one of the parameters governing AuNP interaction with lipid membranes[85].

Since the assay grounds on the assumption that liposomes and model evMBDs have similar stiffness, the real encapsulation yield might have been slightly underestimated.

The modified CONAN assay has strong application potential, as it does not require any type of staining of the biological membranes to work, is sensitive to soluble contaminants and, as such, is adaptable to different experimental needs. These features could pave the way for the application of the assay into quality control field wherever purity check, particle titration, or particle stiffness determination are needed. Future developments of this project involve the refinement of the assay and its extensive application on the BOW products - namely the evMBDs produced starting from synthetic MBDs and EVs produced by EDT-MSC and microalgae. In the specific, the possible effects of stiffness in the detection of evMBDs will be investigated, coupling the modified CONAN assay with in-liquid atomic force microscopy to perform nanomechanical measurements of MBDs, liposomes, EVs and evMBDs (both model and real ones). Further validation of the results here reported using cryo-EM are also planned.

Chapter 11

Materials and Methods

11 PRIN project- Materials and Methods

11.1 Ethical statement and safety procedures

The donation procurement, isolation, and testing were performed in full respect of national guidelines/regulations (Cells and Tissues Directive 2006/17/EC of 8 February 2006 implementing Directive 2004/23/EC and the national Italian Law DL 25/01/2010 n.16). After approval by the Ethical committee of Spedali Civili hospital (Brescia, Nr.NP4761). Written consents of healthy donors according to the Declaration of Helsinki and Local Ethical Committee approval were mandatory requirements to accept the starting material and for further processing.

All the cell manipulation procedures were performed under the Biohazard cabinet (Class II, Type2).

11.2 Cell cultivation

Cell lines. MDA-MB-231 (ATCC HTB-26) cell line was purchased from the American Type Culture Collection (ATCC; Manassas, VA, USA). MDA-MB-453 cell line was purchased from Istituto Zooprofilattico of Brescia (Italy). PC3 (ATCC CRL-1435) and PC3-CD63-GFP cell lines were a kind gift from Prof Alicia Llorente (Oslo University).

The human prostate cancer epithelial cell line (PC3) was stably transfected with the GFP-CD63 expression plasmid (pEGFP-C1 vector, Clontech, USA) encoding for GFP fusion protein with human CD63 under CMV promoter, as described in [86] to yield the cell line PC3-GFP-CD63, the source of GFP-CD63 exosomes.

All these cell lines have adherent properties and grow as monolayers attached to the surface.

Materials. Roswell Park Memorial Institute 1640 (RPMI 1640, Corning), Dulbecco's Modified Eagle's Medium (DMEM, Corning), Ham's *F12* without L-Glutamine (F12, Immunological Sciences). Foetal bovine serum (FBS, Immunological Science), Glutamine 200 mM (Euroclone), Penicillin Streptomycin solution 100X (Pen-Strep, Corning), Geneticin (G418, Thermo Fisher Scientific). 0.25% trypsin/2.21 mM EDTA solution 1X, without Sodium bicarbonate (Trypsin, Corning), Dulbecco's Phosphate-Buffered Saline 1X, without calcium and magnesium (PBS, Corning). Trypan Blue Solution 0.4% (w/v) in PBS (Corning). MycoBlue Mycoplasma Detector Kit (Vazyme Biotech), Nonidet P-40 (NP-40, AppliChem). Nunc™ EasYFlask™ Cell Culture Flasks 75cm^2 (Cat#156472, Thermo Scientific), Nunc™ EasYDish™ Dishes 150mm, 145 cm^2 (Cat#150468, Thermo Scientific), Nunc™ Cell Factory™ Systems 25280 cm^2 (Cat#139446, Thermo Scientific). 50 mL 174×22 mm polypropylene tube (Sarstedt)

FBS complement inactivation was performed at 56°C for 30 minutes before use.

Cell cultivation. MDA-MB-231 and MDA-MB-453 were cultured in RPMI 1640 medium supplemented with 10% (v/v) FBS, 1% (v/v) glutamine, and 1% (v/v) Pen-Strep. The PC3 cells were maintained in DMEM/F12 (1:1 mixture) supplemented with 10% FBS, 1% glutamine, and 1% Pen-Strep. The PC3-CD63-GFP cells were cultivated in a complete medium containing 0.1 mg/ml G418 [86].

All the cultures were maintained at 37 °C in a humidified atmosphere of 5% CO_2. Before confluence, cells were trypsinized and resuspended in a fresh growth medium before plating, at a ratio of 1:3, onto a new growth surface.

Cell counts and viability. Cell counts and viability assays were performed using the Trypan Blue exclusion test.

Mycoplasma Assay. The MDA MB-231, MDA-MB-453, PC3, and PC3-CD63-GFP cell lines were routine testing for mycoplasma contamination. Potential mycoplasma contamination was determined using a MycoBlue Mycoplasma Detector according to the manufacturer's instructions.

Expansion of the culture. In order to collect a massive amount of EV conditioned medium, all the cell lines were expanded from 75cm^2 Flasks to 150mm Dishes, and then to Cell Factory Systems. All the expansions were performed when the cells were at 80% confluence in the previous support. The cells were seeded at 1:3 of the initial cell density after the passage in the larger support.

Starvation and harvesting of the conditioned medium. Briefly, after reaching 70–80% confluence (MDA-MB-231~1.4×10^5 cells/cm^2, MDA-MB-453~2.8×10^5 cells/ cm^2, PC3 and PC3-CD63-GFP~2.2×10^5 cells/cm^2), the cells were meticulously washed with PBS three times to remove cell debris and FBS residual, and the culture medium was replaced with the starvation medium (FBS-free medium). After 24 h, the EV-conditioned medium (CM) was collected from the support in 50 mL tubes and the cultured was switched to a growth medium. Immediately after the collection, the CM was centrifuged at 800 *g* for 30 minutes at 4°C (A-4-44 rotor, 5804R Eppendorf centrifuge) to remove any cell or cell debris remaining in the CM. The clarified supernatant was transferred to new tubes and was used for EV isolation.

Preparation of cell lysates. Whole-cell lysates were prepared with NP-40 buffer (NP-40 0,1% in PBS). Briefly, the culture medium was discarded and the cells were washed twice with ice-cold PBS. The cells were scraped from the surface and collected in 1.5 mL Eppendorf tubes. The cells were pelleted at 13,000 *g* for 10 sec at 4°C and the supernatant was removed. The pellet was resuspended with the NP-40 buffer and was incubated for 15 minutes in ice [87]. The cell lysate was sonicated for 10 sec at 15% of power and then it was centrifuged at 13.000 *g* for 10 minutes at 4°C. The supernatant was transferred to a fresh Eppendorf tube. The protein content was quantified with the Bradford assay and the cell lysate was stored at -20°C.

11.3 Extracellular Vesicle isolation

Chemicals. HPLC grade water (Cat#270733, Sigma Aldrich), Dulbecco's Phosphate-Buffered Saline 1X, without calcium and magnesium (PBS, Corning), Tris(hydroxymethyl)aminomethane (Tris, Cat#T1503, Sigma Aldrich), sucrose 99.5% (Cat#S0389, Sigma Aldrich), Protease Inhibitor Cocktail (P.I., Sigma).

The gradient buffer was made of 10 mM Tris-HCl, pH 7.4.

11.3.1 EV isolation from cell-conditioned medium

11.3.1.1 Medium pre-analytical processing

At 24 h, a conditioned medium (CM) was harvested and EVs were isolated by Differential Centrifugation (DC) and Ultracentrifugation (UC) [67] or Tangential Flow Filtration (TFF). In both methods, a preliminary centrifuge at 800 *×g* for 30 minutes at 4°C (A-4-44 rotor, 5804R Eppendorf centrifuge) was included to eliminate any cells or debris remaining in the CM that could result in misleading results.

The isolation of the EVs from CM was performed using two different method: I) Tangential Flow Filtration (TFF) and, II) Differential centrifugations and ultracentrifugation (dUC) method.

11.3.1.2 Tangential Flow Filtration (TFF)

The EV isolation was performed using the KrosFlo® KR2i TFF System from (Repligen Spectrum Labs) and with the following set of cartridges: I) C1, with a cut-off of 650 nm (D04-E65U-07-N, Repligen Spectrum Labs), II) C2, with a cut-off of 200 nm (D04-P20U-10-N, Repligen Spectrum Labs), and III) C3, with a cut-off of 500KDa~25 nm (D05-E500-10-N, Repligen Spectrum Labs). Before use, the cartridges were washed with sterile water until the output flow solution reaches neutral pH. Moreover, at the end of the filtration, the TFF cartridges were cleaned using NaOH 0.2 M according to the manufacturer's datasheet and stored in NaOH 0.05 M.

Briefly, the EV-conditioned medium was centrifuged at 800 *×g* for 30 minutes at 4°C (A-4-44 rotor, 5804R Eppendorf centrifuge). The resulting pellet was discarded while the supernatant was transferred to a clean bottle. The TFF system was set at the following parameters: I) Concentration mode, II) Concentration factor: 10x, III) Feed flow rate: between 100 mL/minutes and 200 mL/minutes, IV) transmembrane pressure (TMP): 0.5 psi. The supernatant was clarified through C1. The first retentate (R1) was collected and stored at 4°C while the first permeate (P1) was processed with C2. Again, the second retentate (R2) was collected and stored at 4°C and the second permeate (P2) was filtered through C3 to obtain the last retentate (R3) and the last permeate (P3). At the end of the protocol, four fractions were collected I) R1 containing particles with a size > 650 nm, II) R2 containing particles with a size between 650 nm and 200 nm, III) R3 containing particles with a size between 200 nm and 25 nm and, IV) P3 containing particles with a size < 25 nm. The collected fractions were concentrated using Centricon Plus-70 centrifugal filters (MWCO 100kDa, Millipore) following the manufacturer's instructions and the EV preparations were characterised and were frozen at −80 °C until further use.

Despite the promising results, unfortunately, the entire production of cartridges has been entirely devolved to the COVID-19 vaccines. The lack of cartridges has no longer allowed this type of isolation to continue. Experiments based on the TFF isolation were arrested, and all subsequent isolations were conducted via dUC.

11.3.1.3 Differential centrifugations and ultracentrifugation

Cell culture supernatants were centrifuged at 800 *×g* for 30 minutes (A-4-44 rotor, 5804R Eppendorf centrifuge) to obtain the first pellet (P1) containing the large EVs (LEVs). The supernatant was transferred in polycarbonate tubes (Cat#357003 Beckman Coulter) and was centrifuged at 16,000 *×g* for 45 minutes (ja20 rotor, Avanti J25) to reap a medium EV (MEV)-enriched pellet (P2). The supernatant was transferred to polycarbonate tubes (Cat# 355622 Beckmann Coulter) and was ultracentrifuged at 100,000 *×g* for 4 h (TY45i rotor, Optima XP80, Beckman Coulter) to obtain a small EV (SEV)-enriched pellet (P3). The resulting pellets (P1, P2, and P3) were washed by resuspension in filtered PBS (final volume 1.5 mL). P1 and P2 were re-pelleted at the respective *g force* and time (45-30-11 rotor, 5417C Eppendorf centrifuge); P3 was re-pelleted at 100,000 *×g* for 2 h (TLA-55 rotor, Optima MAX, Beckmann Coulter). All steps were performed at 4°C, centrifugations speed decreased with the max brake on. Finally, EV pellets were re-suspended in 100 µL of PBS 1X (or pure water for the Atomic Force Microscopy analysis) supplemented with a 1:1000 P.I. Cocktail. The EV preparations were frozen at −80 °C until further use.

11.3.2 EV isolation from human plasma and from red blood cells

Red Blood Cells EV (RBC-EVs) collection (isolation\separation). RBC-EVs were isolated following the guidelines from Nguyen et al. [88, 89]. Briefly, after blood collection, RBCs were pelleted by centrifugation at 1000 × *g* for 8 minutes at 4°C and washed three times in PBS. RBCs were further washed two times with CPBS (PBS + 0.1g/L calcium chloride) and transferred into a 75mm^2 tissue culture flask. Calcium ionophore (A23187, Sigma Aldrich, St. Louis, USA) was added to the flask (final concentration 10 mM) and incubated overnight at 37°C. RBCs were gently collected from the flask, and cellular debris were removed by differential centrifugation (600 × *g* for 20 minutes, 1600 × *g* for 15 minutes, 3260 × *g* for 15 minutes, and 10,000 × *g* for 30 minutes at 4 °C). The pellet was discarded at every step, transferring the supernatant to a fresh tube. The

supernatants were filtered through 0.45 µm nylon syringe filters. EVs were concentrated by ultracentrifugation at 100,000 × g for 70 minutes at 4 °C (Optima XPN-100, TY45 Ti rotor, Beckman Coulter, USA). EV pellets were then resuspended in cold PBS, layered above 2 ml frozen 60% sucrose cushion, and centrifuged at 100,000 × *g* for 16 h at 4 °C (Optima MAX-XP, MLS-50 rotor, Beckman Coulter, USA), with deceleration speed set to 0. The red layer of EVs was collected and washed twice with cold PBS and spun at 100,000 × *g* for 70 minutes at 4 °C (Optima MAX-XP, TLA-55 rotor, Beckman Coulter). Finally, EVs were resuspended in 1 ml of cold PBS.

Plasma pre-analytical processing. EDTA-blood samples were collected from healthy subjects and were processed within 2 hours from the withdrawal and kept at room temperature[90, 91]. EDTA blood samples were centrifuged at 800 ×*g* for 10 minutes in 15 mL tubes (A-4-44 rotor, 5804R, Eppendorf Centrifuge), and afterwards, the EDTA-plasma samples were centrifuged at 2,500 *g* for 15 minutes, two times. All centrifugation steps were performed at room temperature (22°C) with low acceleration and avoiding the application of the centrifuge brake. After each centrifugation, plasma was collected in a fresh plastic tube, leaving 1 cm of plasma above the buffy layer so as not to disturb it. Plasma was finally polled and transferred into 1.5 mL Eppendorf tubes in 1 ml aliquots and stored at -80C [92].

Differential centrifugation, ultracentrifugation. Plasma EVs were isolated through a protocol of differential centrifugation, ultracentrifugation, and discontinuous sucrose gradient [93]. Briefly, 1 mL plasma was centrifuged at 800 ×*g* for 30 minutes (45-30-11 rotor, 5417C Eppendorf Centrifuge). The supernatant was transferred to a new tube and was centrifuged at 16 000 ×*g* for 45 minutes (45-30-11 rotor, 5417C Eppendorf Centrifuge). Finally, the supernatant was transferred to a 1.5 mL polypropylene microfuge tube (Beckmann Coulter) and was centrifuged at 100 000 ×*g* for 2 h (TLA-55 rotor, Optima MAX, Beckmann Coulter). As previously described, the 800 ×*g* centrifugation step allows sedimentation of LEVs, the 16 000 ×*g* step allows us to pellet MEVs, while the 100,000 ×*g* ultracentrifugation enriches SEVs. All steps were performed at 4°C, centrifugations speed decreased with the max brake on.

Discontinuous sucrose gradient. The discontinuous sucrose gradient was prepared in Open-Top Thinwall Polypropylene Tube (Cat# 326819, Beckmann Coulter) with 15% (0.6 mL), 20, 25, 30, 40, 60% (0.4mL), 70% (0.8mL) sucrose (w/v) in gradient buffer [92–94]. SEV pellet was re-suspended in 1mL of gradient buffer with 250 mM sucrose (8% w/v) and was loaded on top of a discontinuous sucrose gradient. The sucrose gradient was centrifuged at 100,000 ×*g* for 16 h at 4°C (rotor MLS 50, Beckman Optima MAX, Beckmann Coulter). Twelve fractions with equal volumes (0.4 mL) Fractions were collected into a 1.5 mL polypropylene microfuge tube (Beckmann Coulter) from the top of the gradient, were diluted to 1.5 mL with PBS 1X, and were ultracentrifuged at 100 000 ×*g* for 2 h at 4°C (TLA-55 rotor, Optima MAX, Beckmann Coulter). EV pellets were re-suspended in 50µL of PBS 1X (or pure water for the Atomic Force Microscopy analysis) supplemented with a 1:1000 P.I. Cocktail. Fractions were analysed with Sodium Dodecyl Sulphate-PolyAcrylamide Gel Electrophoresis (SDS-PAGE) and Western blot (WB) and then the preparations containing SEV markers (from sixth to ninth, with a density of 1.11–1.22g/cm^3 [93–95]) were frozen at −80 °C until further use.

11.4 Extracellular Vesicle characterisation

11.4.1 CONAN assay

Materials. 1-palmitoyl-2-oleoyl-sn-glycero-3-phosphocholine (POPC, Cat#850457P, Avanti Polar Lipids). Chloroform 100% (Cat#288306, Sigma Aldrich), Methanol 100% (Cat#34860, Sigma Aldrich), HPLC grade water (Cat#270733, Sigma Aldrich), Dulbecco's Phosphate-Buffered Saline 1X, without calcium and magnesium (PBS, Corning).

AuNPs (concentration of 6nM, diameter size between 14nm and 20nm).

POPC liposome synthesis. In CONAN assay, POPC liposomes are used as synthetic, convenient mimic of EVs to create the calibration line used for EVs titration [50].

For liposomes preparation, 7.5 mg of POPC were dissolved in chloroform/methanol 6:1 (v/v) in a glass tube (30 mL, Corex). Solvent was then evaporated using a stream of dry nitrogen and a vacuum pump over-night (O/N). Thus obtaining a thin lipid film on tube walls, which was resuspended in 1 mL of hot (50°C) PBS 1X and vortex mixed 5 minutes for three times, with 5 minutes pauses between each vortex mixing in a water bath at 50°C. Liposome dispersion was tip-sonicated for 20 minutes at 18-20% in ice in order to obtain vesicles with narrow distribution and finally centrifuge at 800 ×*g* for 10 minutes to remove microscopic tip debris. The size distribution of prepared liposomes was checked with DLS (average diameter size 100nm).

Estimation of POPC liposome concentration. The concentration of POPC liposomes can be stoichiometrically estimated by dividing the total lipid amount used for vesicles synthesis by the number of lipids per vesicle (N) obtained by the equation (**Eq. 6**).

Eq. 6
$$N = \frac{\left[4\pi\left(\frac{d}{2}\right)^2 + 4\pi\left(\frac{d}{2} - h\right)^2\right]}{a}$$

Where: d = average of vesicle diameter (measured with DLS); h = lipid bilayer thickness, which can be assumed to be equal to 5nm; a = POPC cross-section, which can be assumed to be equal to 0.5 nm2.

Calibration line. Synthetic POPC liposomes with concentrations ranging from 0.78nM to 25nM were used to build the calibration line. For every standard of liposomes at known concentration, 25 µl of the standard was mixed with 50 µl of AuNPs 6nM (final concentration 3nM), and 25 µl of PBS (final volume 100 µl). After 30 minutes of incubation at RT, the absorbance spectrum from 400 nm to 900 nm was acquired using a 96-well plate reader spectrophotometer (Perkin Elmer Ensight). From the spectra of every standard, AuNP Aggregation Index (AI) and the normalized AI (norm AI or AI%) were calculated and extrapolated using a custom R script.

AI is a useful tool to describe NP's aggregation state. For spherical AuNPs, AI is the ratio between the absorbance at the LSPR peak of pure AuNPs and the absorbance at some significant red-shift wavelength (**Eq. 7**). For the liposomes, the significant shift is the absorbance at 650 nm plus a correction at 850 nm. The AI was normalized on the AI of the AuNPs monodispersed (**Eq. 8**).

Eq. 7
$$AI = \frac{Abs_{LSPR}}{Abs_{650nm} + Abs_{850nm}}$$

Eq. 8
$$normAI = \frac{AI_{sample}}{AI_{\text{AuNPs monodispersed}}}; \quad \text{or} \quad AI\% = \frac{AI_{sample}}{AI_{\text{AuNPs monodispersed}}} \times 100$$

The obtained AI was correlated with the respective liposome concentration to create a calibration line.

Purity CONAN assay and EV quantification. An EV sample was considered "pure", free of single or aggregated protein contaminants (SAP), if its normalized AI (norm AI) was less than 0.2, corresponding to less than 50 ng/µl. To better test the purity of the samples, different dilutions of the same sample were analysed: if AI decreased with a stronger dilution, the EV sample was considered pure (the lower the AI, the less concentrates EV), while if the AI was stable at decrease in the EV concentration, the sample was considered non-pure. For pure EV samples, the CONAN test was also exploited for the quantification of the EVs, by interpolating the AI with the previously created calibration curve.

Briefly, EV samples, resuspended in an appropriate volume of PBS or water, were tested for purity with the CONAN test [50]. Briefly, the experiment was conducted in triplicate as described in [50]. EV samples were diluted 1:1, 1:2, 1:5 and 1:10 in HPLC water. In a 96-well plate, 2 µl of EV preparations were added to 23 µl of HPLC water (final volume 25µl). Subsequently, a 6nM AuNP solution (50 µl) was added to the EV

preparation (final concentration 3nM) and then mixed with 25 µl of 1X PBS (final volume 100 µl). The mixes were incubated for 30 minutes at room temperature and the UV/vis/NIR absorption spectra (400nm to 900nm) were collected using the Ensight multimode plate reader (PerkinElmer). The aggregation index (AI) was extrapolated from the spectra of each sample. Processing of the dataset was done using a custom R script.

11.4.2 Atomic Force Microscopy imaging (AFM)

EV preparations were characterized by size and morphology thanks to the AFM analysis. All AFM experiments were performed in ultrapure water at room temperature. Briefly, EV pellets were diluted 1:10 v/v with sterile H2O (Milli-Q, Merck Millipore). 5 to 10 µL of EV samples were then spotted onto freshly cleaved mica sheets (PELCO® Mica discs Grade V-1, thickness 0.15 mm, 10 mm diameter from Ted Pella Inc.) and air dried over a plate heated at 37-40°C for 10 minutes. Dried samples were then imaged in tapping mode with NaioAFM (Nanosurf AG) equipped with Multi75Al-G (Budget Sensors) tip. Images were collected over different length scales with a scan size ranging from 1µm to 25µm with a and a scan speed of 1s per scanning line. The larger ones allowed the characterisation of the samples as a whole in terms of homogeneity or other collective parameters while those collected at higher magnification showed in detail the shape and size of individual vesicles. The obtained topography images were processed with Gwyddion ver. 2.61 software, while EVs size distributions were obtained by analysing with ImageJ (PSA macro).

11.4.3 Protein concentration assay

BCA Protein Assay. The protein content of EV preparations was measured using the micro-bicinchoninic BCA Protein Assay Kit (Thermo Fishers Scientific) following the manufacturer's instructions. BCA Protein Assay is a colorimetric method that provides a relative concentration to a bovine serum albumin standard (BSA), which was used for the preparation of a calibration curve. The relative absorbance of the BCA soluble compound was measured at 562 nm using a CLARIOstar® Plus multi-mode plate reader (BMG LABTECH).

Bradford assay. The Bradford assay is a colorimetric protein assay based on an absorbance shift of the dye Coomassie Brilliant Blue G-250. The Coomassie Brilliant Blue G-250 dye exists in three forms: anionic (blue), neutral (green), and cationic (red). During the assay, the red form of the dye is converted into the blue form due to the formation of bonds with functional protein groups and the colour change can be measured using UV/Vis spectrophotometer. The blue form of dye has the maximum absorption at 595nm. The increase of absorbance at 595nm is proportional to the amount of bound dye, and thus to the concentration of sample proteins. To determine the EV protein concentration, a BSA (Sigma) standard calibration curve was created with known concentrations (0, 2, 4, 8, 12 and 16µg/µl). Absorbance values of standards, measured with a spectrophotometer (Microplate reader, Model 680, Biorad) were correlated with the respective BSA concentration to create a calibration line. Absorbance values of the samples were interpolated with the calibration curve to obtain the protein concentration.

11.4.4 Nanoparticle Tracking Analysis

Nanoparticle Tracking Analysis (NTA) was performed according to the manufacturer's instructions using a NanoSight NS300 system (Malvern Technologies, Malvern, UK) configured with a 532nm laser. Samples were diluted 1:1000 in filtered PBS to a final volume of 1mL. A syringe pump with constant flow injection was used and three videos of 60s were captured and analyzed with NTA software version 3.2. From each video, the mean, mode, and median EV size were used to calculate sample concentration, expressed in particles/mL.

11.4.5 SDS-PAGE and Western blot

Materials. Loading buffer (reducing SDS sample buffer (80mM Tris, pH 6.8, 2%SDS, 7.5% glycerol, 0.01% bromophenol blue) supplemented with 2% 2-mercaptoethanol (Sigma-Aldrich)), blocking buffer (5% (w/v) non-fat dried skim milk in PBS with 0.05% Tween-20, PBST).

Total cell homogenates and EV preparations were mixed with proper volumes of 6X loading buffer. The samples were boiled at 95°C for 5 minutes, and were separated by SDS-PAGE on acrylamide/bisacrylamide 10% gel.

Immunoblotting. Samples were normalized for EVs concentration when possible (20 µg) or alternatively, equal volumes of each sample were loaded on a SDS−PAGE gel (25 µL). Total cell homogenates (20 µg) of and an equal volume of EVs preparations (25 µL) were loaded on a 10% SDS-PAGE gel and were separated for 1.30 h at 100 V. The proteins were transferred on a PVDF membrane (GE Healthcare) for 1h at 100 V. Membranes were blocked with blocking solution for 1h at 37°C and afterwards, they were washed three times with PBST before the incubation (under agitation, overnight at 4 °C) with primary antibodies diluted in 1% (w/v) non-fat dried skim milk in PBST. The membranes were washed 3 times for 10 minutes with PBS Tween 0.05%, and were incubated with the HRP-conjugated secondary antibody diluted in 1% (w/v) non-fat dried skim milk in PBST for 1h, at RT. After three washes with PBST Blots were detected using Luminata Classic HRP western substrate (Millipore). Images were acquired using a G: Box Chemi XT Imaging system (Syngene, UK). For densitometric analysis, we took advantage of the Image Lab software (Biorad, Hercules, CA, US). For CTX quantification, after the electrophoresis run, the gel was imaged via Odyssey® Fc Imaging System (LI-COR Biosciences, Lincoln, NE, USA) with an acquisition time of 2 minutes and 800 nm wavelength.

The following primary antibodies and dilutions were used: rabbit polyclonal anti-alpha Actinin 4 (1:1000, Cat#GTX101669, Genetex), mouse monoclonal anti-Alix (1:500, Cat#sc-53539, Santa Cruz), rabbit polyclonal anti-Annexin XI (1:1000, Cat#GTX33010, Genetex), mouse anti-CD45 (1:1000, Santa Cruz Biotechnology, USA), mouse anti-CD47 (1:1000, Santa Cruz Biotechnology, USA). Mouse monoclonal anti-CD63 (1:1000, Cat#CBL553, Millipore), mouse monoclonal anti-CD9 (1:500, Cat#sc-7637, Santa Cruz) and rabbit monoclonal anti-CD90 (1:1000, Cat#ab133350, Abcam). Rabbit anti-EGFR (1:1000, Cell Signalling Technology Inc.), mouse anti-GM130 (1:1000, BD Biosciences, Germany), mouse anti-HBA1 (1:1000, Abnova, Jhouzih St., Taipei, Taiwan) and, mouse anti-HBB (1:1000, Abnova, Jhouzih St., Taipei, Taiwan).

The following HRP-conjugated secondary anti- bodies and dilutions were used: rabbit polyclonal anti-mouse and (1:5000, Cat#A90-117P, Bethyl) and goat polyclonal anti-rabbit at (1:5000, Cat#A120-101P, Bethyl), rabbit monoclonal anti-CD63 (1:500, Cat#ab134045, Abcam), rabbit monoclonal anti-APO A1 (1:500, Cat#), (at dilution 1:3000): rabbit anti-mouse and goat anti-rabbit (Zymed).

11.4.6 Cetuximab modification

Materials. Erbitux (Cetuximab, Ctx) 5 mg/mL (Merck Europe B.V.); DBCO STF ester (Click Chemistry Tools); Sulfo Cyanine 7.5 NHS ester (Lumiprobe GmbH); NaN_3 (Sigma Aldrich); azido-Sulfo Cyanine 3 (Lumiprobe GmbH). Storage buffer (sterile PBS + 0.1 mM NaN_3); Reaction buffer (0.1 mM $NaHCO_3$ pH 8.4); Deactivation buffer (1 µM of NaN_3). VivaSpin2000 column (Sartorius Stedim Lab Lid) with 50 KDa cut-off; Vivaspin500 column (Sartorius Stedim Lab Lid) with 30 KDa cut off.

Optimization of the protocol. Cetuximab (CTX) was provided by in storage buffer. The storage buffer was replaced with reaction buffer to grant the optimal functionalization of CTX using the VivaSpin2000 column with 50 KDa cut-off. CTX solutions were centrifuged at 2000 × *g* for 15 minutes. The buffer exchange step was repeated 3 times, adding 2 mL of reaction solution at each step. After the buffer exchange process, CTX concentration was quantified by NanoDrop™OneC (ThermoFisher). For optimization of the antibody functionalization CTX was incubated overnight on continuous mixing at 4°C with 8 equivalents of DBCO STF ester and 8 equivalents of Sulfo Cyanine 7.5 NHS ester, and 6 equivalents of DBCO STF ester and 12 equivalents of Sulfo Cyanine 7.5 NHS ester. Thus obtaining two different preparation of modified CTX (mCTX), CTX: DBCO: Cy7.5 (1:8:8) and CTX: DBCO: Cy7.5 (1:6:12), respectively. DBCO conjugation yield was estimated by incubating a small aliquot of functionalized mCTX with azido-Sulfo Cyanine 3 on continuous mixing at 4°C o/n. Excess of reagents (Sulfo Cyanine 7.5 NHS ester and DBCO STF ester, azido-Sulfo Cyanine 3 or NaN_3) was

removed with Vivaspin500 column with 30KDa cut off. The mCTX solutions were centrifuging the at 12000 × *g* for 15 minutes, and washed with 500µL of PBS until no significant signal from the two free fluorescent dyes could be detected in the washing buffer by UV-Vis spectroscopy. Final concentration of CTX and mCTX functionalisation were verified using UV-Vis spectroscopy. mCTX functionalisation was furtherly observed by SDS-PAGE, on Odyssey Fc. (LI-COR Biosciences).

Final reaction. For the final antibody functionalization, CTX was incubated overnight on continuous mixing at 4°C with 12 equivalents of Sulfo Cyanine 7.5 NHS ester and 6 equivalents of DBCO STF ester, thus obtaining modified CTX (mCTX). For deactivation, mCTX was incubated with deactivation buffer o/n.

11.4.7 EVs functionalization

Materials. N_3-$(Peg)_4$-NHS-Ester (Click Chemistry Tools, 8341 E. Gelding Dr, Scottsdale, AZ, USA); MemGlow™ 488 (Cytoskeleton, Inc., CO, Denver, USA). Vivaspin500 column (Sartorius Stedim Lab Lid, Sperry Way, Stonehouse, UK) with 10 KDa cut off

EVs were functionalized following a two-step labeling strategy. 100µL of $8x10^{11}$ particles/ml EVs was reacted with 200, 500, or 1000 equivalent of N_3-$(Peg)_4$-NHS-Ester overnight on continuous mixing at 4°C. The Peg excess was removed using Vivaspin500 column with 10 KDa cut off, washing the samples 5 times with 500µL of PBS. PEGylated EVs were then reacted overnight on continuous mixing at 4°C with 200, 500, or 1000 equivalent of mCTX. The unreacted mCTX was removed by ultracentrifugation (100,000 × *g*, 2 h), and the pellet was resuspended in 100 µL of PBS and stored at 4°C until use. EV functionalisation with MemGlow™ 488 was performed following standard customer protocols. EV were incubated with MemGlow™ 488 100 nM for 15 minutes, then MemGlow™ 488 excess was removed by ultracentrifugation (100 000 × *g*, 2 hours). The final preparation was performed used RBC-EVs.

11.4.8 Surface Plasmon Resonance evaluation

Materials. Epidermal Growth Factor Receptor (EGFR); Epidermal Growth Factor (EGF, #10605-HNAE-250, Sino Biological Inc. Beijing, China), Erbitux (Cetuximab, Ctx) 5 mg/mL (Merck Europe B.V.). HBS buffer (0.01 M HEPES 0.15 M NaCl pH 7.4); NaOAc buffer (10 mM NaOAc, pH 4.8).

Protocol. EGFR (15 µg/ml) was immobilized onto a CM5 sensor chip using amine coupling according to the manufacturer [96]. The binding kinetics of Epidermal Growth Factor (EGF), CTX, mCTX (CTX:DBCO:Cy7.5(1:8:8) and CTX:DBCO:Cy7.5(1:6:12)), pristine EVs (pEVs) and mCTX-EVs to EGFR were measured using a Biacore platform. EGF was injected at concentrations ranging from 31.25nM to 500nM. CTX and mCTX were injected at concentrations ranging from 0,073nM to 6nM. The binding of pristine EV (pEV) and mCTX-EVs to EGFR were tested at the same concentrations (0.034nM) and the mCTX-EV were injected at concentrations ranging from 0.0021nM to 0.1747nM. mCTX-RBC-EVs were injected at concentrations ranging from 0.0034nM to 0.273nM. EGF/CTX/mCTX were used as positive control while the pEVs as a negative control. Chip regeneration was achieved by injecting glycine pH 2.5 and NaOAc buffer (10 mM NaOAc, pH 4.8), followed by HBS buffer (0.01 M HEPES 0.15 M NaCl pH 7.4). Data coming from the reference flow cell was subtracted to remove the effects of non-specific binding. Sensorgrams were acquired for each concentration and evaluated using the BIA Evaluations program.

11.4.9 Cell mito stress test

Materials. Oligomycin, Carbonyl cyanide-4-(trifluoromethoxy) phenylhydrazone (FCCP), rotenone plus antimycin A (R/A), Seahorse XFe24 Analyzer.

Protocol. The protocol was performed followed the manufacture instructions. MDA-MB cells (MDA-MB-231 and MBD-MB-453) were resuspended in 100µL and were seeded at different amounts (20 000, 40 000, 60 000) in XFe24 cell culture plate. The plate was incubated for 1 hour at RT to promote even cell distribution and reduce edge effects. The plate was incubated in 5% CO_2 atmosphere at 37°C to favour cell adhesion for

5 hours. The cell medium was gently added to a final volume of 250µl and then the plate was incubated in 5% CO_2 atmosphere at 37°C for 24 hours. In the first experiment, the cells were incubated for 24 hours and were I) treated with 20nM CTX or II) left untreated for another 24 hours. In the second experiment, the MDA-MB-231 cells were plated at 40 000 cells/well and after 24 hours were incubated with different CTX concentrations (20nM, 10nM, 2nM, 0.2nM, 0nM) for 24 hours. In this experiment, the best amount of FCCP was optimized.

After the treatment, the medium was replaced with 525uL seahorse medium, with or without CTX. After media changes, the cells were incubated at 37°C w/o CO_2 for 1 hour and measured with the Seahorse platform (Seahorse XFe24 Analyzer). In the Seahorse mesurement I) the ATP synthase inhibitor oligomycin, II) the mitochondrial oxidative phosphorylation uncoupler Carbonyl cyanide-4-(trifluoromethoxy) phenylhydrazone (FCCP) and III) the Complex I inhibitor rotenone plus the complex III inhibitor antimycin A (R/A) were sequentially injected to evaluate basal respiration, ATP production and maximal respiration of primary neuronal cells.

11.4.9.1 Seahorse data analysis

Mitochondrial activity was calculated in the following way (**Figure 35**): I) Basal respiration was calculated from the last rate measurement before Oligomycin injection by subtracting the last step non-mitochondrial oxygen consumption rate (ORC) obtained after Rotenone/Antimycin A (Rot+Ant) injection. II) ATP production was calculated by subtracting the minimum rate measurement after Oligomycin injection from the last rate measurement before Oligomycin injection. III) Proton Leak was calculated by subtracting the minimum rate measurement after Oligomycin injection by subtracting the last step non-mitochondrial ORC. IV) Maximal respiration was calculated after trifluorocarbonylcyanide phenylhydrazone (FCCP) injection by subtracting non-mitochondrial OCR from the maximum rate measurement. V) Spare respiratory capacity was calculating by subtracting basal respiration from maximal respiration. The formula of this parameter were shown (Table 12). From ECAR basal levels of glycolytic activity can be determined but the glycolysis was not directly measured, data on the ECAR is an additional measurement collected while completing the Mito Stress test.

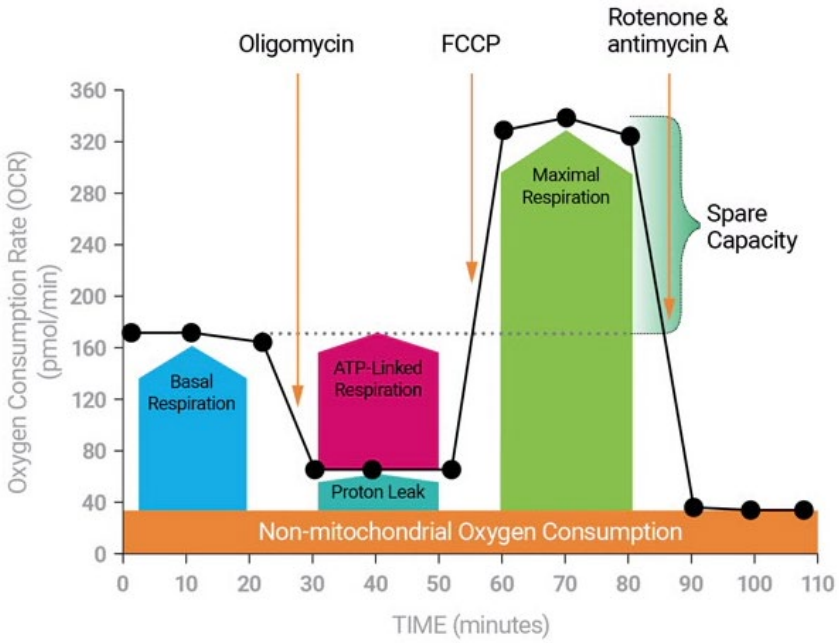

Figure 35. The system to read and process the data of the Mito Stress Test carried out with the Seahorse platform (Seahorse XFe24 Analyzer) were illustrated.

Table 12. The seahorse parameter and their equation.

Parameter Value	Equation
Non-mitochondrial ORC	Minimum rate measurement after Rotenone/antimycin A injection
Basal Respiration	(Last rate measurement before first injection) – (Non-Mitochondrial Respiration Rate)
Maximal Respiration	(Maximum rate measurement after FCCP injection) – (Non-Mitochondrial Respiration)
H+ (Proton) Leak	(Minimum rate measurement after Oligomycin injection) – (Non-Mitochondrial Respiration)
ATP Production	(Last rate measurement before Oligomycin injection) – (Minimum rate measurement after Oligomycin injection)
Spare Respiratory Capacity	(Maximal Respiration) – (Basal Respiration)

1.1.1 *In vitro* uptake assay

MDA-MB-231 cells were seeded as 25000 cells/cm^2 in 96-well plates pre-coated with 50µg/mL collagen. After 24 hours, cells were treated for 4 hours and 24 hours with mCTX, EVs, mCTX-EVs, and mCTX-Peg-EVs previously labeled with Membright488 in media with or without FBS. Each treatment was carried out in triplicate using comparable amounts of EVs (1E+10 EVs/mL) and CTX (1.61E-1nM). Cells were then washed twice with PBS 1X without $CaCl_2$ and $MgCl_2$ and fixed with 3% Paraformaldehyde (PFA) solution for 15 minutes at RT. Then, PFA was quenched with 50 mM NH_4Cl for 10 minutes at RT. Cells were washed twice with PBS 1x and permeabilized with 0.3% Saponin in PBS 1x for 10 minutes at RT. Cells were incubated with DAPI (1:600) for 30 minutes at 37°C in the dark. Cells were finally washed twice with PBA 1X and once with pure water. DAPI, Membright, and CTX fluorescence were acquired with an Ensight multimode reader (Perkine-Elmer) as follows: DAPI Ex/Em 359nm/457nm; Membright Ex/Em 499nm/507nm; CTX 750nm/780nm. For each treatments, membright and CTX fluorescence signals were normalized to DAPI fluorescence. Data from three independent experiments were expressed as mean ± Standard Error of the Mean (SEM). For these experiments the RBC-EVs were used.

1.1.2 Confocal microscopy

MDA-MB-231 cells were seeded on 12 mm-sized coverslips as 200000cells/mL in 150µL of complete media. After 24 hours, cells were treated for 4 hours and 24 hours with mCTX, EVs, mCTX-EVs, and mCTX-Peg-EVs in media with or without FBS as described above. Each treatment was carried out using comparable amounts of EVs (10E+10 EVs/mL) and CTX (1.61E-1nM). Cells were washed once with PBS 1X without CaCl2 and MgCl2 and then fixed with 3% PFA solution. PFA was quenched with 50 mM NH_4Cl for 10 minutes. Cells were washed twice with PBS 1x and permeabilized with 0.3% Saponin in PBS 1x for 10 minutes at RT. Cellular nuclei were stained with DAPI (1:600). Cells were washed twice with PBS 1x, once with pure water, and coverslips were mounted using ProLong™ Gold Antifade Mountant (P36934, Invitrogen). 512x512 pixel images were acquired with a Zeiss LSM510 with a Plan-Apochromat 63x/1.4 Oil DIC objective, with a 0.2% 405nm laser for DAPI and 488nm for Membright488.

Chapter 12

Results and discussion

12 PRIN project - Results and discussion

12.1 Cell lines selection

MDA-MB-231 cells are human epithelial cell line from metastatic mammary adenocarcinoma. MDA-MB-231 is a highly aggressive, invasive and poorly differentiated triple-negative breast cancer (TNBC) cell line as it lacks oestrogen receptor (ER) and progesterone receptor (PR) expression, as well as HER2/neu (human epidermal growth factor receptor 2) amplification. However, MDA-MB-231 presents the epidermal growth factor receptor (EGFR) expression, making these tumours amenable to targeted therapy with EGFR inhibitors. MDA-MB-453 cell line is androgen receptor-positive and "triple-negative" with respect to ER and PR and the HER2/neu protein expression. Furthermore, the expression of EGFR is lacking so it is a good negative control inside our metabolic experiment.

12.2 Extracellular Vesicle production

All experiments require large quantities of EVs isolated from litres of conditioned cell medium (**Table 13**) or human plasma.

Sample ID	N°Estrazione	Cell Type	Source	Confluence	Amount	Starvation	Other	Extra information
E01_P2	1	MDA-MB-231 p29	NUNC	80%	5 x 50 mL	16/06/2021 24h	centrifuga a 800g x 30' prefreeze (-20°C)	06/07/2021 Test Mycoplasma: esito negativo
E01_P3					1 x 50 mL	18/06/2021 n. 2 24h		
E02_P2	2	MDA-MB-231 p29	NUNC	80%	4 x 50 mL	18/06/2021 n. 2 24h	centrifuga a 800g x 30' prefreeze (-20°C)	
E02_P3		MDA-MB-231 p26	Dish 15	65%	1 x 50 mL	02/06/2021 24h		
		MDA-MB-231 p26	Dish 15	70%	1 x 50 mL	04/06/2021 24h		
E03_P2	3	MDA-MB-231 p30	NUNC	60-70%	6 x 50 mL	30/06/2021 24h	centrifuga a 800g x 30' prefreeze (-20°C)	
E03_P3								
E04_P2	4	MDA-MB-231 p30	NUNC	70%	5 x 50 mL	14/07/2021 24h	centrifuga a 800g x 30' prefreeze (-20°C)	
E04_P3					1 x 50 mL	29/06/2021 24h		
E05_P2	5	MDA-MB-231 p30	NUNC	60-70%	4 x 50 mL	01/07/2021 24h	centrifuga a 800g x 30' prefreeze (-20°C)	
E05_P3				70%	2 x 50 mL	29/06/2021 24h		

Sample ID	N°Estrazione	Cell Type	Source	Confluence	Amount	Starvation	Other	Informazioni
	6	MDA-MB-231 p30	NUNC	70%	3 x 50 mL	29/06/2021 24h	centrifuga a 800g x 30' prefreeze (-20°C)	06/07/2021 Test Mycoplasma: esito negativo
		MDA-MB-231 p30						
E06_P2		MDA-MB-231 p27		60-70%		01/07/2021 24h		
E06_P3		MDA-MB-231 p27	Dish 15	60/65/70%	3 x 50 mL	02/06/2021 24h		
	7	MDA-MB-231 p26	Dish 15	80%	25 mL	25/05/2021 24h	centrifuga a 800g x 30' prefreeze (-20°C)	
				85%	25 mL			
				60%	25 mL	02/06/2021 24h		
		MDA-MB-231 p27		75-85%	40 mL	04/06/2021 24h		
		MDA-MB-231 p28		65-70%	2 x 40 mL	08/06/2021 24h		
E07_P2				75-85%	2 x 40 mL			
E07_P3				85%	25 mL	16/06/2021 25h		

Table 13. An extract from the database of the production of conditioned soil for the isolation of EVs. In table the data on I) ID of the sample, II) type of cell line, III) Type of media used, IV) confluence of the cells, V) date of collection and time of contact with the cells, VI) amount of material collected, VII) pre-processing protocol used, and VIII) extra information on cell status.

The method to obtain large quantities of EVs from cellular media is expensive and complex (**Figure 36**). As for the isolation from conditioned media, the greatest challenge is to expand the cells until they occupy a cell factory (632cm^2 per layer). Once the ideal confluence is reached, between 70-80%, the growth medium is replaced with a starvation medium without FBS. After 24 hours, the conditioned medium is collected, aliquoted, and, if the isolation does not occur immediately, centrifuged to remove residues of cells and apoptotic bodies and frozen. Due to the mandatory quarantines imposed by COVID-19, delays in orders, and the lack of material, these expansions and related isolations have been frequently interrupted. Another relevant problem in expanding cells is bacterial, fungal and mycoplasma contamination. The cells were periodically tested for mycoplasma contamination, and the contaminated cultures were immediately eliminated**.**

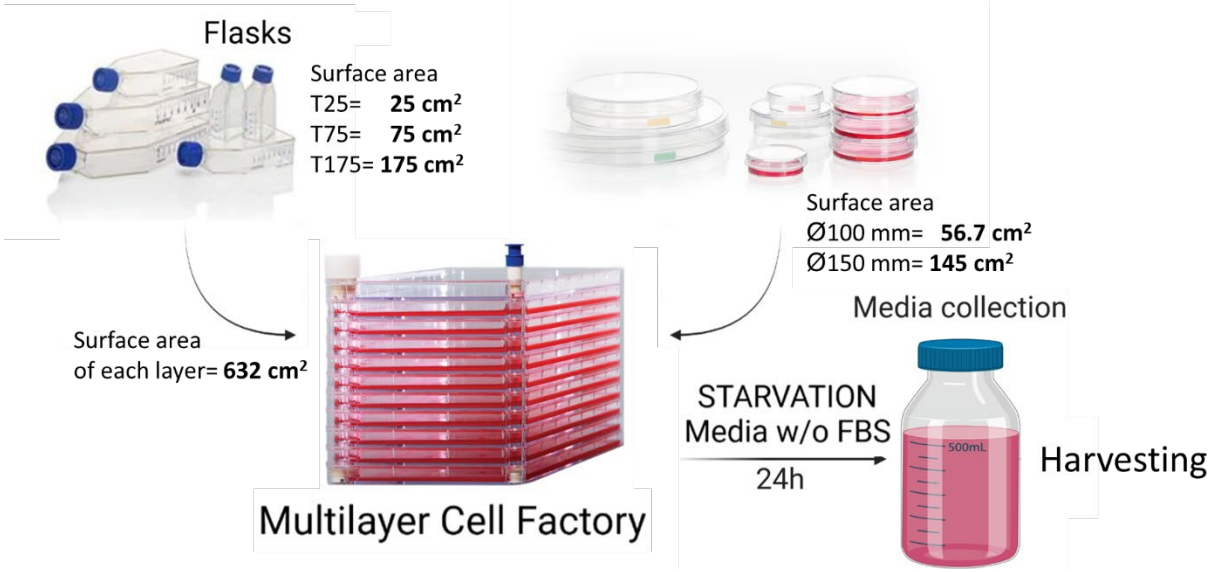

Figure 36. The workflow of the cell expansion and starvation protocol is shown. As can be seen, the cell growth area in the various devices grows exponentially. When the cells reach a confluence of 70-80%, the growth medium is removed, the cells are washed with PBS, and the starvation medium (without FBS) is added. After 24 hours, the conditioned medium is collected for EV isolation.

12.2.1 EV separation and characterization

12.2.1.1 EV isolation from conditioned media

Except for two isolations performed with the PC3-CD63-GFP cell line using the TFF, all other isolations were performed manually using dUC for the cell medium and dUC plus sucrose gradient for the IV isolated from plasma. The volumetric limit for this isolation method is ~ 300mL. An extract from the EV isolation table was displayed (**Table 14**). The table contains all results for both cell lines and human plasma. Each P2 and P3 sample was characterised by the CONAN purity assay and BCA protein analysis. An example of CONAN and BCA analysis is shown (**Figure 37**). The yields, in terms of EV protein content and EV number, were consistent with the estimate of 10E+9 EV particles/µg EV proteins, as reported by Sverdlov and Zendrini *et al.* [81, 97].

Table 14: An extract of the database of EV isolations. In the table was recoding the data about I) Sample ID, II) the isolation date, III) the protocol used for the isolation, and IV)EV characterisation (CONAN, BCA, number of EVs).

EVs name P2=medie P3=piccole	Isolation data	Isolation	CONAN [EV/mL] P2=200nm P3=80nm	CONAN EVs in 80 uL	BCA (proteine) [ug/mL]	BCA ug di proteine in 80 ul	N° EVs da proteine in 80 uL (1ug di prot=2*10^9 Evs)	Extra information
E01_P2	23/6/2021	(16.000g x 45') x2	4,09E+13	3,27E+12	1,91E+03	1,53E+02	3,05E+11	
E01_P3	24/6/2021	(100.000g x 4 h) + (100.000 g x 2h)	1,46E+14	1,17E+13	9,23E+02	7,39E+01	1,48E+11	
E02_P2	24/6/2021	(16.000g x 45') x2	5,86E+12	4,69E+11	NA	NA	NA	
E02_P3	25/6/2021	(100.000g x 4 h) + (100.000 g x 2h)	5,29E+13	4,23E+12	7,07E+02	5,66E+01	1,13E+11	
E03_P2	12/7/2021	(16.000g x 45') x2	NAN	NAN	5,46E+02	4,37E+01	8,74E+10	
E03_P3	13/7/2021	(100.000g x 4 h) +	NAN	NAN	6,10E+01	4,88E+00	9,76E+09	
E04_P2	19/7/2021	(16.000g x 45') x2	NAN	NAN	3,39E+02	2,72E+01	5,43E+10	
E04_P3	20/7/2021	(100.000g x 4 h) +	NAN	NAN	8,71E+01	6,97E+00	1,39E+10	
E05_P2	2/7/2021	(16.000g x 45') x2	NAN	NAN	1,17E+03	9,39E+01	1,88E+11	
E05_P3	3/7/2021	(100.000g x 4 h) +	NAN	NAN	1,01E+02	8,09E+00	1,62E+10	
Usate tutte per l'SPR								
EVs name	Data	Isolation	CONAN [EV/mL]	CONAN EVs	BCA	BCA ug di	N° EVs da proteine in 80 uL	NAN= non testato; NA= testato ma
E06_P2	6/9/2021	(16.000g x 45') x2	NAN	NAN	6,26E+02	5,01E+01	1,00E+11	
E06_P3	7/9/2021	(100.000g x 4 h) +	NAN	NAN	1,73E+02	1,39E+01	2,77E+10	
E07_P2	8/10/2021	(16.000g x 45') x2	NAN	NAN	2,65E+02	2,12E+01	4,23E+10	Pellet filamentoso
E07_P3	8/10/2021	(100.000g x 4 h) +	NAN	NAN	3,92E+00	3,13E-01	6,27E+08	Pellet filamentoso, filtrato a 200 nm

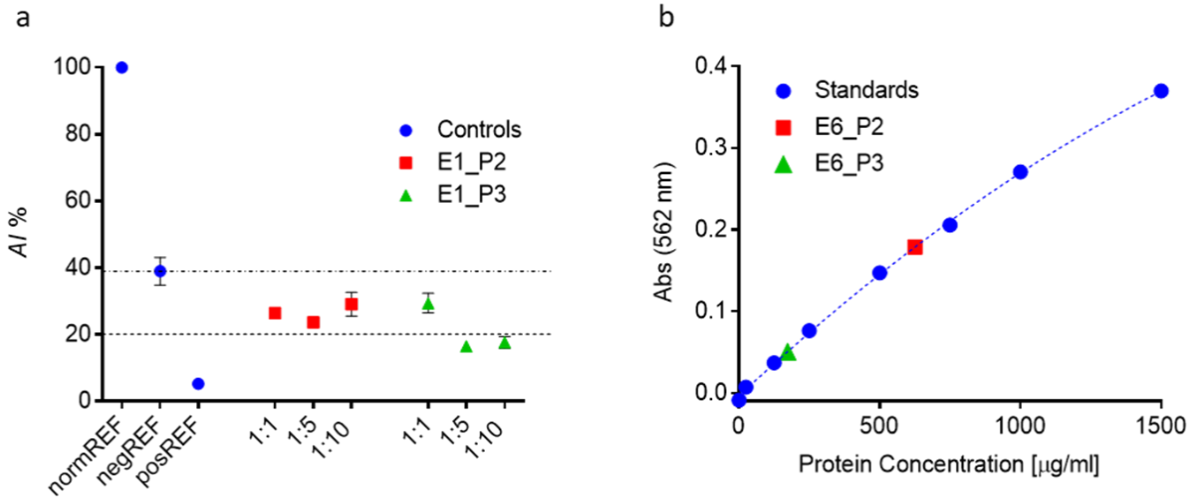

Figure 37. **(a)** Determination of EV preparation purity from protein contaminants using the CONAN assay. An example of CONAN purity assay on MEVs and SEVs Aggregation index (AI) ratios of EV preparations from MDA-MB-231cell line. **(b)** An example of BCA protein assay on MEVs and SEVs.

12.2.1.2 Tangential Flow Filtration (TFF).

TFF seems to be a promising method to separate vesicles because it is more delicate and effective than other isolation methods, such as serial ultracentrifugations. Moreover, it allows the processing of high volumes of samples (such as conditioned culture media) in less time. For this isolation, conditioned media derived from PC3-CD63-GFP cells were used. CD63-GFP is a tetraspanin membrane protein conjugated with GFP protein. CD63 is one of the specific biomarkers in SEVs, so PC3 small-EVs (SEVs) released in the cell culture media are fluorescent. The conditioned medium was filtered with TFF using MidiKros Hollow Fiber Filters (Repligen). The cut-offs of the pore filter were: 1) 650nm, 2) 200nm, 3) 500kDa (25nm circa). In this way, four fractions were obtained: 1) EVs > 650nm, 2) 650nm < EVs < 200nm, 3) 200nm < EVs < 25nm, 4) EVs < 25nm. Fractions

obtained from the filtration were concentrated using Centricon Plus-70 (**Figure 38a**). Finally, EV fractions were analysed by AFM (**Figure 38b**), WB (**Figure 38c**), CONAN assay (**Figure 38d**) and BCA protein assay (**Figure 38e**). The protein analysed are GM130, GFP, CD63, ActIV, Flot1, CD9, Alix, CD81. In particular, fractions with sizes between 200 nm and 650nm (MEVs) and 25nm and 200nm (SEVs) were analysed. As shown, the results obtained are promising. TFF allows to separation and enrich the fluorescent SEVs in the fraction with a size between 25nm and 200nm. Moreover, thanks to the CONAN assay, the purity and the absence of other contaminants in the fractions obtained from TFF were verified. WB results show that CD63 and GFP are both presents and enriched in the TFF fraction of SEVs (they are considerably less concentrated in the MEV fraction), whereas concentrating the other SEV markers.

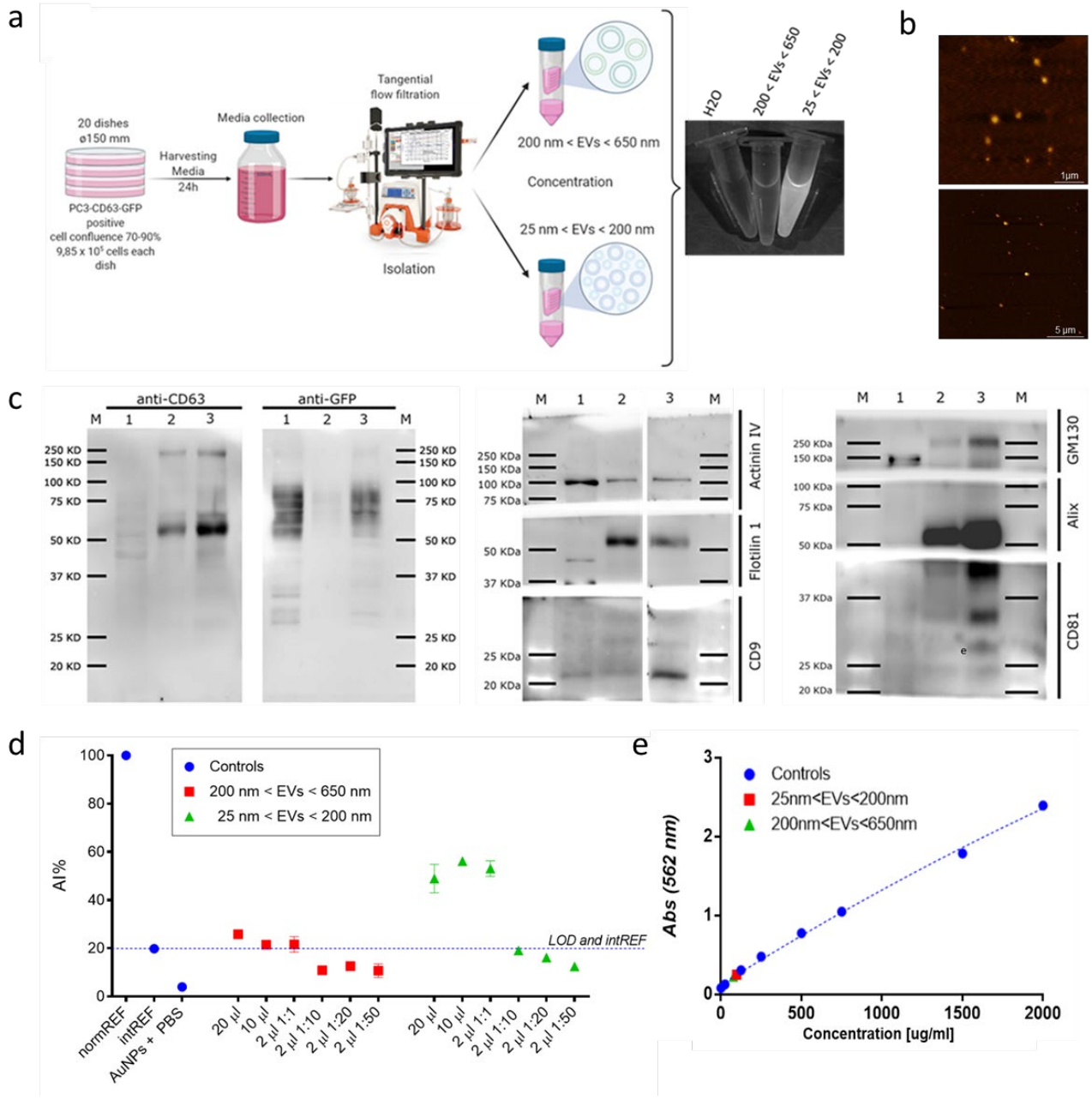

Figure 38. Comparison between fractions obtained from TFF. **(a)** Schematic image of the TFF protocol and image acquired with the program GeneSnap for Syngene: the fraction containing SEVs (25nm < EVs <200 nm) is fluorescent if compared to the fraction containing MEVs (200nm < EVs <650nm) and control (water). **(c)** Biochemical characterisation of EVs by western blot analysis. WB analysis of the TFF fractions and the PC3 homogenate, in which several EV markers were analysed. **(d)** CONAN assay of TFF fractions. **(e)** BCA protein assay of TFF fractions.

12.2.2 EV isolation from human plasma and from red blood cells

The isolation protocol of EV from body fluids (plasma and serum) has been optimised. This type of isolation requires a sucrose gradient to remove the contaminating lipoproteins in the plasma/serum. The input of the gradients was the pellets of the second centrifugation (P2) and the subsequent ultracentrifugation (P3). The EV biomarkers were detected for all the sucrose gradient fractions by WB. The contamination of lipoproteins was localised thanks to the ApoA1 biomarker (**Figure 39**). For the P3 gradient, the lipoprotein contaminants were concentrated in the fractions before the number six. The EV biomarkers were localised in the fraction between fraction seven and fraction ten. Therefore, these fractions were pulled together, cleaned from the sucrose and analysed by CONAN and BCA assay. Unfortunately, for the gradient made with P2, no markers were visible in the fractions. Each P2 and P3 sample was characterised by the CONAN purity assay and BCA protein analysis.

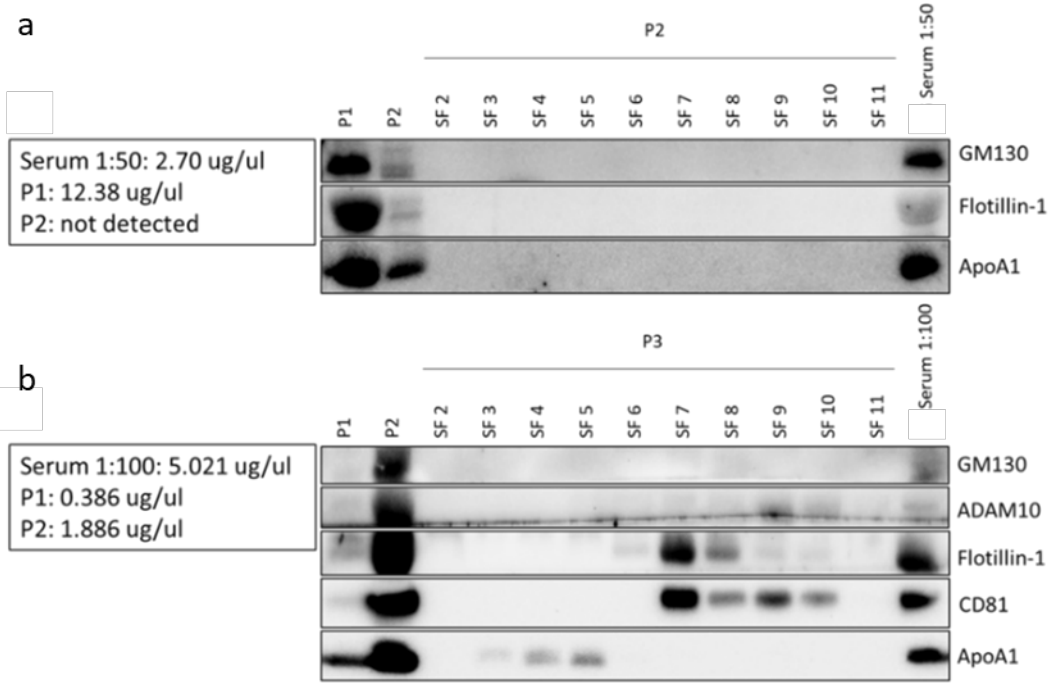

Figure 39. Biochemical characterisation of EVs by WB analysis. **(a)** LEVs pelleted at 800g for 30 minutes (P1), MEVs pelleted at 16.000g for 45 minutes (P2), gradient fractions from P2 obtained with discontinuous sucrose gradient, Serum (1:50). **(b)** P1, P2, gradient fractions from SEV pelleted at 100.000g for 2 hours (P3) obtained with discontinuous sucrose gradient, Serum (1:100). Top numbers refer to the corresponding sucrose gradient fraction (SF).

12.2.2.1 Biophysical and biochemical characterisation of Red Blood Cell-EVs

RBC-EVs were characterized accordingly to the most updated guidelines [32]. In the specific, NTA was used to determine EV particle number and size distribution, AFM was used to evaluate EV morphology, and Western Blot was used to assess EV protein markers. NTA measurements showed a monomodal size distribution, with a peak at 160±2.3nm in diameter (**Figure 40A**) and an EV concentration of 1.81E+12± 8.8E+11 particles/ml. Correlating BCA and NTA data, we found that 2E+9 RBC-EVs correspond to 1,06µg of total proteins (**Figure 40B**), which is in accord with the theoretical calculations by Sverdlov [81] and Zendrini *et al.* . The presence of spherical nano-objects in the size range typical of EVs dried on a flat surface was confirmed by AFM imaging (**Figure 40D**) and image analysis confirmed the size distribution obtained by NTA. Western Blot analysis (**Figure 40C**) revealed the presence of typical EV markers, like Alix and Annexin XI, and hemoglobin subtypes HBB and HBA, confirming the RBC origin of our EVs. The absence of contaminants, such as Golgi-derived vesicles (GM130) or leukocyte-derived EVs (CD45) was verified, together with the expression of CD47. This protein is often referred to as a "don't eat me" signal and highlights RBC EV immune-evasion potential useful for drug delivery applications. Also, the expression of EGFR - the natural ligand of CTX, and

was evaluated and a negligible signal was found (**Figure 40C**). The absence of EFGR on RBC-EVs is mandatory, as it avoids specific, undesired binding of CTX to the surface of RBC-EV during engineering processes.

Finally, the presence of soluble protein-contaminants in the RBC-EV preparations was assessed with the CONAN assay (**Figure 40E**). The fluctuation of the Aggregation Index (AI) at different dilutions and the relative AI value lower than the purity threshold indicated the presence of a negligible amount of no EV-associated soluble proteins, as previously reported. All these data together confirm the quality of our RBC-EV preparations. In particular, the monomodal size distribution and the negligible amount of soluble proteins avoid possible interferences during engineering processes.

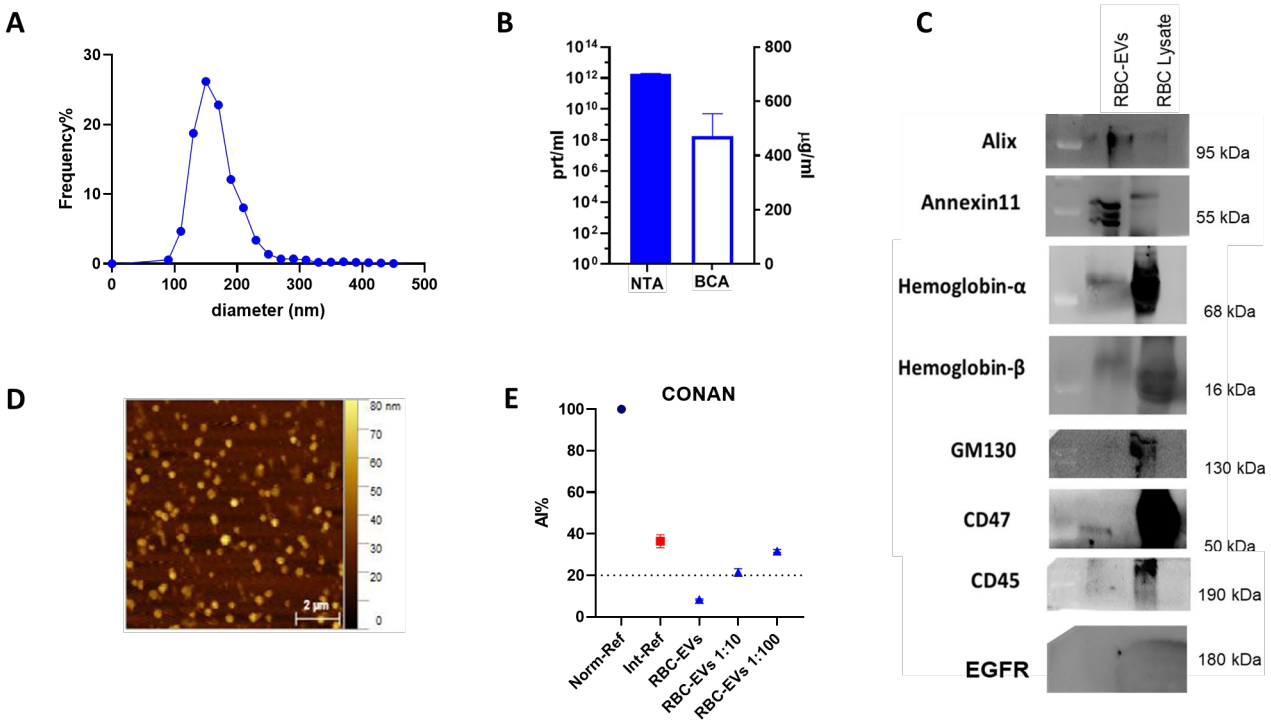

Figure 40. RBC-EV characterisation. **(A)** The size distribution graph obtained by NTA shows a monomodal distribution of our RBC-EVs. Data are expressed in frequency%, and the diameter bin has been selected as 20 nm. *n* = 3. **(B)** The correlation between particle count and protein content of the native RBC-EV samples indicates the absence of soluble proteins. *n* = 3. **(D)** AFM image determines the morphological structure of our RBC-EVs founding spherical nano-objects. **(C)** Representative Western Blot of RBC-EVs and RBC with specific RBC-EV markers, contaminant markers, and EV markers. **(E)** In the CONAN assay, the Int-REF AI ratio defines the threshold below which the spectral redshift is only due to the interaction between the AuNPs and the EVs. The dotted line represents the CONAN assay threshold for soluble proteins detection (<20% AI ratio means that the soluble protein content is ≤0.05 µg/µl).

12.2.3 Cetuximab modification

12.2.3.1 Optimization of the functionalization protocol

The concentration of mCTX and the yield of binding of CTX with DBCO and Cy7.5 were estimated. In the first reaction condition, CTX (1.2E-8 moles) reacted with eight equivalent moles of DBCO and Cy7.5. At the end of the reaction, the actual ratios were 1 CTX (0.00018 n/L): 1.43 DBCO: 1.64 Cy7.5. In the second reaction condition, CTX (1.2E-8 moles) reacted with six equivalents moles of DBCO and 12 equivalent moles of Cy7.5 and the actual ratios were 1 CTX (0.0002 n/L): 1.23 DBCO: 2.01 Cy7.5. After purification by Vivaspin column, mCTX concentration was measured through UV-Vis spectroscopy and attested to be 24,24 µg/µl and 20,33 µg/µl for the first and second reaction condition, respectively. SDS-PAGE was performed on CTX and mCTX (1:6:12) with 1, 5, 10 and 20 µg of protein. Samples were electrophoresed, and the protein bands were visualised in fluorescence (**Figure 41a**) and were later detected with Coomassie Blue (**Figure 41b**).

Considering the reaction yields, the reaction, which presents a more favourable yield, is the reaction with the ratio 1: 6: 12. In this way -on average- only one molecule of DBCO was bound to the CTX and more molecules of Cy7.5 allows for better fluorescence by the compound. The estimated number of molecules of CY7.5 linked to CTX, in the two reactions, led us to prefer the reaction that leads to a product with a higher amount of dye (mCTX(1:6:12)), this is because the greater amount of CY7.5 allows us to better follow the path of the CTX in subsequent experiments.

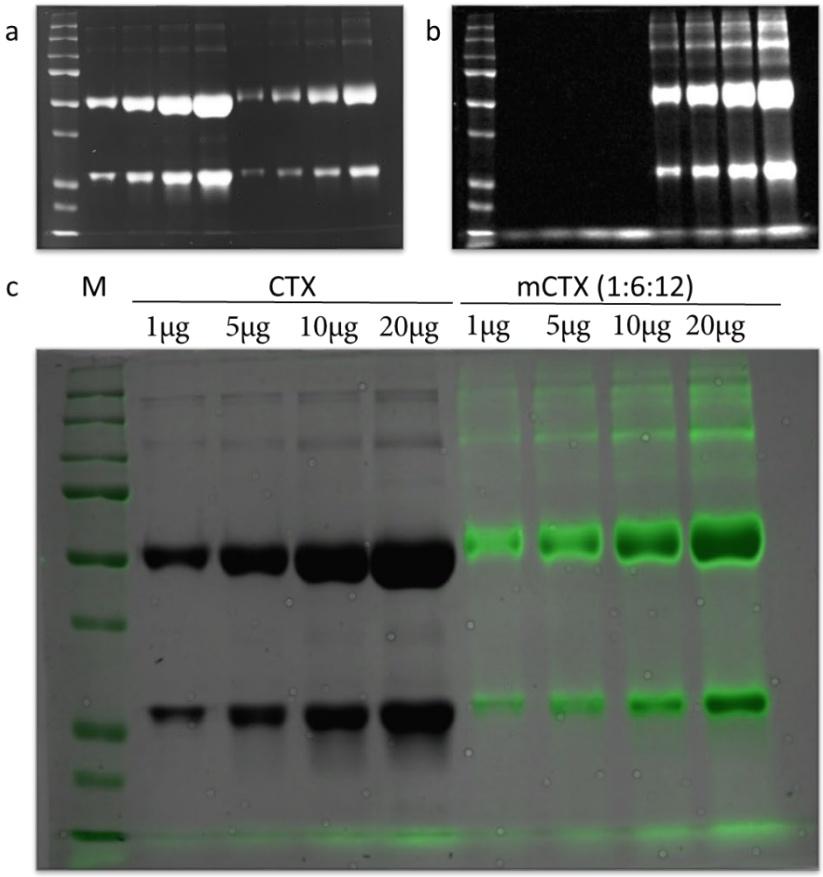

Figure 41. SDS-PAGE analysis: gel was loaded with the marker (M), different amounts of CTX (1, 5, 10, 20 µg) and mCTX (1, 5, 10, 20 µg). **(a)** The SDS-PAGE gel was inspected by Odyssey to highlight the fluorescent signal of the CY7.5 binding to CTX. **(b)** The SDS-PAGE gel was incubated with Coomassie Blue to identify all protein bands. **(c)** Merge image highlights the overlap between the results, in black the protein bands, and in green the fluorescent signal of the Cy7.5.

CTX chemical modification was optimised for RBC-EV surface engineering. To achieve this, we exploited the coupling between the amine present on the side chain of lysines of the antibody and an activated ester (see Material and Methods). We adopted this strategy to covalently bind a fluorophore (Sulfo Cyanine 7.5, allowing its visualisation) and a Dibenzocyclooctyne (DBCO) to make detectable the antibody and to add biorthogonal reactivity towards azido groups. The procedure we followed to functionalised and characterised CTX is resumed (**Figure 42A**). CTX was reacted with an excess of 12 equivalents of NHS-Ester Sulfo Cyanine 7.5 and 6 equivalents of STF-Ester DBCO. After purification, mCTX was characterised by UV-Vis spectroscopy to calculate mCTX concentration and bulk Sulfo Cyanine 7.5 binding yield (**Figure 41B**), using equations (**Eq. 9**) and (**Eq. 10**), respectively.

Eq. 9 $$M = \frac{\mathrm{A280} - (\mathrm{Amax\ x\ C})}{\varepsilon} \mathrm{x\ D}$$

Eq.10 $$\mathrm{R} = \frac{\mathrm{Amax}}{\varepsilon' \mathrm{x\ M}} \mathrm{x\ D}$$

To create a control sample unable to bind to EV surface (de-activated mCTX, DmCTX), an aliquot of mCTX was reacted with the azido group of NaN_3 to deactivate any DBCO (see Material and Methods). DBCO ligation quantification was performed by reacting an aliquot of mCTX or DmCTX with 6 equivalents of azido-Sulfo Cyanine 3. This step is required due to the low molar extinction coefficient of the DBCO, which does not allow direct quantification by UV-Vis spectroscopy. UV-Vis spectra of mCTX-Cy3 and DmCTX-Cy3 (**Figure 41C** and **Figure 41D**) were used to calculate the ligation yield of Cyanine 3 using equations (**Eq. 9**) and (**Eq. 10**), assuming that Cy3 quantification is the same as the DBCO, due to the high kinetics of the reaction and excesses used.

Our calculations showed that CTX bind on average 1.3 molecules of DBCO and 2 molecules of Sulfo Cyanine 7.5. The approximately 1:1 ratio between CTX and DBCO is pivotal to avoid possible bridging structures when engineering multivalent RBC-EVs. Furthermore, DmCTX showed a negligible Cy3 ligation, indicating the successful deactivation of DBCO.

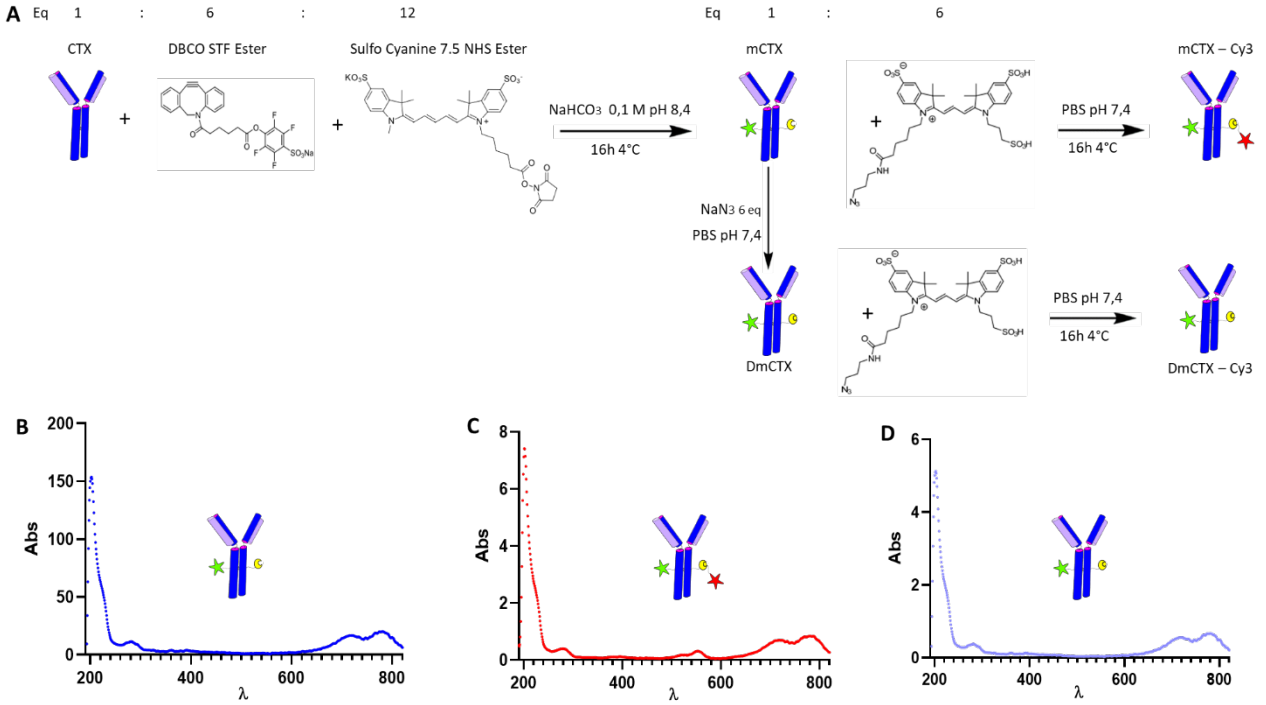

Figure 42. Conjugation and characterisation of mCTX. **(A)** Schematic representation of the mCTX, DmCTX synthesis, and their controls. **(B)** UV-Vis spectra of mCTX showed a peak at 778 nm corresponding to Cy7.5. **(C)** UV-Vis spectra of mCTX-Cy7.5-Cy3 showed peaks at 550 and 778 nm corresponding respectively to Cy3 and Cy7.5. **(D)** UV-Vis spectra of DmCTX-Cy3 showed a peak at 778 nm corresponding to Cy7.5 since Cy3 cannot be bonded to the DBCO.

12.2.4 EVs functionalisation

12.2.4.1 RBC-EV surface engineering

For RBC-EV surface engineering, we followed the experimental workflow resumed (**Figure 42A**). We adopted a two-step chemical labeling strategy (see Material and Methods). RBC-EVs were first reacted with an N_3-$(Peg)_4$-NHS-Ester (reaction ratio 1:200 RBC-EVs:N_3-$(Peg)_4$-NHS-Ester). On the other hand, we also prepared a non-pegylated sample to explore the possibility of physisorption of mCTX and the formation of a PC. Pegylated and non-pegylated samples were reacted with mCTX and DmCTX (reaction ratio 1:200 RBC-EVs:mCTX or DmCTX) and ultracentrifuged to remove unreacted antibodies. The size distribution of RBC-EVs is not affected by the engineering process, indicating no significant morphological changes due to surface functionalization (**Figure 42B**). The CONAN assay was performed on engineered samples to verify the negligible presence of no-EV-associated antibodies. Samples tested showed the same AuNPs aggregation

properties of native EVs, indicating that no-soluble antibodies are detectable (see Figure 4X); hence, the quantified antibody in all the samples is related to the EV surface.

RBC-EVs engineering was quantified by electrophoresis followed by fluorescence imaging. mCTX and DmCTX standards, ranging between 0.02–2µg, were loaded in the same gel as the samples to build a calibration curve. The densitometric fluorescence profile was acquired from the gel image, and significant differences between ^{Peg}RBC-EVs$_{-mCTX}$ and mCTX and RBC-EVs$_{-mCTX}$ were observed (Figure 3C). This data strongly suggests the successful covalent ligation of mCTX with EV proteins; indeed, it causes a different separation pattern due to increased protein molecular weight. Interestingly, RBC-EVs$_{-mCTX}$ has a densitometric profile like free mCTX (**Figure 43C**), indicating that mCTX is in its native form. Hence, these data suggest that the mCTX can be probably physisorbed as PC in the absence of the azido-Peg.

The ratios mCTX per RBC-EV for ^{Peg}RBC-EVs$_{-mCTX}$, RBC-EVs$_{-mCTX}$, and RBC-EVs$_{-DmCTX}$ are the same (approximately 90 molecules of mCTX/DmCTX per EV) (**Figure 43D**). However, ^{Peg}RBC-EVs$_{-DmCTX}$ showed a negligible co-isolation yield indicating that active DBCO is required to bind the azido group on the vesicle. Further, these data foster the anti-fouling properties of the pegylation on the vesicle surface. Peg anti-fouling properties were largely explored and exploited for synthetic NPs and were confirmed in this case as pegylation inhibited the physisorption of DmCTX. All these data together strongly suggest that the two engineering strategies followed can modify the EV surface through different mechanisms. Indeed, one mechanism is carried out by the formation of a covalent bound, and the other by forming a protein corona. To the best of our knowledge, this is the first report about the formation of a PC during EV surface engineering processes.

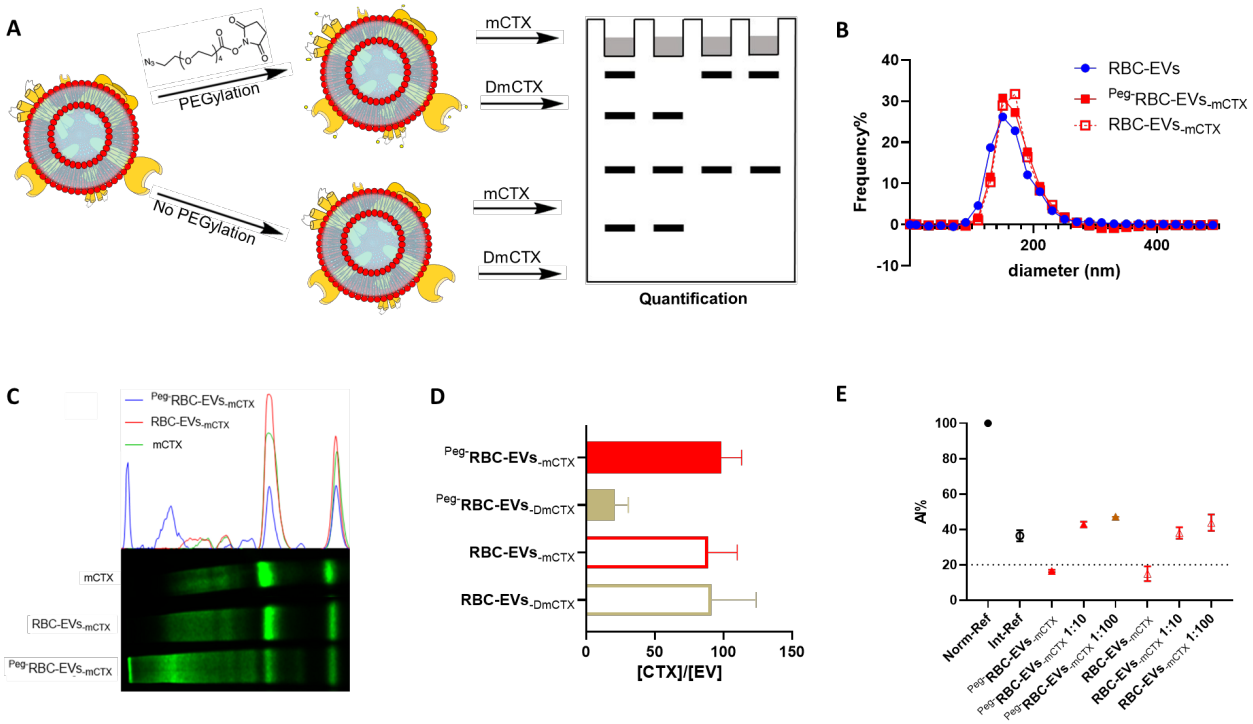

Figure 43. RBC-EVs surface engineering by chemical or physical strategy. **(A)** Schematic representation of the engineering processes followed. **(B)** Size distribution of engineered samples determined by NTA shows no significant differences compared to the native RBC-EVs. Data are expressed in frequency%, and the diameter bin has been selected as 20 nm. *N* = 3. **(C)** Fluorescence densitometric profile of samples engineered with mCTX and mCTX. **(D)** mCTX/DmCTX per RBC-EV yields of engineered samples. Data are elaborated as molecules of mCTX/DmCTX normalized by the number of RBC-EVs of the sample. *N* = 5. **(E)** The dotted line represents the CONAN assay threshold for soluble proteins detection (<20% AI ratio means that the soluble protein content is ≤0.05 µg/µl)

12.2.5 SPR affinity-assay

SPR was conducted on a CM5 dextran-coated chip functionalized with EGFR through amine coupling. Chip functionality was firstly assessed using EGF to validate the chip functionalization. Different concentrations of EGF were injected into the flow channel and then passed over the EGFR-immobilized chip. The same protocol was used for CTX, mCTX(1:8:8) and mCTX(1:6:12) to check whether CTX modification altered its binding capacity, CTX and mCTX (mCTX(1:8:8) and mCTX(1:6:12)) affinity to EGFR were measured (**Figure 44a, Figure 44b,** and **Figure 44c**). As shown (**Figure 44d**), the binding affinity between EGF and EGFR was estimated in terms of the dissociation constant (KD), calculated using the BIA evaluation software. The KD value between EGF and EGFR was approximately 3.4E-8M. The binding affinities of CTX and mCTX to EGFR were also estimated as described above and was approximately 2.6E-9M and 3.2E-9M (**Figure 44d**). These data are compatible with those found in the literature[98].The resulting binding curve of CTX and mCTX are comparable, resulting that the CTX modification did not affect its affinity for EGFR (**Figure 43d**).

pEVs (negative control) and mCTX-EVs were tested at the same molar concentrations to their binding to EGFR (**Figure 44e**). The binding affinity between pEVs or mCTX-EVs to the EGFR was estimated by flowing different concentrations of pEVs or mCTX-EVs onto the EGFR-immobilized sensor chip. The run was performed at the following optimized parameters and solutions: I) Single cycle starts from 0,415nM; II) Serial Dilutions: 1:3; III) Running Buffer: 50% HBS buffer (0.01M HEPES pH 7.4, 0.15M NaCl, 3mM EDTA, 0.005% v/v Surfactant P20) 50% PBS; IV) Contact Time: 90 seconds, V) Flow Rate: 30µL/minute. Sensorchip response to pEVs remained constant regardless pEV concentration used, suggesting their binding to EGFR is not specific (**Figure 44e**). The binding affinity between mCTX-EVs and EGFR was estimated in terms of the dissociation constant (**KD**), calculated using the BIA evaluation software. The KD value between mCTX-EVs and EGFR was approximately 0.20E-9M (**Figure 44f**).

It was demonstrated that the modification of CTX with DBCO and CY7.5, in different ratios, does not influence the binding affinity of the CTX (**Figure 44a**). These results were confirmed by the KD value that does not change respect unmodified CTX. This result was confirmed by the KD value that changes with respect p-EVs. The other open questions regarding the SPR experiments mainly concern the understanding of what kind of bond is formed between the mCTX-EVs and the EGFR on the sensor chip. In particular is it a mono-binding such as between the CTX and the EGFR or a single EVs can bind multiple EGFR sites. This information has yet to be determined. Another important information is the exact estimate of the molarity of the SEVs. SEVs are a heterogeneous population, and it is not easy to correctly determine molarity. This problem was resolved with the RBC-EVs introduction.

Once assessed that RBC-EV can both chemisorb and physisorb mCTX on their surface, we investigated by SPR assays the affinity of the engineered RBC-EVs for the EGFR, the CTX natural target. Hence, we tested Peg-RBC-EVs-mCTX and RBC-EVs-mCTX to evaluate if the chemisorption or the physisorption of the mCTX onto the RBC-EV surface affects its binding affinity. As further controls, we assayed native RBC-EVs and RBC-EVs engineered with DmCTX following the two strategies. Native RBC-EVs showed to have negligible EGFR binding as well as the pEV. The binding curve of Peg-RBC-EVs-mCTX and RBC-EVs-mCTX (**Figure 45B**) resulted very similar, confirming the comparable amount of mCTX present on the surface of the two engineered samples and suggesting that engineering processes didn't affect mCTX binding. On the other hand, Peg-RBC-EVs-DmCTX showed a negligible affinity for EGFR, confirming again that the active form of DBCO is required to bind mCTX on the azido-pegylated EV surface. Besides, the RBC-EVs-DmCTX binding curve resulted stackable to Peg-RBC-EVs-mCTX and RBC-EVs-mCTX ones, confirming that DmCTX has the same affinity for EGFR as mCTX and it can be absorbed on RBC-EV surface as mCTX. pKD were extrapolated to compare the different binding curves obtained. The multifunctionality of engineered RBC-EVs with mCTX led to improve affinity for EGFR compared with mCTX for both chemisorption and physisorption models (**Figure 45C**). Furthermore, RBC-EV surface engineering with DmCTX is functional only for the physisorption strategy, while for the pegylated sample pKD is very low indicating negligible affinity. To summarize, SPR experiments confirmed

that RBC-EVs can be functionalized with mCTX following chemisorption and physisorption strategies and that the two strategies produce samples with the same affinity for the EGFR. Furthermore, SPR of pegylated and unpegylated RBC-EVs functionalized with DmCTX confirmed the co-isolation data previously described. Indeed, DmCTX cannot bind the azido group on the vesicle surface, and, considering the anti-fouling properties of the pegylation, it is not even physisorbed. These considerations suggest the reasons for the negative pKd we observed for Peg-RBC-EVs-DmCTX.

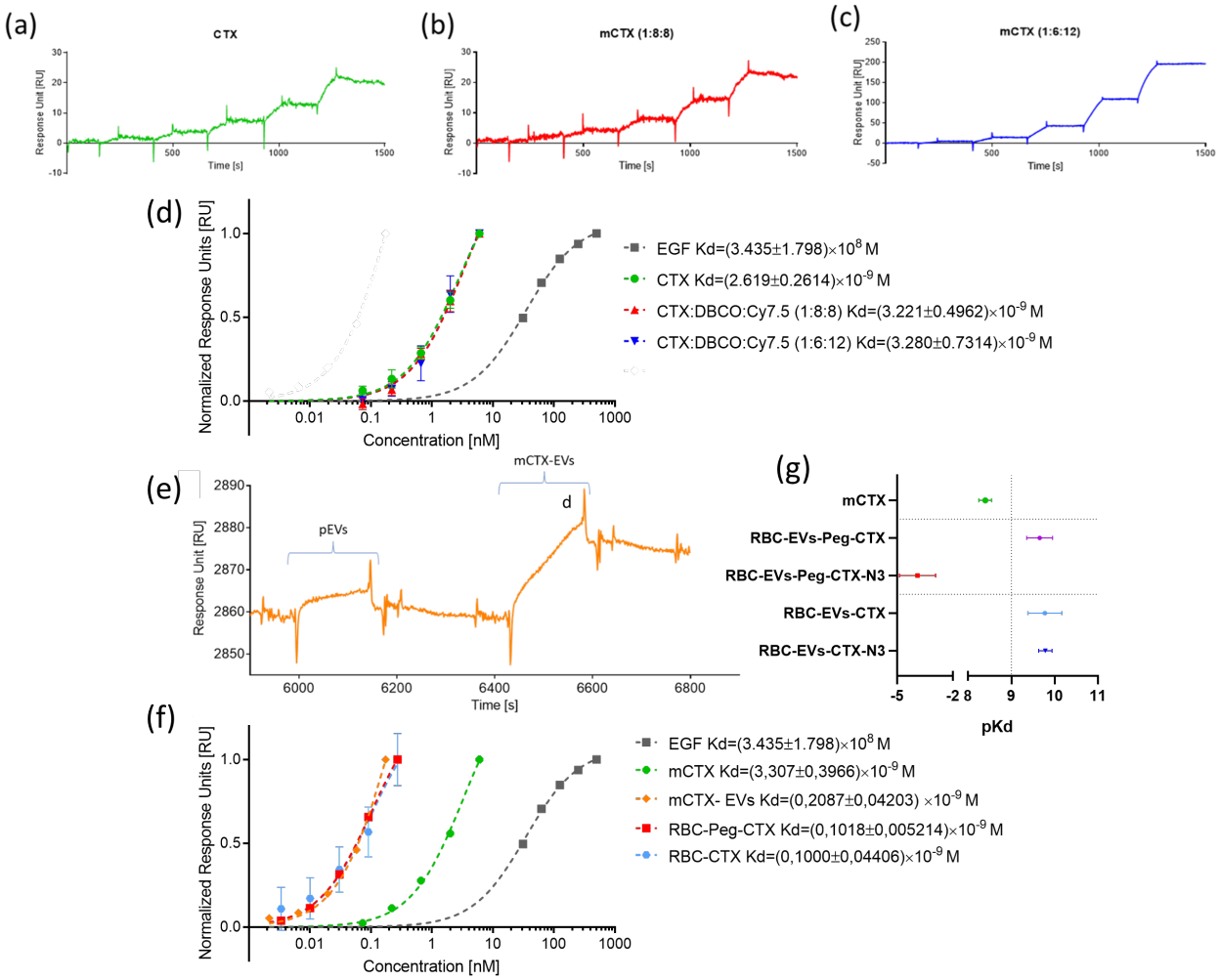

Figure 44: (a) The binding sensorgram between CTX and EGFR. **(b)** The binding sensorgram between mCTX(1:8:8) and EGFR. **(c)** Binding kinetic analysis. The binding sensorgram between mCTX(1:6:12) and EGFR. **(d)** Equilibrium binding responses were fitted to Langmuir isotherms to calculate dissociation constants (KD). The solid lines through the experimental points represent the CTX data obtained by global kinetic analysis followed by mCTX(1:8:8) mCTX(1:6:12), and EGF. **(e)** Biacore sensorgrams of pEVs versus mCTX-EV at the same molar concentration (0,034nM). The run was performed at the following these parameters: Manual run of p-EVs followed by mCTX-EVs; Running Buffer: HBS buffer; Contact Time 150 seconds; Flow Rate 10µL/minute. **(f)** Binding kinetic analysis was optimized with the mCTX-EV isolated from the cell cultures. The experiment was finalized with the mCTX-RBC-EVs. Equilibrium binding responses were normalized and were fitted to Langmuir isotherms to calculate the KDs. Equilibrium binding responses were fitted to Langmuir isotherms to calculate dissociation constants.

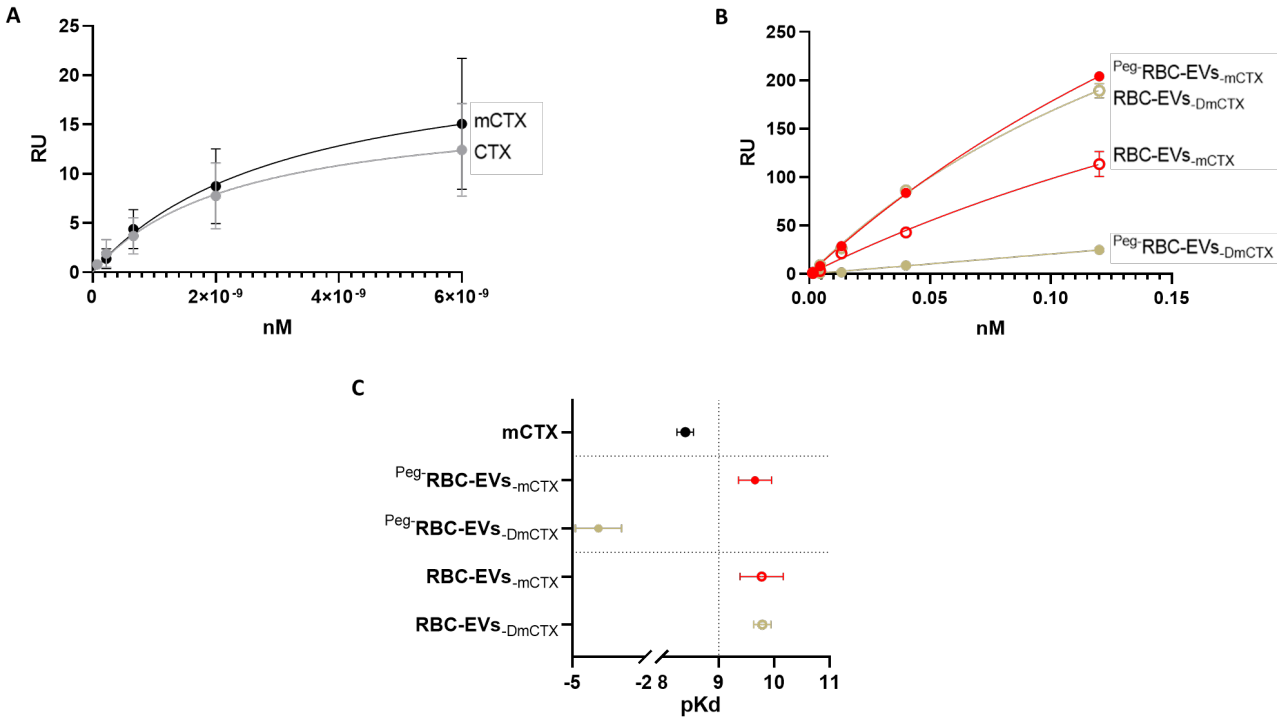

Figure 45. (a) Equilibrium binding responses of CTX and mCTX were fitted to Langmuir isotherms to calculate dissociation constants (KD). The curves are not normalized. **(b)** Equilibrium binding responses of PEG-RBC-EVs, RBC-EVs.DmCYX, RBC-EVs-mCTX, and PEG-RBC-EVs-DmCTX were fitted to Langmuir isotherms to calculate dissociation constants (KD). The curves are not normalized. **(c)** Summary of the pKd of all the reaction conditions.

12.2.6 Cell mito stress test

The Cell Mito Stress Test is a common assay to measure the oxygen consumption rate (OCR) of live cells for the evaluation of mitochondrial respiration function by using Seahorse XFe24. The basal Oxygen Consumption Rate (**OCR**) and Extracellular Acidification Rate (**ECAR**) were then determined *Agilent Seahorse XF Cell Mito Stress Test Report Generator*. Though the measurement requires only a small number of cells, it still has limitations I) compared to the Clark-Type Oxygen Electrode, II) the Cell Mito Stress Test cannot measure the OCR of tissues, but it can measure respiration in isolated mitochondria from tissues. In addition, III) this protocol is strict with cell operations. The experiments conducted with the Seahorse platform have shown that the most delicate phase is the seeding of the cells (step that need optimization based on the cell type), in fact, the uniform distribution of the cell wells is required to obtain a reliable experiment. Accurate cell counting is important for lowering variability between groups. Optimal cell density to ensure cells are uniformly and evenly seeded in a monolayer configuration. If there are cells clusters, it may cause poor cell adhesion and inaccurate measurement of OCR. The MDA-MD-231 seeding protocol was optimized, while the MDA-MD-453 seeding protocol still needs to be optimized due to the natural ability of these cells to clamp together.

In first experiment, CTX was used at molar concentrations of 20nM and different amount of cells was tested (20 000, 40 000, 60 000 cells) for both MDA-MB-231 (**Figure 46**) and MDA-MB-453 (**Figure 47**) cell lines The best condition identified was 40 000 cells and 1 µM FCCP. The second experiment only on MDA-MB-231 because the MDA-MB-453 cells were not affected by the CTX treatment. This experiment will be performed to verify which concentration was the minimal that produced an observable effect on cell metabolism and is essential to verify the no-metabolic response range of CTX on MDA-MB-231 cell line (**Figure 48**). On the same optimized FCCP was identified (1µM). This experiment is essential to verify the no-metabolic response range of CTX on MDA-MB-231 cell line (concentration> 2nM). All the experiments were ran in triplicate. Future experiment have to be done.

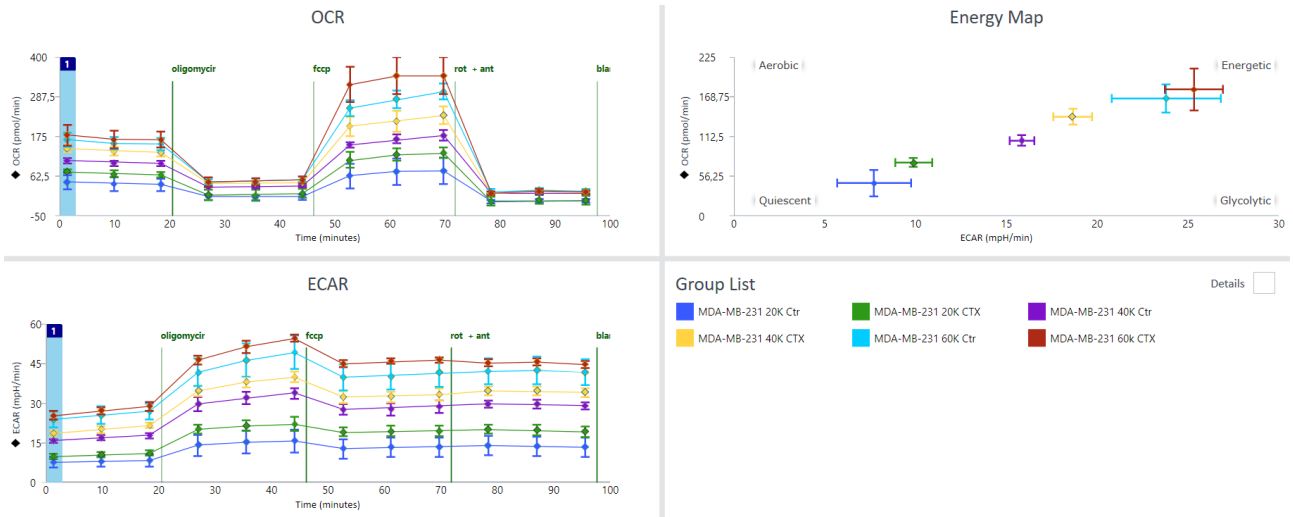

Figure 46. Seahorse-based mito stress test assay on MDA-MB-231 cell line (20K, 40K, 60K cells). The two graphs show time-dependent changes in OCR **(a)** and ECAR **(c)** measured sequentially by injecting oligomycin, FCCP, and rotenone plus antimycin A on MDA-MB-231 with or without the CTX treatment (20nM). **(b)** Basal OCR and ECAR values (before oligomycin injection) were plotted in the energy map to illustrate the difference in the cell metabolic profile.

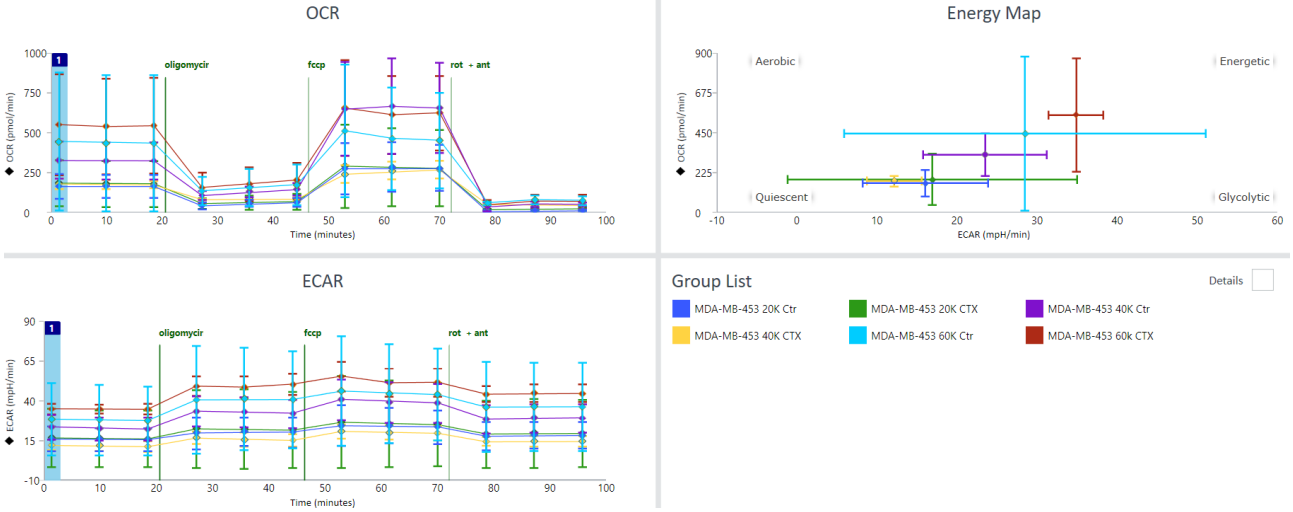

Figure 47. Seahorse-based mito stress test assay on MDA-MB-453 cell line (20K, 40K, 60K cells). The two graphs show time-dependent changes in OCR **(a)** and ECAR **(c)** measured sequentially by injecting oligomycin, FCCP, and rotenone plus antimycin A on MDA-MB-453 with or without the CTX treatment (20nM). **(b)** Basal OCR and ECAR values (before oligomycin injection) were plotted in the energy map to illustrate the difference in the cell metabolic profile.

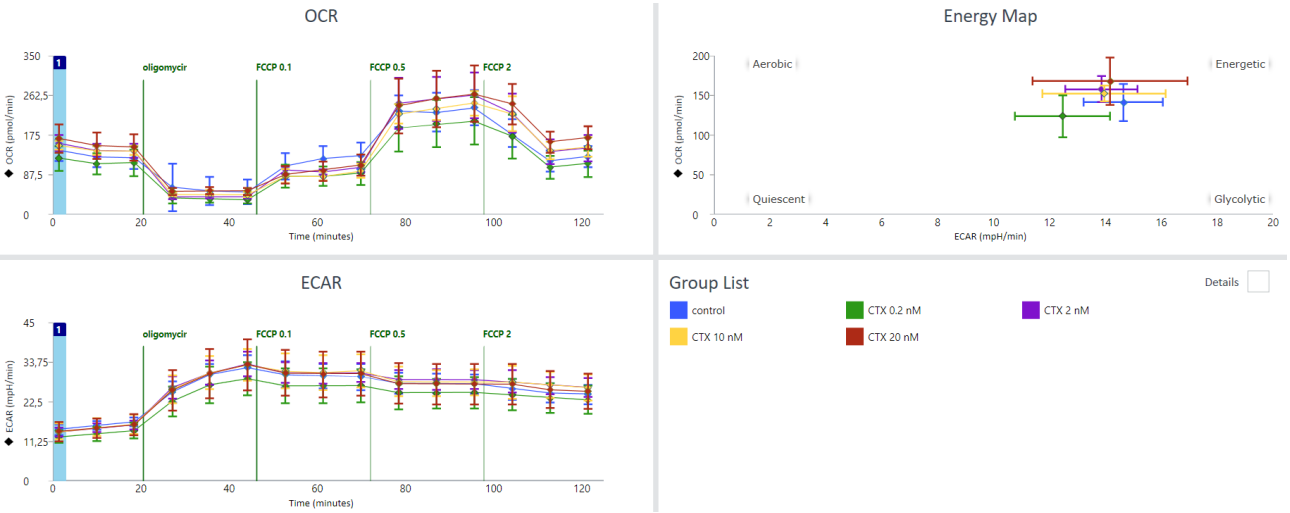

Figure 48. Seahorse-based mito stress test assay on MDA-MB-231 cell line (40K cells). The two graphs show time-dependent changes in OCR **(a)** and ECAR **(c)** measured sequentially by injecting oligomycin, FCCP, and rotenone plus antimycin A on MDA-MB-231 with different amount of CTX treatment (0, 0.2, 2, 10, 20nM). **(b)** Basal OCR and ECAR values (before oligomycin injection) were plotted in the energy map to illustrate the difference in the cell metabolic profile.

12.2.7 *In vitro* mCTX and RBC-EVs uptake

Engineered RBC-EVs targeting ability was assessed in vitro, using MDA-MB-231 cells as TNBC cell model known to express high levels of EGFR. Cells were treated with RBC-EVs engineered following chemisorption or physisorption strategies in the presence or not of Fetal Bovine Serum (FBS). Peg-RBC-EVs-mCTX, RBC-EVs-mCTX, and RBC-EVs were first labeled with MemGlow™ 488. Then, samples were tested after 4h and 24h incubations. Both mCTX and RBC-EVs uptake were evaluated quantifying the fluorescence of the Sulfo Cyanine 7.5 and MemGlow™ 488, respectively.

In absence of FBS, Peg-RBC-EVs-mCTX showed higher mCTX uptake compared with RBC-EVs-mCTX only after 4 hours of treatment, while at 24 hours of treatment there are no significant differences in mCTX uptake between the two samples (**Figure 49A**). Besides, evaluating RBC-EV uptake (**Figure 49B** and **Figure 49C**) we did not notice differences between the two-engineered samples, which showed similar fluorescence intensity. The comparison between unmodified EVs and engineered ones highlights higher uptake of engineered samples only at 24 hours of treatment. This data suggests that at 4 hours of treatment the pivotal mechanism of EV uptake is unspecific and only at 24 hours we can appreciate a CTX-mediated uptake both for chemisorbed and physisorbed samples.

On the other hand, $^{Peg-}$RBC-EVs$_{-mCTX}$ showed significantly higher mCTX uptake compared with RBC-EVs$_{-mCTX}$ both at 4 and 24 hours when treatments were carried out in the presence of FBS (**Figure 50A**). These data are in contrast with the SPR one, where the two samples seem to have the same receptor affinity, and with tests conducted in absence of FBS, which seemed to confirm SPR data. This might be related to the presence of FBS-derived soluble proteins that could exchange with the physisorbed mCTX, leading to a loss of functionality for RBC-EVs-mCTX. Indeed, PC is well known to be a dynamic entity that reflects the environment where the nanoparticle is immersed through a constant exchange of the adsorbed proteins with the others in solution. Confocal microscopy imaging of MDA-MB-231 incubated with RBC-EVs and RBC-EVs$_{-mCTX}$ shows that these two samples' uptake is very similar both at 4 and 24 hours. This data suggests that mCTX functionalization by physisorption does not improve EV targeting ability (**Figure 50B** and **Figure 50C**), as its uptake is like the native RBC-EV control. On the other hand, $^{Peg-}$RBC-EVs$_{-mCTX}$ showed an improved EV uptake mediated by a significantly increased uptake of mCTX compared to RBC-EVs and RBC-EVs$_{-mCTX}$ only after 24 hours of treatment, while after 4 hours the uptake of the chemisorbed sample is like the control. Notably, we observed that, in presence of FBS, the uptake of both mCTX and RBC-EV is lower compared to

the uptake in absence of FBS, suggesting a mechanism of competition between the heterogeneous composition of the FBS and our RBC-EVs. Furthermore, also in presence of FBS, we observed that after 4 hours of treatment the pivotal uptake mechanism is the unspecific one, as all the samples showed the same uptake. To observe a significant effect of the chemisorption of mCTX on the vesicle surface is required a 24-hour incubation. These data together indicate that mCTX covalent binding to the RBC-EV surface is required for efficient functionalization to improve EV targeting ability. Despite having the same EGFR affinity as the chemisorbed one, physisorbed mCTX does not significantly improve EV targeting ability.

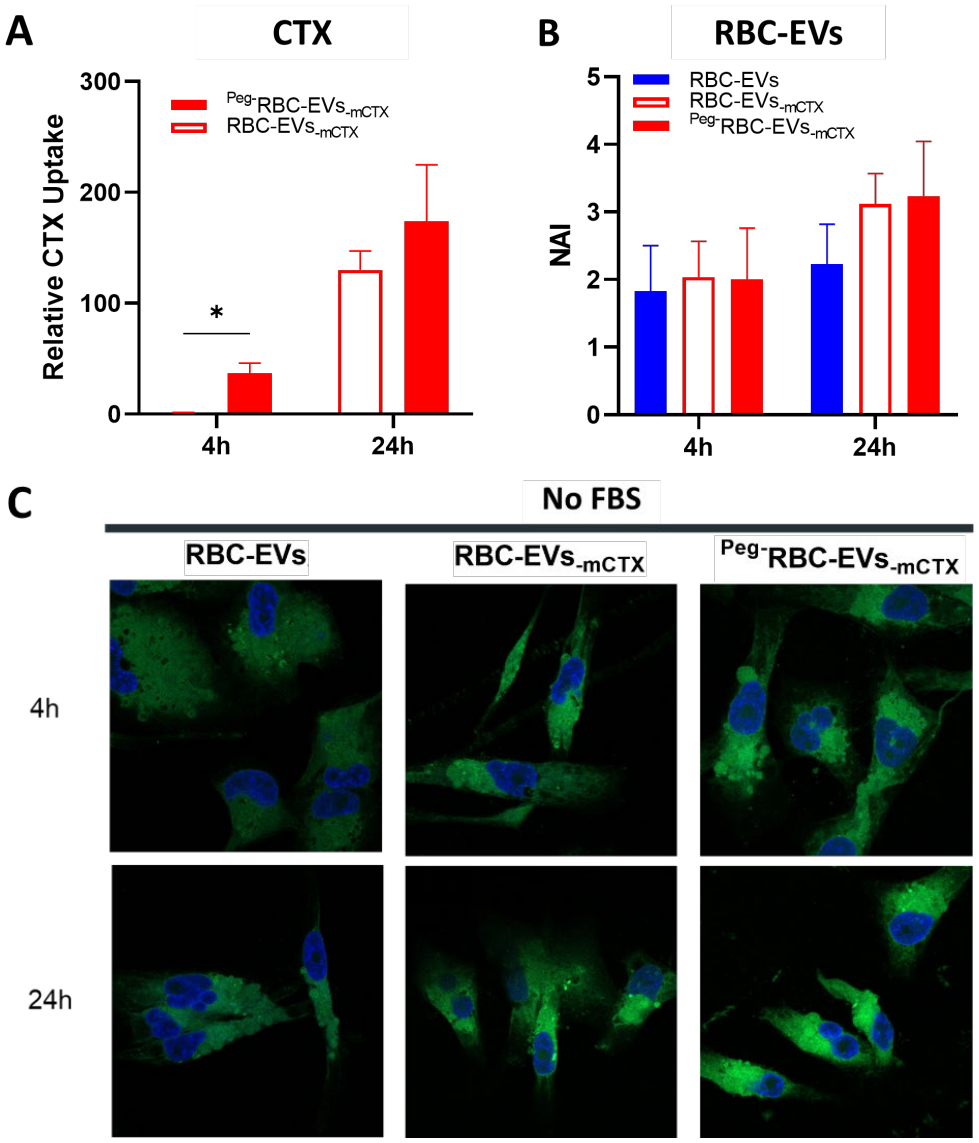

Figure 49. Treatment without FBS. **(A)** Quantification of the cellular uptake at 4 and 24 hours. **(B)** Quantification of the fluorescence intensity at 4 and 24 hours. correlated to the cellular uptake. **(C)** Confocal image of the MDA-MB-231 at 4 and 24 hours treated with RBC-EVs, RBC-EVs-mCTX, and PEG-RBC-EVs-mCTX.

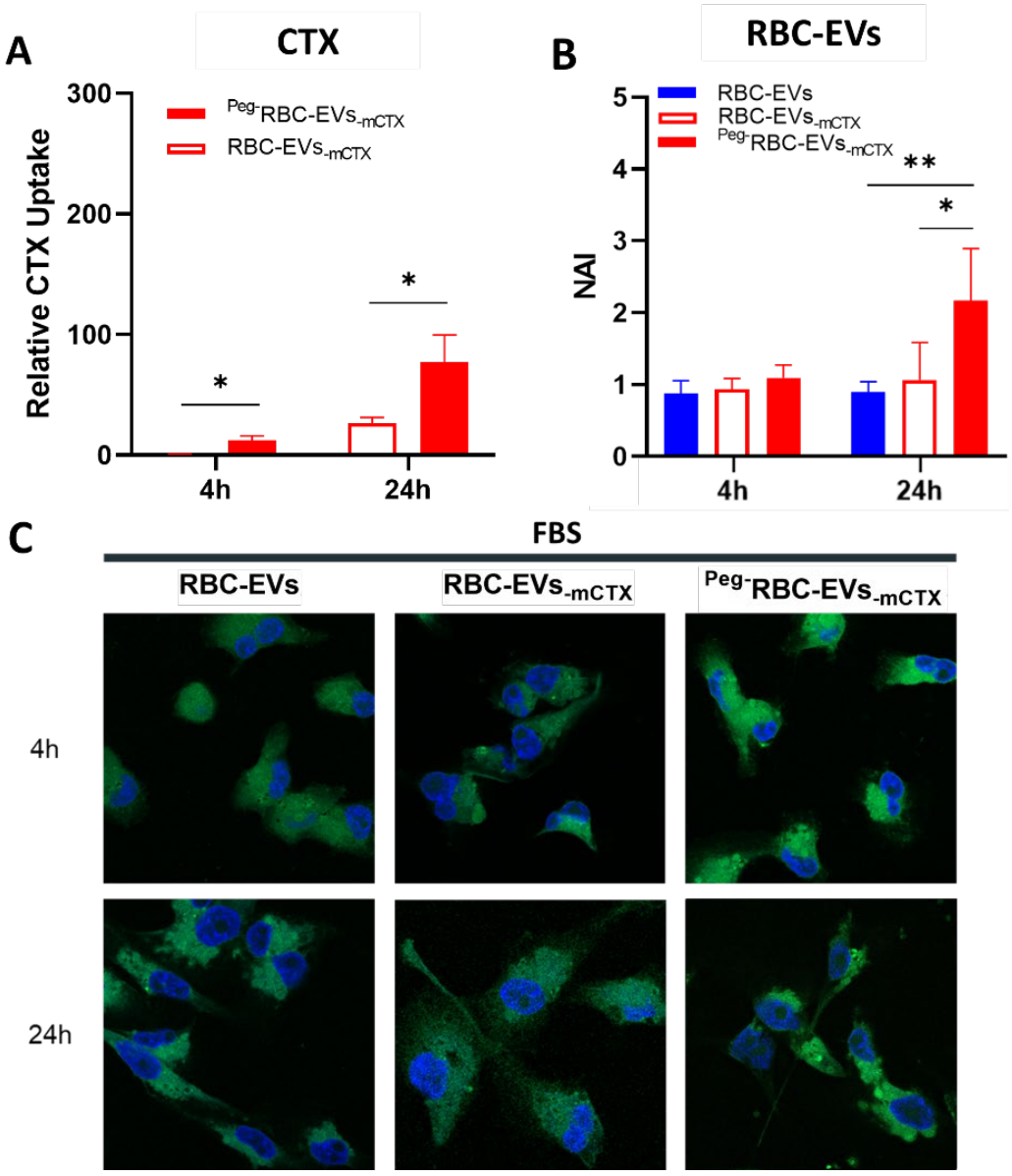

Figure 50. Treatment with FBS. **(A)** Quantification of the cellular uptake at 4 and 24 hours. **(B)** Quantification of the fluorescence intensity at 4 and 24 hours. correlated to the cellular uptake. **(C)** Confocal image of the MDA-MB-231 at 4 and 24 hours treated with RBC-EVs, RBC-EVs-mCTX, and PEG-RBC-EVs-mCTX.

12.3 Conclusion

This work is a first step in understanding the impact of the EV surface engineering processes and will help the field develop new surface-engineered EVs to be exploited as delivery vehicles, imaging agents, or therapeutics. We have developed and optimised the functionalisation of CTX with DBCO and Sulfo-Cyanine 7.5, synthesising mCTX. We demonstrated that mCTX could be used to engineer EV surfaces following a chemical or a physical strategy without affecting EV morphology. The engineering of the EV surface generates a covalent bond between EVs' surface proteins and mCTX, giving rise to changes in the EV protein electrophoretic profile. Besides, mCTX nonspecifically physisorbed on EV surface as PC showed to be dynamic and in equilibrium with the media. Interestingly, we did not notice the physisorption of mCTX on the EV surface after following the chemical strategy, which is probably due to the reported anti-fouling properties of PEGylation.

SPR functional assay demonstrated that both engineered samples are able to bind EGFR with high affinity. However, in vitro tests showed that with FBS, only the chemical strategy leads to an increase in the uptake

of the RBC-EVs correlated with an increased uptake of mCTX. On the other hand, the two samples act very similarly without FBS. This is probably due to the presence of FBS-related proteins during in vitro tests that force an exchange of proteins between the PC present on the vesicle surface and the media, leading to a loss of functionality. This work gives one of the first data about the formation and the effects of the protein corona during EV surface engineering processes. We demonstrated that PC is a phenomenon that must be considered during engineering processes. Its samples act very similar to chemicals engineered once but seem to be less functional in vivo mimicking conditions. For these reasons, it is fundamental to check and characterise reagents and products of engineering processes, to avoid unexpected corona formation.

Further work will aim to characterise PC formation and stability with different proteins and peptides, to support the exploitation of various engineering strategies for developing bio nanotherapeutics.

Chapter 13

General conclusion

13 General conclusion

In these two projects, the BOW project and the PRIN project, the innovative issues of nanoparticle engineering at the mesoscale and molecular length scale were addressed. In the BOW project, the visionary hybridisation between inorganic NPs and natural organic NPs promises to become the new frontier of the application of nanotechnology and medical diagnostics. In the PRIN project, the molecular engineering of the surface of extracellular vesicles and the optimisation and characterisation of conjugation methods aimed at specific targeting promise to improve nanomedicine in the therapeutic field, targeting the drug at the target site and decreasing the side effects of therapy. The common thread that connects the two projects is the characterisation of these nanoparticles. The characterisation process is fundamental for the medical translation of these technologies, from research to clinic, and is primary to use these nanomaterials for application purposes. It is necessary to check every single step and be sure that, for example, the production, the isolation, and the engineering took place in the desired way. This is fundamental for biological samples containing a high degree of heterogeneity. The "luck" of being able to induce the vesiculation of red blood cells by chemical methods allows one to obtain a massive homogeneous pool of extracellular vesicles. This possibility is usually unattainable with cell cultures if not with tools for isolation and massive production (bioreactors, TFF ...). Still, many studies have to be done both for engineering on the molecular scale and the mesoscale, more massive efforts must be made to learn how to characterise innovative hybrid products such as evMBDs, and more immense efforts must be made to standardise regular synthesis and characterisation protocols.

Chapter 14

Acknowledgments

14 Acknowledgments

The work presented in this thesis benefited from the supervision and help of many people. Therefore, I would like to thank:

Prof. Paolo Bergese, Section of Biotechnology, Department of Molecular and Translational Medicine, University of Brescia, mentor, supervisor, and tutor.

Prof. Giuseppe Pomarico, Section of Biotechnology, Department of Molecular and Translational Medicine, University of Brescia, mentor and co-tutor.

Prof. Annalisa Radeghieri, Section of Biotechnology, Department of Molecular and Translational Medicine, University of Brescia, mentor and co-tutor.

Dr. Lucia Paolini, Section of Biotechnology, Department of Molecular and Translational Medicine, University of Brescia, mentor.

Dr. Andrea Zendrini, Section of Biotechnology, Department of Molecular and Translational Medicine, University of Brescia, mentor.

Prof. Paolo Arosio, Biochemical Engineering Laboratory at Eidgenössische Technische Hochschule Zürich, ETHZ, the supervisor at the ETHZ, Zürich, Switzerland.

Karl Normak and Dr Michael Sebastian Gerlt worked with me on the BOW project during my visiting period at the Eidgenössische Technische Hochschule Zürich, Switzerland.

All the colleagues from ETHZ, Dr Umberto Capasso Palmiero, Dr Miriam Linsenmeier, Dr Itzel Condado-Morales, Dr Marcos Gil Garcia, Dr Raphaël P.B Jacquat, Dr Katarzyna Makasewicz, Philippe Lenzen, Dominik Zürcher, Chiara Morelli, Florence Stoffel, Charlotte Seiffert, Michael Ullmann, Marcell Papp, Francesca and Severin.

A special thanks to Ingrid Chantal Gröbli Copat, Annina Luciana Eichenberger, Dr. Carolina Paganini, and Sabrina Picciotto.

All the colleagues from the bioCSI lab Dr. Serena Ducoli, Dr. Miriam Romano, Silvia Alacqua and Angelo Musicò, worked with me during these three years and Ing Franco Rabbi.

All the partners involved in the PRIN project: Prof. Marco Rusnati and Eva Chiara Urbinati, and Prof. Alessandra Valerio and Dr. Maurizio Ragni.

All the partners involved in the BOW project: Center for Colloid and Surface Science (Italy), National Research Council (IRIB, IBBR, IBF, ISMN, Italy), Nanotechnology and Magnetism Group-NANOMAG, at the University of Santiago de Compostela (Spain), Max-Planck-Institut für Polymerforschung (Germany), Helmholtz Zentrum München, München (Germany) Zabala Innovation (Spain), German Research Center for Environmental Health (Germany), Institute Of Technology Sligo (Ireland), Federal Polytechnical School, ETH Zurich

(Switzerland), Hansabiomed Life Sciences Ou (Estonia), Biodevice Systems (Czech Republic), Rigenerand Srl (Italy).

Special mentions go to Prof. Eugenio Monti, Head of the Section of Biotechnology, Department of Molecular and Translational Medicine, University of Brescia and Prof. Marco Presta, Coordinator of the Ph.D. Course in Precision Medicine, Department of Molecular and Translational Medicine, University of Brescia.

14.1 Ringraziamenti

Alle persone che mi vogliono e mi hanno voluto bene.

Ai miei compagni di lavoro. Alla mia famiglia che mi ha sempre sostenuto, ai miei amici nuovi, storici , sia vicini che lontani... e un po' anche a me (Figura 51).

Figura 51: **(a)** I miei due gruppi di laboratorio (italiano e Svizzero). **(b)** La mia famiglia, le mie coinquiline/i, i miei amici vecchi/nuovi, vicini e lontani.

Chapter 15

Bibliography

15 Bibliography

[1] S. Busatto *et al.*, "The nanostructured secretome," *Biomaterials Science*, vol. 8, no. 1, pp. 39–63, 2020, DOI: 10.1039/c9bm01007f.

[2] "BOW project." https://www.bowproject.eu/

[3] R. P. Feynman, "There's Plenty of Room at the Bottom," *Engineering and Science*, vol. 23, no. 5, pp. 22–36, 1960, DOI: 10.1201/9780429500459.

[4] S. Prasad, V. Kumar, S. Kirubanandam, and A. Barhoum, *Engineered nanomaterials: Nanofabrication and surface functionalization*. Elsevier Inc., 2018. DOI: 10.1016/B978-0-323-51254-1.00011-7.

[5] V. Gubala *et al.*, "Engineered nanomaterials and human health: Part 1. Preparation, functionalization and characterization (IUPAC Technical Report)," *Pure and Applied Chemistry*, vol. 90, no. 8, pp. 1283–1324, 2018, DOI: 10.1515/pac-2017-0101.

[6] S. Bayda, M. Adeel, T. Tuccinardi, M. Cordani, and F. Rizzolio, "The History of Nanoscience and Nanotechnology: From Chemical–Physical Applications to Nanomedicine," *Molecules*, vol. 25, no. 1, p. 112, Dec. 2019, DOI: 10.3390/molecules25010112.

[7] A. Barhoum *et al.*, "Review on Natural, Incidental, Bioinspired, and Engineered Nanomaterials: History, Definitions, Classifications, Synthesis, Properties, Market, Toxicities, Risks, and Regulations," *Nanomaterials*, vol. 12, no. 2, 2022, DOI: 10.3390/nano12020177.

[8] I. Khan, K. Saeed, and I. Khan, "Nanoparticles: Properties, applications and toxicities," *Arabian Journal of Chemistry*, vol. 12, no. 7, pp. 908–931, Nov. 2019, DOI: 10.1016/j.arabjc.2017.05.011.

[9] Cytodiagnostics, "Introduction to Gold Nanoparticle Characterization." https://www.cytodiagnostics.com/pages/introduction-to-gold-nanoparticle-characterization

[10] "Duomo di Milano." https://www.duomomilano.it/en/event/2019/08/15/feast-of-the-assumption-of-the-blessed-virgin-mary/266/

[11] NanoComposix, "Plasmonic Nanoparticles." https://nanocomposix.com/collections/application-plasmonic

[12] A. A. AbdelHamid, A. Mendoza-Garcia, and J. Y. Ying, "Advances in and prospects of nanomaterials' morphological control for lithium rechargeable batteries," *Nano Energy*, vol. 93, p. 106860, 2022, DOI: 10.1016/j.nanoen.2021.106860.

[13] J. Jeevanandam, A. Barhoum, Y. S. Chan, A. Dufresne, and M. K. Danquah, "Review on nanoparticles and nanostructured materials: History, sources, toxicity and regulations," *Beilstein Journal of Nanotechnology*, vol. 9, no. 1, pp. 1050–1074, 2018, DOI: 10.3762/bjnano.9.98.

[14] P. García Acevedo *et al.*, "Fluorescent Single-Core and Multi-Core Nanoprobes as Cell Trackers and Magnetic Nanoheaters," *Magnetochemistry*, vol. 8, no. 8, p. 83, 2022, DOI:

10.3390/magnetochemistry8080083.

[15] A. V. Samrot, C. S. Sahithya, J. Selvarani A, S. K. Purayil, and P. Ponnaiah, “A review on synthesis, characterization and potential biological applications of superparamagnetic iron oxide nanoparticles,” *Current Research in Green and Sustainable Chemistry*, vol. 4, no. November 2020, p. 100042, 2021, DOI: 10.1016/j.crgsc.2020.100042.

[16] C. Janko *et al.*, “Functionalized Superparamagnetic Iron Oxide Nanoparticles (SPIONs) as Platform for the Targeted Multimodal Tumor Therapy,” *Frontiers in Oncology*, vol. 9, no. FEB, pp. 1–9, Feb. 2019, DOI: 10.3389/fonc.2019.00059.

[17] Y. Moldes-Diz *et al.*, “A novel enzyme catalysis reactor based on superparamagnetic nanoparticles for biotechnological applications,” *Journal of Environmental Chemical Engineering*, vol. 6, no. 5, pp. 5950–5960, Oct. 2018, DOI: 10.1016/j.jece.2018.09.014.

[18] Y. Moldes-Diz *et al.*, “Development of a Superparamagnetic Laccase Nanobiocatalyst for the Enzymatic Biotransformation of Xenobiotics,” *Journal of Environmental Engineering*, vol. 144, no. 3, pp. 1–8, 2018, DOI: 10.1061/(asce)ee.1943-7870.0001333.

[19] W. Park, H. Shin, B. Choi, W. K. Rhim, K. Na, and D. Keun Han, “Advanced hybrid nanomaterials for biomedical applications,” *Progress in Materials Science*, vol. 114, no. May 2018, p. 100686, 2020, DOI: 10.1016/j.pmatsci.2020.100686.

[20] V. Gubala *et al.*, “Engineered nanomaterials and human health: Part 2. Applications and nanotoxicology (IUPAC Technical Report),” *Pure and Applied Chemistry*, vol. 90, no. 8, pp. 1325–1356, Aug. 2018, DOI: 10.1515/pac-2017-0102.

[21] G. Sanità, B. Carrese, and A. Lamberti, “Nanoparticle Surface Functionalization: How to Improve Biocompatibility and Cellular Internalization,” *Frontiers in Molecular Biosciences*, vol. 7, no. November. Nov. 26, 2020. DOI: 10.3389/fmolb.2020.587012.

[22] D. Walczyk, F. B. Bombelli, M. P. Monopoli, I. Lynch, and K. A. Dawson, “What the cell ‘sees’ in bionanoscience,” *Journal of the American Chemical Society*, vol. 132, no. 16, pp. 5761–5768, 2010, DOI: 10.1021/ja910675v.

[23] M. T. Manzari, Y. Shamay, H. Kiguchi, N. Rosen, M. Scaltriti, and D. A. Heller, “Targeted drug delivery strategies for precision medicines,” *Nature Reviews Materials*, vol. 6, no. 4, pp. 351–370, 2021, DOI: 10.1038/s41578-020-00269-6.

[24] V. Harish *et al.*, “Review on Nanoparticles and Nanostructured Materials: Bioimaging, Biosensing, Drug Delivery, Tissue Engineering, Antimicrobial, and Agro-Food Applications,” *Nanomaterials*, vol. 12, no. 3, p. 457, Jan. 2022, DOI: 10.3390/nano12030457.

[25] NIST, “Metrology for Nanomaterials in Medicine.” https://www.nist.gov/programs-projects/metrology-nanomaterials-medicine

[26] P. Liu, G. Chen, and J. Zhang, “A Review of Liposomes as a Drug Delivery System: Current Status of Approved Products, Regulatory Environments, and Future Perspectives,” *Molecules*, vol. 27, no. 4, 2022, DOI: 10.3390/molecules27041372.

[27] P. Nakhaei *et al.*, “Liposomes: Structure, Biomedical Applications, and Stability Parameters With Emphasis on Cholesterol,” *Frontiers in Bioengineering and Biotechnology*, vol. 9, no. September, pp. 1–23, 2021, DOI: 10.3389/fbioe.2021.705886.

[28] E. D. Castañeda-Reyes, M. de J. Perea-Flores, G. Davila-Ortiz, Y. Lee, and E. G. de Mejia, “Development, characterization and use of liposomes as amphipathic transporters of bioactive compounds for melanoma treatment and reduction of skin inflammation: A review,” *International Journal of Nanomedicine*, vol. 15, pp. 7627–7650, 2020, DOI: 10.2147/IJN.S263516.

[29] V. R. da Costa *et al.*, "Exosomes in the Tumor Microenvironment: From Biology to Clinical Applications," *Cells*, vol. 10, no. 10, p. 2617, Oct. 2021, DOI: 10.3390/cells10102617.

[30] L. van der Koog, T. B. Gandek, and A. Nagelkerke, "Liposomes and Extracellular Vesicles as Drug Delivery Systems: A Comparison of Composition, Pharmacokinetics, and Functionalization," *Advanced Healthcare Materials*, vol. 11, no. 5, 2022, DOI: 10.1002/adhm.202100639.

[31] T. Skotland, K. Sagini, K. Sandvig, and A. Llorente, "An emerging focus on lipids in extracellular vesicles," *Advanced Drug Delivery Reviews*, vol. 159, pp. 308–321, 2020, DOI: 10.1016/j.addr.2020.03.002.

[32] C. Théry *et al.*, "Minimal information for studies of extracellular vesicles 2018 (MISEV2018): a position statement of the International Society for Extracellular Vesicles and update of the MISEV2014 guidelines," *Journal of Extracellular Vesicles*, vol. 7, no. 1, p. 1535750, Dec. 2018, DOI: 10.1080/20013078.2018.1535750.

[33] M. Battistelli and E. Falcieri, "Apoptotic bodies: Particular extracellular vesicles involved in intercellular communication," *Biology*, vol. 9, no. 1, 2020, DOI: 10.3390/biology9010021.

[34] E. Woith, G. Fuhrmann, and M. F. Melzig, "Extracellular vesicles—connecting kingdoms," *International Journal of Molecular Sciences*, vol. 20, no. 22. p. 5695, Nov. 14, 2019. DOI: 10.3390/ijms20225695.

[35] J. J. Richardson and H. Ejima, "Surface Engineering of Extracellular Vesicles through Chemical and Biological Strategies †," *Chemistry of Materials*, vol. 31, no. 7, pp. 2191–2201, 2019, DOI: 10.1021/acs.chemmater.9b00050.

[36] M. Richter, P. Vader, and G. Fuhrmann, "Approaches to surface engineering of extracellular vesicles," *Advanced Drug Delivery Reviews*, vol. 173, pp. 416–426, Jun. 2021, DOI: 10.1016/j.addr.2021.03.020.

[37] H. Choi, Y. Choi, H. Y. Yim, A. Mirzaaghasi, J. K. Yoo, and C. Choi, "Biodistribution of Exosomes and Engineering Strategies for Targeted Delivery of Therapeutic Exosomes," *Tissue Engineering and Regenerative Medicine*, vol. 18, no. 4, pp. 499–511, 2021, DOI: 10.1007/s13770-021-00361-0.

[38] J. P. K. Armstrong, M. N. Holme, and M. M. Stevens, "Re-Engineering Extracellular Vesicles as Smart Nanoscale Therapeutics," *ACS Nano*, vol. 11, no. 1, pp. 69–83, 2017, DOI: 10.1021/acsnano.6b07607.

[39] H. Qi *et al.*, "Blood Exosomes Endowed with Magnetic and Targeting Properties for Cancer Therapy," *ACS Nano*, vol. 10, no. 3, pp. 3323–3333, 2016, DOI: 10.1021/acsnano.5b06939.

[40] I. Parolini *et al.*, "Microenvironmental pH is a key factor for exosome traffic in tumor cells," *Journal of Biological Chemistry*, vol. 284, no. 49, pp. 34211–34222, 2009, DOI: 10.1074/jbc.M109.041152.

[41] P. Meers, T. Mealy, N. Pavlotsky, and A. I. Tauber, "Annexin I-mediated vesicular aggregation: mechanism and role in human neutrophils," *Biochemistry*, vol. 31, no. 28, pp. 6372–6382, Jul. 1992, DOI: 10.1021/bi00143a003.

[42] J. L. Hood, M. J. Scott, and S. A. Wickline, "Maximizing exosome colloidal stability following electroporation," *Analytical Biochemistry*, vol. 448, no. 1, pp. 41–49, 2014, DOI: 10.1016/j.ab.2013.12.001.

[43] L. Zhu, N. Xu, Z. L. Zhang, and T. C. Zhang, "Cell derived extracellular vesicles: From isolation to functionalization and biomedical applications," *Biomaterials Science*, vol. 7, no. 9, pp. 3552–3565, 2019, DOI: 10.1039/c9bm00580c.

[44] B. György, M. E. Hung, X. O. Breakefield, and J. N. Leonard, "Therapeutic Applications of Extracellular Vesicles: Clinical Promise and Open Questions," *Annual Review of Pharmacology and Toxicology*, vol. 55, no. 1, pp. 439–464, Jan. 2015, DOI: 10.1146/annurev-pharmtox-010814-124630.

[45] S. Araujo-Abad, M. Saceda, and C. de Juan Romero, "Biomedical application of small extracellular

vesicles in cancer treatment," *Advanced Drug Delivery Reviews*, vol. 182, p. 114117, 2022, DOI: 10.1016/j.addr.2022.114117.

[46] G. Adamo *et al.*, "Nanoalgosomes: Introducing extracellular vesicles produced by microalgae," *Journal of Extracellular Vesicles*, vol. 10, no. 6, 2021, DOI: 10.1002/jev2.12081.

[47] S. Picciotto *et al.*, "Isolation of extracellular vesicles from microalgae: Towards the production of sustainable and natural nanocarriers of bioactive compounds," *Biomaterials Science*, vol. 9, no. 8, pp. 2917–2930, 2021, DOI: 10.1039/d0bm01696a.

[48] S. Picciotto *et al.*, "Extracellular Vesicles From Microalgae: Uptake Studies in Human Cells and Caenorhabditis elegans," *Frontiers in Bioengineering and Biotechnology*, vol. 10, no. March, pp. 1–11, 2022, DOI: 10.3389/fbioe.2022.830189.

[49] P. Arosio, "Biochemical Engineering Laboratory." https://arosiogroup.ethz.ch/

[50] A. Zendrini *et al.*, "Augmented COlorimetric NANoplasmonic (CONAN) Method for Grading Purity and Determine Concentration of EV Microliter Volume Solutions," *Frontiers in Bioengineering and Biotechnology*, vol. 7, no. February, pp. 1–10, 2020, DOI: 10.3389/fbioe.2019.00452.

[51] D. Maiolo *et al.*, "Colorimetric nanoplasmonic assay to determine purity and titrate extracellular vesicles," *Analytical Chemistry*, vol. 87, no. 8, pp. 4168–4176, 2015, DOI: 10.1021/ac504861d.

[52] R. L. Barbieri, "Breast," in *Yen & Jaffe's Reproductive Endocrinology: Physiology, Pathophysiology, and Clinical Management: Eighth Edition*, vol. 419, Elsevier, 2019, pp. 248-255.e3. DOI: 10.1016/B978-0-323-47912-7.00010-X.

[53] S. M. Fragomeni, A. Sciallis, and J. S. Jeruss, "Molecular Subtypes and Local-Regional Control of Breast Cancer.," *Surgical oncology clinics of North America*, vol. 27, no. 1, pp. 95–120, Oct. 2018, DOI: 10.1016/j.soc.2017.08.005.

[54] M. J. Haney, Y. Zhao, Y. S. Jin, and E. V. Batrakova, "Extracellular Vesicles as Drug Carriers for Enzyme Replacement Therapy to Treat CLN2 Batten Disease: Optimization of Drug Administration Routes," *Cells*, vol. 9, no. 5, p. 1273, May 2020, DOI: 10.3390/cells9051273.

[55] W. S. Liao *et al.*, "Targeting EGFR of triple-negative breast cancer enhances the therapeutic efficacy of paclitaxel- and cetuximab-conjugated nanodiamond nanocomposite," *Acta Biomaterialia*, vol. 86, pp. 395–405, 2019, DOI: 10.1016/j.actbio.2019.01.025.

[56] S. I. Ohno *et al.*, "Systemically injected exosomes targeted to EGFR deliver antitumor microrna to breast cancer cells," *Molecular Therapy*, vol. 21, no. 1, pp. 185–191, 2013, DOI: 10.1038/mt.2012.180.

[57] S. Yue, Y. Zhang, Y. Wei, R. Haag, H. Sun, and Z. Zhong, "Cetuximab-Polymersome-Mertansine Nanodrug for Potent and Targeted Therapy of EGFR-Positive Cancers," *Biomacromolecules*, vol. 23, no. 1, pp. 100–111, 2022, DOI: 10.1021/acs.biomac.1c01065.

[58] D. Patel *et al.*, "Monoclonal antibody cetuximab binds to and down-regulates constitutively activated epidermal growth factor receptor vIII on the cell surface," *Anticancer Research*, vol. 27, no. 5 A, pp. 3355–3366, 2007.

[59] S. Höbel, D. Vornicescu, M. Bauer, D. Fischer, M. Keusgen, and A. Aigner, "A novel method for the assessment of targeted PEI-based nanoparticle binding based on a static surface plasmon resonance system," *Analytical Chemistry*, vol. 86, no. 14, pp. 6827–6835, 2014, DOI: 10.1021/ac402001q.

[60] J. Che *et al.*, "A new approach for pharmacokinetics of single-dose cetuximab in rhesus monkeys by surface plasmon resonance biosensor," *Journal of Pharmaceutical and Biomedical Analysis*, vol. 50, no. 2, pp. 183–188, 2009, DOI: 10.1016/j.jpba.2009.04.009.

[61] H. Lu, X. Li, Z. Luo, J. Liu, and Z. Fan, "Cetuximab Reverses the Warburg Effect by Inhibiting HIF-1–

Regulated LDH-A," *Molecular Cancer Therapeutics*, vol. 12, no. 10, pp. 2187–2199, Oct. 2013, DOI: 10.1158/1535-7163.MCT-12-1245.

[62] F. L. Graham, J. Smiley, W. C. Russell, and R. Nairn, "Characteristics of a human cell line transformed by DNA from human adenovirus type 5," *Journal of General Virology*, vol. 36, no. 1, pp. 59–72, 1977, DOI: 10.1099/0022-1317-36-1-59.

[63] C. Paganini *et al.*, "Rapid Characterization and Quantification of Extracellular Vesicles by Fluorescence-Based Microfluidic Diffusion Sizing," *Advanced Healthcare Materials*, vol. 11, no. 5, pp. 1–6, 2022, DOI: 10.1002/adhm.202100021.

[64] F. Rossignoli *et al.*, "Isolation, Characterization, and Transduction of Endometrial Decidual Tissue Multipotent Mesenchymal Stromal/Stem Cells from Menstrual Blood," *BioMed Research International*, vol. 2013, pp. 1–14, 2013, DOI: 10.1155/2013/901821.

[65] V. Álvarez *et al.*, "The immunomodulatory activity of extracellular vesicles derived from endometrial mesenchymal stem cells on CD4+ T cells is partially mediated by TGFbeta," *Journal of Tissue Engineering and Regenerative Medicine*, vol. 12, no. 10, pp. 2088–2098, Aug. 2018, DOI: 10.1002/term.2743.

[66] G. Robert R, L, "Culture of phytoplankton for feeding marine invertebrates," *Culture of marine invertebrate animals*, pp. 29–60, 1975.

[67] L. Paolini *et al.*, "Fourier-transform Infrared (FT-IR) spectroscopy fingerprints subpopulations of extracellular vesicles of different sizes and cellular origin," *Journal of Extracellular Vesicles*, vol. 9, no. 1, p. 1741174, Sep. 2020, DOI: 10.1080/20013078.2020.1741174.

[68] A. Zendrini *et al.*, "Supplementary material Augmented COlorimetric NANoplasmonic (CONAN) Method for Grading Purity and Determine Concentration of EV Microliter Volume Solutions," *Frontiers in Bioengineering and Biotechnology*, vol. 7, 2020, DOI: 10.3389/fbioe.2019.00452.

[69] R. Massart, "Preparation of aqueous magnetic liquids in alkaline and acidic media," *IEEE Transactions on Magnetics*, vol. 17, no. 2, pp. 1247–1248, Mar. 1981, DOI: 10.1109/TMAG.1981.1061188.

[70] Y. Fang, W. S. Loc, W. Lu, and J. Fang, "Synthesis of In2O3@SiO2 core-shell nanoparticles with enhanced deeper energy level emissions of In 2O3," *Langmuir*, vol. 27, no. 23, pp. 14091–14095, Dec. 2011, DOI: 10.1021/la203333d.

[71] Y. Han, J. Jiang, S. S. Lee, and J. Y. Ying, "Reverse microemulsion-mediated synthesis of silica-coated gold and silver nanoparticles," *Langmuir*, vol. 24, no. 11, pp. 5842–5848, Jun. 2008, DOI: 10.1021/la703440p.

[72] Z. Zhou *et al.*, "Anisotropic shaped iron oxide nanostructures: Controlled synthesis and proton relaxation shortening effects," *Chemistry of Materials*, vol. 27, no. 9, pp. 3505–3515, 2015, DOI: 10.1021/acs.chemmater.5b00944.

[73] U. Capasso Palmiero *et al.*, "Use of RAFT macro-surfmers for the synthesis of transparent aqueous colloids with tunable interactions," *Soft Matter*, vol. 13, no. 37, pp. 6439–6449, 2017, DOI: 10.1039/c7sm01084b.

[74] S. T. Camli, F. Buyukserin, O. Balci, and G. G. Budak, "Size controlled synthesis of sub-100nm monodisperse poly(methylmethacrylate) nanoparticles using surfactant-free emulsion polymerization," *Journal of Colloid and Interface Science*, vol. 344, no. 2, pp. 528–532, Apr. 2010, DOI: 10.1016/j.jcis.2010.01.041.

[75] J. Turkevich, P. C. Stevenson, and J. Hillier, "A study of the nucleation and growth processes in the synthesis of colloidal gold," *Discussions of the Faraday Society*, vol. 11. pp. 55–75, 1951. DOI: 10.1039/DF9511100055.

[76] W. Haiss, N. T. K. Thanh, J. Aveyard, and D. G. Fernig, “Determination of size and concentration of gold nanoparticles from UV-Vis spectra,” *Analytical Chemistry*, vol. 79, no. 11, pp. 4215–4221, 2007, DOI: 10.1021/ac0702084.

[77] W. Haiss, N. T. K. Thanh, J. Aveyard, and D. G. Fernig, “Supporting Information. Determination of Size and Concentration of Gold Nanoparticles from UV/vis Spectra,” *Scanning Electron Microscopy*, 2007.

[78] C. Théry, S. Amigorena, G. Raposo, and A. Clayton, “Isolation and Characterization of Exosomes from Cell Culture Supernatants and Biological Fluids,” *Current Protocols in Cell Biology*, vol. 30, no. 1, pp. 1–29, 2006, DOI: 10.1002/0471143030.cb0322s30.

[79] S. Busatto *et al.*, “Tangential flow filtration for highly efficient concentration of extracellular vesicles from large volumes of fluid,” *Cells*, vol. 7, no. 12. 2018. DOI: 10.3390/cells7120273.

[80] C. Paganini, U. Capasso Palmiero, G. Pocsfalvi, N. Touzet, A. Bongiovanni, and P. Arosio, “Scalable Production and Isolation of Extracellular Vesicles: Available Sources and Lessons from Current Industrial Bioprocesses,” *Biotechnology Journal*, vol. 14, no. 10, 2019, DOI: 10.1002/biot.201800528.

[81] E. D. Sverdlov, “Amedeo Avogadro’s cry: What is 1μg of exosomes?,” *BioEssays*, vol. 34, no. 10, pp. 873–875, Oct. 2012, DOI: 10.1002/bies.201200045.

[82] M. Stobiecka and M. Hepel, “Multimodal coupling of optical transitions and plasmonic oscillations in rhodamine B modified gold nanoparticles,” *Physical Chemistry Chemical Physics*, vol. 13, no. 3, pp. 1131–1139, 2011, DOI: 10.1039/c0cp00553c.

[83] J. Zhang, Z. Huang, Y. Xie, and X. Jiang, “Modulating the catalytic activity of gold nanoparticles using amine-terminated ligands,” *Chemical Science*, vol. 13, no. 4, pp. 1080–1087, 2022, DOI: 10.1039/d1sc05933e.

[84] C. Liu *et al.*, “Microfluidic Sonication to Assemble Exosome Membrane-Coated Nanoparticles for Immune Evasion-Mediated Targeting,” *Nano Letters*, vol. 19, no. 11, pp. 7836–7844, 2019, DOI: 10.1021/acs.nanolett.9b02841.

[85] L. Caselli *et al.*, “A plasmon-based nanoruler to probe the mechanical properties of synthetic and biogenic nanosized lipid vesicles,” *Nanoscale Horizons*, vol. 6, no. 7, pp. 543–550, 2021, DOI: 10.1039/d1nh00012h.

[86] L. Sadovska *et al.*, “A novel 3D heterotypic spheroid model for studying extracellular vesicle-mediated tumour and immune cell communication,” *Biochemical and Biophysical Research Communications*, vol. 495, no. 2, pp. 1930–1935, Jan. 2018, DOI: 10.1016/j.bbrc.2017.12.072.

[87] H. Ji, “Lysis of cultured cells for immunoprecipitation,” *Cold Spring Harbor Protocols*, vol. 5, no. 8, 2010, DOI: 10.1101/pdb.prot5466.

[88] D. B. Nguyen *et al.*, “Characterization of Microvesicles Released from Human Red Blood Cells,” *Cellular Physiology and Biochemistry*, vol. 38, no. 3, pp. 1085–1099, 2016, DOI: 10.1159/000443059.

[89] W. M. Usman *et al.*, “Efficient RNA drug delivery using red blood cell extracellular vesicles,” *Nature Communications*, vol. 9, no. 1, p. 2359, Dec. 2018, DOI: 10.1038/s41467-018-04791-8.

[90] K. W. Witwer *et al.*, “Standardization of sample collection, isolation and analysis methods in extracellular vesicle research,” *Journal of Extracellular Vesicles*, vol. 2, no. 1, 2013, DOI: 10.3402/jev.v2i0.20360.

[91] F. A. W. Coumans *et al.*, “Methodological guidelines to study extracellular vesicles,” *Circulation Research*, vol. 120, no. 10. pp. 1632–1648, 2017. DOI: 10.1161/CIRCRESAHA.117.309417.

[92] I. Grossi *et al.*, “MicroRNA-34a-5p expression in the plasma and in its extracellular vesicle fractions in subjects with Parkinson’s disease: An exploratory study,” *International Journal of Molecular Medicine*,

vol. 47, no. 2, pp. 533–546, 2021, DOI: 10.3892/ijmm.2020.4806.

[93] G. Di Noto G. *et al.*, “Immunoglobulin free light chains and GAGs mediate multiple myeloma extracellular vesicles uptake and secondary NfκB nuclear translocation,” *Frontiers in Immunology*, vol. 5, no. OCT, 2014, DOI: 10.3389/fimmu.2014.00517.

[94] L. Paolini *et al.*, “Residual matrix from different separation techniques impacts exosome biological activity,” *Scientific Reports*, vol. 6, no. 1, p. 23550, Sep. 2016, DOI: 10.1038/srep23550.

[95] A. Radeghieri *et al.*, “Active antithrombin glycoforms are selectively physiosorbed on plasma extracellular vesicles,” *bioRxiv*, pp. 1–20, 2021, DOI: 10.1101/2021.07.16.452649.

[96] G. E. Healthcare, “Biacore ™ X100”.

[97] A. Zendrini, G. Guerra, K. Sagini, T. Vagner, D. Di Vizio, and P. Bergese, “On the surface-to-bulk partition of proteins in extracellular vesicles,” *Colloids and Surfaces B: Biointerfaces*, vol. 218, no. April, p. 112728, 2022, DOI: 10.1016/j.colsurfb.2022.112728.

[98] W. T. Kuo *et al.*, “Quantitative analysis of ligand-EGFR interactions: A platform for screening targeting molecules,” *PLoS ONE*, vol. 10, no. 2, 2015, DOI: 10.1371/journal.pone.0116610.